Towards a Net-zero Carbon Energy System: High Efficiency Photovoltaics and Electrocatalysts

Thesis by

Stefan Omelchenko

In Partial Fulfillment of the Requirements for
the degree of
Doctor of Philosophy

CALIFORNIA INSTITUTE OF TECHNOLOGY
Pasadena, California

2019
Defended September 27, 2018

Stefan Thomas Omelchenko
ORCID: 0000-0003-1104-9291

"Adventure is when everything goes wrong. That's when the adventure starts."
- Yvon Chouinoard

To those who don't know how they got here or where they're going. Welcome to an adventure.

Acknowledgements

I am indebted to many people, without whom I would not be here writing this thesis.

First, I would like to thank my advisors Harry Atwater and Nathan Lewis. Sir Isaac Newton once said "If I have seen further it is by standing on the shoulders of giants," and that is certainly applicable for my relationship with Harry and Nate, whose breadth of knowledge seem limitless and whose support and inspiration is also so. I am incredibly grateful to have been in your groups and been given the freedom to make (many) mistakes and find my own way.

I would also like to thank the rest of my committee, Professors Bill Johnson and Keith Schwab for their helpful discussion and time in reviewing this thesis. Professor Johnson is an incredible lecturer and the deep insights into thermodynamics in his courses proved to be an invaluable foundation in many of my research projects. I am honored to have Professor Schwab as the chair of my committee and as a friend whom I can always turn to for academic and professional advice and the latest in garbage culture.

My road to Caltech started in high school where I was fortunate enough to have stellar calculus and physics teachers. I would like to thank Mr. Poska and especially, Mr. Walz for showing me the intimate connections math and physics have in our world and for inspiring me – one person can have a huge difference in your life.

My research at Caltech would not have been possible without the guidance of my mentor, Yulia Tolstova, The Fearless Leader. As a scientist, she taught me to be skeptical of everything and be meticulously detail oriented. As a friend, I am grateful for all the cups of tea and for the lessons you taught me about our motherland and Ukranian vodka.

The works in this thesis would not have been possible alone and I am thankful for my colleagues and co-authors: Samantha Wilson, Raymond Blackwell, Amanda Shing, Carlos Read, Michael Lictherman, Heping Shen, Daniel Jacobs, Joeson Wong, and all the others who contributed to my studies.

I would like to thank everyone in the Atwater Group and the Lewis Group for making our groups the two best on campus and for providing friendship and scientific guidance throughout my time at Caltech. I am particularly thankful for those who put up with me on a daily basis in G131. Xinghao

Zhou, Jingjing Jiang, Weilai Yu, Katie Hamann, Madeline Meier, Katie Chen and Kathleen Kennedy, thank you for making our office so clearly superior to G135. I would like to thank Erik Verlage for daring himself to wax his legs and then actually doing it when he missed his deadline. Ke Sun was an invaluable office resource who, no matter how busy, would help me solve any problem I might have. I would also like to thank Paul Nuñez for bearing the brunt of my presence and sitting next to me for 5 years and enlightening me to alternative lifestyles where checking email is taboo. Although the faces in the office changed a lot over my tenure, Kimberly Papadontanakis was there with me for the long haul. I will be hard pressed to find an office mate again who is as cynical and as giving and kind as you. If you were to ever leave, the Lewis Group would miss you dearly. I would also like to thank Katherine "Chatty Kathy" Rinaldi for the cups of tea we shared.

Caltech and (the Lewis and Atwater Groups in particular) would not run without the work of many people behind the scenes. This is no more evident than in Harry's administrators who function as schedulers, therapists, advisors, and genuinely make life easier for all of the A-Team – thank you to Jennfier Blakenship, Liz Jennings, and Lyann Lau. I would also like to thank Barbara Miralles who plays a similar role in the Lewis Group and without whom the group would be lost. I would especially like to thank Jonathan Gross, Tiffany Kimoto, and Christy Jenstad for being friends foremost. People like you are the reason that Caltech is a special place.

I am most indebted to my family and friends. Thank you to my friends at Caltech who helped me escape life as a graduate student and helped keep me grounded. The soccer crew of Chris Kucharczyk, Saneyuki Ohno, Réda Boumasmoud, Ottman Tertuliano, Marius Lemm, Leon "The Knee" Harding, and Philipp Moesta were always down for a game (or a beer) and will always be a source of international companionship while watching a match. During the work day, my friends at lunch were always a source of a midday escape and interesting conversation – thank you to Mikhail Hanewich-Hollatz, Vatsal "My Wife" Jahlani, and Nathan Schoepp for always being there and to everyone else that I have shared lunch with over the years. Thanks to Sisir Yalamanchili who was helped distract me from the doldrums of RCA cleaning silicon with silly YouTube videos, music, and philosophical discussions and for also being my travel partners to conferences and for making me part of your family in India. Thanks to Azhar Carim for being the Czar of Liibations and always being down to watch college football and to Fadl Saadi for always making me laugh and for being my pseudo-mentor in the Lewis Group. I must also thank my roommates Thom Bohdanowicz, Fish Mattman, and Christian Fagan who have managed to survive living with me and tell the tale. Nafeesa Andrabi, Cody Finke, Justin Jasper, Marisa Palucis, Cooper Jasper, and Matt Shaner were always down to help

me get rad and teach me a thing or two during the long car rides to and from climbing, skiing, trail running, or mountain biking. Nafeesa and Cody are owed special thanks for always accepting me as their constant third wheel. Thank you to Thuy Jacobson for always being down to work out, get rad, and eat way too much food afterwards and of course, thank you for all your future healing once you are a certified PT. I owe the love of my life, Teddy Albertson, and the love of his life, Lorinda Dajose, for always being there for me and coming with me on climbing trips even when we had to walk really far ("We're almost there Lori"). I cannot forget Greeeeeg Smetana even if he is lurking quietly in the shadows – you were my first friend at Caltech and continue to be one of my best. Out of all my friends, I owe Will and Sarah Whitney the most; thank you for simultaneously being my best friends, life coaches, adventure partners, and for sheltering me on your couch for almost half a year– I will forever owe you. But I am certainly most indebted to my parents without whom none of this would have been possible. Thank you so much for your love and support over the years. If anything, life has taught me that I am incredibly lucky to have such good role models and to be your son. Thank you to Michael and Monica for being the best siblings (and friends) that I could ever ask for and for being the test subjects on which I honed my skills for annoyance. I love you all.

Stefan Omelchenko
September 2018
Pasadena, CA

Abstract

Modern society is dependent on energy. Despite increases in energy efficiency, human development and economic goals are expected to increase the global demand for energy by almost 30% in the next 20 years. At the same time, anthropogenic carbon dioxide emissions must approach zero to stabilize global temperatures below the 2°C target set out by international climate agreements. Realizing a net-zero carbon energy system will depend on the development of a highly reliable, sustainable electricity grid to power society and the ability to produce chemicals and fuels in a carbon-free manner. Developing cheap, efficient solar photovoltaics and highly active and selective electrocatalysts is thus pivotal to achieving this goal.

In this work, we address issues limiting photovoltaics and electrocatalysts. Our work on photovoltaics analyzes two effects often neglected in the evaluation of efficiency limits for photovoltaic materials. We show that the shape of the band tail and, in particular, the extent of sub-gap absorption, controls the open-circuit voltage, emission, and ultimately the achievable efficiency of a solar cell. These findings are generalizable to any luminescent material and our analysis suggests that efficiency limits for a material can be determined through simple experimental characterization. In addition, we develop a device physics model which accounts for the presence of excitons, which are the fundamental excitation in a host of emerging photovoltaic materials. A case study in cuprous oxide shows that excitonic effects can play a large role in the device physics of materials with large exciton binding energies and that standard models can drastically underestimate the efficiency limits in these systems. Our work on photovoltaics, culminates in the realization of a novel device architecture for tandem silicon/perovskite solar cells that opens the possibility of achieving efficiencies >30%. Finally, we develop a method to tune the catalytic activity of electrocatalysts for the oxygen-evolution and chlorine-evolution reactions. Our method is based on group electronegativity and is likely generalizable to other reactions and catalysts. The analyses and technologies developed herein are promising steps towards a zero-carbon energy system.

Published Content and Contribution

Portions of this thesis have been drawn from the following publications

S. T. Omelchenko*, J. Wong*, N. S. Lewis, H. A. Atwater, "Effects of imperfect bandgaps and disorder on photovoltaic efficiency," *in preparation.*
S.T.O and J.W. conceived the theory, designed the model, and performed the simulations for this work along with co-authors. The manuscript was prepared by S.T.O and J.W. with input from co-authors.

H. Shen*, **S. T. Omelchenko***, D. Jacobs*, S. Yalamanchili*, Y. Wan, Y. Wu, P. Phang, T. Duong, J. Peng, Y. Yin, D. Yan, C. Samundsett, N. Wu, T. P. White, G. G. Andersson, N. S. Lewis, K. R. Catchpole, "Ohmic p-Si/titania contact enables high efficiency, interconnect-free monolithic perovskite/silicon tandem solar cells", *Science Advances,* 4, 12, 2019
doi: 10.1126/sciadv.aau9711
S.T.O, S.Y., and N.S.L. conceived of the device structure for this work. S.T.O, S.Y., H.S., and D.J. designed and fabricated the structure, conceived of the experiments, and conducted the measurements, along with co-authors. The manuscript was prepared by H.S., S.T.O., S.Y., and D.J. with input from co-authors.

C. E. Finke, **S. T. Omelchenko**, J. Jasper, M. F. Lichterman, C. G. Read, N. S. Lewis, M. R. Hoffmann, "Enhancing the activity of oxygen-evolution and chlorine-evolution electrocatalysts by atomic layer deposition of TiO_2," *Energy Environ. Sci,* 12, 358, 2019
doi: 10.1039/c8ee02351d
S.T.O contributed to the concept of this work along with co-authors. S.T.O. assisted with the design of experiments, collection of measurements, and analysis of data. The manuscript was prepared by C.F. and S.T.O. with input from co-authors.

S. T. Omelchenko, Y. Tolstova, H. A. Atwater, Jr., N. S. Lewis, "Excitonic Effects in Emerging Semiconductors: A Case Study in Cu_2O", *ACS Energy Lett.*, 2, 431, 2017
doi: 10.1021/acsenergylett.6b00704
S.T.O was responsible for the conception of this work along with co-authors. S.T.O. designed the experiments, collected the measurements, and analyzed the data. The manuscript was prepared by S.T.O. and Y.T. with input from co-authors.

Y. Tolstova, **S. T. Omelchenko**, R. E. Blackwell, A. M. Shing, H. A. Atwater, Jr., "Polycrystalline Cu_2O Photovoltaic Devices Incorporating Zn(O,S) Window Layers", *Sol. Energy Mater. and Sol. Cells*, 160, 340, 2017
doi: 10.1016/j.solmat.2016.10.049
S.T.O contributed to the concept of this work along with co-authors. STO assisted with device fabrication, design of experiments, collection of measurements, and analysis of data. The manuscript was prepared by Y.T. and S.T.O. with input from co-authors.

S. T. Omelchenko, Y. Tolstova, H. A. Atwater, N. S. Lewis, "Excitonic Effects in Materials with Large Excitonic Binding Energies," *43nd IEEE PVSC* (2016)
doi: 10.1109/PVSC.2016.7750347
S.T.O was responsible for the conception of this work along with co-authors. S.T.O. designed the experiments, collected the measurements, and analyzed the data. The manuscript was prepared by S.T.O. and Y.T. with input from co-authors.

S. T. Omelchenko, Y. Tolstova, S. S. Wilson, H. A. Atwater, N. S. Lewis, "Single crystal Cu_2O Photovoltaics by the floating zone method," *42nd IEEE PVSC* (2015)
doi: 10.1109/PVSC.2015.7355920
S.T.O was responsible for the conception of this work along with co-authors. S.T.O. grew the samples, designed the experiments, collected the measurements, and analyzed the data. The manuscript was prepared by S.T.O. and Y.T. with input from co-authors.

Table of Contents

Acknowledgements ..... **iii**

Abstract ..... **vii**

List of Publications ..... Error! Bookmark not defined.

Table of Contents ..... **x**

List of Figures ..... **xiii**

List of Tables ..... **xxii**

Chapter 1 Introduction **1**
1.1 A Net-Zero Carbon Emission Energy System 1
1.2 Challenges to Realizing Net-Zero Carbon 3
1.3 Solar Photovoltaics 4
1.3.1 The Solar Cell Market 4
1.3.2 Basics Operating Principles of Photovoltaics 6
1.4 Electrocatalysis for Production of Fuels and Chemicals 10
1.5 Scope of This Thesis 12

Chapter 2 Efficiency Limits of Light Absorbers **14**
2.1 Detailed Balance Limit 14
2.2 Imperfect Absorption and Modified Detailed Balance 16
2.2.1 Absorption in real materials 16
2.2.2 Modified Detailed Balance 19
2.3 Sub-gap Absorption and Solar Cell Performance 21

Chapter 3 The Effect of Excitons on Photovoltaic Performance: A Case Study in Cu_2O **32**
3.1 Introduction 32
3.2 Equilibrium Concentration of Excitons 34
3.3 Experimental Observations of Excitons in Cu_2O Photovoltaics 38
3.3.1 Growth of Cu_2O substrates 39
3.3.2 Photoluminescence of the Exciton Peak in Cu_2O 40
3.3.3 Excitons in the Spectral Response of Cu_2O-based Photovoltaics 42
3.4 The Role of Excitons in Photovoltaic Device Physics 44
3.4.1 Device Model Including Excitons 45
3.4.2 Model Parameters for Cu_2O 48
3.4.3 Effects of Excitons on Carrier Diffusion Length in Cu_2O 51
3.4.4 Equilibrium Concentration of Excitons and Free Carriers 53
3.4.5 Absorption, Generation, and J_{sc} 54
3.4.6 V_{oc}, FF, and Efficiency 55
3.4.7 Model Results 56
3.5 Conclusion 62

Chapter 4 Interconnect-free Perovskite/Silicon Tandems **63**

4.1 Increasing Silicon Efficiency: Tandem Si Solar Cells....63
4.2 The Rise of Perovskites and Silicon/Perovskite Tandems....63
4.3 Interconnect-free Perovskite Silicon Tandem....67
4.3.1 Interconnect-free Cell Architecture and Fabrication....68
4.3.2 Current-Voltage and TiO_2/Si Contact Characteristics....71
4.3.3 TiO_2/Si Band Alignment and Charge Transport Mechanism....79
4.3.4 Cell Stability....90
4.4 Conclusion....94

Chapter 5 Tuning the Catalytic Activity of Oxygen- and Chlorine-Evolution Electrocatalysts with Atomic Layer Deposition....96
5.1 Introduction....96
5.2 Material Selection, Sample Preparation, and Characterization....97
5.2.1 Material Selection and Group Electronegativity....97
5.2.2 Sample Preparation....98
5.2.3 Catalyst Microstructure....100
5.3 Catalyst Performance....105
5.3.1 Catalyst Overpotential....106
5.3.2 Specific Activity....109
5.3.3 Stability of Enhanced Catalyst Performance....111
5.4 Catalyst Surface Electronics....115
5.4.1 Potential of Zero Charge Measurements....116
5.4.2 XPS Characterization of TiO_2 Coated Catalysts....118
5.5 Conclusion....126

Chapter 6 Conclusion and Outlook....127

Appendix A Band Tailing Code....130

Appendix B Floating Zone Crystal Growth....190
B.1 Zone Melting Background....190
B.2 The Floating Zone Method....194
B.2.1 General Growth Process Overview....195
B.3 The Caltech System....196
B.3.1 The Floating Zone Furnace....196
B.3.2 Growth of Feed Rods....197
B.3.3 Tips for Floating Zone Growth....199

Appendix C Electrochemical Methods for Catalysis....201
C.1 Experimental Setup and Catalyst Testing....201
C.2 Calculating Overpotentials....202
C.2.1 Electronegativity and Overpotential Calculations....202
C.3 Calculating Faradaic Efficiency....203
C.4 Determination of Solution and System Resistance....204
C.5 Determination of the Double Layer Capacitance and Electrochemically Active Surface Area....206
C.6 Calculating Specific Activities using ECSA and Surface Area Measured by AFM....209
C.7 Determination of E_{ZC} by Electrochemical Impedance Spectroscopy....210

Appendix D Details of XPS Analysis....217

D.1 XPS Data Collection and Peak Fitting 217

List of Figures

Figure 1.1 A sustainable energy system with near zero carbon emissions, reproduced from(*6*). Renewable electricity is used directly as a source of energy for transportation or to produce fuels, chemicals and materials electrochemically.....2

Figure 1.2 Power output from a 4.6 MW solar photovoltaic power plant in Arizona on a cloudy day. From (*20*).....6

Figure 1.3 A simplified semiconductor energy band diagram depicting absorption, thermalization, and radiative recombination. The semiconductor has a band gap $Eg = hvgreen$ and thus absorbs green photons and photons with higher energy (shorter wavelength) while photons with less energy are transmitted (red photon). Upon absorption electrons (filled gray circle) in the valence band (*VB*) are excited to the conduction band (*CB*) leaving behind an effectively positively charged hole (white circle) in the valence band. Absorption of a photon with excess energy (blue photon) promotes an electron to an excited state in the conduction band above the band gap. The excited electron rapidly decays back to the valence band edge in a process known as thermalization (dark red steps), transferring its energy to the semiconductor lattice in the process. In radiative recombination, electrons recombine across the band gap emitting a photon in the process.....7

Figure 1.4 Current density-voltage characteristics of an ideal solar cell. In the dark, the solar cell operates as an ideal diode (red dashed curve) with an exponential dependence on the applied voltage. The light curve (blue) is a superposition of the dark curve and the absorbed photon flux. The short circuit current is equal to the total absorbed photon flux and corresponds to the point $V = 0$, where there is no radiative recombination. By contrast, the V_{oc} is at the point when the incident photon flux is completely balanced by the radiative emission of the cell and occurs when the light curve intersects the abscissa. The power producing region of the light curve is thus in the fourth quadrant. The maximum power point is represented by the dark gray box. The ratio of the area of the dark gray box to the light gray box is the fill-factor, which is a measure of resistance and non-idealities in the cell. 9

Figure 1.5 Reaction energetics for a reaction X to Y with (red) and without (blue) a catalyst. The catalyst lowers the activation energy (E_A) for the reaction resulting in greater kinetics and reaction efficiency. 11

Figure 2.1 a) The AM1.5G photon flux. b) The Shockley-Queisser Limit for the AM 1.5G spectrum: photovoltaic cell efficiency as a function of band gap.....15

Figure 2.2 The band edge absorption of GaAs adapted from (*34*). GaAs exhibits an exponential band tail below the band gap and band to band absorption above gap.17

Figure 2.3 The deficit in the experimentally achieved open-circuit voltage from that of the S-Q Limit as a function of Urbach parameter for common photovoltaic materials. 19

Figure 2.4 a) The spectral response of a solar cell with a 1.5 eV band gap for different Urbach energies in units of k_BT. using the absorption model outlined in Section 2.2.2. The sub-gap absorption increases deeper into the gap with increasing Urbach parameter b) The modified detailed balance efficiency as a function of cell band gap for

different Urbach energies. Increasing the Urbach parameter has a deleterious effect on cell performance. 22
Figure 2.5 Line cuts at 1.5 eV (left) and contour plots (right) of the photovoltaic figures of merit as a function of Urbach parameter. The red dashed line in the left figures indicates the thermal energy k_BT (25.8 meV at 300 K)....24
Figure 2.6 Effect of sub-gap absorption on a 1.5 eV band gap solar cell. a) Current density-voltage characteristics with different Urbach parameters. b) The FF as a function of Urbach parameter. The red dashed line indicates k_BT. 25
Figure 2.7 a) Spectral response (solid lines) and photoemission (dashed lines) for an absorber with a 1.5 eV band gap for different Urbach parameters. The dot-dashed lines indicate the effective band gap distribution. b) The ratio of sub-gap photoemission to the total photoluminescence.The red dashed line indicates k_BT. 27
Figure 2.8 The photoluminescence peak shift for a 1.5 eV band gap absorber as a function of Urbach parameter. 28
Figure 2.9 Spectral response for a 1.5 eV band gap solar cell with different absorber thicknesses and an Urbach parameter of 0.1 k_BT....29
Figure 2.10 Photovoltaic performance metrics for a 1.5 eV solar cell as a function of Urbach energy for different levels of incomplete above-gap absorption. The red lines indicate the thermal energy k_BT. 30
Figure 2.11 Photovoltaic figures of merit as a function of Urbach parameter for a 1.5 eV band gap solar cell with varying sub-gap carrier collection efficiencies. The red dashed lines indicate the thermal energy k_BT. 31
Figure 3.1 The fraction of free electrons and holes relative to the total excitation density $x = nehN$ in Cu_2O. The upper limit of the branching ratio between excitons and free electrons and holes during photovoltaic operation is 27.7%, suggesting that substantial exciton densities should be present during typical device operating conditions. 38
Figure 3.2 Photoluminescence spectra of the free exciton peak in Cu_2O at room temperature under different visible light excitation. The free exciton peak is observed for all excitations above the Cu_2O band gap. 41
Figure 3.3 Photoluminescence spectrum of the free exciton peak in thermally oxidized, polycrystalline Cu_2O wafers at room temperature using a 2.4 mW, 514 nm excitation. 42
Figure 3.4 Spectral response of a polycrystalline Cu_2O /Zn(O,S) solar cell. The red dashed line indicates the Cu_2O electronic band gap beyond which, in the shaded region, are wavelengths for which only excitons can exist. 44
Figure 3.5 The simulated electron, exciton and effective diffusion lengths for Cu_2O for doping densities a) 10^{12}, b) 10^{14}, and c) 10^{16}. 52
Figure 3.6 The equilibrium ratio of excitons to free carriers as a function of doping density for temperatures ranging from 200 to 500 K. 54
Figure 3.7 Comparison between the simulated device performance of a p-n^+ Cu_2O-based solar cell using a model incorporating excitonic effects relative to the FC model, denoted by the superscript *x* and *fc*, respectively. (a) The simulated dark saturation current density. (b) The ratio of the dark current density, when excitons are included,

to the dark current density using the FC model. The dark current density increases substantially when excitonic effects are included. (c) The calculated short-circuit current density. Experimental J_{sc} values (the circles) agree well with the J_{sc} values obtained using the excitonic model (*103, 104*). (d) The absolute difference in short-circuit current density between the excitonic and FC models. At room temperature and a doping density of 10^{16}, excitonic effects account for an additional 2.84 $mA \cdot cm^{-2}$. (e) The open-circuit voltage obtained from the excitonic and FC models. In the low temperature limit, the V_{oc} approaches the exciton band edge and electronic band gap for the excitonic model and the FC model, respectively. The turquoise circle represents the record experimental V_{oc} for Cu_2O solar cells (*105*). (f) The difference between the open-circuit voltage as calculated from the excitonic model and the FC model. The change in voltage is small over the calculated temperature range. (g) The simulated photovoltaic efficiency under the AM 1.5 spectrum. (h) The absolute difference in the practical efficiency in Cu_2O-based solar cells between the excitonic model and the FC model. At room temperature, the FC model underestimates the efficiency by 1.9 absolute percent. 59

Figure 3.8 The simulated fill-factor for the excitonic and FC models. The fill factors were in close agreement except at the highest doping densities, where large enhancement in the J_{sc} dominates and leads to an increase in the solar-cell efficiency relative to the FC case. 61

Figure 4.1 Perovskite record cell efficiency, adapted from (*30, 122*). The record at the time of writing is 23.3%. 65

Figure 4.2 Simplified diagram of the 2-terminal (left) and 4-terminal (right) tandem solar cell device architectures. In each design, the top contact is a transparent electrode (TE), which allows the light to pass through to the two cells, while the bottom contact need not be transparent. In the 2-terminal design the high and low band gap sub-cells are in ohmic contact by means of either a transparent conductive oxide (TCO) or tunnel junction (TJ). In a 4-terminal design two additional transparent electrode contacts are needed on the rear side of the high band gap sub-cell and on the top of the low band gap sub-cell. 67

Figure 4.3(A) Schematic of the interconnect-free monolithic perovskite/c-Si tandem solar cell (not to scale). Initial tests were carried out on homojunction Si cells with Spiro-OMeTAD as the top perovskite contact; however, our best performance was obtained with polysilicon bottom-cells and PTAA as the top hole-selective layer. (B) Cross-sectional scanning-electron microscope (SEM) image of the tandem device based on Si homojunction subcell from the top surface to the p^+-Si layer (Spiro-OMeTAD is used as HTM). The anti-reflection layer was not included due to the large thickness of ~ 1 mm, (C) Scanning transmission-electron microscopy (STEM) bright field (BF) image and (D) high-resolution STEM BF image of the TiO_2/p^+-Si interface. 70

Figure 4.4 AFM image of TDMAT-ALD TiO_2 on a p^+-Si substrate. 71

Figure 4.5 (A) *J-V* behavior of the proof-of-concept tandem device with both reverse and forward scanning at 0.05 V/s based on heterojunction poly-Si subcell. (B) Absorbance (1-R, where R is the reflectance) of the tandem device (grey shading),

external quantum efficiency (EQE) of the perovskite top cell (blue), and EQE of the c-Si bottom sub-cell (red). 72

Figure 4.6 (A) *J-V* behavior of the proof-of-concept tandem device with both reverse and forward scanning at 0.05 V/s based on Si homojunction subcell. (B) Absorbance (1-R, where R is the reflectance) of the tandem device (grey shading), external quantum efficiency (EQE) of the perovskite top cell (blue), and EQE of the c-Si bottom sub-cell (red). (C) schematic of single-junction Si homojunction solar cell including ALD-TiO_2 on a flat p^+-Si emitter (not to scale), (D) photovoltaic performance of a single-junction homojunction Si solar cell. 73

Figure 4.7(A) Schematic of the structure used for measuring contact resistivity. (B) Comparison of the *J-V* behavior of ITO/p^+-Si and various TiO_2/p^+-Si structures before and after annealing at 400 °C in air. $TiCl_4$-ALD TiO_2 listed here is deposited with the reactor chamber temperature of 75 °C. (C) Simulated band diagram of the TiO_2/p^+-Si at equilibrium assuming n-type doping of $5x10^{18}$ cm^{-3} on the TiO_2 and 10^{19} cm^{-3} for p^+-Si (appropriate for our test structure with TDMAT TiO_2, see table S3. The unknown interfacial energy gap Δ is shown here for illustrative purposes as 600 meV, which falls within the range of reported measurements (*152*)). Both mechanisms of direct- and tunneling assisted capture by interfacial defects are shown. 75

Figure 4.8 *J-V* curves of the $TiCl_4$-ALD TiO_2 deposited at low temperatures on different p+-Si wafers. The samples receive no further heat-treatment. TiO_2 deposited at 150 °C on top of p^+-Si with a doping density of (A) ~9.3×10^{19} cm^{-3}, the extracted contact resistivity is ~850 $m\Omega cm^2$ and (C) ~1.7×10^{20} cm^{-3}, the extracted contact resistivity is ~445 $m\Omega cm^2$. TiO_2 deposited at 200 °C on top of p+-Si with a doping density of (B) ~9.3×10^{19} cm^{-3}, the extracted contact resistivity is ~210 $m\Omega cm^2$ and (D) ~1.7×10^{20} cm^{-3}, the extracted contact resistivity is ~99.6 $m\Omega cm^2$....76

Figure 4.9 *J-V* data of a 2-T perovskite/Si tandem device with ITO as the recombination layer. 77

Figure 4.10 *J-V* data of monolithic perovskite/Si tandem solar cells with (top) TTIP-ALD TiO_2, (bottom) $TiCl_4$–ALD TiO_2 (deposited at 75°C). 78

Figure 4.11 (A) Combined UPS valence band spectrum and IPES, and (B) the secondary electron cut-off region, and (C) calculated energy diagram from the above measurement, of an annealed TDMAT-ALD TiO_2 layer. The error for the work function was ±0.2 eV, and the extraction of valence band and conduction band had an error of ±0.1 eV....80

Figure 4.12 (A) Combined UPS valence band spectrum and IPES, and (B) the secondary electron cut-off region representative, and (C) calculated energy diagram from the above measurement of an annealed TTIP-ALDTiO_2 layer. 80

Figure 4.13 (A) Combined UPS valence band spectrum and IPES, and (B) the secondary electron cut-off region representative, and (C) calculated energy diagram from the above measurement of an annealed TiCl4-ALD TiO2 layer (deposited at 75°C). ..81

Figure 4.14 (A) Simulated *J-V* curves for varying interfacial gaps Δ. A single neutral mid-gap SRH defect was included with $Sn = Sp = 10^5$ cm/s. The dashed curves are computed with tunneling to defects included. (B) Simulated small voltage resistivity

$\rho = dVdI|V = 0$ with the TiO_2 donor density fixed at 10^{18} cm^{-3} and variable p-Si acceptor doping. Measurements are included as data points in red. Calculations for neutral (solid lines), acceptor-type (dotted lines) and donor-type (dot-dashed lines) are shown to demonstrate the important effect of defect charge on the interfacial carrier balance. (C) Simulated band diagram of the full tandem device based on homojunction Si subcell with high work-function cp-TiO_2 at illuminated open-circuit. The inset depicts the two important energetic offsets Δ and δ, respectively, defined as the valence-to-conduction band offset at the TiO_2-Si interface and the difference in work functions between our solution-processed mesoporous TiO_2 layer and that of the ALD compact layer. 82

Figure 4.15 Calculated small-voltage resistivity as in Fig. 4B of the main text, this time showing the effect of tunneling. Tunneling has a minor effect for neutral and acceptor-type defects, but significantly affects the donor-defect models when the acceptor doping is large because tunneling effects are most significant when the depletion region is small which occurs for large acceptor doping concentrations... 84

Figure 4.16 V_{oc} yield of transparent single-junction perovskite solar cells (with p^+-Si as the substrate) with and without mesoporous-TiO_2. Results for TDMAT-ALD TiO_2 are shown on the left while results for TTIP-ALD TiO_2 are shown on the right. Both titania compact layers have high work functions with the deposition conditions used in this work..... 87

Figure 4.17 Simulated band diagram at 0 V (left) and *J-V* behavior (right) of a single-junction perovskite solar cell with and without an additional "mesoporous" titania layer inserted between the perovskite and high work-function compact titania. This represents a 1D simplification of the complex 3-dimensional mesoporous structure present in our tandem cell design, but captures the qualitative effect of including titania layers with contrasting work functions. The mesoporous layer functions primarily to maintain the built-in voltage in the perovskite cell, as seen in the band diagram (left) and consequently discrepant open-circuit voltages (right). Here electron affinities of 4.1 eV and 4.5 eV were used for the compact and mesoporous titania layers respectively. 87

Figure 4.18 *J-V* curve of a monolithic perovskite/Si tandem solar cells with as-deposited $TiCl_4$-ALD TiO_2 (200 °C). The top perovskite subcell has a planar structure without the inclusion of the mesoporous TiO_2 film, and is fabricated with low-temperature processes. 88

Figure 4.19 *J-V* curves of the $TiCl_4$-ALD TiO_2 deposited at low temperatures on different p+-Si wafers. The samples receive no further heat-treatment. TiO_2 deposited at 150 °C on top of p^+-Si with a doping density of (A) ~9.3×10^{19} cm^{-3}, the extracted contact resistivity is ~850 $m\Omega cm^2$ and (C) ~1.7×10^{20} cm^{-3}, the extracted contact resistivity is ~445 $m\Omega cm^2$. TiO_2 deposited at 200 °C on top of p+-Si with a doping density of (B) ~9.3×10^{19} cm^{-3}, the extracted contact resistivity is ~210 $m\Omega cm^2$ and (D) ~1.7×10^{20} cm^{-3}, the extracted contact resistivity is ~99.6 $m\Omega cm^2$..... 89

Figure 4.20 (A) Excess carrier lifetime of a Si substrate with and without TiO_2 passivation ($TiCl_4$-ALD TiO_2 deposited at 150 °C without further annealing) as a function of the measured injection level. The implied V_{oc} (iV_{oc}) is increased by ~50 mV with the

$TiCl_4$ TiO_2 coating. (B) *J-V* curve of a $TiCl_4$-ALD (150 °C) TiO_2/p^+-Si sample (p^+-Si has a doping density of ~$1.5*10^{19}$ cm^{-3}). 90
Figure 4.21 Damp heat test (85 °C in a relative humidity level of 85%) of a semitransparent perovskite solar cell. Evolution of the photovoltaic characteristics including (a) V_{oc}, (b) J_{sc}, (c) FF and (d) PCE during damp heat stability of an encapsulated single-junction perovskite device for 1414 h. 91
Figure 4.22 PCE evolution of the proof-of-concept perovskite/Si homojunction tandem device undergoing four different aging stages. (A) Stage 1: 1 Sun continuous illumination in air for ~2.1 h, biased near maximum power point); (B) Stage 2: device stored in dark in a N_2 cabinet for ~1224 h; (C) Stage 3: device under 1 Sun continuous illumination in air for ~19 h, biased at ~1.3 V, and Stage 4: device underwent light/dark cycles for seven cycles, with total illumination of over 800 h. The measurement under light was taken at 25 °C. Corresponding V_{oc} evolution (D-F) of the same device under the same conditions. 94
Figure 5.1 X-ray diffraction patterns for typical IrO_2 and RuO_2. All observed peaks were indexed to standard diffraction patterns for IrO_2 and RuO_2, respectively. 100
Figure 5.2 Material characterization of typical electrocatalyst samples. (A) SEM image of an IrO_2 catalyst with 1000 ALD TiO_2 cycles. (B) AFM map of IrO_2 with 10 ALD cycles of TiO_2. (C) HAADF-STEM image of an IrO_2-based electrocatalyst with 10 ALD cycles of TiO_2. The underlying crystalline material is IrO_2 while the hair-like material at the surface is TiO_2. (D,E) Energy dispersive X-ray spectroscopy (EDS) maps of IrO_2-based electrocatalysts with 10 and 40 ALD cycles of TiO_2, respectively. The red color indicates Ir and green indicates Ti. Note that green and red intermix throughout this cross section due to the inherent roughness of the sample. 101
Figure 5.3 Representative topographic atomic force microscopy images of IrO_2, RuO_2, and FTO each with 0, 3, 10, and 1000 ALD cycles of TiO_2. 102
Figure 5.4 Representative conductive atomic force microscopy tunneling current images of IrO_2, RuO_2, and FTO each with 0, 3, 10, and 1000 ALD cycles of TiO_2. 103
Figure 5.5 High-Angle Annular Dark-Field Scanning Transmission Electron Microscopy (HAADF-STEM) images of different IrO_2 + 10 ALD cycles of TiO_2 samples. The crystalline sublayer is IrO_2 and the "hairy" top layer is amorphous TiO_2. 105
Figure 5.6 Specific activities (j_s) and overpotentials (η) for the OER and CER on IrO_2, RuO_2, and FTO coated at various ALD cycles of TiO_2. Overpotentials were measured at 10 mA/cm^2_{geo} for the OER and at 1 mA/cm^2_{geo} for the CER (normalized to geometric surface area). Specific activities for the OER were measured at 350 mV (IrO_2 and RuO_2) or 900 mV (FTO). Specific activities for the CER were measured at 150 mV (IrO_2 and RuO_2) or 700 mV (FTO). The red squares indicate available literature values. 107
Figure 5.7 Group electronegativity vs overpotential at 1 mA/cm^2_{AFMSA}. Overpotential data was taken from Seh *et al.* (blue and orange circles) and from this work (red circles). For $LaCrO_3$, $LaMnO_3$, $LaFeO_3$, $LaCoO_3$, $LaNiO_3$, RuO_2, IrO_2, and PtO_2 group electronegativites were estimated by taking the geometric mean of the Allen Scale electronegativities of the constituent atoms. For $IrO_x/SrIrO_3$, Ir_2SrO_7 was assumed for group electronegativity calculations (*208*). For IrO_2/TiO_2, $IrTiO_4$ was assumed for group electronegativity calculations For $NiFeO_x$, $NiFe_2O_4$ was was assumed for

group electronegativity calculations (*200*). For $NiCoO_x$ $NiCo_2O_4$ was assumed for group electronegativity calculations (*200*). For $NiCoO_x$, $NiCo_2O_4$ was assumed for group electronegativity calculations (*200*). For $CoFeO_x$, $FeCo_2O_4$ was assumed for group electronegativity calculations (*200*). For CoO_x, $CoO_{1.5}$ was assumed for group electronegativity calculations (*200*). For NiO_x, Ni_2O_3 was assumed for group electronegativity calculations (*200*). 108

Figure 5.8 Tafel plots from IrO_2 coated with 0 (dark blue), 3 (orange), 6 (yellow), 10 (purple), and 20 (green) ALD cycles of TiO_2 all from this work are shown next to those of $IrO_x/SrIrO_3$ at 0 (red) and 30 (light blue) hrs of activation as taken from literature (*208*). To calculate the current density, the surface area was measured by AFM (Table 4.1). 110

Figure 5.9 Example stability testing data of IrO_2 + 0 (blue), 10 (orange), and 40 (yellow) ALD cycles in 1 M H_2SO_4 at 10 mA/cm^2_{geo}. 112

Figure 5.10 X-ray photoelectron spectroscopy of the Ti 2p region for IrO_2, RuO_2, and FTO electrocatalysts with 10 cycles, 10 cycles, and 30 cycles of TiO_2, respectively, before and after stability testing for the OER. Note the peak still visible in the "after" RuO_2 spectra is associated with the Ru 3p core levels. 114

Figure 5.11 X-ray photoelectron spectroscopy of the Ti 2p region for an RuO_2 electrocatalyst with 60 cycles of before and after 24-hour stability testing for the CER. The TiO_2 is still present after testing. 115

Figure 5.12 E_{ZC} of IrO_2 (blue), RuO_2 (red), and FTO (green) anodes coated with various ALD cycles of TiO_2. Black dots and circles with black borders indicate the catalysts with the highest specific activity for each catalyst for the OER and CER, respectively. 118

Figure 5.13 X-ray photoelectron spectroscopy of the Ti $2p_{3/2}$ region for IrO_2, RuO_2, and FTO catalysts with varying TiO_2 thicknesses. Bulk TiO_2 is shown as the blue peak in each spectrum. The slightly and highly reduced Ti peaks are shown in green and red, respectively, and the most highly oxidized Ti peak is shown in orange. 120

Figure 5.14 X-ray photoelectron spectroscopy of the Ti 2p region for IrO_2, RuO_2, and FTO catalysts. Bulk TiO_2 is shown as the blue peak in each spectrum. The slightly and highly reduced Ti peaks are shown in green and red, respectively, and the most highly oxidized Ti peak is shown in orange. 121

Figure 5.15 Ti $2p_{3/2}$ overall peak shift relative to bulk TiO_2 as a function of TiO_2 cycle thickness for IrO_2, RuO_2, and FTO. 122

Figure 5.16 X-ray photoelectron spectroscopy of the Ir 4f, Ru 3d, and Sn $3d_{5/2}$ region for IrO_2- RuO_2- and FTO-based electrocatalysts as a function of TiO_2 thickness. 124

Figure 5.17 Overall peak shift of the main peak of the Ir 4f, Ru 3d, and Sn $3d_{5/2}$ spectra relative to the bare metallic (0 cycle) metal-oxide substrate as a function of TiO_2 cycle thickness for IrO_2, RuO_2, and FTO, respectively. 125

Figure B.1 (Top) Diagram of the typical solidification process, known as normal freezing. The distribution of solute (impurities) in the solid is controlled by the distribution coefficient *k*, the rate of the advance of the solid-liquid interface, and the mixing in the liquid. (Bottom) The solute concentration for a normal freezing process as a function of the fraction of solidification for different distribution coefficients *k*. . 192

Figure B.2 (Top) Diagram of the zone melting process, in which a molten zone is passed along the length of a solid. (Bottom) The solute concentration for the zone melting process as a function of the fraction of solidification for different distribution coefficients *k*. Zone melting results in regions of purification and uniform solute distribution. 193

Figure B.3 Image of a floating zone during growth of single crystalline Cu_2O. The bright regions in the background are the halogen lamps which serve as the heat source. 194

Figure B.4 Typical floating zone setup before (left) and after (right) the feed and seed rods are brought into contact..... 195

Figure B.5 The optical floating zone furnace from Crystal Systems Inc. Adapted from (*211*). 197

Figure B.6 The Bridgeman vertical tube furnace and crane assembly (*211*). 198

Figure B.7 Top view of a seed rod sample holder (gray) with an improperly sized seed rod (red) during different stages of rotation. The sample holder is sized for a sample of the size traced out by the black dashed circle. The center of a seed rod this size is collinear with the rotational axis (black dot) of the sample holder and feed rod. The improperly sized seed rod, however, has a rotational axis (red dot) different than that of the sample holder. Thus, rotation of the sample holder leads to the center of the seed rod tracing a circle around the axis of rotation of the float zone assembly (black dot). This leads to a "wobbly", unstable molten zone. 200

Figure C.1 System resistance as measured by electrochemical impedance spectroscopy in 5.0 M NaCl at pH 2.0 (CER) and 1.0 M H_2SO_4 (OER). The resistivity of the system did not appreciably change between 0 and 60 ALD cycles of TiO_2. For IrO_2 based electrodes, the average system resistance was 9.1 ± 0.6 Ω for CER condtions and 5.4 ± 0.6 Ω for OER conditions. For RuO_2 based electrodes, the average system resistance was 8.0 ± 1.0 Ω for CER condtions and as 5.3 ± 0.7 Ω for OER conditions. For FTO-based electrodes, the average system resistance was 30 ± 7 Ω for CER condtions and 23 ± 6 Ω for OER conditions..... 205

Figure C.2 Example double-layer capicitance measurements for determining ECSA for IrO_2 with 10 cycles of ALD TiO_2 in 1.0 M H_2SO_4. (Left) Cyclic voltamogramms in the non-Faradaic region at 0.005, 0.01, 0.025, 0.05, 0.1, 0.2, 04, and 0.8 V/s. (Right) Cathodic (yellow disks) and anodic (blue disks) charging currents measured at 0.95 V vs SCE plotted as a function of scan rate..... 207

Figure C.3 Example impedence spectroscopy for IrO_2 with 0 cycles of ALD TiO_2 in 5.0 M NaCl pH 2.0 at E_{oc}. These data were fit to a resistor in series with a parallel combination of a capacitor and a shunt resistor. The resulting capacitance was taken as the C_d which in this case was was 3.24×10^{-6} F. 208

Figure C.4 ECSA for IrO_2, RuO_2, and FTO based catalysts in 1.0 M H_2SO_4 and 5.0 M NaCl, pH 2.0. All catalysts presented here had a geometric surface area of 0.13 cm^2, yielding electrochemical roughness factors between 0.1 and 6.0..... 209

Figure C.5 Sample Bode (above) and Nyquist (below) plots of electrochemical impedence spectroscopy data of IrO_2 coated with 10 ALD cycles of TiO_2. The Bode plot shows the frequency of the alternating current signal (Hz) versus the phase shift of the impedance response (degrees). The Nyquist plot shows the real (Z') and imaginary (Z'') components of the impedance response to the alternating current signal. Data

presented in the figure were collected at 105 mV vs SCE in 5.0 M $NaNO_3$ at pH 2.0. The resulting equivelent circuit [R_s-(R_p-C)] fit of these data yielded a capacitance of 5.8× 10^{-6} F. 213

Figure C.6 Electrochemical impedance spectroscopy of (A) IrO_2, (B) RuO_2, (C) and FTO coated with various ALD cycles of TiO_2 at 25 mV intervals in 5.0 M $NaNO_3$ at pH 2.0. The resulting Nyquist plots were modeled as R_s-(C-R_p) circuits. The calculated capacitance values (dots) for each sample (set of dots) are shown here. The minimum value of each curve represents the E_{ZC}. The magnitude of the capacitance represents the surface area of the sample. 214

Figure C.7 Sample Mott-Schottky (E vs $1/C^2$) plots of RuO_2 with 0 (red), 1000 (blue) ALD TiO_2 cycles. The fit, using a geometric surface area of 7.1 X 10^{-6} m^2, yielded N_d = of 5.4 X 10^{19} cm^{-3}. 215

Figure C.8 Potential of zero charge as a function of TiO_2 cycle number for IrO_2, RuO_2, and FTO electrocatalysts. Black dots and disks with black borders indicate the catalysts with the highest specific activity for each substrate for the OER and CER, respectively. 216

Figure D.1 X-ray photoelectron spectroscopy of the Ti 2p region for a bulk TiO_2 film. The peak associated with Ti^{4+} is shown in blue. The slightly and highly reduced Ti peaks are shown in green and red, respectively, and the most highly oxidized Ti peak is shown in orange. 218

Figure D.2 X-ray photoelectron spectroscopy of the Ti 2p region for a bare RuO_2 film. The 3 orange, red, and purple peaks define the Ru 3p core level photoemission associated with RuO_2 219

List of Tables

Table 2.1 Experimentally observed Urbach parameters of common photovoltaic materials. 18
Table 3.1 Exciton binding energies (E_x) and dielectric constants for established and emerging photovoltaic materials. The exciton binding energy scales with the inverse square of the dielectric constant. 33
Table 4.1 Hall-effect measurements for annealed TDMAT-ALD TiO_2 85
Table 5.1 Surface area (measured by AFM) as a percent of geometric surface area. Dividing these values by 100 yields topographic roughness factors. 104
Table 5.2 A summary of the Tafel slopes and exchange current densities from this work (IrO_2 + TiO_2 catalyts) and previous work ($SrIrO_3$ catalysts) (*208*). All current density data reported here is based on surface area that is measured by AFM (Table S1). 110
Table 5.3 Summary of overpotential data as measured from CVs to reach 10 mA/cm^2_{geo} in 1 M H_2SO_4 for the OER and 1 mA/cm^2_{geo} in 5 M NaCl pH 2.0 for CER at 0 min, 10 min, 2 h, and 24 h of testing in constant current mode. The right-most column displays the overpotential that was reported in the main text. N/A indicates that a rapid loss in activity was noticed before the time of measurement. 113
Table 5.4 The areal peak ratios of the main peak to the satellite peak for the Ir 4f, Ru 3d, and Sn 3d core-level photoemission. 125

Table B.1 Faradaic efficiencies for the OER and CER 204

Chapter 1
Introduction

1.1 A Net-Zero Carbon Emission Energy System

The rapid increase in human development over the last several centuries has come with an increased dependence on energy to provide the services that society relies on. Despite increases in energy efficiency, the global energy demand is expected to increase by almost 30% in the next 20 years as emerging economies continue to develop (*1, 2*). At the same time, net emissions of carbon dioxide (CO_2) from anthropogenic sources must approach zero (or negative values) if global temperatures are to stabilize at or below the 2ºC target of international climate agreements (*3-5*).

Electricity production, transportation, and industrial chemical production together account for the vast majority of global annual CO_2 emissions; 22.3 Gt of the 33.9 Gt of CO_2 emitted each year (*6*). Of this total, electricity generation is responsible for 38% of annual carbon dioxide emissions as ~80% of the global electricity generation was still derived from fossil fuel sources in 2017 (*6, 7*). Transportation accounts for an additional 22% of annual CO_2 emissions. While roughly 70% of these emissions are from short distance transport where electrification is already playing a role in decarbonization, the remaining 30% is due to aviation, long distance rail and road transport, and long-route shipping where electrification is much more difficult (*6, 8, 9*). Chemicals and chemistry are used to make almost everything that society produces. The chemical industry is energy intensive, often requiring high temperatures and pressures to run reactions efficiently and in the process producing ~6% of the world's annual CO_2 emissions – a number that is expected to grow as developing economies grow and the demand for industrial chemicals increases (*10*). Thus, a transition to a near zero net emissions future will likely require a robust, emissions-free grid system capable of producing vast amounts of inexpensive electricity; electrification of most fuel

consuming devices and carbon-neutral fuels for the parts of the transportation system that are not easily electrified; and new electrochemical methods and catalysts for electrification of commodity chemical production.

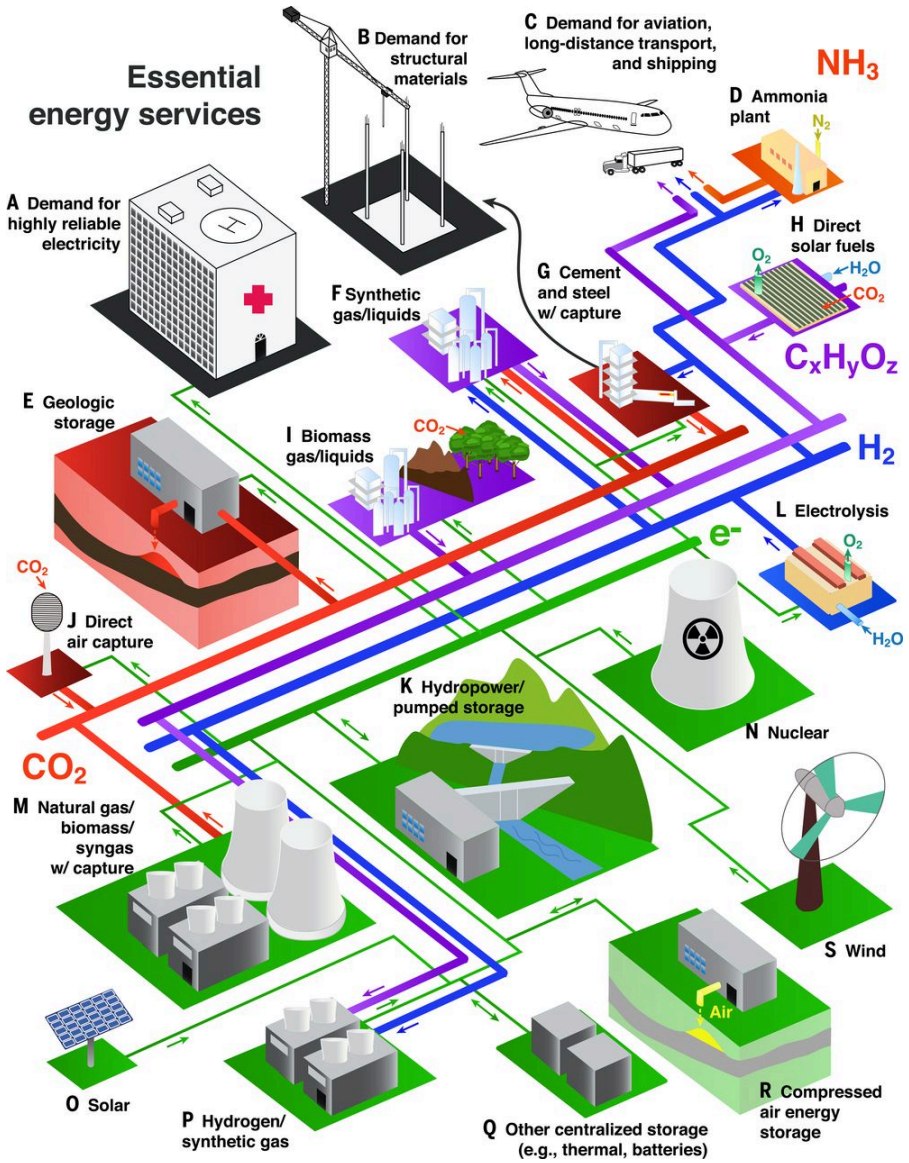

Figure 1.1 A sustainable energy system with near zero carbon emissions, reproduced from(*6*). Renewable electricity is used directly as a source of energy for transportation or to produce fuels, chemicals and materials electrochemically.

An example of a near net zero carbon energy system is depicted in Fig. 1.1. In such a system, a cheap, reliable electricity grid primarily powered by renewable energy (solar, wind or

hydro) is used as the major energy source to power the rest of the energy services. Light-duty and short-distance medium- and heavy-duty vehicles have been electrified or consume clean burning fuels (e.g. hydrogen). Major industrial chemicals and transportation fuels are produced (photo)electrochemically and are thus powered by the vast amounts of inexpensive, renewable electricity. Other industries that are more difficult to decarbonize (e.g. cement and steel manufacturing) can use carbon capture and storage technology to offset their emissions. Despite an increased societal awareness of anthropogenic climate change and an increased adoption of renewable energy technologies, the world is far from realizing a net-zero carbon emissions energy system.

1.2 Challenges to Realizing Net-Zero Carbon

Creating a global net-zero carbon energy system is not an easy task. The largest and most immediate barrier preventing the implementation of a carbon-neutral energy system is the substantial cost associated with known technological alternatives to the current carbon emitting system. These costs are exacerbated by current economic and development goals and trends in international trade and travel that are expected to fully double the global energy demand by 2100, such that difficult-to-eliminate emissions could be in the future comparable to current total emissions (*6*). Beyond cost reductions, rapid innovation is needed to increase efficiency and develop new processes and technologies to replace difficult to those energy services which are difficult to decarbonize. Nowhere is this truer than in the electricity generation, energy storage, and chemical production sectors which largely rely on technologies developed over 100 years ago. This thesis focuses on cost reductions and technological innovations in solar photovoltaics, a promising renewable electricity generation technology, and catalysis for the electrochemical production of fuels and industrial chemicals.

1.3 Solar Photovoltaics

The majority of CO_2 emissions related to electricity generation can be mitigated by switching to renewable energy sources (e.g. solar, wind, and hydro). Solar photovoltaics, which convert solar energy directly into electricity and are commonly referred to as solar cells, are a particularly attractive carbon-free technology. More energy from sunlight is incident on the Earth's surface in an hour and a half than was consumed globally in 2014 (*11, 12*) and yet, photovoltaics make up only a miniscule fraction of the total global electricity generation, less than 2% in 2017 (*13*).

1.3.1 The Solar Cell Market

The global solar cell market began as a fledgling industry in the early years of the second half of the 20th century, scraping by in niche applications. Since then the solar cell market has grown at a near exponential rate to a robust market with over 400 GW of installed global capacity (*14*). The market is dominated by crystalline silicon (Si) photovoltaics, which at present account for 95% of global solar energy production. The growth of the solar cell market has been largely driven by a drastic reduction in Si module cost and increase in cell efficiency, such that photovoltaic electricity generation is now cost competitive with traditional electricity generation technologies (*15*). Indeed, at the time of writing, the balance of system costs (installation, permitting, support structure, electrical wiring, etc.) account for over 70% of the cost of a fully installed Si module (*16*).

Despite the recent decrease in the cost of Si solar modules, further cost reductions are needed to account for the high cost of solar energy storage if solar is to replace baseload power at large penetrations (*16, 17*). Reductions in the recombination losses at the Si surface and metal contacts through better passivation and minimization of shadow losses at the top contacts have resulted in incremental improvements in the Si cell efficiency. The current laboratory record power-conversion efficiency (η) for single-junction Si solar cells is 26.6% (*18*), closely approaching the theoretical limit of 29.4% (record module efficiencies are closer to

23%) (*19*). Further reductions in the cost of Si photovoltaics can be most readily met by increasing the module efficiency, and thereby reducing the area-related balance of systems costs. For example, replacing a 15% efficient solar module with a 20% efficient module, all else being equal, leads to a 25% reduction in land acquisition, installation, cleaning, and permitting costs on a per watt basis. Thus, other approaches beyond the incremental improvement of Si cells are needed to increase cell efficiencies past the Si single junction theoretical limit.

Beyond improvements in efficiency, the electricity produced from photovoltaics is inherently time-varying (the sun is not always shining) as is illustrated in Fig. 1.2. The diurnal day-night cycle and weather limit the capacity factor of photovoltaics to only ~25%, even in the most favorable locations. This intermittency necessitates so-called "load following" electricity generation, which is typically supplied by natural gas-fired generators that can ramp up and down quickly to meet the time varying gap between the supply and demand (*6*). One renewable alternative is to store the solar energy in a chemical fuel which can be used later (when demand peaks and sunlight wanes) using a photovoltaic-powered electrolyzer. However, improvements in the electrocatalysis and system efficiencies are needed (see Section 1.4).

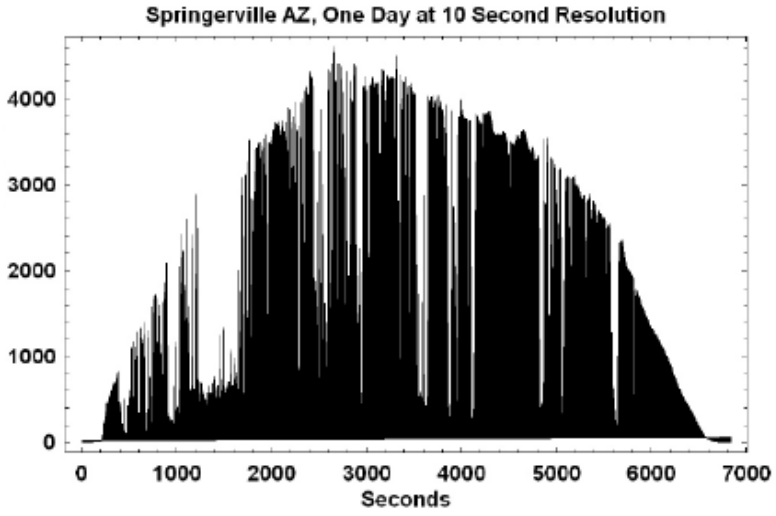

Figure 1.2 Power output from a 4.6 MW solar photovoltaic power plant in Arizona on a cloudy day. From (*20*).

1.3.2 Basics Operating Principles of Photovoltaics

In order to understand how to improve the efficiency of solar cells we must first understand how they work. The operating principle behind solar cells is the photovoltaic effect – the spontaneous generation of a voltage by a material under illumination. Though first observed in photosensitive electrodes immersed in an electrolyte by Becquerel in 1839, modern photovoltaics are solid-state devices that consist of one or more semiconductor materials. A brief description is provided below for the lay reader but there are many thorough treatments of the device physics of photovoltaics and the interested reader is directed to references (*21-23*).

By far, the most common type of solar cell is the single-junction consisting of a single absorbing semiconductor material with a p-n homojunction device architecture. A semiconductor. A semiconductor is characterized by a distribution of electronic states in bands separated by forbidden gaps in which no electronic states exist. At thermal equilibrium, the electrons in a semiconductor are governed by Fermi-Dirac statistics and will occupy states up to the Fermi-energy. The highest occupied band is referred to as the valence

band (VB) and the lowest lying band above the Fermi level is known as the conduction band (CB). The difference in energy between the VB and the CB is known as the band gap (E_g), which typically ranges from 50 meV to 3.5 eV (though the distinction between a very wide band gap semiconductor and an insulator is somewhat arbitrary).

The energy band gap gives rise to the characteristic optical response of a semiconductor (Fig. 1.3). When light is absorbed by a semiconductor, an electron in the valence band is excited to a conducting state in the conduction band, leaving behind an effective positive charge, which can be treated as a quasiparticle. Hence, in order for a semiconductor to absorb a photon, the photon must have an energy at least equal to the band gap $E_{photon} \geq E_g$; photons with a lower energy are not absorbed and are transmitted through the semiconductor. Photons with an energy greater than the band gap are absorbed and electrons are promoted to higher states in the conduction band. However, this excess energy is lost rapidly as the electron couples to the semiconductor's crystal lattice vibrations (phonons) in a process known as thermalization and the electron decays back to the conduction band edge.

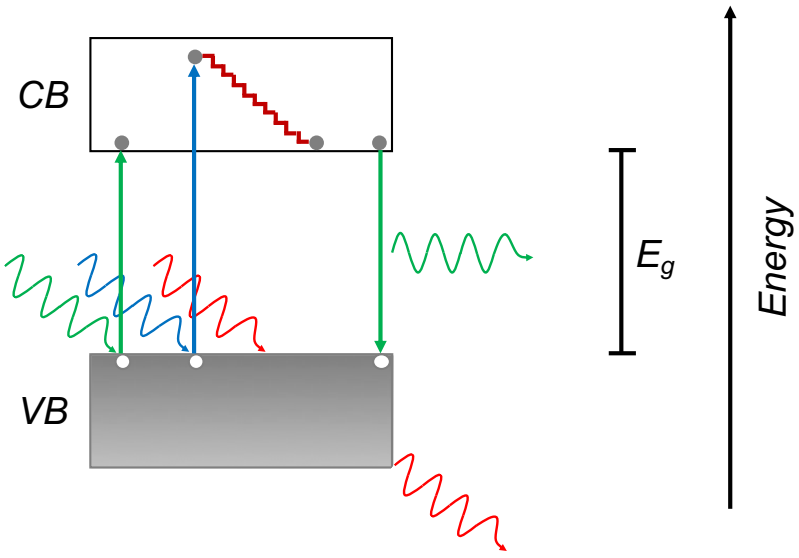

Figure 1.3 A simplified semiconductor energy band diagram depicting absorption, thermalization, and radiative recombination. The semiconductor has a band gap $E_g = h\nu_{green}$ and thus absorbs green photons and photons with higher energy (shorter wavelength) while photons with less energy are transmitted (red photon). Upon absorption

electrons (filled gray circle) in the valence band (*VB*) are excited to the conduction band (*CB*) leaving behind an effectively positively charged hole (white circle) in the valence band. Absorption of a photon with excess energy (blue photon) promotes an electron to an excited state in the conduction band above the band gap. The excited electron rapidly decays back to the valence band edge in a process known as thermalization (dark red steps), transferring its energy to the semiconductor lattice in the process. In radiative recombination, electrons recombine across the band gap emitting a photon in the process.

Electrons excited to the conduction band have a finite lifetime, eventually they will recombine with the hole in the valence band. In an ideal material, this process is always radiative – a photon is emitted when the electron and hole recombine, which is emitted to free space or reabsorbed by the semiconductor. However, non-radiative recombination is always present in real materials and represents a major loss mechanism in most solar cells. This non-radiative recombination is often mediated through defect states either at semiconductor surfaces or in the bulk (or both!).

Under continuous illumination, a steady-state population of electrons and holes are generated. In response, the electron and hole systems develops electrochemical potential and the cell builds up a voltage equal to the electrochemical potential difference between the two carrier populations. Thus, the voltage is limited to the band gap of the solar cell, though for realistic solar cells the voltage is always lower due to imperfections and entropic losses.

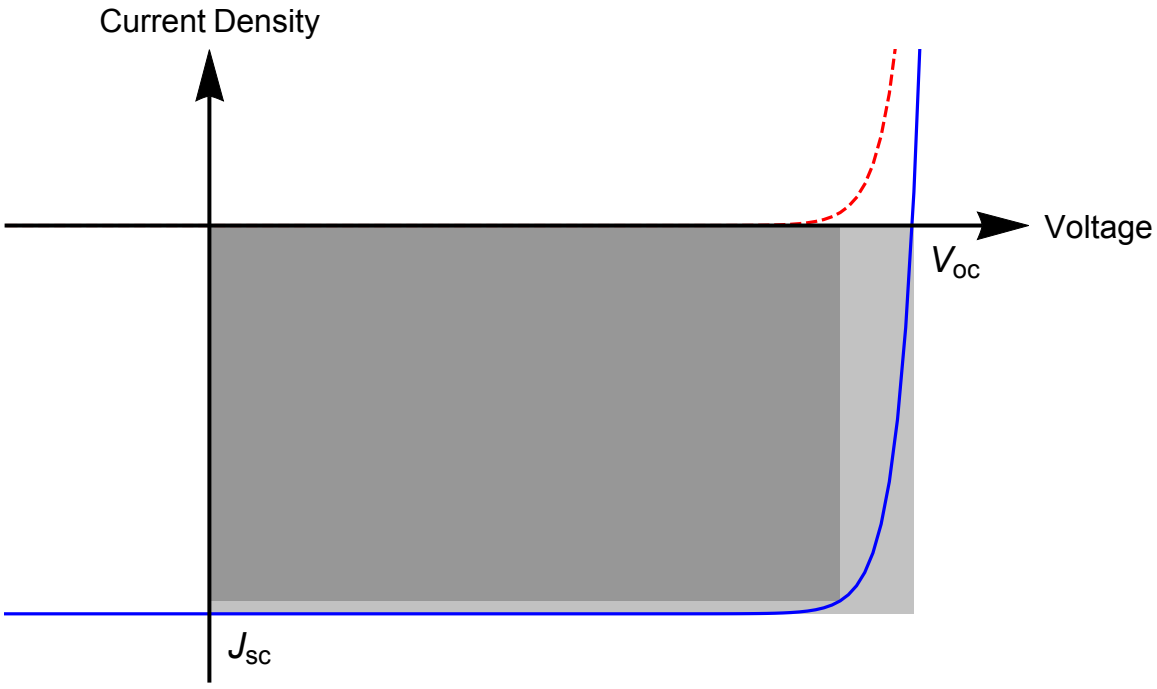

Figure 1.4 Current density-voltage characteristics of an ideal solar cell. In the dark, the solar cell operates as an ideal diode (red dashed curve) with an exponential dependence on the applied voltage. The light curve (blue) is a superposition of the dark curve and the absorbed photon flux. The short circuit current is equal to the total absorbed photon flux and corresponds to the point $V = 0$, where there is no radiative recombination. By contrast, the V_{oc} is at the point when the incident photon flux is completely balanced by the radiative emission of the cell and occurs when the light curve intersects the abscissa. The power producing region of the light curve is thus in the fourth quadrant. The maximum power point is represented by the dark gray box. The ratio of the area of the dark gray box to the light gray box is the fill-factor, which is a measure of resistance and non-idealities in the cell.

The recombination in the solar cell is (intuitively) voltage dependent. The current-voltage characteristics of an ideal solar cell are illustrated in Fig. 1.4. In the dark, the solar cell is simply a p-n junction diode with an exponential dependence on voltage. Under illumination, the solar cell absorbs photons and a photocurrent is generated. Hence, the light curve is a superposition of the dark curve. At short-circuit, the conduction band and the valence band in the semiconductor are connected via an external conductor such that the radiative

recombination is zero and thus the short-circuit current density J_{sc} is simply the total photogenerated current. Because each absorbed photon corresponds to a single electron hole pair, the magnitude of the J_{sc} indicates the efficiency of absorption. At open-circuit there is no current pathway and the absorbed photon flux exactly balances the radiative emission from the cell. Therefore, the open circuit voltage V_{oc} is indicative of the material and junction quality, being higher for cells with lower non-radiative recombination. The cell produces power equal to the product of the current and voltage in the region of the curve between the J_{sc} and V_{oc}. The voltage and current density at the maximum power point of the cell (V_{mpp} and J_{mpp}, respectively) are determined by minimizing the power density ($M_{pp} = \frac{d}{dV}P = \frac{d}{dV}J(V) * V = 0$). The efficiency of the cell η is then determined by dividing the maximum power by the power incident on the cell from the solar spectrum (~1000W/m^2 at the Earth's surface). The fill factor *FF* is the ratio of the maximum power produced by the cell and the product of the J_{sc} and V_{oc} and is a measure of the resistive losses, non-radiative recombination, and general non-ideality of the cell. Thus, the J_{sc}, V_{oc}, *FF*, and η are the key performance metrics for photovoltaics.

1.4 Electrocatalysis for Production of Fuels and Chemicals

Society relies on chemistry and chemical products for almost everything we produce. Catalysts lower the thermodynamic barrier necessary to run a reaction and improve reaction kinetics (Fig. 1.5) and are used in the vast majority (> 90%) of chemical processes. The chemical industry in its vastness is (unsurprisingly) a large consumer of energy (10% of global energy consumption was consumed by chemical processes in 2013). Thus, improving catalysis is a large lever to reducing the CO_2 emissions of the entire chemical industry.

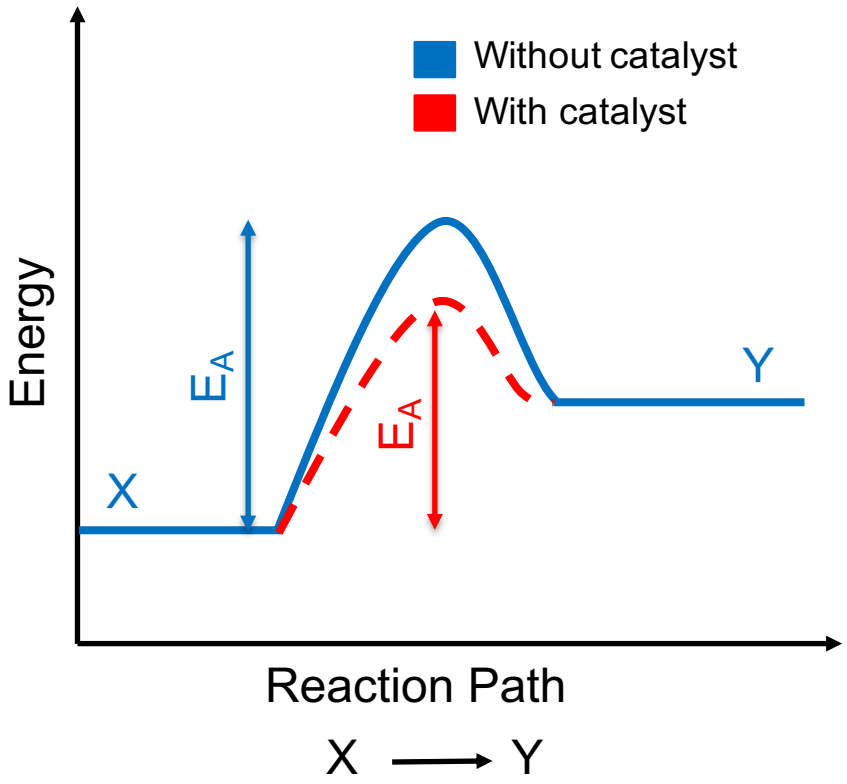

Figure 1.5 Reaction energetics for a reaction X to Y with (red) and without (blue) a catalyst. The catalyst lowers the activation energy (E_A) for the reaction resulting in greater kinetics and reaction efficiency.

Indeed, catalysts play an integral in the production of widely consumed chemicals, such as, hydrogen (50 Mt/yr), ethylene (115 Mt/yr), and ammonia (175 Mt/yr), which are possible to produce sustainably by coupling electrochemical production with a renewable electricity grid, but which remain much more expensive and less efficient than conventional production methods (*6, 9*). In fact, chlorine is one of the only major commodity chemicals produced electrochemically. Thus, development of improved electrocatalysts with higher efficiencies and selectivities is imperative not only to realizing a variety of electrochemical transformations at scale but also to improving the energy efficiency of existing reactions.

In this thesis, we focus on improving catalysts for the oxygen-evolution and chlorine-evolution reactions (OER and CER, respectively), because of their major role in the global economy and zero-carbon future.

The OER is the limiting half reaction in water splitting, which produces hydrogen through water electrolysis. Stored electrolytic hydrogen can be used in a variety of energy scenarios. In a power-to-gas-to power system, stored hydrogen is converted back to electricity through combustion in hydrogen burning turbines or in fuel cells. Hence, P2G2P systems can be used to complement the time variability of renewable sources such as wind and solar. The high energy efficiency of hydrogen fuel cells also makes hydrogen an attractive choice for a clean transportation fuel. Indeed, Toyota has recently introduced a line of fuel cell cars and a heavy-duty fuell cell/battery hybrid truck with impressive ranges and there are large investments planned in hydrogen for transportation Germany and in California (*24-26*). Thus, development of new, efficient OER electrocatalysts is need to usher in an era of clean hydrogen.

The CER is the largest electrochemical process in the world, accounting for 2% of global energy usage alone. Chlorine is used in 50% of industrial chemical processes, 85% of all pharmaceuticals and 95% of all crop protection chemicals as well as in almost all water treatment facilities (*27*). The operating expenses of a chlor-alkali plant make are dominated by electricity costs and make up 50% of the total cost of chlorine (*28*). Improving the efficiency of existing OER catalysts, thus represents a large potential reduction in CO_2 emissions.

1.5 Scope of This Thesis

This thesis works towards a net-zero carbon emission future by focusing on improvements in photovoltaic efficiency and electrocatalysis through fundamental understanding and development of new technologies. In Chapter 2, we extend the classical Shockley-Quiesser detailed balance model to include non-ideal band edge shapes. We find that even with perfect

above gap absorption significant below gap band tailing severely limits the solar cell efficiency and external radiative efficiency. In Chapter 3, we investigate the effects of bound electron-hole pairs (excitons) on photovoltaic performance using an emerging semiconductor, cuprous oxide, as a case study. Chapter 4, develops a novel, interconnect-free tandem perovskite/silicon solar cell architecture. We demonstrate that our cell contacting scheme is highly efficient, transparent, and has the promise to push cell efficiencies beyond 30%. In Chapter 5, we demonstrate a new tool to tune the catalytic activity of heterogeneous electrocatalysts for the chlorine-evolution and oxygen-evolution reactions, which are important componenets of industrial chlorine production and the fuel-forming water splitting reaction, respectively. Finally, we conclude in Chapter 6 by summarizing our findings and providing outlook for future work in these directions.

Chapter 2
Efficiency Limits of Light Absorbers

2.1 Detailed Balance Limit

Understanding the fundamental energy conversion limits of how efficiently a photovoltaic device can operate is important; it yields insight into effective strategies for device design, and materials selection. A solar energy converter operating as a heat engine with the hot reservoir at the temperature of the sun (~5800 K) and the cold reservoir at the temperature of the earth (~300 K), could operate at a maximum Carnot efficiency of 94.8%. However, the Carnot efficiency is much larger than that achieved by photovoltaic devices and ignores fundamental entropic and thermalization losses that are associated with absorption and emission in traditional photovoltaic devices.

The reciprocity between absorption and emission in photovoltaic devices was first outlined by Shockley and Queisser (S-Q) in their seminal paper on the fundamental efficiency limits of photovoltaics in 1961 (*29*). The theory laid out by S-Q is known as detailed balance because it balances the absorbed solar flux with the luminescent emission and current extraction from the solar cell. The S-Q theory is subject to three key assumptions: 1) the solar cell operates in the radiative limit (the external radiative efficiency is unity) and there is no non-radiative recombination, 2) perfect carrier collection (the internal quantum efficiency, IQE, is unity) so that every absorbed photon creates an electron-hole pair that is collected as current, and 3) that the semiconductor absorber has a perfect forbidden energy gap with perfect absorption above gap and zero sub-gap absorption. Under these assumptions, the current-voltage characteristics of an ideal solar cell are given by the balance of the light generated current from the absorbed solar flux and the radiative current:

$$J(V) = -q \int_{E_g}^{\infty} \Phi_{Sun}(E) a(E) dE + \int_{E_g}^{\infty} b(E, V, T_{cell}) a(E) dE$$

$$-\int_{E_g}^{\infty} b(E,0,T_{earth})a(E)dE \quad (1)$$

where, J is the current-density, V is the voltage, q is the fundamental electron charge, E_g is the band gap, $\Phi_{Sun}$is the incident solar flux, a is the absorptivity, and we have employed Kirchoff's law to substitute $a(E) = \epsilon(E)$ in the second term and

$$b(E,V,T) = \frac{2\pi}{h^3c^2}\frac{E^2}{e^{\frac{E-qV}{k_BT}}-1} \quad (2)$$

is the Planck blackbody formula accounting for the chemical potential of the cell (i.e. the quasi-Fermi level splitting taken here as the cell voltage, $\Delta\mu = qV$) where, E is the photon energy, V is the voltage and T is absolute temperature in Kelvin. The first term is the absorbed solar flux, the second is the radiative current and the third term is the absorbed solar flux from the blackbody radiation of the Earth. The performance metrics of a single junction solar cell with band gap E_g are thus readily calculated from Eq. 1 as follows: J_{sc} occurs at V=0, the V_{oc} is determined by solving for the roots of Eq. 1., and the efficiency η is found by finding the maximum power produced from the cell with respect to voltage ($\frac{d}{dV}P = \frac{d}{dV}V * J(V) = 0$) and dividing by the incident power.

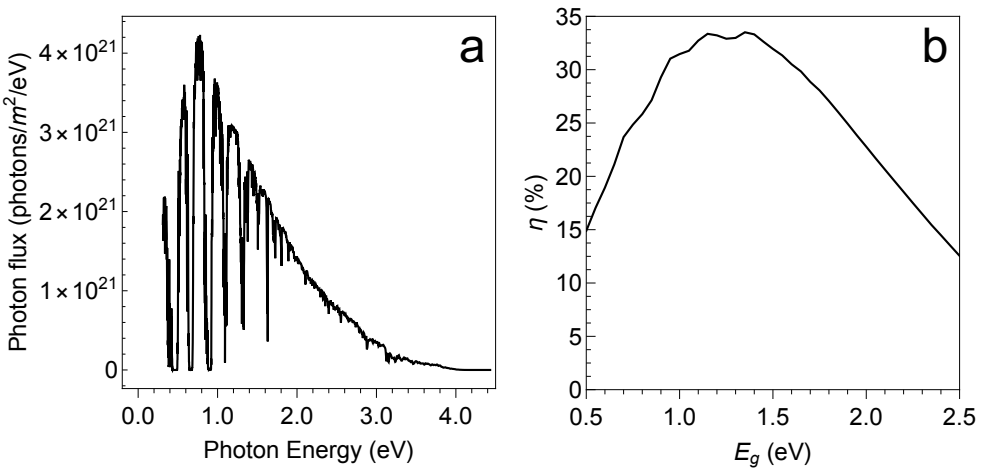

Figure 2.1 a) The AM1.5G photon flux. b) The Shockley-Queisser Limit for the AM 1.5G spectrum: photovoltaic cell efficiency as a function of band gap.

Unsurprisingly, the band gap of the absorber material plays a central role in determining the ultimate device efficiency as it controls the absorption characteristics of the cell. Increasing a cell's bandgap increases the V_{oc} at the expense of the J_{sc}. These opposing driving forces, in concert with the spectral make-up of the incident solar flux, lead to an optimal band gap for a photovoltaic converter. Figure 2.1a shows the Air Mass 1.5 Global (AM 1.5G) photon flux, so called because it refers to the incident solar photon flux at 37º latitude such that sunlight passes through the equivalent of 1.5 atmospheres before reaching the Earth's surface. Global includes both direct and diffuse sunlight and is relevant for cells without concentration. The detailed balance efficiency for the AM 1.5G spectrum is plotted as a function of band gap energy in Fig. 2.1b. The optimum efficiency of 33.6% occurs at a band gap $E_g = 1.34$ eV, though there are multiple peaks owing to the spectral profile. As a comparison, at the time of writing the record single junction efficiency is 28.8% for a GaAs ($E_g = 1.42$ eV) solar cell (*30*).

2.2 Imperfect Absorption and Modified Detailed Balance

The Shockley-Queisser Limit is a useful tool to understand the ultimate limits of perfect photovoltaic energy conversion. However, in practice, semiconductors are far from ideal owing to a variety of defect states that present themselves in the fundamental optoelectronic processes governing solar cell performance. Herein, we develop a modified detailed balance model that accounts for these no idealities, namely the non-zero sub-gap absorption exemplified by typical photovoltaic materials.

2.2.1 Absorption in real materials

A key assumption of the S-Q model is that the solar cell is a perfect absorber - all photons of energy higher than the band gap are absorbed and the absorption below gap is zero. However,

real materials exhibit sub-gap absorption due to impurities and disorder as illustrated in Fig. 2.2. (*31-33*). This sub-gap absorption is typically characterized by a linear exponential band tail below the gap and has been observed in a wide range of absorber materials including amorphous, organic, perovskite and II-VI, III-V and group IV semiconductors (*31, 34-42*). This phenomenon was first observed by Urbach in 1953 for AgBr and other ionic materials and band tails with the form $\alpha(E) = \alpha_0 \exp\left(\frac{E-E_0}{\gamma}\right)$ are known as Urbach tails, with the steepness of the decay determined by the Urbach parameter γ (*43*). Though the exact physical origin of the band tailing is material dependent, any band tail with a linear exponential can be characterized with an Urbach parameter.

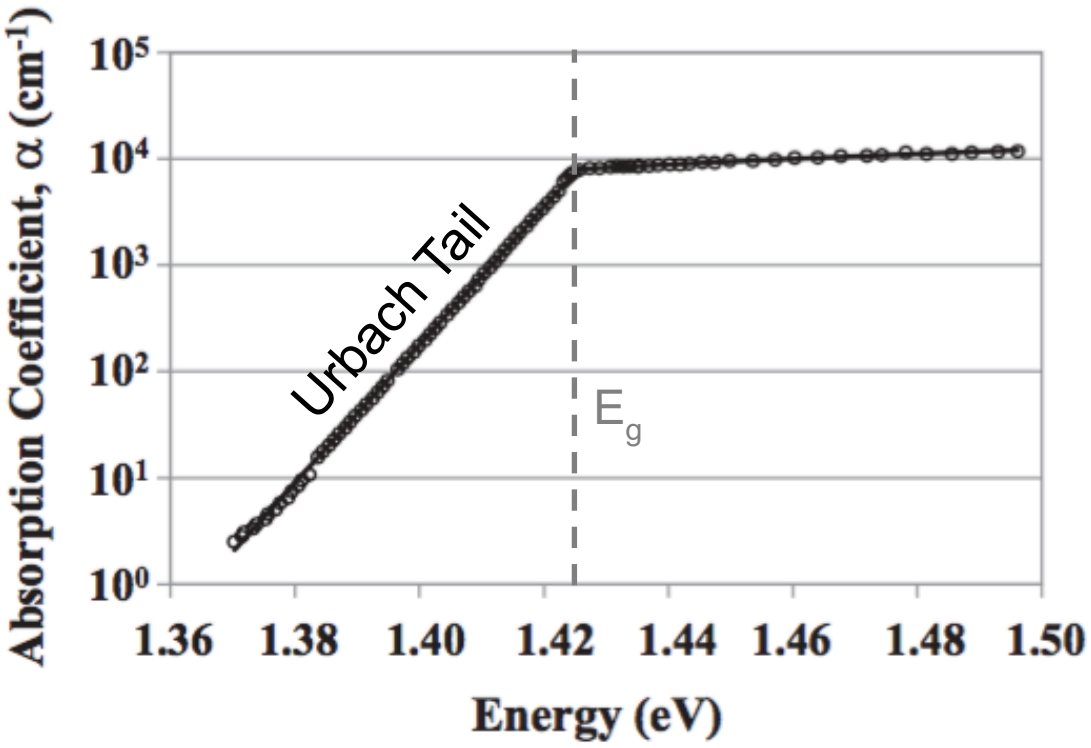

Figure 2.2 The band edge absorption of GaAs adapted from (*34*). GaAs exhibits an exponential band tail below the band gap and band to band absorption above gap.

The Urbach parameters for photovoltaic The Urbach parameters for photovoltaic absorber materials varies widely based on material quality and inherent disorder (*31*). The

experimentally derived Urbach parameters for common photovoltaic parameters are tabulated in Table 2.1. High quality materials (e.g. GaAs, InP) have Urbach parameters in the range of a few meV, whereas more disordered materials (e.g. a-Si, CZTS) typically exhibit Urbach parameters on the order of several k_bT (~25.8 meV at 300 K).

Material	E_0 **(meV)**
GaAs	6.7 (*34*)
InP	7.1 (*35*)
CdTe	9.0 (*36*)
c-Si	11 (*37*)
Cu_2O	14 (*38*)
$CH_3NH_3PbI_3$	15 (*39*)
CIGS	24 (*40*)
a-Si	48 (*41*)
CZTS	65 (*42*)

Table 2.1 Experimentally observed Urbach parameters of common photovoltaic materials.

Although the sub-gap absorption in an Urbach tail is exponentially small (see Fig. 2.2) there is a relationship between the experimental photovoltaic performance and Urbach parameter for a given photovoltaic materials. Figure 2.3 plots the difference between the open-circuit voltage predicted by the detailed balance from S-Q and the experimentally achieved open-circuit voltage for different materials as a function of their Urbach parameters. Small values of $V_{oc,S-Q} - V_{oc,Exp}$ indicate larger experimental open-circuit voltages and more ideal cell performance. There is a striking correlation between a material's Urbach parameter and the ideality of the cell: high quality materials (GaAs, Si, InP, perovskites) have open-circuit voltages approaching that of the S-Q Limit, whereas more disordered materials exhibit open-circuit voltages that are far from ideal.

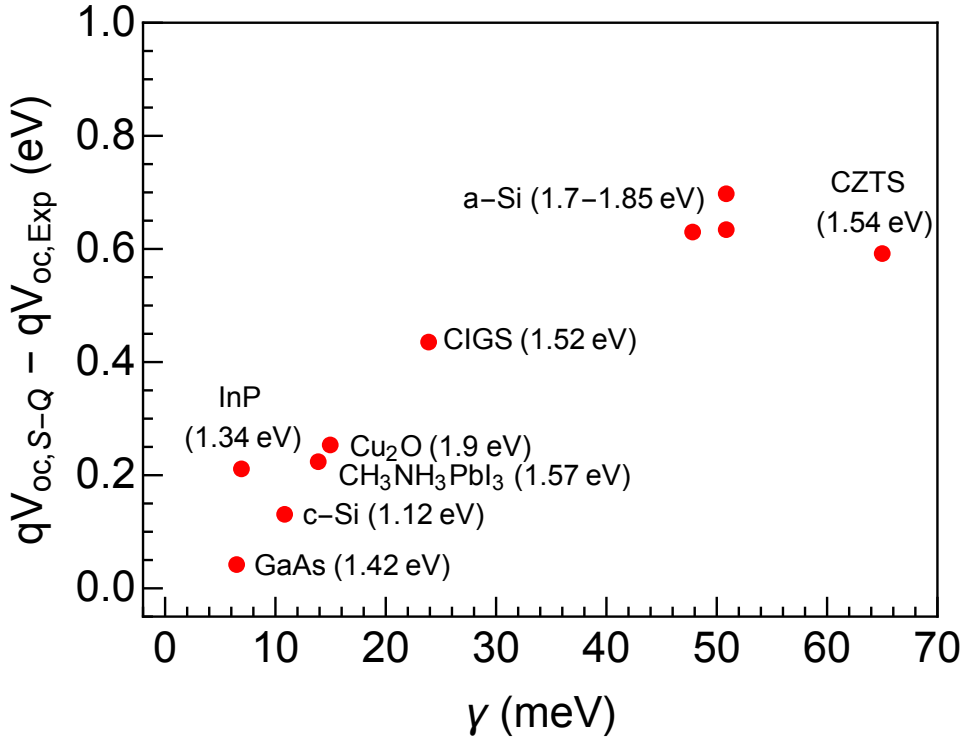

Figure 2.3 The deficit in the experimentally achieved open-circuit voltage from that of the S-Q Limit as a function of Urbach parameter for common photovoltaic materials.

2.2.2 Modified Detailed Balance

To better understand the correlation between photovoltaic performance and sub-gap absorption we develop a modified detailed balance model for single junction solar cells that includes the effects of band tailing:

$$J(V) = -q \int_0^\infty \left(\Phi_{AM1.5G}(E) + \Phi_{bb}(E, 0, T_{Earth})\right) a(E,V)\,dE + \frac{q}{\eta_{ext}(V)} \int_0^\infty \Phi_{bb}(E, V, T_{cell})\, a(E,V)\,dE \quad (3)$$

where, η_{ext} is the external radiative efficiency of the solar cell and we have again used Kirchoff's law to replace the emissivity with the absorptivity in the second term on the right. As in S-Q's original detailed balance model, the current collected *J(V)* is a balance of the photogenerated current and the carrier loss from radiative and non-radiative

recombination. For simplicity, we assume that our cell operates in the radiative limit with perfect carrier collection efficiency where $\eta_{ext} = 1$ and $IQE = 1$, such that $EQE(E,V) = IQE(E,V)a(E,V) = a(E,V)$ (see Section 2.3.1 for analysis of the non-radiative limit and imperfect carrier collection. We consider a flat plate solar cell with zero-front surface reflection and perfect back reflector so that the absorptivity is described by Beer-Lambert absorption:

$$a(E,V) = 1 - \exp(-2\alpha L) \tag{4}$$

where, L is the cell thickness. To parameterize the band-edge we use an absorption model that convolutes a sub-gap exponential density of states with a parabolic density of states above gap that describes band-to-band absorption (*44*), which yields:

$$\alpha_{0K}(E) = \alpha_0\sqrt{\gamma}G\left(\frac{E - E_g}{\gamma}\right)$$

with

$$G(x) = Re\left(\frac{1}{2\Gamma\left(1+\frac{1}{\theta}\right)}\int_{-\infty}^{\infty}\exp\left(-|x'|^{\theta}\right)\sqrt{x-x'}dx'\right)$$

where, $\alpha_{0K}(E)$ is the absorption coefficient at absolute zero and $\theta = 1$ represents the case of an Urbach tail. It is important to note that this absorption accounts only for the density of states but not for the occupation of these states and leads to a divergence in the generalize Planck law (*44, 45*) and an overestimation of the effects described below (*46, 47*). The resolution is to include an occupation factor $f_v - f_c$ where f_v is the occupation of holes in the valence band and f_c is the occupation of electrons in the conduction band. Then, the total absorption coefficient is:

$$\alpha(E,V) = \alpha_{0K}(E) * (f_v - f_c)$$

We consider the case of perfectly parabolic density of states with equal electron and hole effective masses. Under such conditions, the occupation factor has the following form:

$$(f_v - f_c) = \tanh\left(\frac{E - V}{4k_B T}\right)$$

and thus, the solar cell's absorption is not only dependent on the incident photon energy but also on the cell's operating voltage. While the occupation factor of real material systems is more complicated, we note that $f_v - f_c$ is generally a function with limiting values from -1 to 1 with a sign flip at $E = \Delta\mu$, which is captured by the simple expression above.

In the following sections, we use this modified detailed balance model to analyze the performance metrics of the solar cell when the effects of sub-gap absorption are included. Although, the absorption model presented here is general it can easily be fit to capture the optical response of any semiconductor absorber in general so that more specific results can be obtained (*44*).

2.3 Sub-gap Absorption and Solar Cell Performance

Using the modified detailed balance model developed in Section 2.2.2 we analyze the effects of sub-gap absorption on solar cell performance. The calculations below assume $\alpha_0 L = 10$, which leads to full absorption above gap (the effects of incomplete absorption are treated later) and that the cell and Earth are at room temperature $T_{cell} = T_{Earth} = 300$ K. Urbach parameters ranging from 1 meV to 1 eV are considered. The Mathematica code used to calculate the findings below can be found in Appendix A.

The spectral response of a solar cell with a 1.5 eV band gap is shown in Figure 2.4a for different Urbach parameters in units of $k_B T$. Naively from Fig. 2.4a, sub-gap absorption would seem to have a muted effect on the solar cell performance, as the cell exhibits unity photoconversion above gap for all Urbach parameters and shows exhibits only some band tailing below the gap with absorption extending deeper into the gap with increasing Urbach

parameter. Though, one should note that even for the lowest Urbach parameters the cell spectral response is not perfect as in the S-Q case. However, we find that the increasing the Urbach parameter to even ~3 k_BT has detrimental effects on the maximum theoretical efficiency, especially for band gaps less than the optimum 1.34 eV band gap from the S-Q Limit (Fig. 2.4b). For the lowest Urbach parameters the efficiency approaches that of the S-Q Limit with a maximum efficiency near 33.6%, but for Urbach parameters > k_BT there is a significant penalty and at $3k_BT$ the maximum efficiency is only half of the S-Q limit with an efficiency of only 16.7%.

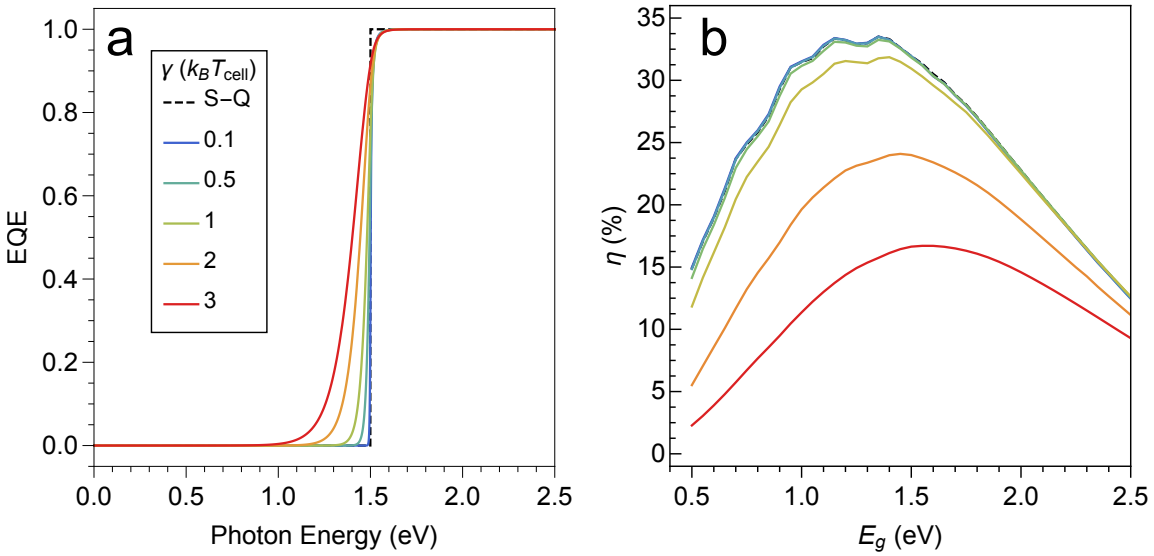

Figure 2.4 a) The spectral response of a solar cell with a 1.5 eV band gap for different Urbach energies in units of k_BT. using the absorption model outlined in Section 2.2.2. The sub-gap absorption increases deeper into the gap with increasing Urbach parameter b) The modified detailed balance efficiency as a function of cell band gap for different Urbach energies. Increasing the Urbach parameter has a deleterious effect on cell performance.

The drastic decrease in solar cell efficiency can be understood by examining the figures of merit of solar cell performance as a function of increasing Urbach parameter as illustrated in Fig. 2.5. For small increases in the Urbach parameter $\gamma < k_BT$, increasing sub-gap absorption leads to a monotonic decrease in the open-circuit voltage and monotonic increase in short-circuit current density that effectively cancel out and result in only a slight decrease

in the limiting efficiency as compared to that of the S-Q analysis. For $\gamma > k_B T$, there is a drastic decrease in the achievable efficiency which can only be attributed to a dramatic decrease in the V_{oc}, which trends to zero for exceedingly large values of γ, and subsequent decrease in fill factor (see Fig. 2.6b below). Meanwhile, the the tailing of absorption below the gap has a lesser effect on the J_{sc} because the marginal increase in absorption below gap is small in comparison to the total absorption, which is dominated by band-to-band transitions above gap. Indeed, the short-circuit currenty density does not significantly until $\gamma > 100$ meV and asymptotes at the total incident solar flux for the largest Urbach parameters. The significant reduction in V_{oc} with increasing γ dominates the effects on the solar cell efficiency, which shows a similar trend with Urbach parameter, approaching the S-Q efficiency at low γ and decreasing significantly for $\gamma > k_B T$. These qualitative effects are true irrespective of band gap (see the contour plots in Fig. 2.5)

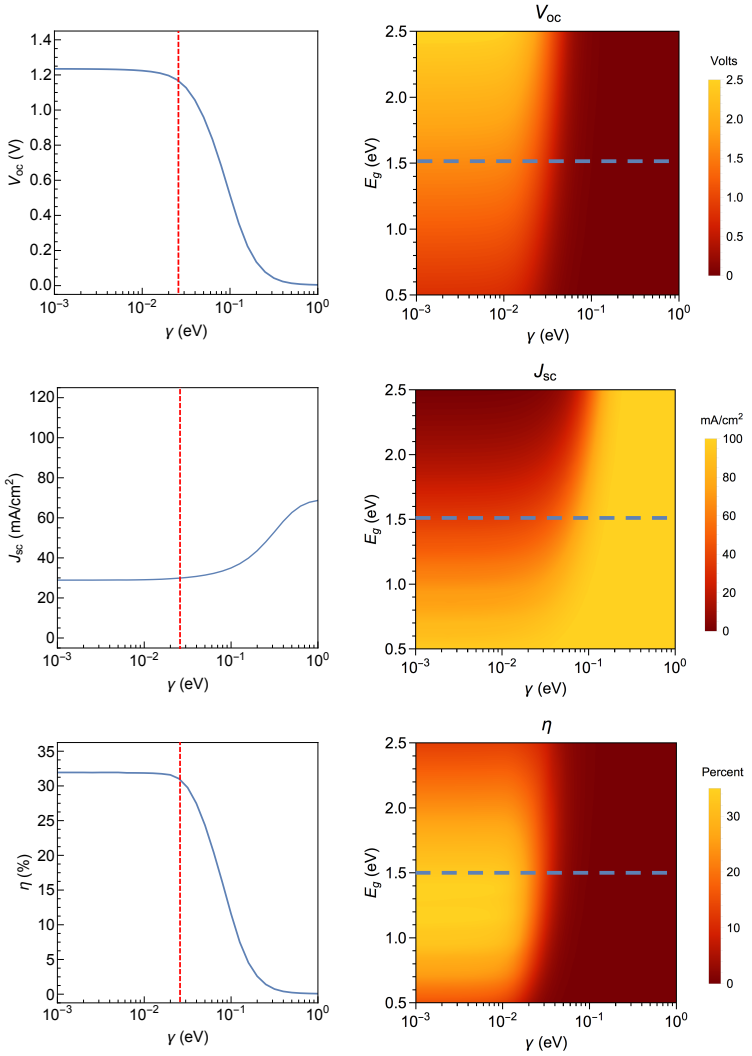

Figure 2.5 Line cuts at 1.5 eV (left) and contour plots (right) of the photovoltaic figures of merit as a function of Urbach parameter. The red dashed line in the left figures indicates the thermal energy k_BT (25.8 meV at 300 K).

Unsurprisingly, the effects of increasing Urbach parameter on the V_{oc} and J_{sc} manifest in the solar cell's current-voltage characteristics, as depicted in Fig. 2.6. As is expected, small values of the Urbach parameter lead to current voltage characteristics similar to the S-Q limit, while larger values of γ lead to non-ideal diode behavior (Fig. 2.6a). For $\gamma > k_BT$ there is a drastic decrease in the *J-V* curve's fill-factor before it levels off to 25.8%.

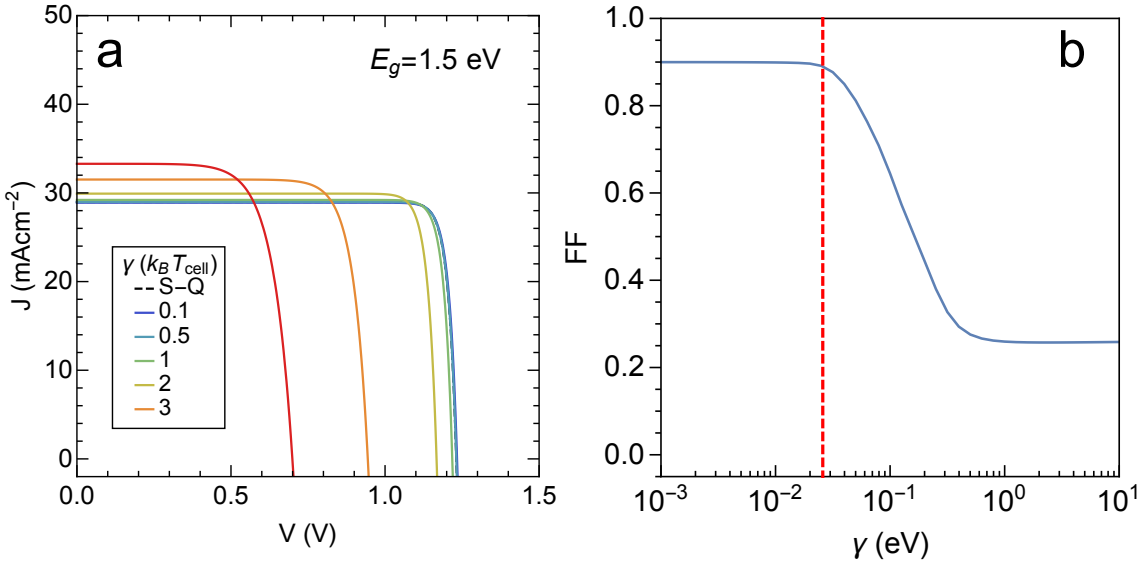

Figure 2.6 Effect of sub-gap absorption on a 1.5 eV band gap solar cell. a) Current density-voltage characteristics with different Urbach parameters. b) The FF as a function of Urbach parameter. The red dashed line indicates k_BT.

It is interesting to note that the open-circuit voltage decreases dramatically at $\gamma \sim k_BT$. To further understand this phenomenon, we can examine the photoluminescence (PL) of the solar cell as a function of Urbach parameter. Assuming all carriers are thermalized and hence, can be described by a single Fermi distribution, the reciprocity between absorption and emission dictates that the solar cell emit radiation according to the generalized Kirchoff (Lasher-Stern-Würfel) law (*45*). The photoluminescence (dashed lines) along with the spectral response (solid lines) of a 1.5 eV band gap semiconductor with different Urbach parameters is plotted in Fig. 2.7a. There is qualitatively different behavior for $\gamma < k_BT$ and $\gamma > k_BT$. Increasing Urbach energies for $\gamma < k_BT$ leads to a broadening of the PL, though the peak remains essentially at the band-edge. In contrast, increasing γ beyond k_BT leads to a broadened PL peak that is Stoke's shifted (Fig. 2.8) to lower energy relative to the EQE band edge. Indeed, the total photoluminescence in this case is dominated by sub-gap PL (Fig. 2.7b), which is indicative of a shift in the dominant radiative recombination pathways from band-to-band to tail-to-tail, tail-to-band, or band-to-tail. At $\gamma \sim k_BT$ the luminescence is almost entirely from sub-gap states.

Upon further analysis of the Stokes shift, we find that the peak position of the luminescence actually occurs roughly at the quasi-Fermi level splitting. In other words, $E_{PL}^{max} \approx qV_{oc}$. This peculiar fact can be reconciled with the physical picture shown in Fig. 2.9. In an ideal semiconductor with a perfect band-edge, the quasi-Fermi levels are below the band-edge (assuming 1-Sun illumination). Thus, as carriers are excited into the conduction band, they relax to the band-edge and eventually luminescence with a photon energy given by the bandgap. With the introduction of sub-gap absorption, the notion of a perfect forbidden energy gap is destroyed and rather the semiconductor effectively has a distribution of bandgaps, which can be calculated from the effective distribution of bandgaps by taking a derivative of the spectral response with respect to energy (*48*). For $\gamma < kT$, the situation is similar to the ideal case because the band gap is still well defined (Fig. 2.7a and Fig. 2.9b). However,s when the width of the band gap distribution is larger than kT (which occurs roughly when $\gamma \sim kT$), the Stokes shift occurs, suggesting that luminescence at the band-edge only occurs for a sufficiently well-defined bandgap.

For $\gamma > kT$, the physics of luminescence drastically changes, as shown in the right-most schematic of Figure 2.9. In this case, as carriers are excited into the conduction band, they rapidly thermalize as they did in the perfect semiconductor. On the other hand, since the band-edge is no longer well-defined, it is possible in principle for carriers to completely thermalize to the valence band without emitting a photon. For sufficiently slow thermalization between the valence and conduction band, an out-of-equilibrium population can form in the semiconductor in steady-state operation, characterized by two quasi-Fermi levels. While the quasi-Fermi level splitting is lower for increasing γ, the role of the quasi-Fermi levels in this scenario is two-fold: it Pauli-blocks incoming photons with energies beneath this splitting and also prevents excited carriers from rapidly relaxing to the valence band, forming an electron bottle neck. The carriers, therefore, eventually luminescence as the quasi-Fermi splitting position, and the quasi-Fermi level splitting becomes an effective bandgap for the semiconductor. Thus, the Stokes shift can be qualitatively described by a

two-bandgap picture, where the peak position of the distribution of bandgaps defines the higher energy bandgap, while the quasi-Fermi level splitting defines the lower energy bandgap.

The qualitative picture described above illustrates the importance of including band-filling when applying Würfel's generalized Planck's law to examine sub-gap absorption. Indeed, without including band-filling, we get quantitative and qualitatively different results that are physically inconsistent with experiment

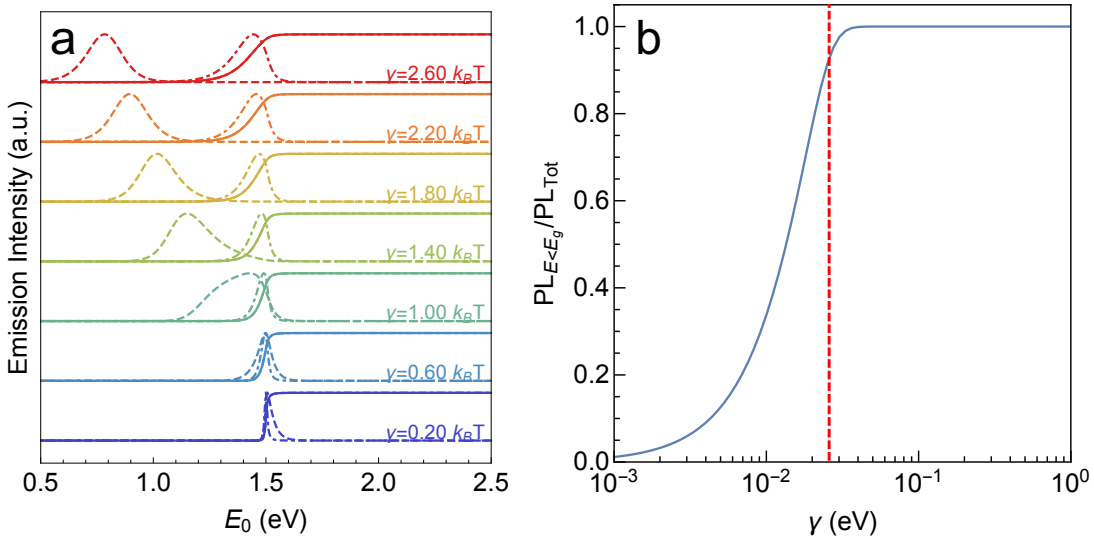

Figure 2.7 a) Spectral response (solid lines) and photoemission (dashed lines) for an absorber with a 1.5 eV band gap for different Urbach parameters. The dot-dashed lines indicate the effective band gap distribution. b) The ratio of sub-gap photoemission to the total photoluminescence. The red dashed line indicates k_BT.

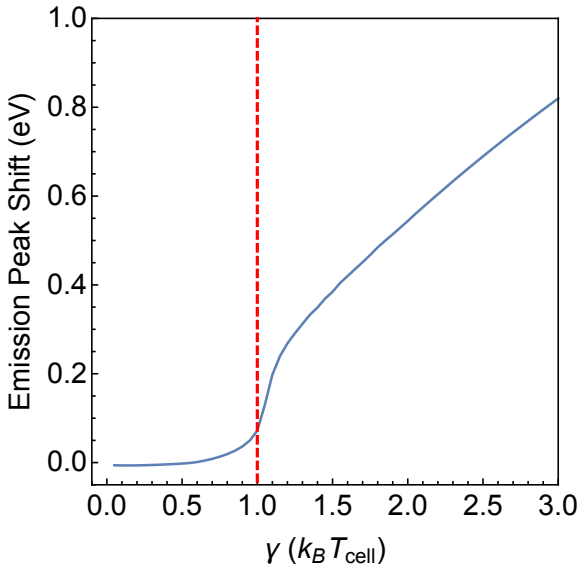

Figure 2.8 The photoluminescence peak shift for a 1.5 eV band gap absorber as a function of Urbach parameter.

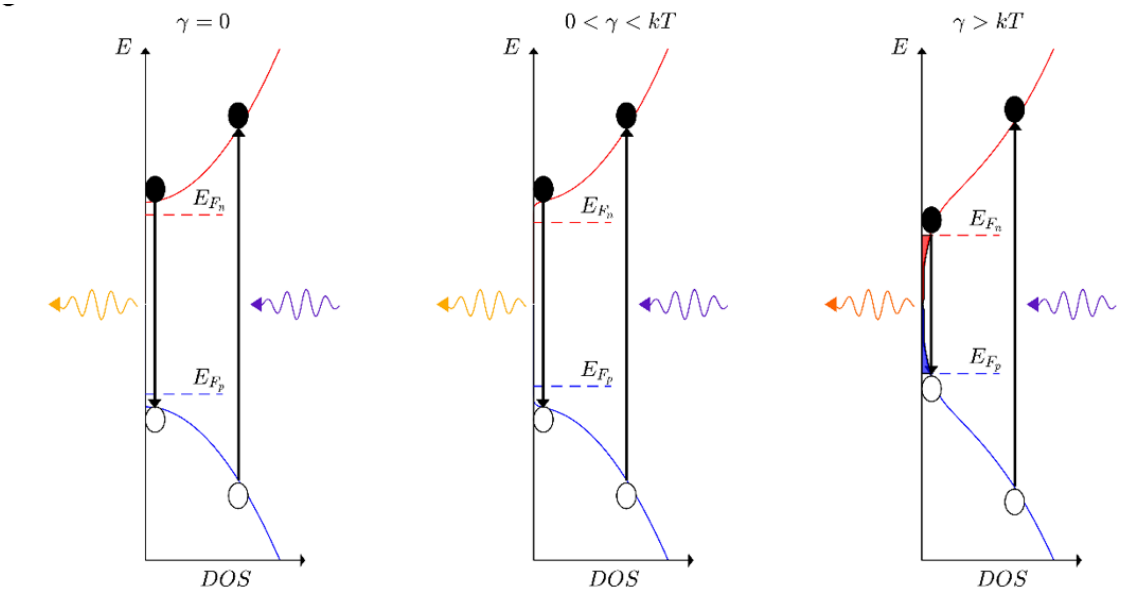

Figure 2.9 Schematic depiction of the density of states profile along and photogeneration, relaxation and radiative recombination of carriers for a semiconductor with different Urbach parameters.

2.3.1 Effect in Weakly Absorbing Limit and Limit of Imperfect Sub-gap Carrier Collection

The effects outlined above assumed that $\alpha_0 L = 10$ so that the cell was thick enough to absorb all incident photons and the EQE above gap was unity. In addition, we assumed that the sub-gap carrier collection was perfect. Below, we detail the effect of sub-gap absorption in the weakly absorbing limit and in the limit of imperfect sub-gap carrier collection.

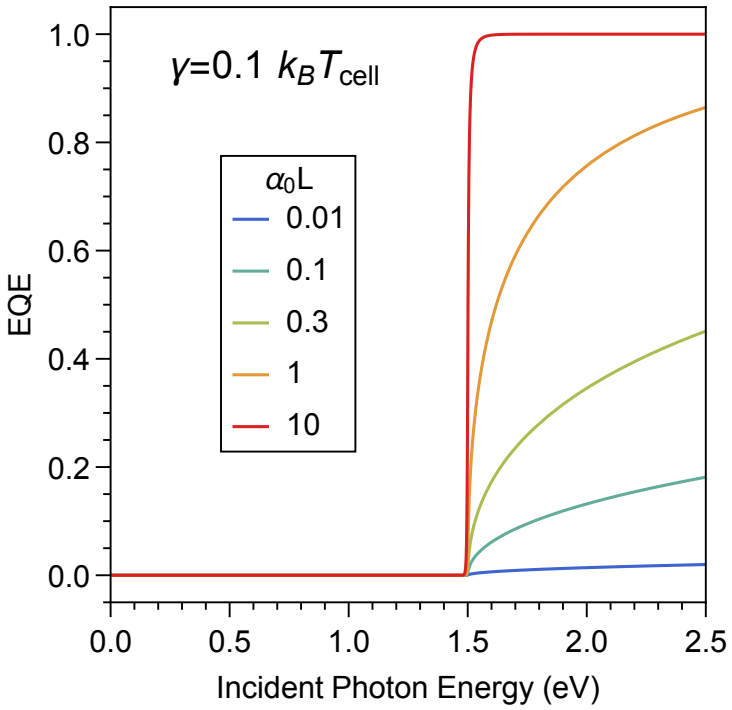

Figure 2.10 Spectral response for a 1.5 eV band gap solar cell with different absorber thicknesses and an Urbach parameter of 0.1 k_BT.

Figure 2.10 shows the spectral response of a 1.5 eV band gap solar cell with an Urbach energy equal to 0.1 k_BT for varying ranges of incomplete absorption. In the weakly absorbing limit the effect of the Urbach parameter on the photovoltaic figures of merit is much the same as in the case of complete absorption (Fig. 2.11). The V_{oc} decreases significantly for $\gamma > k_BT$ but the V_{oc} is slightly less than that predicted by S-Q theory for weaker absorption. This stems

from the significant decrease in the photogenerated current and thus $J_{sc,}$ owing to incomplete absorption of the incident solar spectrum. Again, this drastic decrease in open-circuit voltage leads to a significant decrease in the ultimate device efficiency for large Urbach parameters, though the obtainable efficiency is lower than the S-Q limit even at low values of γ due to the deficit in J_{sc}.

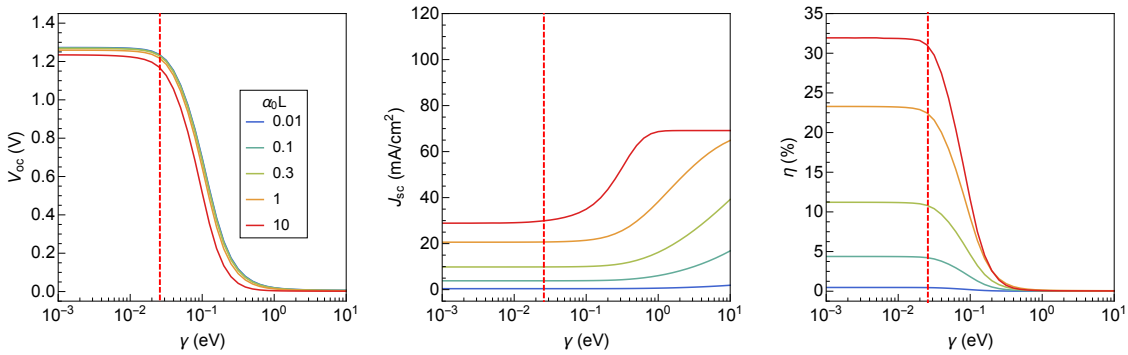

Figure 2.11 Photovoltaic performance metrics for a 1.5 eV solar cell as a function of Urbach energy for different levels of incomplete above-gap absorption. The red lines indicate the thermal energy k_BT.

In contrast, to the weakly absorbing limit, imperfect carrier collection has the effect to tolerate larger amounts of sub-gap absorption. In reality, the sub-gap carrier collection efficiency is a complicated function of the physical origin of the defects and of the sub-gap band structure. For simplicity, here we consider constant below-gap carrier collection efficiencies ranging from 10^{-8} to 1 (Fig. 2.12) and assume we are still in the radiative limit, though we note that further analysis of the exact relationship between carrier collection and external radiative efficiency is needed. Decreasing the sub-gap carrier collection efficiency effectively makes the sub-gap states dark, preventing carrier collection from those states. Thus, for low carrier collection efficiencies, increased sub-gap absorption from an increase in the Urbach parameter has a muted effect and the figures of merit for solar cell performance are only effected at subsequently larger Urbach parameters.

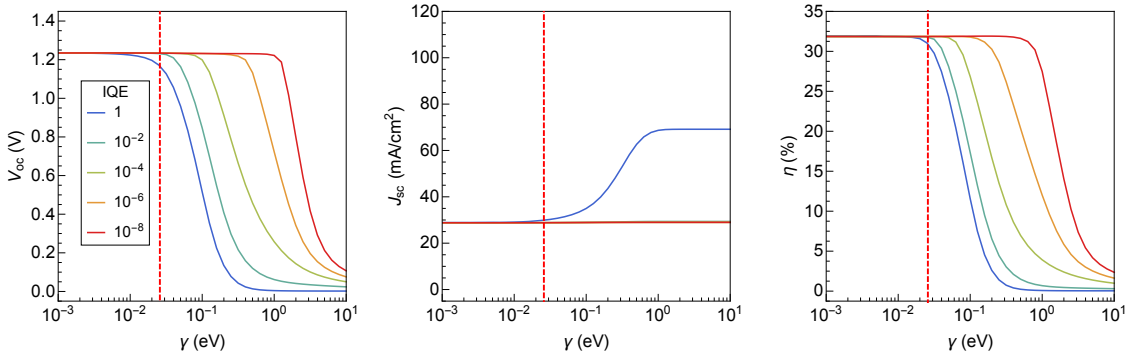

Figure 2.12 Photovoltaic figures of merit as a function of Urbach parameter for a 1.5 eV band gap solar cell with varying sub-gap carrier collection efficiencies. The red dashed lines indicate the thermal energy k_BT.

2.4 Conclusion and Outlook

Detailed balance is a useful tool to analyze absorbing (and by reciprocity, emitting) materials. In the case of solar cells, our modified detailed balance model can be used to calculate the realistic efficiency limits of photovoltaic materials with sub-gap absorption that arises from defects and disorder. Using this model, we find that the S-Q model drastically overestimates the efficiency limits of materials with large sub-gap absorption (i.e. large Urbach parameters) and that even weak sub-gap absorption can have significant effects on the cell's achievable open-circuit voltage and efficiency. The effects on V_{oc} manifest in the cell's photoluminescence leading to a broadening and red-shift of the luminescence peak. Our work therefore suggests that it is prudent to carefully measure the absorption edge (or photoluminescence) when evaluating photovoltaic materials. Furthermore, the general nature of this model and the fundamentality of the sub-gap density of states in semiconductors implies that our findings are likely relevant for other luminescent devices (e.g. lasers and light emitting diodes).

Chapter 3

The Effect of Excitons on Photovoltaic Performance: A Case Study in Cu_2O

3.1 Introduction

Materials that can act as the top cell in a dual-junction architecture with traditional solar cells like silicon (Si), cadmium telluride (CdTe), and copper indium gallium diselenide (CIGS) could potentially reduce the levelized cost of electricity by producing increased photovoltaic efficiencies (*16*). Novel materials could also provide optionality for ultrathin, flexible photovoltaic technologies (*16, 49-51*). The performance of photovoltaics is generally evaluated using the "free carrier" (FC) device model, in which the negatively charged electron and positively charged hole are treated as independent, non-interacting particles. However, substantial interactions between charge carriers can lead to the formation of excitons, comprising a coulombically bound state between a photo-excited electron in the conduction band and a hole in the valence band. For Si, CdTe, and GaAs, the interaction between the electron and hole is weak, with exciton binding energies of 15, 10 and 4 meV, respectively (*52-54*). Excitonic binding energies less than the thermal energy at room temperature (25.6 meV) allow for facile dissociation of photogenerated excitons into free electrons and holes at room temperature. Even in these devices, the role of excitons may be important in certain device configurations (*55-57*).

Many emerging photovoltaic materials, however, exhibit large exciton binding energies ($>>k_BT$, see Table 3.1), so appreciable exciton densities are present at room temperature. For example, cuprous oxide (Cu_2O), a promising candidate material for the top cell in a tandem solar cell with Si, has an exciton binding energy (E_x) of 151 meV (*58*). Cu_2O has been the subject of intense investigation of the Bose-Einstein condensation phenomenon, which

requires extremely large exciton densities (~10^{18} cm^{-3}) (*59-62*). Additionally, these large exciton densities lead to excitonic charge transport in Cu/Cu_2O Schottky junctions even at room temperature (*63-65*).

Material	E_x [meV]	ϵ
GaAs	4.2 (*54*)	12.9 (*54*)
Si	15.0 (*52*)	11.9 (*21*)
CdTe	10.0 (*53*)	11.0 (*36*)
ZnO	60 (*66*)	8.6 (*67*)
Cu_2O	150 (*68*)	7.0 (*69*)
m-WS_2	710 (*70*)	20 (*71*)
m-MoS_2	910 – 1100 (*72, 73*)	25 (*71*)

Table 3.1 Exciton binding energies (E_x) and dielectric constants for established and emerging photovoltaic materials. The exciton binding energy scales with the inverse square of the dielectric constant.

In the following, we examine how photovoltaic device performance is effected by the incorporation. In particular, we demonstrate that in materials with large exciton binding energies, such as Cu_2O, excitons play a fundamental role in photovoltaic operation and that the FC model consequently underestimates the potential photovoltaic device efficiency. Specifically, the Saha-Langmuir equation, which governs ionization events, has been used to calculate the branching ratio at quasi-equilibrium between free electrons and holes and excitons as a function of temperature and total-excitation density. The exciton densities have been investigated experimentally under visible illumination by examination of a free exciton peak in the photoluminescence spectrum of Cu_2O at room temperature. The photovoltaic device performance has also been evaluated by comparing traditional FC device physics models to models that include levels of excitonic transport that are consistent with both theoretical and experimental results.

3.2 Equilibrium Concentration of Excitons

When an exciton is created by absorption of a photon, the exciton diffuses to the device junction, where a strong electric field ionizes the exciton into a free electron and hole that are subsequently collected as current. The extent of excitonic effects in a photovoltaic device is therefore governed during solar cell operating conditions by the branching ratio between free carriers and excitons.

The exciton Bohr radius of technologically relevant semiconductors is typically 1-50 nm, which implies that exciton-exciton interactions occur only for exceedingly large exciton densities (> 10^{19}-10^{20} cm^{-3}). This process can, therefore be neglected during normal photovoltaic operation, under 1-100 Sun illumination intensities for most photovoltaic semiconductors (*74*). Under such conditions, the interchange between the charge-neutral exciton and its ionized state, a free electron and hole, can be modeled in accord with the ionization of an ideal gas.

Consider the entropy of a "gas" containing the concentration n_x of excitons in coexistence with their ionized states electrons and holes with concentrations n_e and n_h, respectively,

$$S = k_B \ln\left(\frac{M_e!}{(M_e-n_e)!n_e!}\right) + k_B \ln\left(\frac{M_h!}{(M_h-n_h)!n_h!}\right) + k_B \ln\left(\frac{M_x!}{(M_x-n_x)!n_x!}\right) \quad (1)$$

where M_i is the concentration of available states for the i^{th} particle and k_B is Boltzmann's constant. Then using Sterling's approximation $\ln(n!) \approx n\ln(n) - n$ for large n gives:

$$k_B \ln\left(\frac{M_i!}{(M_i-n_i)!n_i!}\right) \approx k_B[M_i \ln(M_i) - n_i \ln(n_i) - (M_i - n_i)\ln(M_i - n_i) - M_i - (M_i - n_i)]$$

$$= k_B\left[M_i \ln(M_i) - n_i \ln\left(M_i \frac{n_i}{M_i}\right) - (M_i - n_i)\ln\left(M_i\left(1 - \frac{n_i}{M_i}\right)\right) + n_i\right]$$

$$= k_B\left[M_i \ln(M_i) - n_i \ln\left(M_i \frac{n_i}{M_i}\right) - (M_i - n_i)\ln\left(M_i\left(1 - \frac{n_i}{M_i}\right)\right) + n_i\right]$$

$$= k_B\left[M_i \ln(M_i) - n_i\left(\ln(M_i) + \ln\left(\frac{n_i}{M_i}\right)\right) - (M_i - n_i)\ln M_i \ + \ln(1 - \frac{n_i}{M_i}) + n_i\right]$$

Then cancelling terms and using $M_i \gg n_i$ yields

$$\approx k_B\left[-n_i \ln\left(\frac{n_i}{M_i}\right) + n_i\right] \tag{2}$$

So that the entropy of the exciton-free carrier system is

$$S = k_B\left[-n_e \ln\left(\frac{n_e}{M_e}\right) - n_h \ln\left(\frac{n_h}{M_h}\right) - n_x \ln\left(\frac{n_x}{M_x}\right) + n_e + n_h + n_x\right]$$

Then the total free energy is given by

$$G = n_e E_g + n_x(E_g - E_x) + k_B T\left[-n_e \ln\left(\frac{n_e}{M_e}\right) - n_h \ln\left(\frac{n_h}{M_h}\right) - n_x \ln\left(\frac{n_x}{M_x}\right) + n_e + n_h + n_x\right]$$

where we have set the potential energy scale to zero at the valence band such that $U_e = E_c = E_g$, and $U_x = E_c - E_b = E_g - E_x$ and E_x is the exciton binding energy. The total density of states is simply given by the inverse of the volume occupied by each quasiparticle (taken as the cube of the particles thermal wavelength) $M_i^{-1} = v_i = \lambda_i^3,\ \lambda_i = \frac{h}{\sqrt{2\pi m_i k_B T}}$, where m_i is the mass of the i^{th} particle and h is the Planck constant. Substituting into the free energy yields

$$G = n_e E_g + n_x(E_g - E_x) + k_B T[-n_e \ln(n_e v_e) - n_h \ln(n_h v_h) - n_x \ln(n_x v_x) + n_e + n_h + n_x] \tag{3}$$

Under illumination, the total photo-generated carrier density N, is equal to the sum of the density of photo-generated excitons and electrons, i.e., $N = n_e + n_x$, then $n_e = N - n_x$. Substituting into Eq. 3.3 and using the fact that the electron and hole concentrations are equal ($n_h = n_e = N - n_x \equiv n_{eh}$, where n_{eh} is the free carrier concentration) gives

$$G = (N - n_x)E_g + n_x(E_g - E_x) + k_B T\left[-2(N - n_x)\ln\left((N - n_x)v_e\right) - n_x \ln(n_x v_x) + 2N - n_x\right]$$

Thermal equilibrium occurs at the minimum of the free energy (namely, $\frac{dG}{dn_x} = 0$) resulting in the following equation

$$E_x + k_B T\left[\ln\left(\frac{\left((N-n_x)v_e\right)^2}{n_x v_x}\right)\right] = 0$$

Rearranging and defining the fraction of free carriers $x = \frac{n_{eh}}{N}$ gives the Saha-Langmuir equation (*75*):

$$\frac{x^2}{1-x} = \frac{1}{N} * \left(\frac{2\pi\mu k_B T}{h^2}\right)^{\frac{3}{2}} e^{-\frac{E_x}{k_B T}} \quad (4)$$

where μ is the reduced exciton mass. Thus, the concentration of free electrons and holes and the concentration of excitons depends on the exciton binding energy E_x, which determines the time before excitons dissociate into free carriers, as well as the total excitation density N, which governs the probability of a free electron and free hole interacting to form an exciton. In particular, Equation 3.4 shows that the fraction of free carriers (x) increases with temperature, as the thermal energy approaches E_x and a larger number of excitons thus dissociate into free carriers. The fraction of excitons also increases with increasing excitation density, because the probability of free electron and holes binding into excitons also increases.

The Saha-Langmuir equation is a powerful tool to estimate the quasi-equilibrium exciton density in material systems and requires only knowledge of the reduced exciton mass and exciton binding energy (*76, 77*). For materials with large binding energies (>> $k_B T$), Equation 3.4 implies large exciton densities may occur even at room temperature. Figure 3.1 shows the calculated free electron and hole fractions in Cu_2O as a function of the total excitation density, as T is varied form room temperature down to 40 K. The shaded region labeled "PV

Regime" refers to the total, steady-state generated excitation density in Cu_2O (where an excitation can be either an exciton or free carriers) under standard photovoltaic operating conditions. The absorbed solar flux was estimated by integrating the absorption in Cu_2O over the standard Air Mass (AM) 1.5 solar spectrum, that is,

$$N_{gen} = \tau_x \int AM\ 1.5(E)\ \alpha(E)\ dE$$

In Cu_2O, the ground-state exciton is split by the spin exchange into a spin singlet "paraexciton" state and a spin triplet "orthoexciton" state, with the orthoexciton lying 12 meV higher than the paraexciton (*78, 79*). The inversion symmetry of the Cu_2O crystal makes the paraexciton transition dipole- and quadrupole-forbidden, and the orthoexciton dipole-forbidden. This characteristic leads to long exciton lifetimes for both the paraexciton and orthoexciton. The small energetic splitting between the ortho- and paraexcitons causes fast exchange (on the picosecond timescale) between the two states. Consequently, for temperatures relevant to photovoltaic operation, the ortho- and paraexciton lifetimes are mutually similar, and the "excitonic" lifetime is given by the fastest radiative decay. The paraexciton lifetime has been measured to be as large as 14 μs – 10 ms (*59, 80, 81*). However, at room temperature, the orthoexciton lifetime has been measured to be 350 ns (*82, 83*). We have thus conservatively estimated the lifetime as 100 ns to 10 μs, which yields a steady-state excitation density between 10^{15} and 10^{17} cm^{-3}. Hence, at the excitation densities expected during photovoltaic cell operation, excitons represent a substantial fraction, greater than 20%, of the total excitation density in Cu_2O. In the high exciton lifetime limit, the branching ratio is as high as 28% at T = 300 K, and at lower temperatures, excitons become the dominant charge-carrier population.

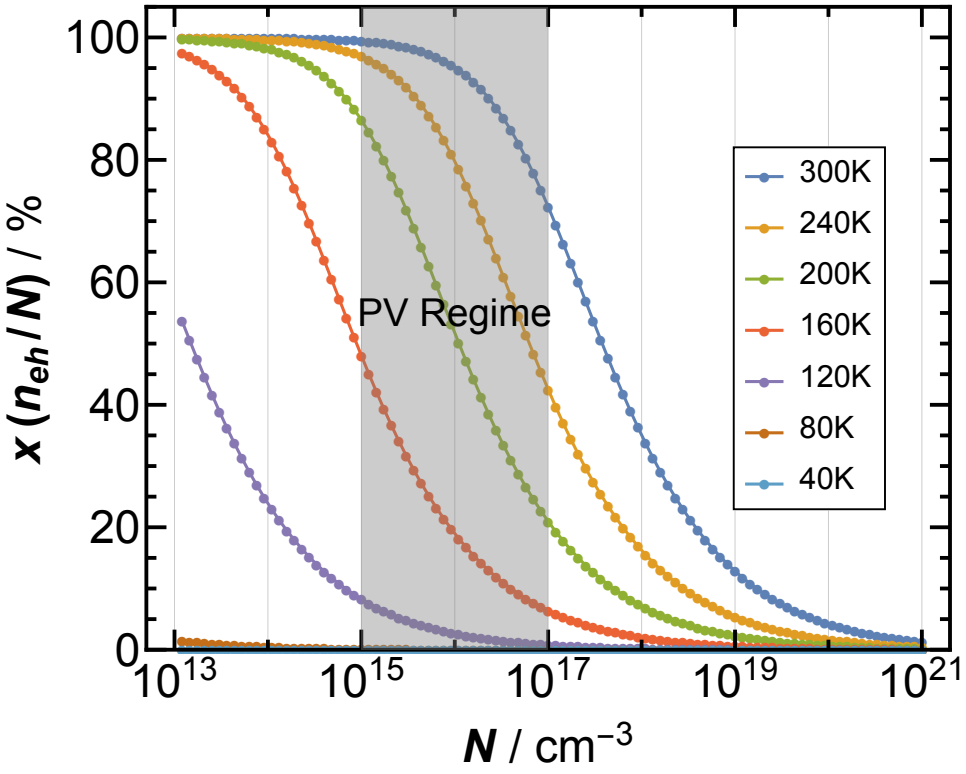

Figure 3.1 The fraction of free electrons and holes relative to the total excitation density $\left(x = \frac{n_{eh}}{N}\right)$ in Cu_2O. The upper limit of the branching ratio between excitons and free electrons and holes during photovoltaic operation is 27.7%, suggesting that substantial exciton densities should be present during typical device operating conditions.

3.3 Experimental Observations of Excitons in Cu_2O Photovoltaics

The large exciton concentrations predicted by the Saha-Langmuir equation (as much as 28% of the total photo-generated carrier population at room temperature under photovoltaic operating conditions) suggest that excitonic signatures should be experimentally observable in Cu_2O and Cu_2O-based devices. In this section, we detail the experimental methods and results for the growth of Cu_2O substrates, exciton photoluminescence measurements, and photovoltaic device fabrication and characterization.

3.3.1 Growth of Cu_2O substrates

Cu_2O substrates were prepared by two different techniques: 1) thermal oxidation of Cu foil, which tended to lead to polycrystalline samples, and 2) the floating zone method, which produced single crystalline substrates.

High purity (99.9999%, 0.5 mm thick, Alfa Aesar) Cu foil was used to produce the polycrystalline Cu_2O wafers. The growth process used in this study was based off of other growth procedures from our labs and elsewhere that resulted in high efficiency Cu_2O based devices (*84-86*). Our preparation is as follows. The foils were cut into squares with ~ 1 cm sides, cleaned, and suspended from a quartz hanger. The hanger assembly was heated in a quartz tube under N_2(g) to 1025 °C at 1000 °C/h. The foils were then oxidized in air for 24 h and cooled under N_2(g) to room temperature. The resulting substrates were ~ 0.8 mm thick and the grain size of these wafers was typically of the order of several millimeters and in some cases almost the size of the entire wafer (~1 cm^2). Hall measurements indicated that the polycrystalline wafers had carrier concentrations of ~10^{13} cm^{-3} and hole mobilities ~65 $cm^2/V \cdot s$. The polycrystalline substrates were used to fabricate Cu_2O/Zn(O,S) heterojunction photovoltaics (whose fabrication is discussed in detail later).

The other Cu_2O growth technique, the floating zone method, was used to produce high-quality, single crystalline substrates. Feed and seed rods were grown by the thermal oxidation of high-purity Cu rods (Alfa Aesar, 99.999%) in a vertical tube furnace (Crystal Systems Inc.) in air for 100 h at 1050 °C. The rods were then cooled in N_2 at 120 °C/h. Prior to growth, the rods were cleaned in acetone and etched using dilute nitric acid (0.1 M) for 60 seconds. The rods were suspended by either Cu or Pt wire. Single crystals were grown in an optical floating zone furnace (CSI FZ-T-4000-H-VII-VPO-PC). Crystals were grown in air with the seed and feed rods counter-rotating at 7 rpm. Single crystallinity was confirmed using x-ray diffractometry and pole figure analysis. The resulting single crystalline boules were diced into wafers along the growth axis and mechanically polished to a specular finish using diamond grit. For further information regarding the floating zone process and single crystal preparation and characterization see Appendix B.

3.3.2 Photoluminescence of the Exciton Peak in Cu_2O

At low temperature (4 K), cuprous oxide exhibits a peak in its photoluminescence (PL) spectrum due to the recombination of the free orthoexciton at 610 nm as well as several phonon-assisted exciton luminescence peaks at slightly lower energies (*59, 87-90*). At higher temperature the peak redshifts and thermally broadens, becoming convoluted with the Γ_{12} phonon-assisted peak, which is only separated by 13.6 meV from the exciton peak (*82, 90*).

A Ti:sapphire laser (Libra, Coherent Inc.) with a fundamental 800 nm laser pulse, 120 fs pulse width, and 10 kHz repetition rate was used to pump an optical parametric amplifier (Opera Solo, Coherent Inc.) and generate visible light. Single crystalline Cu_2O wafers grown by the float-zone method were illuminated with wavelengths ranging from 400 to 550 nm. The time-averaged photoluminescence spectra were collected using a time-correlated single-photon-counting method using a streak camera (Hamamatsu Inc.) with 20 ps time resolution.

Figure 3.2 shows the photoluminescence spectra of the orthoexciton peak in our single crystalline Cu_2O samples grown by the floating zone method for a selection of optical excitation wavelengths at $T = 300$ K. The orthoexciton peak was observed for all excitation energies below the Cu_2O electronic band edge (2.1 eV, 590 nm). Observation of the orthoexciton peak at 300 K under visible light excitation is direct evidence of the photo-generation of excitons at room temperature under conditions relevant to photovoltaic operating conditions.

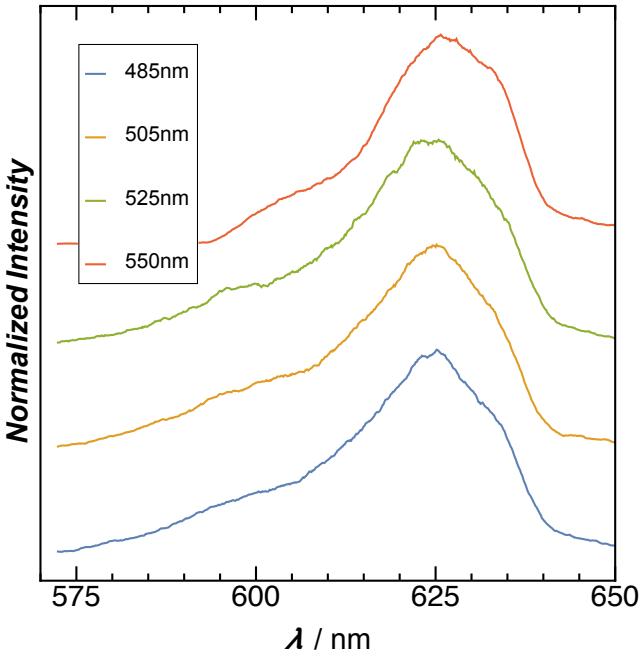

Figure 3.2 Photoluminescence spectra of the free exciton peak in Cu_2O at room temperature under different visible light excitation. The free exciton peak is observed for all excitations above the Cu_2O band gap.

Room temperature photoluminescence spectra were also collected for the polycrystalline Cu_2O wafers grown by thermal oxidation, which were used in device fabrication. The spectra were collected using a 514 nm excitation for powers ranging from 85 μW to 5.4 mW. The photoluminescence spectrum near the orthoexciton luminescence peak is shown in Figure 3.3. The unusual peak shape is due to the convolution of the orthoexciton peak and the phonon-assisted exciton peak, which broadens and grows at higher temperatures where the absorption probability of phonons by excitons is large (*88-90*). The peak was evident even at the lowest of excitation powers (0.85 μW). Thus, excitons are generated under visible excitation even in polycrystalline Cu_2O substrates used in photovoltaic fabrication.

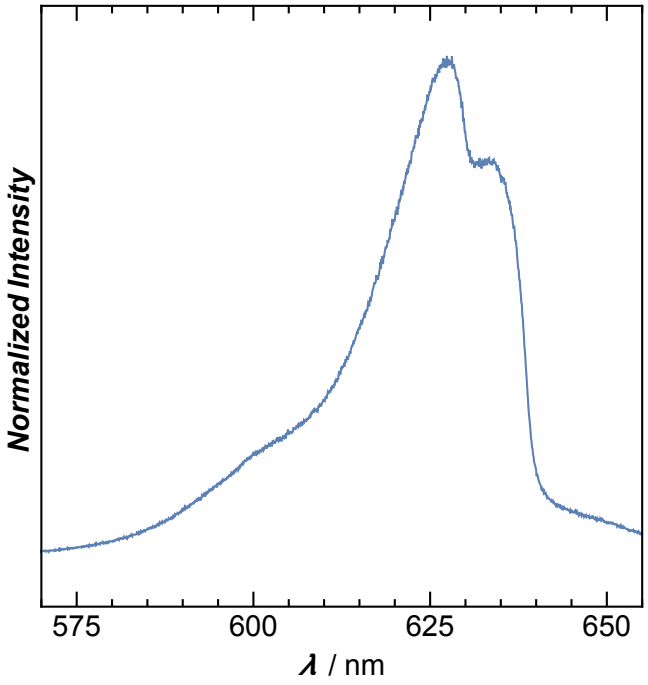

Figure 3.3 Photoluminescence spectrum of the free exciton peak in thermally oxidized, polycrystalline Cu_2O wafers at room temperature using a 2.4 mW, 514 nm excitation.

3.3.3 Excitons in the Spectral Response of Cu_2O-based Photovoltaics

Given the large exciton densities observed in Cu_2O through photoluminescence measurements, Cu_2O-based photovoltaics were fabricated in order to investigate excitonic signatures in solar cell performance. Photovoltaic devices in this work were fabricated on the polycrystalline Cu_2O wafers grown by thermal oxidation of copper foil with a sputtered Zn(O,S) window layer, and an indium tin oxide (ITO) top contact and a Au back contact (*84*). The photovoltaic cells in this study were fabricated using a circular shadow mask resulting in an ultimate cell size ~0.02 cm^2 so that individual solar cells were generally isolated to only 1 or 2 grains.

Prior to fabrication, the polycrystalline Cu_2O substrates were cleaned with isopropanol and loaded into a magnetron sputtering system with a base pressure of 1.7×10^{-7} Torr. The Cu_2O

wafers were heated in vacuum for 90 min at 100 °C. A 45 nm layer of Zn(O,S) was co-sputtered from ZnO and ZnS targets at a working pressure of 5 mTorr Ar. The power on the ZnO target was 100W and the power on the ZnS target was 85W. After deposition, the samples were cooled to room temperature in vacuum and removed from the chamber. A shadow mask was placed over the samples and a 60 nm ITO layer was sputtered at 50 W in an Ar atmosphere with a working pressure of 3 mTorr at room temperature. A 100 nm Au back-contact was then sputter deposited on the back of the sample.

Figure 3.4 shows the spectral response of a typical Cu_2O /Zn(O,S) cell. The spectral response measurements were performed using a Xe arc lamp and slit monochromator (Newport Inc.), and a calibrated reference Si photodiode (Thor Labs Inc.) with a known spectral responsivity. The external quantum yield approached zero at 650 nm, which is consistent with the 1.91 eV optical band edge in Cu_2O. However, the quantum yield was substantial in the region between the Cu_2O electronic band gap (2.1 eV, 591 nm) and the Cu_2O optical band gap (1.91 eV, 650 nm). In this region, absorption of a photon generates an exciton, so the current collection below 2.1 eV must be attributed solely to excitonic transport (*60, 88*). A similar spectral response characteristic has been observed in high-quality Cu/Cu_2O Schottky diodes with the current collection in the exciton region explained by exciton diffusion to the Schottky junction followed by ionization of the exciton into an electron and hole by the strong electric field in the depletion region (*65, 91*). The current in the excitonic region accounts for 9.3% of the short-circuit current density of the Cu_2O/Zn(O,S) cells. Although this value is less than the ~27% predicted by the branching ratio, the 9.3% value does not account for excitonic transport in the region having excitation energies greater than 2.1 eV, where the PL data indicate that excitons are also generated. Aside from direct generation through bandgap absorption of a photon, excitons may also form via free carrier relaxation processes, such as when “hot” carriers that arise from above-band-gap photon absorption thermally relax to the band edge. These free carrier cooling mechanisms may further contribute to excitonic transport in the region in which excitation energies are > 2.1 eV. The presence of substantial external quantum yield in our Cu_2O/Zn(O,S) solar cells even at the low light intensities (<< 1 Sun) of spectral response measurements is clear evidence that

exciton diffusion provides a fundamental charge transport mechanism in Cu_2O photovoltaics.

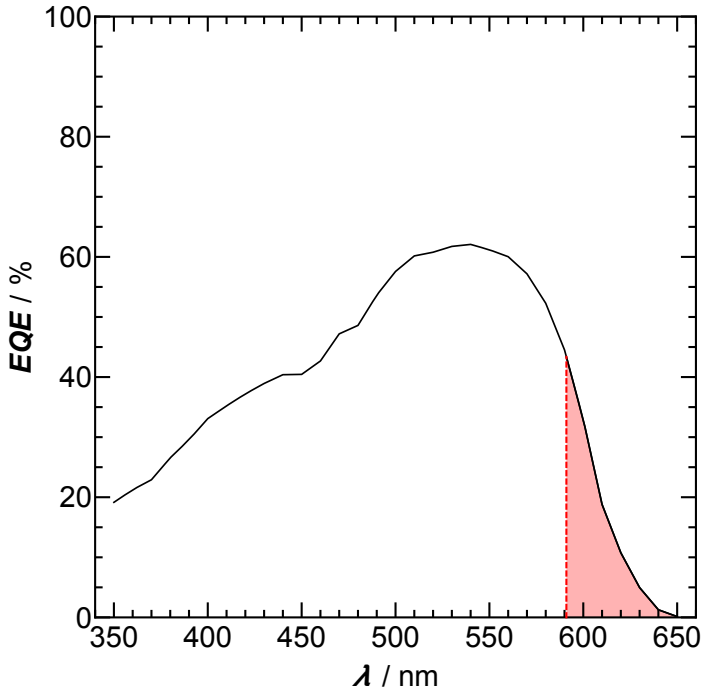

Figure 3.4 Spectral response of a polycrystalline Cu_2O /Zn(O,S) solar cell. The red dashed line indicates the Cu_2O electronic band gap beyond which, in the shaded region, are wavelengths for which only excitons can exist.

3.4 The Role of Excitons in Photovoltaic Device Physics

The current-voltage characteristics of a solar cell can be expressed by the diode equation:

$$J = J_0 \left[e^{\frac{q(V-JR_S)}{k_B T}} - 1 \right] + \frac{V+JR_S}{R_{sh}} - J_{sc} \tag{5}$$

where J is the total current density, J_0 is the dark saturation current density, q is the unsigned fundamental electronic charge, V is the voltage, R_s is the area-normalized series resistance, R_{sh} is the area-normalized shunt resistance, and J_{sc} is the short-circuit current density. Thus,

J_0 and J_{sc} are fundamental parameters that ultimately govern the solar-cell efficiency. Traditionally, J_0 and J_{sc} are solved for using the free-carrier model in which electrons and holes are treated as independent, non-interacting particles and any exciton effects are neglected. However, several studies have shown that even materials with relatively small steady-state exciton densities (e.g., Si, CdTe), excitons can have a large effect on photovoltaic performance in certain device configurations (*55-57*). Hence, it is expected that in materials with room temperature exciton densities, such as Cu_2O, excitons could play a significant role in the device physics. We therefore use a device model that accounts for excitonic effects.

3.4.1 Device Model Including Excitons

Cu_2O is intrinsically p-type due to the thermodynamic favorability of copper vacancy formation and the absence of an n-type doping scheme. Our cell has thus been modeled as a simplified, "one-sided" p-n^+ junction with an infinite p-type base and a negligibly thin n-type emitter subject to the following assumptions: (1) the depletion approximation; (2) the drift and diffusion currents are opposite and equal in magnitude within the depletion region; (3) recombination is neglected in the depletion region; (4) the solar cell is operating in low-level injection; (5) in the bulk, minority carriers flow by diffusion (*92*). The inclusion of excitons requires the modification of the "free carrier" model to include an additional term that accounts for the exchange between the excitons and free-carrier populations. In this case, the excess minority- carrier (Δn_e) and excess exciton (Δn_x) concentrations are governed by the following coupled differential equations:

$$D_e \frac{d^2 \Delta n_e}{dz^2} = \frac{\Delta n_e}{\tau_e} - G_e e^{-\alpha z} + b(\Delta n_e N_A - \Delta n_x n^*) \quad (6)$$

$$D_x \frac{d^2 \Delta n_x}{dz^2} = \frac{\Delta n_x}{\tau_x} - G_x e^{-\alpha z} - b(\Delta n_e N_A - \Delta n_x n^*) \quad (7)$$

where D is the diffusion coefficient, τ is the lifetime, and G is the wavelength-dependent generation rate (*55*). The subscripts e and x refer to electrons and excitons, respectively. The third term in Eq. 3.6 and 3.7 is the net rate at which electrons and holes bind to form excitons, and is derived from the law of mass action, where b is the coefficient for binding free carriers into excitons, N_A is the p-type doping density and n^* is the equilibrium constant for the exchange between excitons and free carriers (in equilibrium $n^* n_x = n_e n_h$). Further, free carriers and excitons were assumed to be in quasi-equilibrium at the edge of the depletion region. The coupled differential equations yield analytical solutions for the dark saturation current density, J_0, and the short-circuit current density, J_{sc},:

$$J_0 = eD_e n_0 \left(\frac{\gamma}{L_1} + \frac{1-\gamma}{L_2}\right) + eD_x n_x^0 \left(\frac{\zeta}{L_1} + \frac{1-\zeta}{L_2}\right) \tag{8}$$

$$J_{sc} = eG_e \left(\frac{\gamma}{\alpha + L_1^{-1}} + \frac{1-\gamma}{\alpha + L_2^{-2}}\right) + eG_x \left(\frac{\zeta}{\alpha + L_1^{-1}} + \frac{1-\zeta}{\alpha + L_2^{-2}}\right) \tag{9}$$

where e is the fundamental unsigned charge on an electron; n_0 and the n_x^0 are the equilibrium concentrations of electrons and excitons, respectively; and α is the wavelength-dependent absorption coefficient (*56*). Additionally:

$$\gamma = \frac{1}{2} - \frac{M_\Delta + \frac{2M_{21}D_x}{D_e}}{2\sqrt{\delta}} \tag{10}$$

$$\zeta = \frac{1}{2} + \frac{M_\Delta - \frac{2M_{12}D_e}{D_x}}{2\sqrt{\delta}} \tag{11}$$

$$L_1 = \frac{1}{\sqrt{\varepsilon_1}} \tag{12}$$

$$L_2 = \frac{1}{\sqrt{\varepsilon_2}} \tag{13}$$

$$\varepsilon_1 = \frac{1}{2}(M_{11} + M_{22} - \sqrt{\delta}) \tag{14}$$

$$\varepsilon_2 = \frac{1}{2}(M_{11} + M_{22} + \sqrt{\delta}) \tag{15}$$

$$M_{\Delta} = M_{11} - M_{22} \tag{16}$$

$$\delta = M_{\Delta}^2 + 4M_{12}M_{21} \tag{17}$$

$$M_{11} = \left(\frac{1}{\tau_e} + bN_A\right)\frac{1}{D_e} \tag{18}$$

$$M_{22} = \left(\frac{1}{\tau_e} + bn^*\right)\frac{1}{D_x} \tag{19}$$

$$M_{12} = -\frac{bn^*}{D_e} \tag{20}$$

$$M_{21} = -\frac{bN_A}{D_x} \tag{21}$$

The "free carrier" solutions for the dark saturation and short-circuit current densities, respectively, for an *p*-n^+ solar cell are given by:

$$J_{0,FC} = -\frac{eD_e\Delta n_0}{L_e} \tag{22}$$

$$J_{sc,FC} = \frac{eG_e}{\alpha + L_e^{-1}} \tag{23}$$

Equation 3.22 and 3.23 were used to compare the performance of the excitonic model to that of the traditional "free carrier" model. The major effect of excitons, effecting a coupling between the electron and hole population and exciton population, alters the diffusion characteristics of both free carriers and excitons, as can be seen from Eqs. 3.8-3.9 and 3.22-3.23. Thus, a fraction γ of photogenerated electrons move with a diffusion length L_1 and the remaining photogenerated electrons (1-γ) diffuse with a diffusion length L_2, where L_1 and L_2 are effective diffusion lengths that account for the interactions between the exciton and free carrier populations. Similarly, a portion of photogenerated excitons ζ and the remaining exciton fraction (1-ζ) have diffusion lengths L_1 and L_2, respectively.

3.4.2 Model Parameters for Cu_2O

Equation 3.8 and 3.9 are fundamentally dependent on the experimentally measured parameters D and τ, which are affected by temperature and doping density. The performance of the p-n^+ Cu_2O solar cell can then be evaluated a function of temperature and N_A. The dependence of the exciton binding energy on doping density can be estimated assuming that the exciton binding energy falls off to zero as the doping density approaches the Mott density:

$$E_x = E_{x\infty}\left[1 - \sqrt{\frac{N_A}{n_{Mott}}}\right]^2 \tag{24}$$

where $E_{x\infty}$ is the unscreened exciton binding energy, 150 meV in Cu_2O (*91, 93*). The Mott density was estimated using the value for Si as a function of temperature:

$$n_{Mott} = 10^{16}\frac{a_B^{Si}}{a_B^{Cu_2O}}\frac{\varepsilon^{Si}}{\varepsilon^{Cu_2O}}\,T \tag{25}$$

where a_B is the exciton Bohr radius and ε is the dielectric constant. The superscripts Si and Cu_2O refer to silicon and Cu_2O, respectively. The unscreened exciton binding energy is assumed to be independent of temperature.

The electronic band gap E_g of Cu_2O was measured down to 4 K using the threshold energy of the free exciton peak in the photoluminescence spectrum. The temperature dependence of E_g was fit using an oscillator model that accounts for exciton-phonon coupling:

$$E_g(T) = E_g(0) + S\hbar\omega - S\hbar\omega\coth\left(\frac{\hbar\omega}{2k_BT}\right) \tag{26}$$

where $E_g(0) = 2.173$ eV is the electronic band gap at $T = 0$ K, $S = 1.89$ is a material specific constant, and $\hbar\omega = 13.6$ meV is the phonon energy of the phonon (Γ_{12}^-) emitted during exciton luminescence (*90*).

The electron mobility was estimated from majority-carrier data in literature. The effect of temperature and doping density on the majority carrier mobility was estimated as:

$$\frac{1}{\mu_h} = \frac{1}{\mu_T} + \frac{1}{\mu_I} \tag{27}$$

where

$$\mu_T = 8511 \times 10^{-0.00643T} \tag{28}$$

is the mobility caused by lattice vibrations, with the value determined from as-grown Cu_2O crystals (*94, 95*). Empirical data for the mobility as a function of hole concentration due to Na doping was used as an interpolating function in the model for μ_I (*96*).

The minority-carrier lifetime is an important materials property that plays a significant role in determining the performance of solar cells in the free carrier model. Generally, the electron lifetime is estimated from the electron diffusion length fit from the external quantum efficiency, and varies from ~100 ns for undoped samples to on the order of ~ 1 ns for doped samples (*85, 97*). As such, we have estimated the electron lifetime as:

$$\tau_e = \frac{100}{1+10^{-16}\, N_A} \tag{29}$$

The lowest lying exciton states in Cu_2O are the spin singlet "paraexciton" and spin triplet "orthoexciton", which are split by a spin exchange, with the paraexciton lying 12 meV lower than the orthoexciton. The paraexciton transition is dipole- and quadrupole-forbidden, and the transition is dipole-forbidden for the orthoexciton due to inversion symmetry of the Cu_2O crystal. This behavior leads to long-lived exciton states; the paraexciton lifetime, for example, has been measured to be > 14 μs at low temperatures (*59*). The small energetic splitting between the two states causes the orthoexciton to decay into the paraexciton state on the picosecond time scale, while paraexcitons up-convert to orthoexcitons at the same rate (*82, 98*). Consequently, for temperatures relevant to photovoltaic operation, the ortho- and paraexciton lifetimes are the same, given by the most rapid recombination pathway. Thus,

the temperature-dependent orthoexciton lifetime data from Ref. [14] was used for τ_x (implemented as an interpolating function in our code), assuming that the exciton lifetime is < 1μs (*83*).

The mean time for excitons to form is given by $\tau_b = \frac{1}{bn^*}$, where n^* is found by treating the exciton and electron-hole system as an ideal gas mixture and neglecting exciton-exciton interactions:

$$n^* = \frac{n_{0e}n_{0h}}{n_{0x}} T^{3/2} e^{-E_x/k_B T} \tag{30}$$

with the density of states,

$$n_{0i} = \frac{g_i(2\pi m_i k_B)^{3/2}}{h^3} \tag{31}$$

where g_i is the degeneracy term, m_i is the translational mass and h is Planck's constant. For Cu_2O $g_e = 2, g_h = 2$ and $g_x = g_e g_h = 4$ and $m_e = 0.99m_0, m_h = 0.58m_0$, and $m_x = 3.0m_0$, where m_0 is the fundamental electron mass. The exciton binding coefficient b has not been measured in Cu_2O, so we have used the variation of b with temperature for Si:

$$b = 10^{-3}T^{-2} + 2.5 \times 10^{-6}T^{-1/2} + 1.5 \times 10^{-7} \tag{32}$$

in units of $cm^3 \cdot s^{-1}$ (*99*). This is likely an underestimation of b in Cu_2O, because the exciton binding energy in Cu_2O is approximately an order of magnitude larger than that in Si.

The diffusion lengths of electrons and excitons were calculated by use of:

$$L_e = \sqrt{D_e \tau_e} \tag{33}$$

$$L_x = \sqrt{D_x \tau_x} \tag{34}$$

The diffusion coefficient of electrons in Cu_2O has yet to be measured, so D_e was estimated using the Einstein relation:

$$D_e = \frac{1}{e}\frac{m_h}{m_e}\mu_h k_B T \quad (35)$$

where the electron mobility was estimated by weighting the hole mobility by the ratio of the electron and hole translational masses. This approach yields values of ~2 μm for L_e, which agrees well with measured values from the literature (*65, 85, 97, 100*). Similarly, the exciton diffusion length was calculated using:

$$D_x = \mu_x k_B T \quad (36)$$

The exciton mobility μ_x has been measured accurately down to low temperatures. Above 10 K, the following expression was found to be in good accord with the experimentally measured exciton mobility:

$$\mu_x = \frac{2\sqrt{2\pi}\hbar^4 \rho v_l^2}{3\mathcal{D}^2 m_x^{5/2}} (k_B T)^{-3/2} \quad (37)$$

where, $\rho = 6.11$ g·cm^{-3} is the mass density of the Cu_2O crystal, $v_l = 4.5 \times 10^5$ m·s^{-1} is the thermal velocity, and $\mathcal{D} = 1.2$ is the deformation potential (*101*).

3.4.3 Effects of Excitons on Carrier Diffusion Length in Cu_2O

The principal effect of excitons on solar cell performance is to modify the diffusion characteristics of photogenerated species by effectively coupling the motion of free carriers and excitons (*55, 56*). Figure 3.5 shows the effect of temperature and doping density on the diffusion lengths L_e, L_x, L_1, and L_2. The exciton diffusion length is approximately constant with temperature, and is almost an order of magnitude greater than L_e, which varies significantly with temperature. For low-to intermediate doping densities, this behavior causes L_1 to approach L_e, especially at high temperatures. At low temperatures, where excitons dominate, L_1 tends towards L_x. L_2 is substantially lower than L_1 for all temperatures.

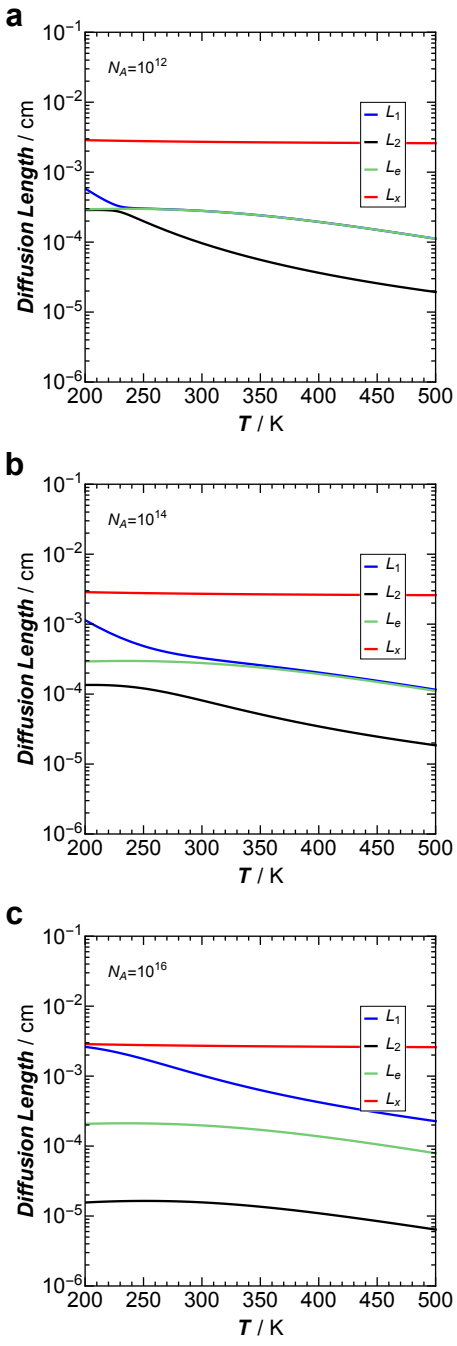

Figure 3.5 The simulated electron, exciton and effective diffusion lengths for Cu_2O for doping densities a) 10^{12}, b) 10^{14}, and c) 10^{16}.

3.4.4 Equilibrium Concentration of Excitons and Free Carriers

A fundamental assumption in our model is that excitons and free carriers are in equilibrium in the Cu_2O bulk up to the edge of the depletion region, such that:

$$n_i^2 = n_0 p_0 = n_x^0 n^* \tag{38}$$

where, n_0, p_0, and n^0_x are the electron, hole concentrations, respectively. Here, we assume that the hole concentration is given by the ionized dopant density N_A and thus, in equilibrium, the ratio of excitons to free electrons is given by:

$$\frac{n_x^0}{n_0} = \frac{N_A}{n^*} \tag{39}$$

The equilibrium exciton ratio is shown in Figure 3.6. As expected, the excitonic fraction of the photogenerated population increases with decreasing temperature and increasing doping density. The exciton density is greater than the free carrier population at room temperature for large doping densities. From, Eq. 3.37 and 3.38 the equilibrium exciton concentration is given by:

$$n_x^0 = \frac{n_i^2}{n^*} \tag{40}$$

and the equilibrium electron concentration is given by the typical expression:

$$n_0 = \frac{n_i^2}{N_A} \tag{41}$$

The intrinsic carrier concentration can be calculated from the effective density of states in the valence and conduction bands, respectively:

$$N_C(T) = 2\left(\frac{2\pi m_e k_B T}{h^2}\right)^{\frac{3}{2}} = 4.75 \times 10^{15} T^{3/2} \tag{42}$$

$$N_V(T) = 2\left(\frac{2\pi m_h k_B T}{h^2}\right)^{\frac{3}{2}} = 2.14 \times 10^{15} T^{3/2} \quad (43)$$

$$n_i^2(T) = N_C N_V e^{-\frac{E_g(T)}{k_B T}} = 1.014 \times 10^{31} T^{3/2} \quad (44)$$

in cm^{-3} (*21*). Using these values and the parameters outlined above, the dark saturation current density J_0 can be calculated.

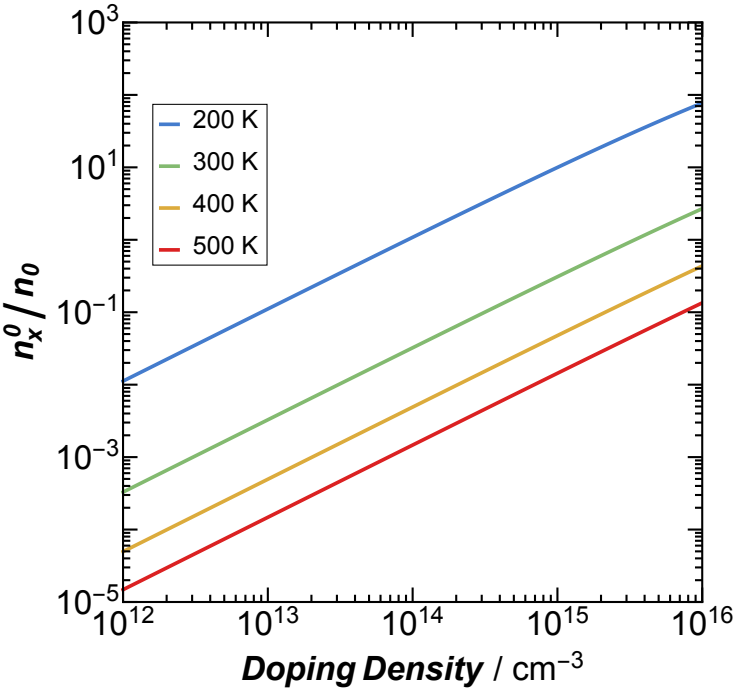

Figure 3.6 The equilibrium ratio of excitons to free carriers as a function of doping density for temperatures ranging from 200 to 500 K.

3.4.5 Absorption, Generation, and J_{sc}

The calculation of J_{sc} requires knowledge of the generation rate of excitons and free carriers, as well as the absorption coefficient in the visible spectrum. We have calculated J_{sc} using the full wavelength dependence of G_e and α. The experimentally determined absorption coefficient was used, and the absorption coefficient of Cu_2O was assumed to not vary

substantially over the temperature range evaluated in this study (200 – 500 K) (*102*). The wavelength-dependent electron and exciton generation rate were estimated by:

$$G(\lambda) = \alpha(\lambda)\Phi(\lambda) \tag{45}$$

where Φ is the photon flux from the global AM 1.5 solar spectrum. To differentiate between exciton and free carrier generation, the free carriers were assumed to be generated for absorption of a photon with energy above the electronic band gap, and excitons were assumed to be generated only in the case for photon excitation with an energy between the electronic band gap and the excitonic band edge (E_g-E_x). Thus, the short-circuit current density is the summation of two parts, one free-carrier and one excitonic:

$$J_{sc} = e\int_{E_g}^{\infty} \alpha(\lambda)\Phi(\lambda)\left(\frac{\eta}{\alpha(\lambda)+L_1^{-1}} + \frac{1-\eta}{\alpha(\lambda)+L_2^{-2}}\right)d\lambda + e\int_{E_g-E_x}^{E_g} \alpha(\lambda)\Phi(\lambda)\left(\frac{\zeta}{\alpha(\lambda)+L_1^{-1}} + \frac{1-\zeta}{\alpha(\lambda)+L_2^{-2}}\right)d\lambda \tag{46}$$

This approach is an oversimplification, as we have demonstrated experimentally in the previous section. Even above-band-gap illumination leads to excitonic generation that is observable as a free-exciton peak in the photoluminescence spectrum.

3.4.6 V_{oc}, *FF*, and Efficiency

The open-circuit voltage (V_{oc}) can be calculated by solving Equation (3.5) for the case when $J = 0$. To calculate the fill-factor (*FF*), a *J-V* characteristic was generated by numerically solving Eq. 3.1 for *J*, with $R_s = 20\ \Omega\cdot\text{cm}^2$ and $R_{sh} = 875\ \Omega\cdot\text{cm}^2$, as a function of *V* (*103*). The *J-V* behavior was then used to determine the power density so that the current and voltage at the maximum power point (J_{mpp} and V_{mpp}, respectively) could be extracted by maximization

of the power density. These parameters were then used to calculate the fill factor *FF* and ultimately the photovoltaic efficiency η, according to

$$FF = \frac{J_{mpp} V_{mpp}}{J_{sc} V_{oc}} \tag{47}$$

where, J_{mpp} and V_{mpp} are the current-density and voltage at the maximum power point and

$$\eta = \frac{V_{oc}\, J_{sc}\, FF}{P_{in}} \tag{48}$$

where P_{in} is the power incident on the Cu_2O cell, in this case, the standard AM 1.5 solar spectrum.

3.4.7 Model Results

The magnitude of the excitonic effects is dependent on the temperature and total excitation density (see Figure 3.1), so the photovoltaic behavior was evaluated as a function of doping density over temperatures relevant to solar cell operation (200 – 500 K) using empirical data from the literature (see Section 3.4.2, above). Intrinsic hole concentrations in high-quality Cu_2O are typically ~ 10^{12} cm^{-3}, however, recently Cu_2O doped with Na has shown carrier concentrations as high as 10^{16} cm^{-3} while maintaining the high mobility necessary for efficient carrier collection. We have therefore considered doping densities (N_A) ranging from 10^{12} to 10^{16} cm^{-3} (*96, 103*). Higher-order excitonic effects, such as the binding of excitons to impurities, have been neglected, to provide an upper bound of solar cell performance when excitons are considered.

Figure 3.7 compares the predictions obtained from the excitonic model and the FC model. At intrinsic doping levels, J_0 is similar for both models across all temperatures. However, at large doping densities, J_0^x increased substantially compared to the value of J_0 produced by the FC model, due to the extra recombination created by excitons that is not considered in the FC model. At lower temperatures and large doping densities, the concentration of

excitons increases and J_0^x increases substantially compared to J_0^{fc}. The simulated dark current densities when excitonic effects were either included or neglected were substantially smaller than experimental results for J_0. This discrepancy is likely due to recombination sources that were not included in the model, such as interfacial defects and surface states.

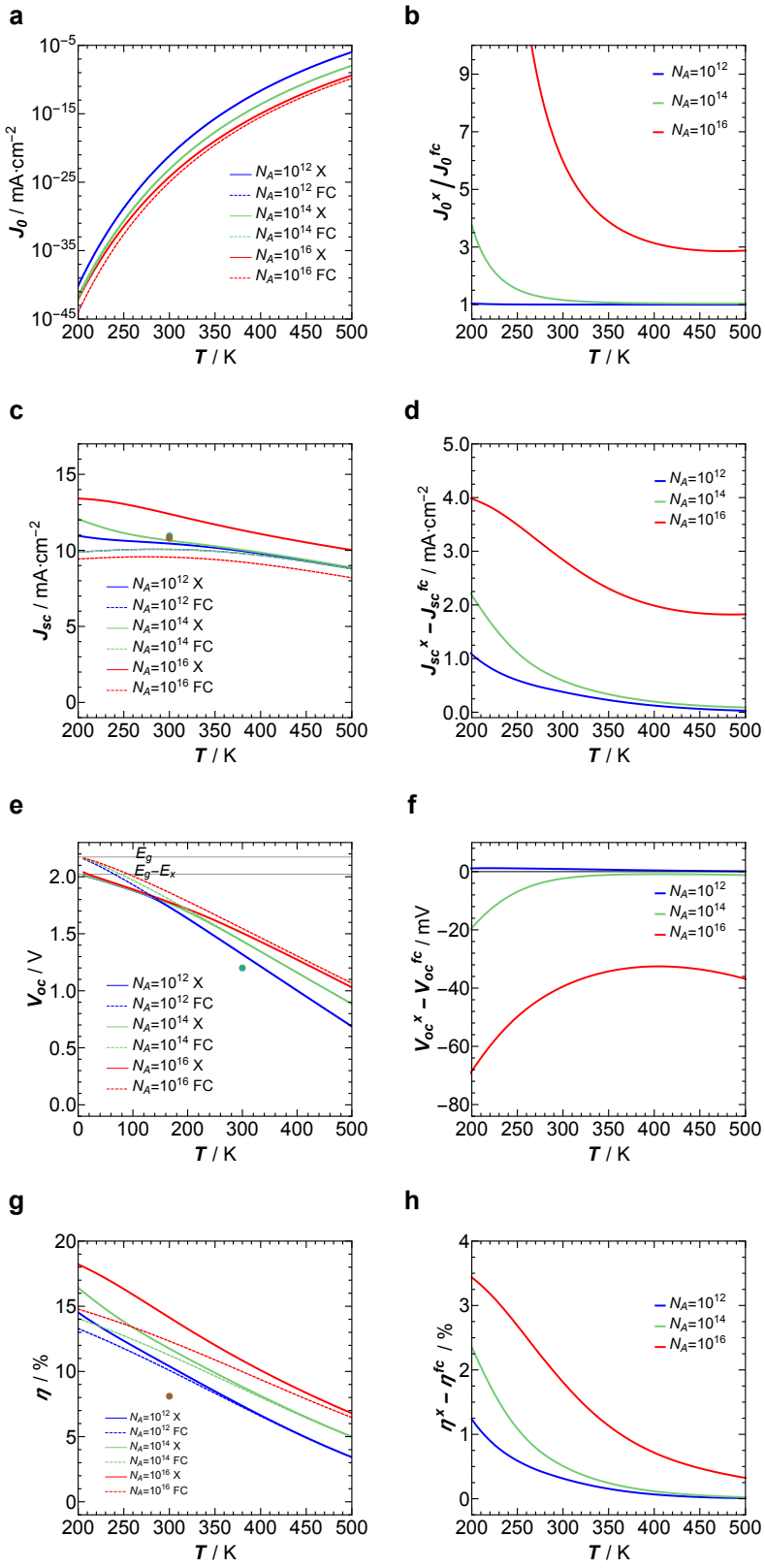
a
b
c
d
e
f
g
h
J_0 / mA·cm^{-2}
J_0^x / J_0^{fc}
J_{sc} / mA·cm^{-2}
$J_{sc}^x - J_{sc}^{fc}$ / mA·cm^{-2}
V_{oc} / V
$V_{oc}^x - V_{oc}^{fc}$ / mV
η / %
$\eta^x - \eta^{fc}$ / %
T / K
E_g
E_g–E_x
N_A=10^{12} X
N_A=10^{12} FC
N_A=10^{14} X
N_A=10^{14} FC
N_A=10^{16} X
N_A=10^{16} FC
N_A=10^{12}
N_A=10^{14}
N_A=10^{16}

Figure 3.7 Comparison between the simulated device performance of a p-n^+ Cu_2O-based solar cell using a model incorporating excitonic effects relative to the FC model, denoted by the superscript x and fc, respectively. (a) The simulated dark saturation current density. (b) The ratio of the dark current density, when excitons are included, to the dark current density using the FC model. The dark current density increases substantially when excitonic effects are included. (c) The calculated short-circuit current density. Experimental J_{sc} values (the circles) agree well with the J_{sc} values obtained using the excitonic model (*103, 104*). (d) The absolute difference in short-circuit current density between the excitonic and FC models. At room temperature and a doping density of 10^{16}, excitonic effects account for an additional 2.84 $mA \cdot cm^{-2}$. (e) The open-circuit voltage obtained from the excitonic and FC models. In the low temperature limit, the V_{oc} approaches the exciton band edge and electronic band gap for the excitonic model and the FC model, respectively. The turquoise circle represents the record experimental V_{oc} for Cu_2O solar cells (*105*). (f) The difference between the open-circuit voltage as calculated from the excitonic model and the FC model. The change in voltage is small over the calculated temperature range. (g) The simulated photovoltaic efficiency under the AM 1.5 spectrum. (h) The absolute difference in the practical efficiency in Cu_2O-based solar cells between the excitonic model and the FC model. At room temperature, the FC model underestimates the efficiency by 1.9 absolute percent.

Figure 3.7c shows the calculated short-circuit density. The experimental values for J_{sc} are larger than the current densities predicted by the FC model at $T = 300$ K but agree well with values for J_{sc} predicted using the excitonic model (*103, 104*). At low temperature, the inclusion of excitons leads to an enhancement of J_{sc} (Figure 3.7d). This enhancement of J_{sc} decreases with increasing temperature, and converges to the value of J_{sc} calculated from the FC model at higher temperatures, when the excitation density is primarily due to free electrons and holes. The increase of J_{sc} is driven predominantly by the effective band gap narrowing of Cu_2O from the electronic band gap (2.1 eV) to the exciton band edge (1.91 eV), which increases by E_x = 150 meV the range over which Cu_2O absorbs light. The large increase in J_{sc} at the highest doping level is caused by a decrease in the electron lifetime and the subsequent decrease in the electron diffusion length, due to increased scattering off of impurity centers (Figure 3.5). The decrease in the electron diffusion length has a more substantial effect on the FC model because only a small fraction of the photogenerated minority carriers in the excitonic model move with the electron diffusion length, whereas the remaining electrons diffuse with an effective diffusion length between that of excitons and electrons (*56*).

The enhancements in the excitonic model of J_0 and J_{sc} counteract one another, so that V_{oc} is essentially unchanged compared to that produced by FC model, except for the largest doping density where the enhancement in J_0 exceeds that of J_{sc}. Excitons therefore produce a decrease in V_{oc} for the largest doping density compared to what is expected from the FC model (Figure 3.7e/f). At T = 300 K, the difference between the models is at most ~40 mV (for the highest doping density considered), and this difference decreases as free carriers begin to dominate as the temperature is further increased. For a photovoltaic cell in the radiative recombination limit, V_{oc} should approach the band edge of the absorber material as the temperature goes to T = 0 K (*106*). In the low-temperature limit of our simulations, V_{oc} tends to the excitonic band edge when excitonic effects are included. In contrast, V_{oc} tends to the electronic band edge for the FC model, which suggests that the models correctly capture the physics of solar cell operation in both cases. Intrinsically doped Cu_2O-based photovoltaics have exhibited open-circuit voltages as high as 1.20 V at room temperature (the turquoise dot in Figure 3.7e), within 100 mV of the results of our simulations (*105*). Such high-quality Cu_2O junctions have exhibited V_{oc} that extrapolates to the exciton band edge (1.91) at 0 K, again demonstrating that the device physics of Cu_2O photovoltaics under such conditions are governed primarily by excitonic effects.

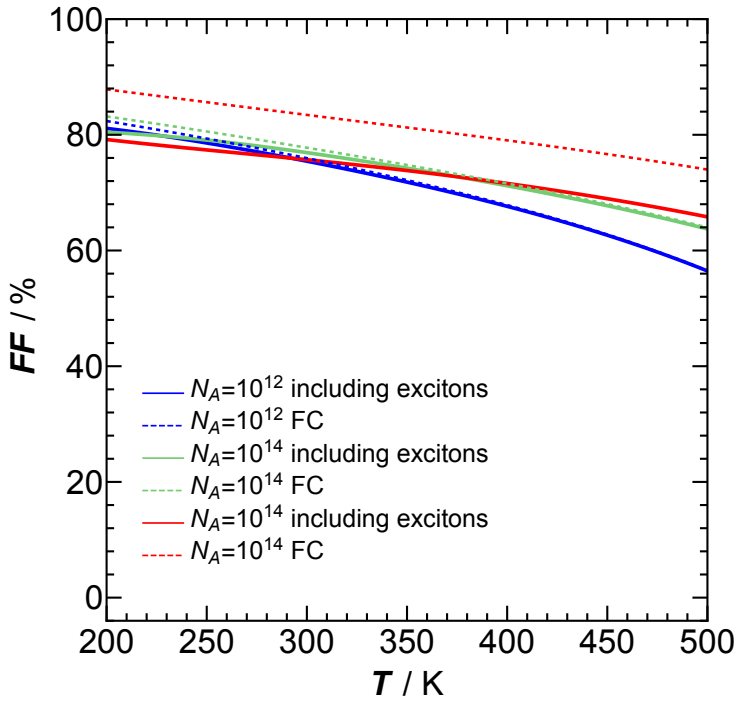

Figure 3.8 The simulated fill-factor for the excitonic and FC models. The fill factors were in close agreement except at the highest doping densities, where large enhancement in the J_{sc} dominates and leads to an increase in the solar-cell efficiency relative to the FC case.

The calculated fill factor (~75-80% at room temperature) is comparable for both models (see Figure 3.8). The difference in efficiency between the models is thus dominated by the substantial changes in J_{sc} when excitons are included, which can intuitively be seen from Eq. 3.9. The photovoltaic efficiency calculated from each model (Figure 3.7g) is less than the detailed-balance efficiency limit for Cu_2O, which is 20.5% at 300 K. The source of this difference is the non-ideality of Cu_2O charge transport that has been represented in our model by using empirical data from the literature. As in the case of J_{sc}, the simulated efficiency using the excitonic model is enhanced relative to the efficiency obtained from the FC model at low temperatures, where excitons dominate, and converges to the efficiency obtained from the FC model at high temperatures, where the photogenerated population consists entirely of free electrons and holes. Hence, at temperatures relevant to photovoltaic operation, the free-

carrier model substantially underestimates the performance of Cu_2O solar cells, with the difference as much as 1.9 absolute percent for the case when $N_A = 10^{16}$ cm^{-3} at $T = 300$ K.

3.5 Conclusion

In conclusion, neglecting excitonic effects by adopting the traditional "free carrier" model fails to capture a fundamental photoconversion and charge-transport mechanism in Cu_2O. Using a thermodynamic model that governs ionization events, the quasi-equilibrium branching ratio between excitons and free carriers in Cu_2O indicates that during photovoltaic operation up to 28% of photogenerated carriers are excitons. These large exciton densities were directly observed as a free-exciton peak in the photoluminescence spectrum of Cu_2O at room temperature under visible-light excitation. Spectral response measurements of a Cu_2O/Zn(O,S) solar cell indicated substantial excitonic current collection at energies below the Cu_2O electronic band gap, under conditions for which only excitons are generated. In the case of Cu_2O, the "free carrier" model was shown to underestimate the efficiency of a Cu_2O solar cell by as much as 2 absolute percent at room temperature.

Chapter 4
Interconnect-free Perovskite/Silicon Tandems

4.1 Increasing Silicon Efficiency: Tandem Si Solar Cells

Combining multiple junctions in a single device is one of the most practical and well-demonstrated approaches to exceed the single absorber Shockley-Queisser limit (*29*). In such a design, each sub-cell is optimized to absorb a different part of the solar spectrum, producing two separate quasi-Fermi level splittings, thereby reducing thermalization losses. The utilization of tandem device architectures with Si bottom cells would increase the theoretical cell efficiency beyond 40% and ultimately allow the production of photovoltaic modules in excess of 30%, all while leveraging Si's already dominant market share (*107*).

To that end there has been considerable effort to develop efficient Si-based tandem solar cells. For over two decades, research has primarily focused on Si-based tandems which utilize III-V semiconductors as the top cell material owing to III-V's maturity, reliability and high efficiency (*108-115*). Indeed, Si/III-V tandems have obtained efficiencies above the single-junction Shockley-Queisser limit of 32% (*116*) under one-sun illumination, however, a number of obstacles impede the commercial viability of this pairing, including the high materials and fabrication costs of III-V semiconductors.

4.2 The Rise of Perovskites and Silicon/Perovskite Tandems

Recently, the inorganic-organic metal-halide perovskites (henceforth, simply perovskite) have emerged as an alternative to III-Vs as a top cell material in a tandem structure with Si.

Since their introduction as purely organic, dye-sensitized solar cells in 2009 (*117, 118*), the efficiency of single junction, solid-state perovskite solar cells has risen from 10.9% (*119*) at a near meteoric rate to 23.3% (Fig. 4.1). Along with the drastic increase in efficiency of perovskite solar cells has come a significant increase in device stability. Initially, perovskite devices were unstable in air, their performance rapidly decayed in the presence of oxygen and moisture in a matter of seconds. The introduction of multication perovskites incorporating cesium (Cs) and/or formamidinium (FA), in addition to methylammonium (MA), has led to stable solar cell performance that are now capable of passing the standard 1,000 hour damp heat test (*120*). Additionally, the band gap of perovskites, like that of the III-Vs, can be tuned over a large range (*121*) making the perovskites attractive candidates for multijunction solar cells on top of Si (and other narrower band gap materials on the market, such as, cadmium telluride and copper indium gallium selenide). However, unlike the III-Vs, the perovskites have simple processing requirements and low materials cost, thus presenting a pathway to improving efficiency to over 30% while preserving low module cost. Perovskite tandems with Si have now attained monolithic perovskite/Si tandem device with world-record efficiencies of 27.3%, though no details of this record-efficiency cell structure have yet been provided (*122*).

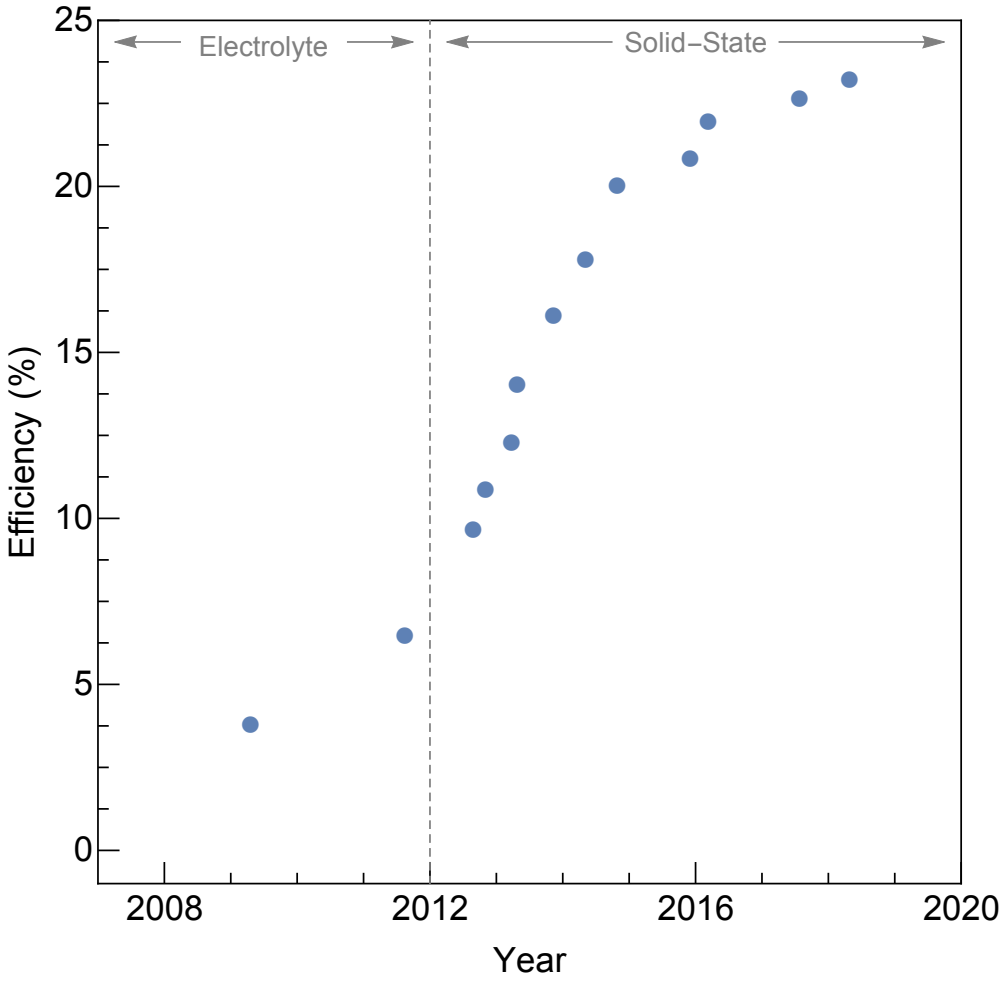

Figure 4.1 Perovskite record cell efficiency, adapted from (*30, 123*). The record at the time of writing is 23.3%.

Design approaches for creating tandem cells have either two or four electrical terminals per tandem pair (Fig. 4.2). While four-terminal Si/perovskite tandems have been the focus of many works (*124-127*) and have demonstrated efficiencies close to the single junction Si record (26.7%) (*128*), the added wiring complexity and need for multiple transparent contacts has prevented their widespread use commercially. The two-terminal (2-T) configuration allows for monolithic fabrication, in which the cells are constructed as a single unit, allowing simple electrical integration at the system level and relaxing the need for additional front and rear transparent electrodes. In place of transparent electrodes, however, the monolithic

approach requires an interconnection layer that effectively facilitates the flow of photogenerated carriers from one sub-cell to the other. Ideally this should be achieved with low electrical and optical losses and at minimal processing cost. Tunnel junctions consisting of two heavily doped p^+ and n^+ regions are a common choice for such an interconnection layer (*129*). Indeed, the first demonstration of a 2-T perovskite/Si tandem device used a partially crystallized, heavily doped n-type Si layer to form a tunnel junction on top of a crystalline p^+-Si emitter in its Si homojunction bottom cell, resulting in η =13.7% (*130*). Improved light management, combined with advances in perovskite photovoltaics, yielded η = 22.7% by use of heavily-doped hydrogenated nanocrystalline Si (nc-Si:H) tunneling layers on a Si heterojunction with intrinsic thin-layer (HIT) bottom cell (*131*). This approach has been further developed recently by texturing the HIT bottom cell whilst conformally depositing the perovskite and contact layers using thermal evaporation. Reduced reflection and an improved infrared response in this design has yielded an efficiency of 25.2% for a monolithic perovskite/Si tandem solar cell (*132*). An alternative to utilizing tunnel junctions for interconnection is to employ a recombination layer, typically in the form of a transparent conductive oxide (TCO), common choices being indium-doped tin oxide (ITO) (*120, 133, 134*) and indium-doped zinc oxide (IZO) (*135*). The previous record efficiency of 23.6% for monolithic perovskite/Si tandems was obtained accordingly by incorporating an ITO intermediate layer to connect a HIT bottom cell and perovskite top cell (*120*). Impediments to further improvements in such TCO-containing interconnection systems include substantial parasitic absorption due to free-carrier absorption at long wavelengths, and the prevalence of shunt paths through the top cell, caused by surface roughness (*131*).

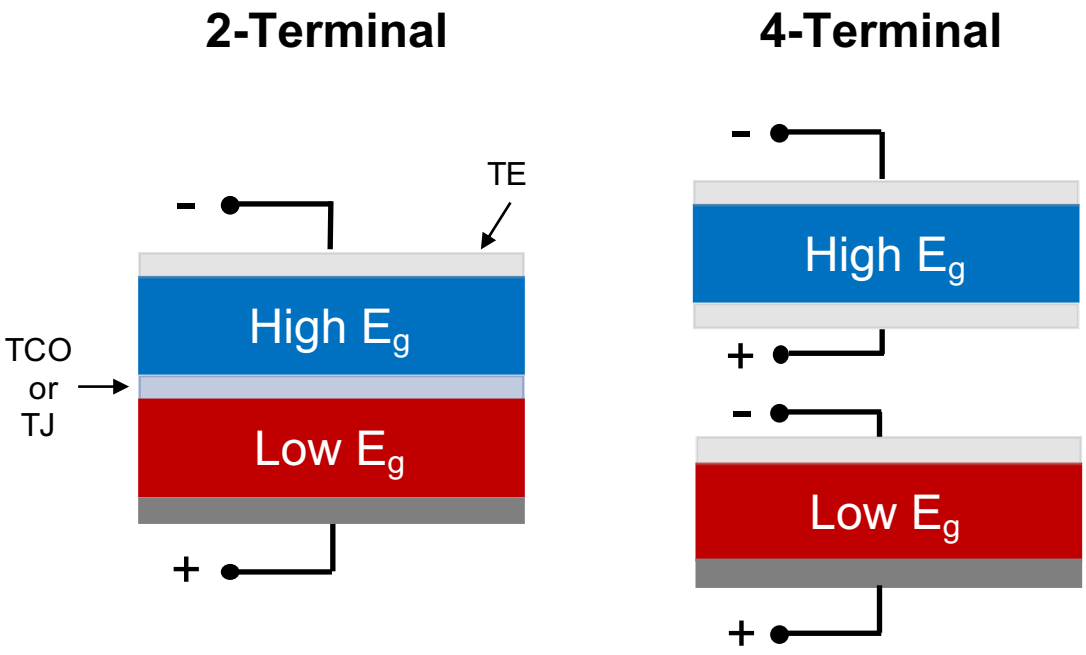

Figure 4.2 Simplified diagram of the 2-terminal (left) and 4-terminal (right) tandem solar cell device architectures. In each design, the top contact is a transparent electrode (TE), which allows the light to pass through to the two cells, while the bottom contact need not be transparent. In the 2-terminal design the high and low band gap sub-cells are in ohmic contact by means of either a transparent conductive oxide (TCO) or tunnel junction (TJ). In a 4-terminal design two additional transparent electrode contacts are needed on the rear side of the high band gap sub-cell and on the top of the low band gap sub-cell.

4.3 Interconnect-free Perovskite Silicon Tandem

We demonstrate herein a third and distinct strategy for fabrication of efficient monolithic, two-terminal perovskite/Si tandem solar cells. The approach forgoes the use of a conventional interconnection layer and instead places the perovskite top cell in direct contact with the Si bottom cell (Fig. 4.3A). Development of this concept was stimulated by the observation of highly Ohmic contact between TiO_2 deposited by atomic-layer deposition (ALD) and p-type Si in photoanodes that efficiently and stably evolve O_2(g) from water (*136*). Preliminary testing revealed that despite the absence of an intentional recombination layer between the two materials, a sufficiently conductive contact can be produced to enable

the operation of an efficient tandem cell. The contact resistance was subsequently found to be strongly dependent on the band alignment at the TiO_2/p^+-Si interface and on the relative doping densities of the TiO_2 and p-Si, both of which are sensitive to the TiO_2 preparation method. Although in our work the TiO_2 was prepared by atomic-layer deposition, other studies have shown that under certain deposition and annealing conditions TiO_2 films with similar behavior can be obtained using sputtering (*137*). Hence analogous behavior may be obtainable with other deposition techniques, including spin-coating or spray-coating. For our first proof-of-concept tandem devices we employed n-type homojunction Si cells, making their p^+ emitter the substrate for a conventional (semi-transparent) solution-processed perovskite top cell based on TiO_2 and 2,2',7,7'-Tetraakis-(N,N-di-4-methoxyphenylamino)-9,9'-spirobifluorene (Spiro-OMeTAD). Subsequently we found that Ohmic contact can also be achieved between TiO_2 and the boron-doped, recrystallized a-Si layer of a heterojunction cell (*138*), yielding even higher tandem voltages relative to the homojunction. We discuss both cell types herein to demonstrate the general applicability of the interconnect-free concept, but primarily make use of the homojunction cells with their physically simpler structure to perform our mechanistic analyses.

4.3.1 Interconnect-free Cell Architecture and Fabrication

The perovskite top cell in our demonstration devices consisted of a conventional n-i-p structure with a stack of cp-TiO_2 (compact TiO_2) /ms-TiO_2 (mesoporous-TiO_2) /perovskite /Spiro-OMeTAD or PTAA (poly[bis(4-phenyl)(2,4,6-trimethylphenyl)amine)/MoO_x / IZO /Au grid, as illustrated in the cross-sectional SEM image in Fig. 4.3B. The ALD-deposited TiO_2 was uniform and conformal with a low surface roughness of ~0.77 nm (Fig. 4.4). A ~54 nm thickness of TiO_2 was found to be optimal, covered by a ~70-80 nm ms-TiO_2 layer and an ultra-thin PCBM (Phenyl-C61-butyric acid methyl ester) /PMMA (Poly(methyl methacrylate)) passivation layer to improve the cell voltage and reduce hysteresis in the current-voltage (*J-V*) characteristics (*139*). Multi-cation perovskites, which have consistently outperformed their single-cation originators (*140*), were used in the cells and fabricated using an anti-solvent one-step method (*141*). A composition of

$Cs_{0.05}Rb_{0.05}FA_{0.765}MA_{0.135}PbI_{2.55}Br_{0.45}$ yielded stable films with an appropriate bandgap (E_g= 1.63 eV) (*142*). Current matching between the two sub-cells was obtained by deposition of a relatively thin (~310 nm) perovskite layer. For both four-terminal and two-terminal Si tandems, a bandgap of ~1.7 -1.8 eV is expected to yield higher cell voltages (*143*), all other things being equal, than the 1.63 eV bandgap material used herein. At present, the high bandgap perovskites show a greater difference between the bandgap and cell V_{oc} than the more optimized lower bandgap compositions (*127, 128, 140, 144*), mitigating the potential gains in voltage. Layer thicknesses of ~120 nm and ~50 nm (*128*) were used for the organic hole selective layers (Spiro-OMeTAD and PTAA respectively). Before sputtering ~40 nm of IZO for the front contact, a 10 nm MoO_x buffer layer was deposited to protect the underlying organic layer from sputter damage.

For the Si bottom cells, we have used both n-type homojunction cells and passivating-contact heterojunction cells with pyramidally textured and passivated rear surfaces. Si homojunction cells constitute > 80% of the current PV market share for the moment, primarily on p-type wafers, although a trend towards using n-type substrates as employed here is widely anticipated (*145*). Passivating-contact cells are an emerging technology well suited for tandems, due to their higher cell voltages, simple processing requirements (*146*) and strong performance in the infrared (*147*). The heterojunction cell we employed incorporated a thin (<1.4 nm) oxide layer buried beneath ~50 nm of heavily boron-doped, recrystallized a-Si (*138*). For brevity, these devices will be referred to as “polysilicon” (poly-Si) cells, although the top layer is likely a mix of amorphous and partially crystallized silicon.

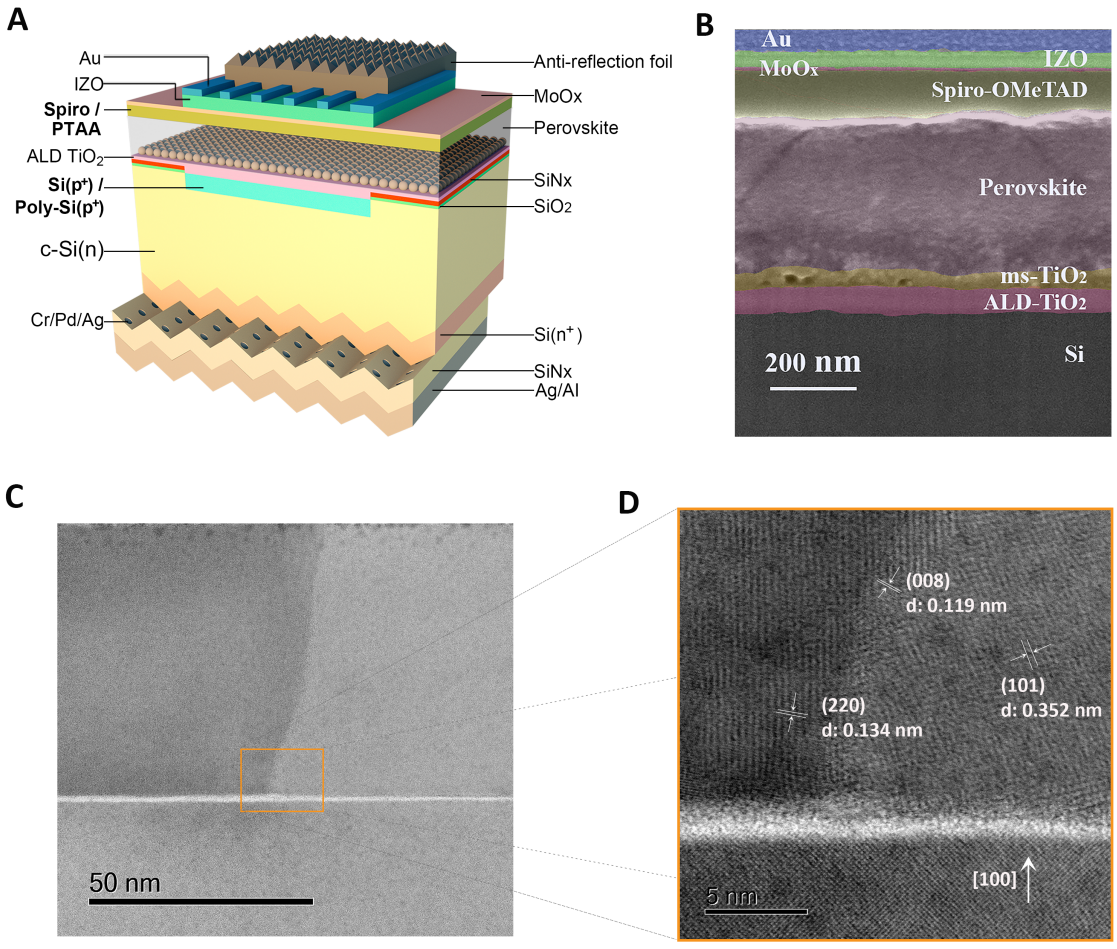

Figure 4.3(A) Schematic of the interconnect-free monolithic perovskite/c-Si tandem solar cell (not to scale). Initial tests were carried out on homojunction Si cells with Spiro-OMeTAD as the top perovskite contact; however, our best performance was obtained with polysilicon bottom-cells and PTAA as the top hole-selective layer. (B) Cross-sectional scanning-electron microscope (SEM) image of the tandem device based on Si homojunction subcell from the top surface to the p^+-Si layer (Spiro-OMeTAD is used as HTM). The anti-reflection layer was not included due to the large thickness of ~ 1 mm, (C) Scanning transmission-electron microscopy (STEM) bright field (BF) image and (D) high-resolution STEM BF image of the TiO_2/p^+-Si interface.

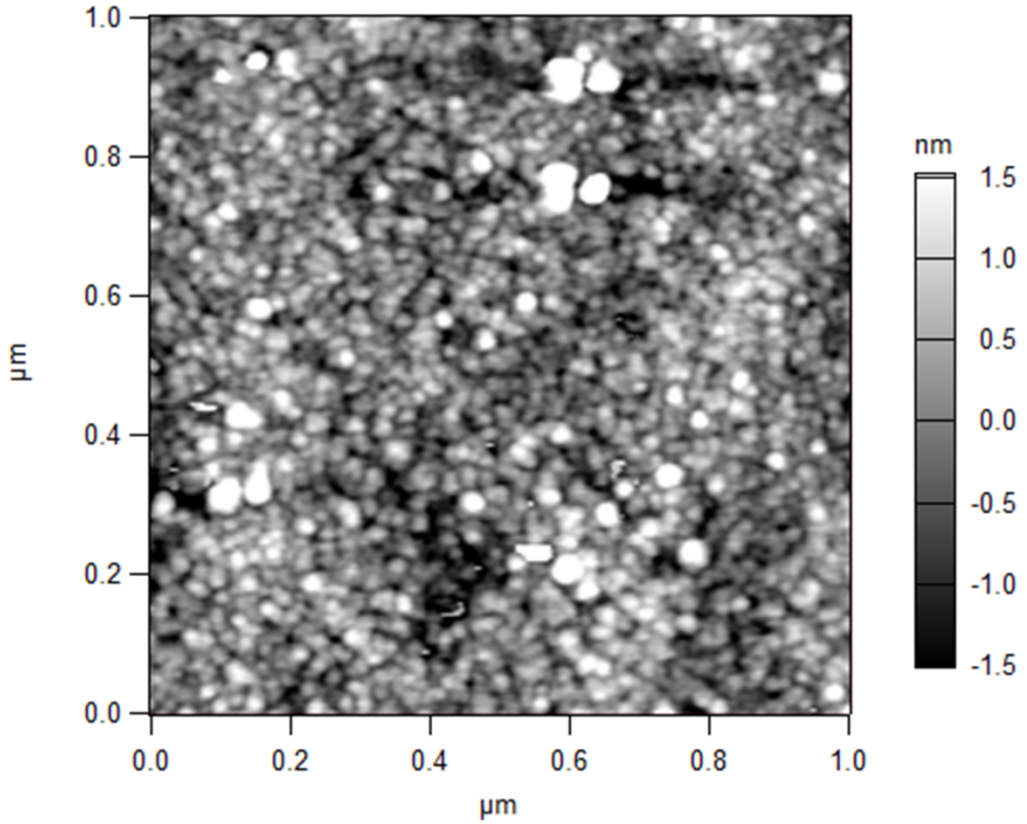

Figure 4.4 AFM image of TDMAT-ALD TiO_2 on a p^+-Si substrate.

4.3.2 Current-Voltage and TiO_2/Si Contact Characteristics

As a direct demonstration of the interconnect-free concept, Fig. 4.5A shows the photovoltaic *J-V* performance exhibited by our highest-performing polysilicon tandem cell and the corresponding photovoltaic metrics. The performance of the homojunction tandem is likewise shown in Fig. 4.6. A steady-state efficiency of 24.1% was obtained for the polysilicon interconnect-free tandem under 100 mW cm^{-2} of simulated Air Mass 1.5G illumination, with a V_{oc} of ~1.76 V, a short-circuit current (J_{sc}) of 17.8 mA cm^{-2}, and a fill factor (*FF*) of ~0.78. Compared to the polysilicon tandems, the best homojunction tandems had a steady-state efficiency of 22.9% (Fig. 4.9A) with slightly lower voltages of ~1.70 V and currents densities of 17.2 mA cm^{-2}. Although both efficiency values are uncertified, the spectral response data predicts short-circuit current densities under standard illumination test

conditions that are in close agreement with those observed experimentally herein. We thus expect that certified efficiencies would be very similar to the values reported herein. Any spectral mismatch would have its greatest effect on the short-circuit current density, whereas the voltage and fill factor would be mostly unaffected. These latter metrics are our main concerns for evaluating the interconnect-free concept, as they pertain to the passivation and electrical connection at the sub-cell interface, respectively.

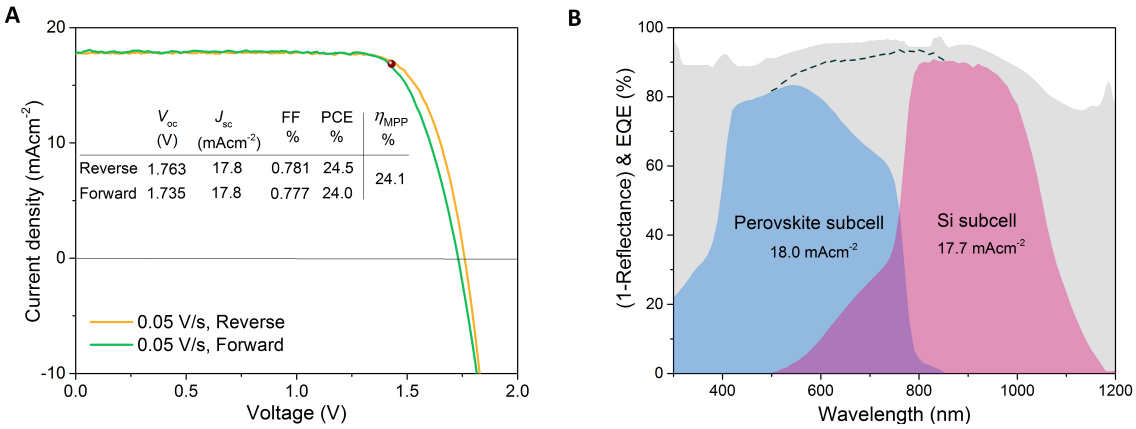

Figure 4.5 (A) *J-V* behavior of the proof-of-concept tandem device with both reverse and forward scanning at 0.05 V/s based on heterojunction poly-Si subcell. (B) Absorbance (1-R, where R is the reflectance) of the tandem device (grey shading), external quantum efficiency (EQE) of the perovskite top cell (blue), and EQE of the c-Si bottom sub-cell (red).

Efficient operation of the interconnect-free tandem device requires facile charge transfer between the Si cell's front-surface and the TiO_2 layer. Specifically, photogenerated electrons collected in the TiO_2 layer must be able to recombine, while incurring minimal voltage loss, with corresponding holes from the Si emitter region. The n-type character of TiO_2 would be expected to produce a rectifying p-n heterojunction with p-type Si, whether monocrystalline, polycrystalline or amorphous. (*148, 149*) Despite this, the *J-V* characteristics of our tandem devices did not exhibit S-shaped curves, nor the fill-factor losses that would be expected if a rectifying contact were present (*150, 151*).

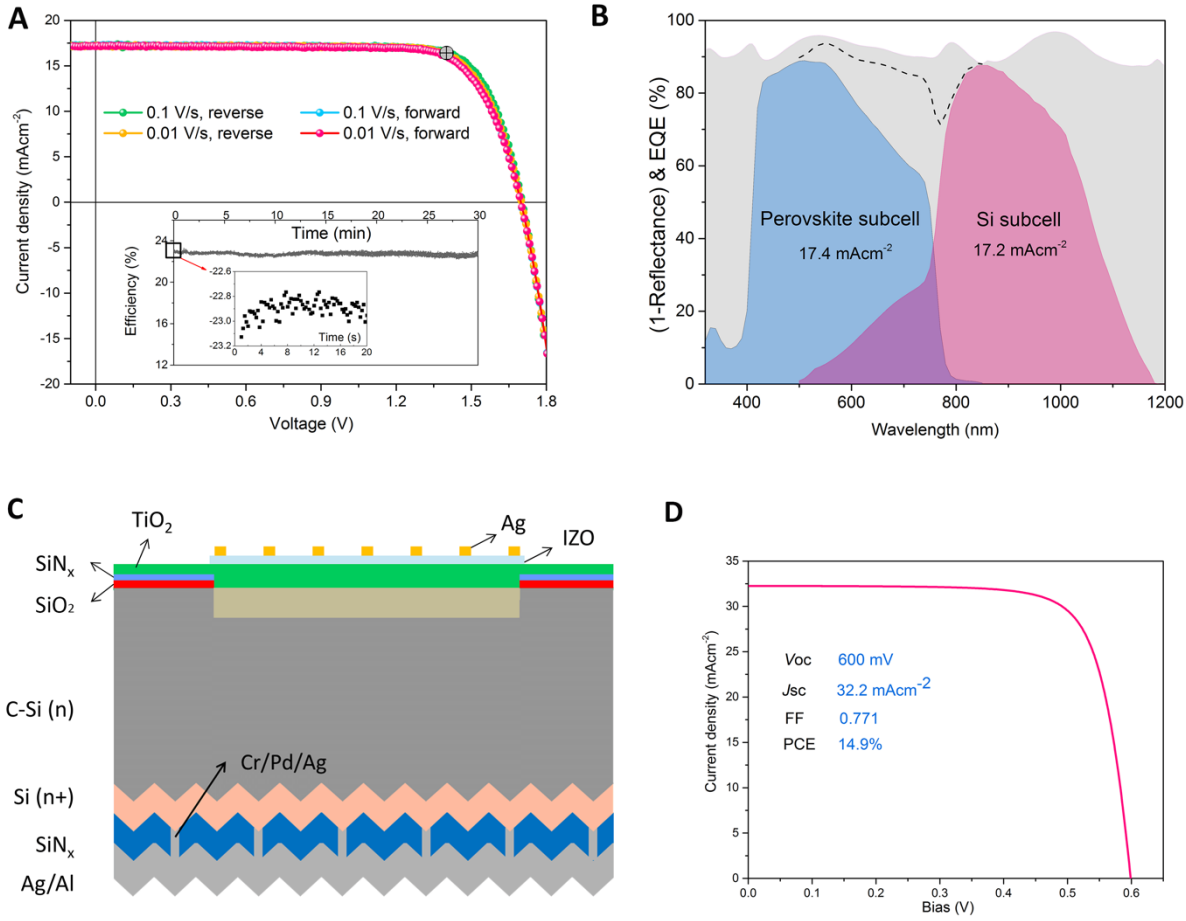

Figure 4.6 (A) *J-V* behavior of the proof-of-concept tandem device with both reverse and forward scanning at 0.05 V/s based on Si homojunction subcell. (B) Absorbance (1-R, where R is the reflectance) of the tandem device (grey shading), external quantum efficiency (EQE) of the perovskite top cell (blue), and EQE of the c-Si bottom sub-cell (red). (C) schematic of single-junction Si homojunction solar cell including ALD-TiO_2 on a flat p^+-Si emitter (not to scale), (D) photovoltaic performance of a single-junction homojunction Si solar cell.

To explicitly demonstrate the existence of facile electrical contact between TiO_2 and p-type Si, the structure depicted in Fig. 4.7A was used to investigate the electrical properties of the TiO_2/p^+-Si interface in our homojunction tandem devices – the operating principles for our polysilicon tandems presumably being similar. Analogous test structures were also fabricated using an ITO film instead of TiO_2 to emulate the recombination layer used in previous tandem designs (*120, 133, 134*). The contact resistivity (ρ_c) of a given film with respect to

p^+-Si was determined via the method devised by Cox and Strack (*152*). We note values so derived include not only the desired metal oxide/p^+-Si contact resistivity, also the bulk metal oxide as well as the oxide/Al contact resistance, so these measurements are to be interpreted as an upper bound on the former quantity. In our initial tests of the TiO_2/p^+-Si interface all samples exhibited a relatively high contact resistance as seen in Fig. 4.7B, which was only improved upon annealing at 400 °C in dry air. After annealing, the highest performing TiO_2 samples achieved a contact resistance better than 30 $m\Omega cm^2$, surpassing that of the ITO samples at ~230 $m\Omega cm^2$ by a wide margin. By contrast, annealing had a detrimental effect on the ITO/p^+-Si contact, correlating with a previous observation of reduced bulk conductivity when annealing ITO on quartz (*133*). Subsequent testing has revealed that whilst helpful, the annealing step is not strictly necessary for the TiO_2/p^+-Si contact because acceptable resistivity (~100 $m\Omega cm^2$) can be achieved without annealing, by instead increasing the ALD chamber temperature from 75 °C to 200 °C (Fig. 4.8).

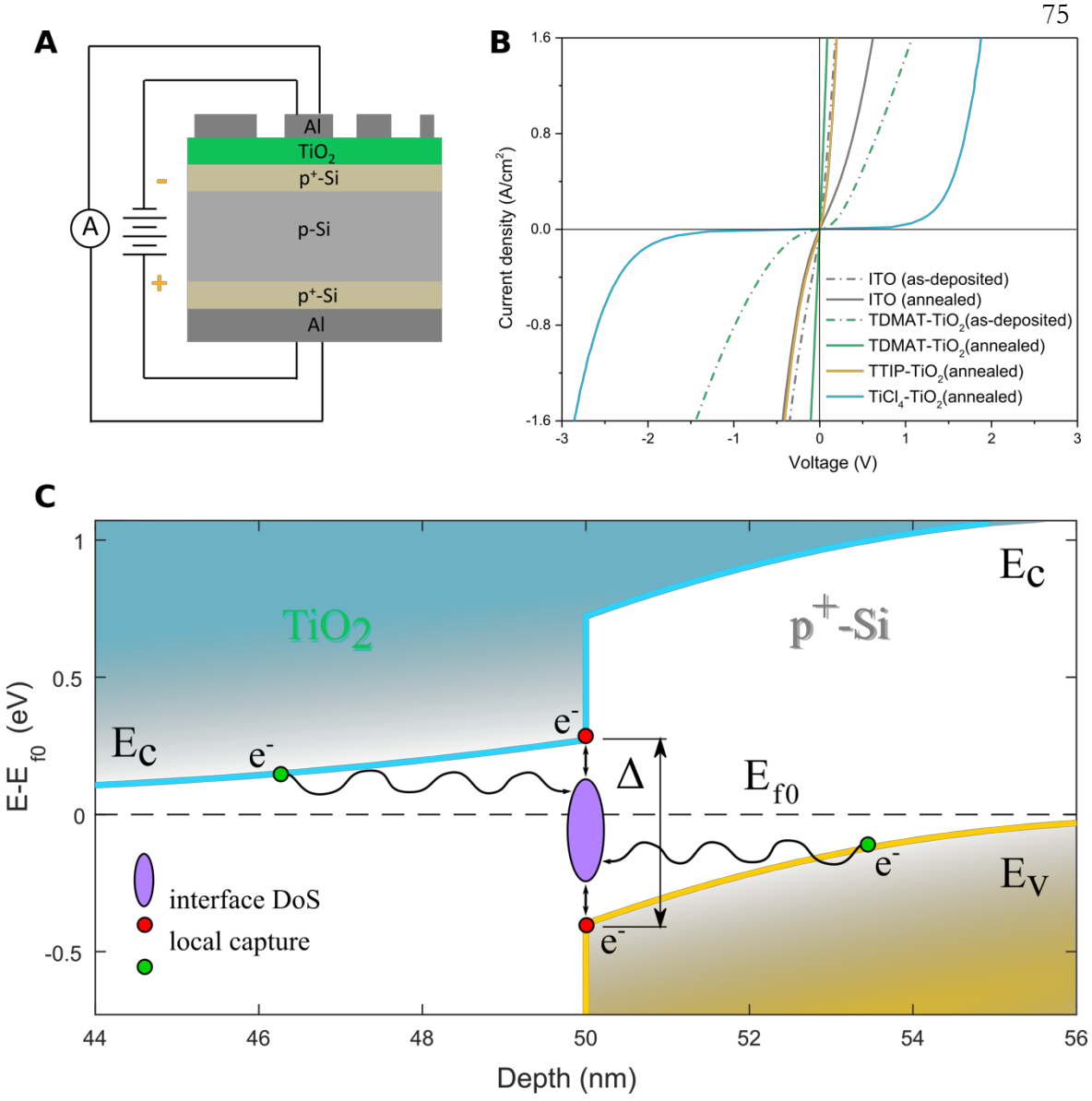

Figure 4.7(A) Schematic of the structure used for measuring contact resistivity. (B) Comparison of the *J-V* behavior of ITO/p^+-Si and various TiO_2/p^+-Si structures before and after annealing at 400 °C in air. $TiCl_4$-ALD TiO_2 listed here is deposited with the reactor chamber temperature of 75 °C. (C) Simulated band diagram of the TiO_2/p^+-Si at equilibrium assuming n-type doping of $5x10^{18}$ cm^{-3} on the TiO_2 and 10^{19} cm^{-3} for p^+-Si (appropriate for our test structure with TDMAT TiO_2, see table S3. The unknown interfacial energy gap Δ is shown here for illustrative purposes as 600 meV, which falls within the range of reported measurements (*153*)). Both mechanisms of direct- and tunneling assisted capture by interfacial defects are shown.

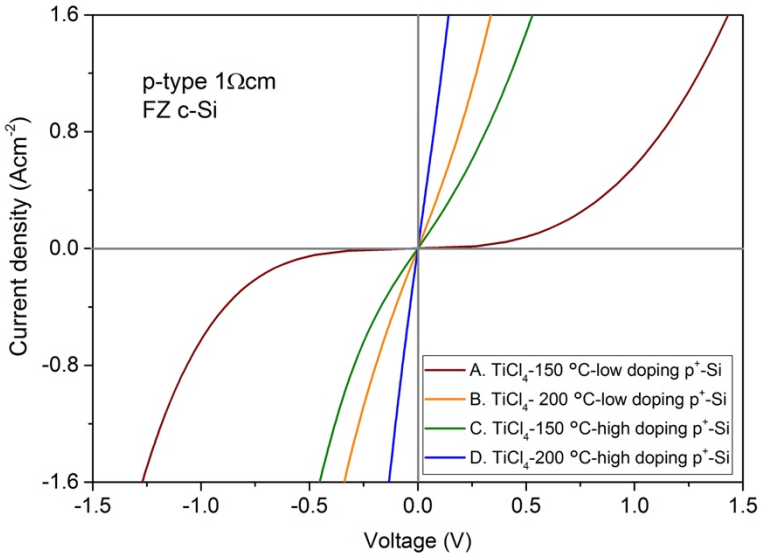

Figure 4.8 *J-V* curves of the $TiCl_4$-ALD TiO_2 deposited at low temperatures on different p+-Si wafers. The samples receive no further heat-treatment. TiO_2 deposited at 150 °C on top of p^+-Si with a doping density of (A) ~9.3×10^{19} cm^{-3}, the extracted contact resistivity is ~850 mΩcm^2 and (C) ~1.7×10^{20} cm^{-3}, the extracted contact resistivity is ~445 mΩcm^2. TiO_2 deposited at 200 °C on top of p+-Si with a doping density of (B) ~9.3×10^{19} cm^{-3}, the extracted contact resistivity is ~210 mΩcm^2 and (D) ~1.7×10^{20} cm^{-3}, the extracted contact resistivity is ~99.6 mΩcm^2.

Regarding the comparison with ITO, tandem devices fabricated with ITO as a recombination layer exhibited overall inferior photovoltaic performance as determined by all device metrics, with V_{oc} = 1.510 V, J_{sc} = 15.8 mA/cm^2 and FF = 0.637 (Fig. 4.9). The current loss in this test device is likely a result of parasitic absorption in the ITO layer and reflection loss on the ITO/Si interface, and the reduced V_{oc} and FF are ascribable to inferior contact between the sub-cells (as supported by the *J-V* measurements of Fig. 4.7B), as well as shunting due to pinholes in sputtered ITO layers. This indicates that our interconnect-free tandem cells can not only be fabricated in fewer steps, but enjoy performance benefits relative to the standard design incorporating an ITO-based recombination layer.

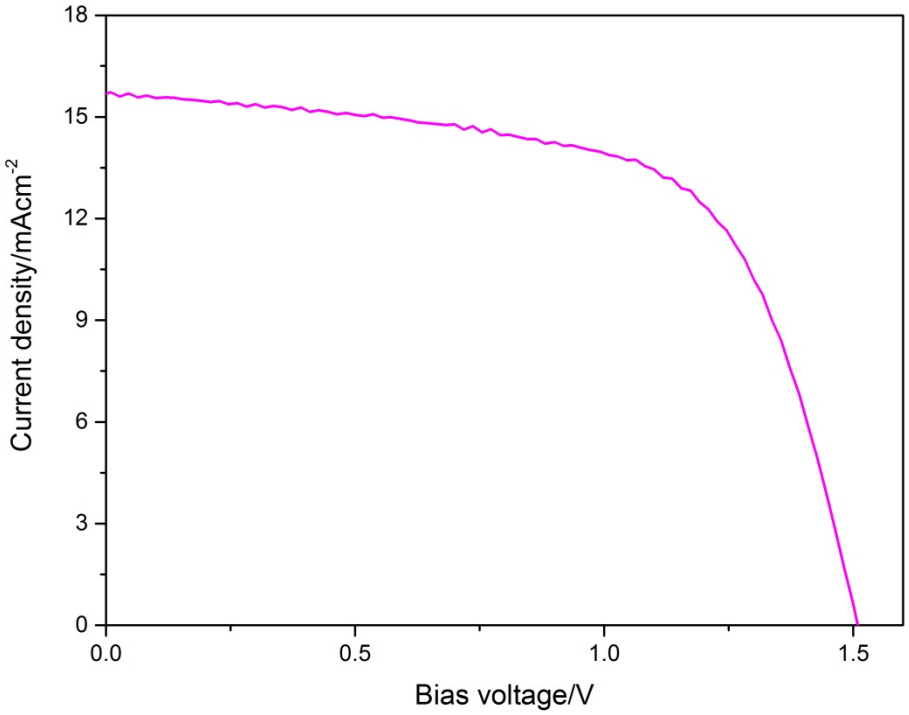

Figure 4.9 *J-V* data of a 2-T perovskite/Si tandem device with ITO as the recombination layer.

It is notable that TiO_2 layers prepared using different ALD precursors yielded quite drastically different *J-V* characteristics in our TiO_2/p^+-Si test structures, as highlighted in Fig. 4.7B. Ohmic, highly conductive behavior between TiO_2 and p^+-Si was observed in samples with TiO_2 prepared using tetrakisdimethylamidotitanium (TDMAT) as the ALD precursor (Fig. 3B, green solid line), whereas by contrast very low conductivity (ρ>10 Ωcm^2) in the low-bias region was obtained when using titanium tetrachloride ($TiCl_4$) instead (Fig. 4.7B, blue solid line), despite otherwise identical processing conditions. The use of titanium tetraisopropoxide (TTIP) resulted in intermediate performance, displaying conductive but distinctly non-linear *J-V* behavior (Fig. 4.7B, yellow solid line). The conductivity of these TiO_2/p^+-Si test structures was found to correlate well with the behavior of tandem devices constructed using the same material, with η =21% obtaining for homojunction tandems using TTIP as the precursor and η =3.6% for $TiCl_4$ as the precursor (75 °C deposition) (Fig. 4.10). These drastic variations motivated the need for a fundamental understanding of the contact

between TiO_2 and p-Si. Below we present arguments which indicate that the contact is mediated by interfacial defects, a distinct mechanism to the one that predominates in conventional p-n tunnel junctions.

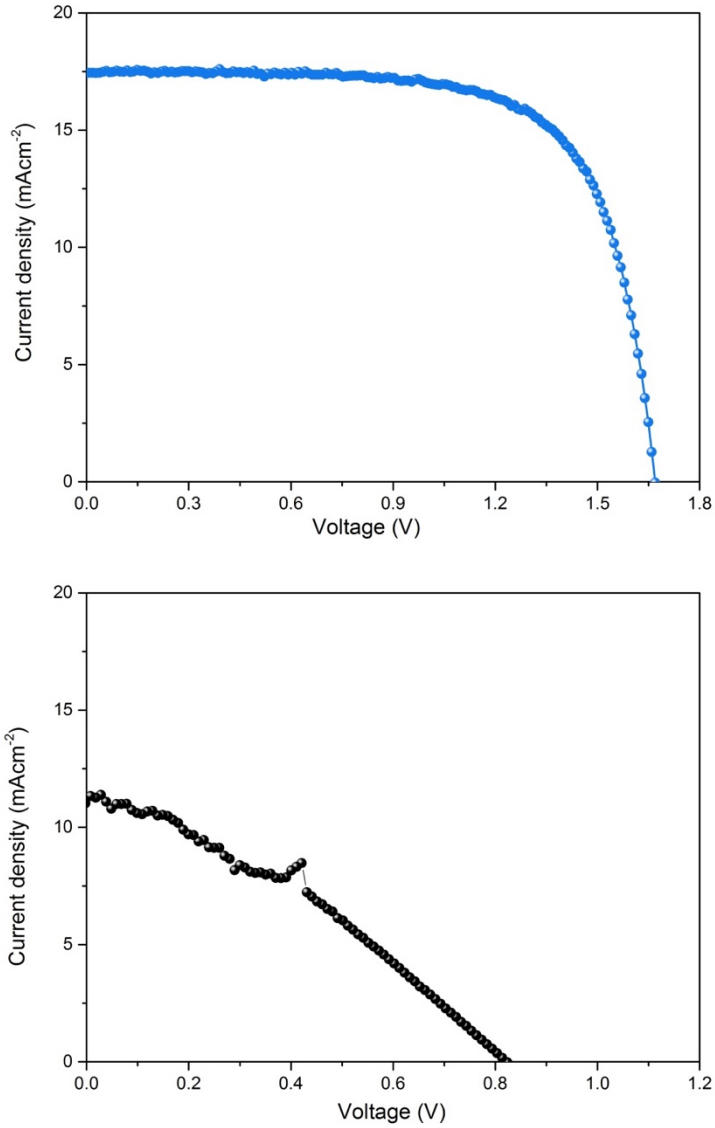

Figure 4.10 *J-V* data of monolithic perovskite/Si tandem solar cells with (top) TTIP-ALD TiO_2, (bottom) $TiCl_4$–ALD TiO_2 (deposited at 75°C).

4.3.3 TiO_2/Si Band Alignment and Charge Transport Mechanism

One aspect of clear relevance to the transport of carriers between TiO_2 and Si is the interfacial band alignment, whatever the underlying mechanism. Based on X-ray photoelectron spectroscopic (XPS) measurements of the electron affinity (χ^{TiO_2}) for our TiO_2 samples (4.35-4.7 eV, Figures 4.11, 4.12, 4.13) and the Si ionization energy ($I.E.^{Si}$), taken here as 5.15 eV, the band alignment at an idealized TiO_2/p^+-Si junction should result in an energy gap of $\Delta = E_c^{TiO_2} - E_v^{Si} = \chi^{TiO_2} - I.E.^{Si} \approx$ 0.45-0.8 eV, between the top of the Si valence band and the bottom of the TiO_2 conduction band (Fig. 4.7C). Less idealized, experimental determinations of Δ that include the surface dipole contribution require combining data from several techniques, and have only been reported rarely for TiO_2/p-Si interfaces (*153, 154*). In those studies values of Δ between 0.45 eV and 0.8 eV were obtained depending strongly on the 1-2 nm interlayer composition, which could partly account for our observation of a pronounced sensitivity to processing. A non-vanishing gap at the TiO_2/p^+-Si interface prohibits band-to-band tunneling between the TiO_2 conduction band and the Si valence band at 0 V as would occur in a standard tunnel junction, due to a lack of overlap in the bulk density of states at equilibrium (see Fig. 4.7C). Under sufficient reverse bias the necessary overlap will occur, but carriers would then need to tunnel through the sum of the depletion and interlayer widths, estimated to be 10's of nanometers for TiO_2 doping in the range of 10^{17}-10^{19} cm^{-3}. This distance is at the upper limit of what is physically reasonable, and indicates that band-to-band tunneling at reverse bias is only likely to occur when both depletion regions are very small, corresponding to high doping (*155*). At forward bias, the band overlap is decreased and band-to-band tunneling becomes prohibited, requiring a separate mechanism to explain the presence of a high forward current. In place of tunneling, at forward bias a current could be carried via the thermionic emission of conduction-band electrons from TiO_2 over the barrier due to the conduction-band offset $E_g^{Si} - \Delta$, but this would predict a strong tradeoff between the forward and reverse current, contrary to the observed Ohmic behavior (i.e., large gaps Δ would provide a small barrier for the forward thermionic emission current while enlarging the threshold voltage for reverse tunneling current, and vice versa). We conclude that our observation of high conductivity in both the

forward and reverse direction are indicative of an operating mechanism distinct from that of a familiar p-n tunnel junction.

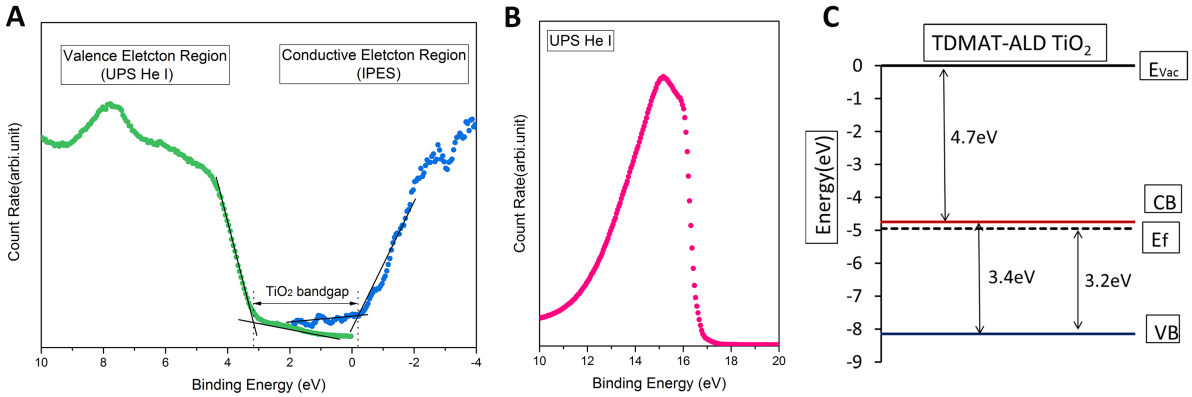

Figure 4.11 (A) Combined UPS valence band spectrum and IPES, and (B) the secondary electron cut-off region, and (C) calculated energy diagram from the above measurement, of an annealed TDMAT-ALD TiO_2 layer. The error for the work function was ±0.2 eV, and the extraction of valence band and conduction band had an error of ±0.1 eV.

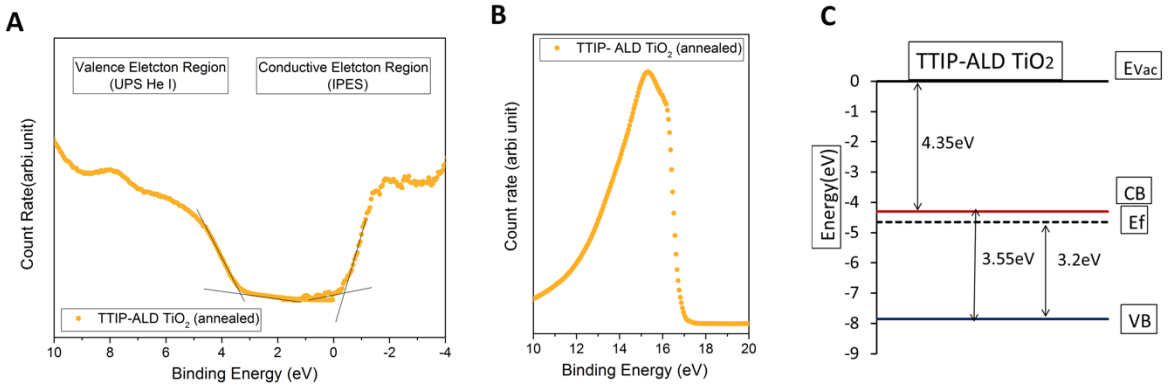

Figure 4.12 (A) Combined UPS valence band spectrum and IPES, and (B) the secondary electron cut-off region representative, and (C) calculated energy diagram from the above measurement of an annealed TTIP-ALDTiO_2 layer.

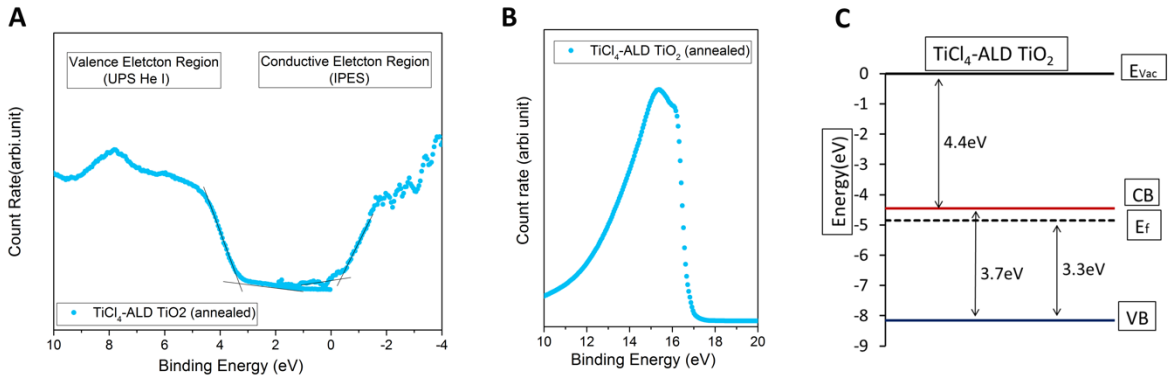

Figure 4.13 (A) Combined UPS valence band spectrum and IPES, and (B) the secondary electron cut-off region representative, and (C) calculated energy diagram from the above measurement of an annealed TiCl4-ALD TiO2 layer (deposited at 75°C).

The considerations above indicate that the presence of a pristine interfacial energy gap Δ is not readily compatible with the observed highly conductive contact between TiO_2 and p^+-Si. A more likely alternative is the presence of a substantial density of localized mid-gap states at the interface between Si and TiO_2. Such interfacial states can facilitate band-to-band tunneling at reverse bias and act as generation-recombination centers at all bias voltages (*150, 156-158*). In such a scenario, electrons move into and out of the defects states via local capture/emission as well as tunneling (Fig. 4.7C). As generation-recombination centers, the interface states would have a substantial influence on charge transport by facilitating the recombination of majority carriers in Si at forward bias without requiring emission over the interfacial barrier. At reverse-bias, every recombination center becomes a source of generation, and high conductivity can be obtained by thermally generated carriers. Conceptually this situation is similar to having a recombination-layer of atomic dimensions between the TiO_2 and p-Si, created in situ and intrinsically via the native material contact, without the introduction of substantial optical losses. For the contact resistance, the relevant recombination induced by the interfacial defects occurs between majority holes in the p-Si and electrons in TiO_2, just as in a conventional (e.g. ITO) recombination layer. Such defects may also induce unwanted recombination between majority holes and the minority electrons in p-Si, thereby degrading the open-circuit voltage of the bottom cell. In homojunction cells, minority carriers are capable of reaching the TiO_2 interface, making this a relevant concern.

In contrast, in passivating-contact cells these defects will not affect the degree of passivation due to the selective barrier (buried oxide in the polysilicon design) between minority carriers and the TiO_2 interface. Hence, in homojunction cells the interfacial defects must be carefully controlled so as not to overly compromise the silicon cells' voltage, whereas in selective-contact designs this tradeoff should be largely alleviated, depending on the degree of selectivity.

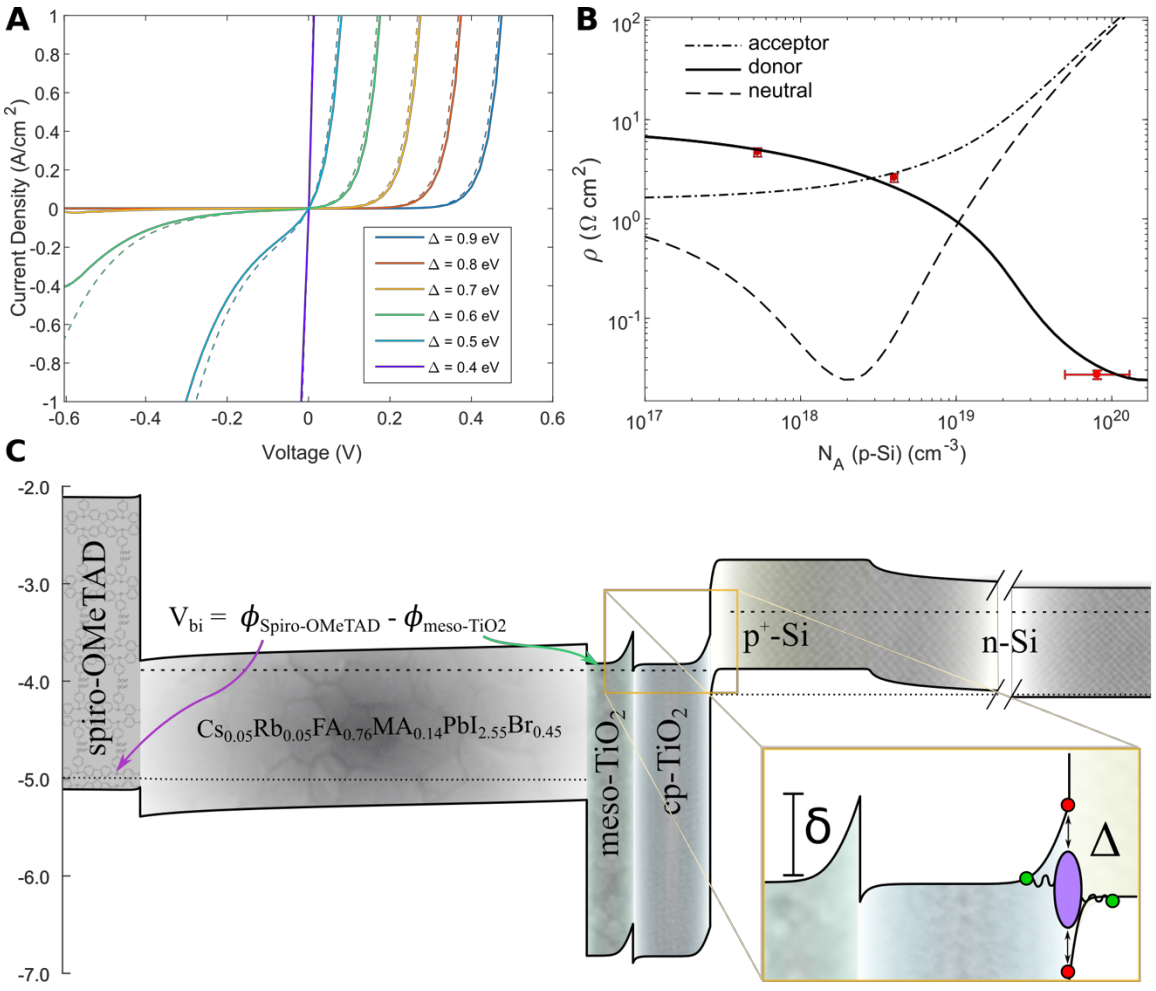

Figure 4.14 (A) Simulated *J-V* curves for varying interfacial gaps Δ. A single neutral mid-gap SRH defect was included with $S_n = S_p = 10^5$ cm/s. The dashed curves are computed with tunneling to defects included. (B) Simulated small voltage resistivity $\left(\rho = \frac{dV}{dI}|_{V=0}\right)$ with the TiO_2 donor density fixed at 10^{18} cm^{-3} and variable p-Si acceptor doping. Measurements are included as data points in red. Calculations for neutral (solid lines), acceptor-type (dotted lines) and donor-type (dot-dashed lines) are shown to demonstrate

the important effect of defect charge on the interfacial carrier balance. (C) Simulated band diagram of the full tandem device based on homojunction Si subcell with high work-function cp-TiO_2 at illuminated open-circuit. The inset depicts the two important energetic offsets Δ and δ, respectively, defined as the valence-to-conduction band offset at the TiO_2-Si interface and the difference in work functions between our solution-processed mesoporous TiO_2 layer and that of the ALD compact layer.

Numerical drift-diffusion models based on SCAPS (*159*) were used to investigate the impact of interfacial generation-recombination centers on the interfacial contact resistance. These models were designed to compute the current across a TiO_2/p^+-Si heterojunction assuming Ohmic metal contacts on both sides, and therefore mainly addressed the junction current, with only minor contributions from bulk conduction through the small layers thicknesses (50 nm and 100 nm for TiO_2 and Si, respectively). Shockley-Read-Hall (SRH) recombination centers were added at the TiO_2/p^+-Si interface to physically correspond to localized states that are expected to form in the interfacial energy gap. Such defects are likely to occur at a high density, given the relatively low degree of lattice matching between TiO_2 and Si, the possibility of precursor remnants, Si dangling bonds, and the presence of a 1-2 nm amorphous alloy interlayer observed in our samples between the two bulk crystals (Figures 4.3C, D). Interlayers are known to have a profound effect on the interface dipole or band-alignment of semiconductor-semiconductor contacts (*160*), as well as on the mechanisms of charge transfer (*161*), and may therefore play a key role in our experimental system. For simplicity in our modeling, the contribution of the interlayer capacitance was neglected, while the defect density of the interlayer was captured in the interfacial SRH parameters. Tunneling due to defects was not accurately modeled due to a lack of detailed knowledge of the interface parameters, but calculations with tunneling processes included are presented in Fig. 4.14A and Fig. 4.15 to illustrate qualitatively the behavior that results from this effect.

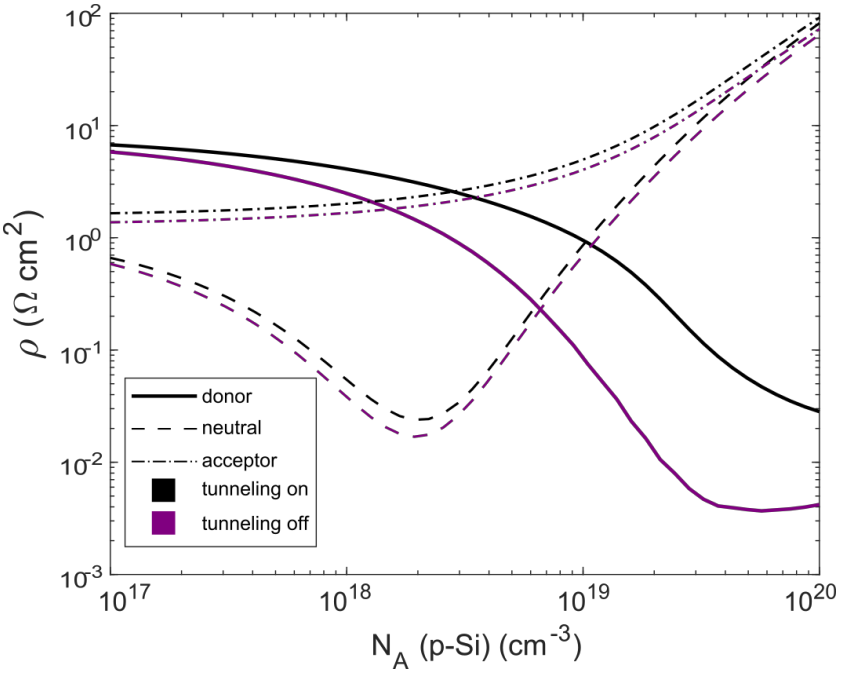

Figure 4.15 Calculated small-voltage resistivity as in Fig. 4B of the main text, this time showing the effect of tunneling. Tunneling has a minor effect for neutral and acceptor-type defects, but significantly affects the donor-defect models when the acceptor doping is large because tunneling effects are most significant when the depletion region is small which occurs for large acceptor doping concentrations.

Fig. 4.14A shows the computed *J-V* characteristics of a TiO_2/p^+-Si heterojunction with varying gaps Δ in the range of 0.4-0.9 eV, and with a high density of neutral mid-gap defects (recombination velocities $S_n = S_p = 10^5$ cm/s), all other parameters being equal (see Table 4.1). These *J-V* characteristics bear a striking resemblance to the experimental behavior of Fig. 4.7B in that they both exhibit the full range of qualitative characteristics seen experimentally, namely highly conductive Ohmic behavior (e.g. Δ = 0.4), asymmetric exponential-type curves (Δ = 0.5, 0.6 eV) and strong rectification (Δ = 0.7-0.9 eV). The detrimental effect of a large band offset can only be compensated by higher recombination velocities up to the physical limit of $S_{n,p} = v_{th} \approx 10^7$ cm/s, likely ruling out high defect-mediated conductivity for band offsets greater than ~0.7 eV. A somewhat less trivial prediction of the SRH model concerns the balance of carrier densities at the interface. According to equation S1 (supplementary information), the interfacial carrier densities must be balanced to achieve maximal conductivity (in particular $v_n n_0 \approx v_p p_0$ where n_0, p_0 are

the equilibrium carrier densities at the interface and $v_{n,p}$ their quasi-recombination velocities). Experimentally the interfacial conductivity was found to benefit from a high substrate doping (Fig. 4.14B, red markers), which is consistent with donor type defects at the interface that require excess acceptors to achieve the relevant balance. Donor defects are frequently present at both TiO_2 and un-passivated Si surfaces in the form of oxygen vacancies (*162*) and dangling bonds (P_b centers) (*163*), respectively. The SRH theory thus consistently accounts for the Ohmic conductivity between TiO_2/p^+-Si, in accord with the behavior observed previously for TiO_2-protected Si photoanodes (*136, 164*).

Field [G]	Resistivity [ohm cm]	Hall Coefficient [cm³/C]	Type	Carrier Density [1/cm³]	Hall Mobility [cm²/(VS)]
$1.0000x10^3$	$8.4670x10^{-1}$	$-8.2446x10^{-1}$	n	$7.5713x10^{18}$	$9.8962x10^{-1}$
$3.0000x10^3$	$8.4615x10^{-1}$	$-7.8738x10^{-1}$	n	$7.9278x10^{18}$	$9.4511x10^{-1}$
$5.0001x10^3$	$8.4497x10^{-1}$	$-7.8614x10^{-1}$	n	$7.9403x10^{18}$	$9.5362x10^{-1}$

Table 4.1 Hall-effect measurements for annealed TDMAT-ALD TiO_2

According to the SRH theory outlined above, the diverse behavior seen in Fig. 4.7B with respect to preparation conditions likely results from variations in the band offset between the TiO_2 conduction-band edge and the Si valence band (Δ), as well as in the TiO_2 doping density and interfacial defect properties. In accordance with this picture our highest-performing material in the homojunction designs was TDMAT-ALD TiO_2, which exhibited relatively large electron affinities for anatase (Fig. 4.11). Although vacuum levels are only an approximate indicator of the actual band alignment, the data suggest a small Δ, in addition to sufficiently conductive TiO_2 layer (Table 4.1), is helpful for obtaining a high-conductivity contact between to p^+-Si. This raises a related issue regarding the TiO_2 work function's influence on the perovskite cell's built-in or flat-band voltage. A larger n-type selective contact work function predicts a reduced built-in voltage, all other things being equal, and therefore a reduced perovskite V_{oc}. This is contrary to our experimental observation that the perovskite cells on TDMAT-ALD TiO_2 function without substantial losses to their open-circuit voltage. The observed cell performance is thus indicative that the mesoporous TiO_2 layer inserted between the compact TiO_2 layer and the perovskite in the standard cell

architecture functions to maintain the top-cell voltage, likely due to its smaller work function (*139*). Indeed, single-junction perovskite cells fabricated without a mesoporous TiO_2 layer (i.e. directly on the TDMAT-ALD TiO_2 compact layer) exhibited drastically reduced open-circuit voltages as predicted by the preceding argument (Fig. 4.16: note that this does not indicate an intrinsic limit of planar cells, as solution-processed compact layers yielded uncompromised, high open-circuit voltages (*165*)). This reasoning is also supported by our drift-diffusion simulations of single-junction perovskite solar cells with and without a mesoporous layer (Fig. 4.17). The mechanism of work function adjustment imputed to the mesoporous titania is illustrated in the simulated band diagram of Fig. 4.14C. Devices whose compact titania layers have a large work function (e.g. our TMDAT-ALD TiO_2) therefore seem to benefit substantially from inclusion of the mesoporous layer. Mesoporous layers are typically annealed at high (~400 °C) temperatures to drive off the organic suspension agents, but options exist for low temperature preparation (*166, 167*), and for the deposition of layers with analogous functionality that do not require heat treatment (*168*). As a preliminary demonstration of a low-temperature interconnection-free process, we fabricated tandems with open-circuit voltages as high as ~1.75 V (Fig. 4.18) without exceeding 200 °C in the processing sequence, by optimizing the $TiCl_4$-ALD TiO_2 (Fig. 4.19). With its lower work-function, $TiCl_4$-ALD TiO_2 allows uncompromised top-cell voltages in a planar architecture without mesoporous TiO_2, although wetting issues in the perovskite deposition seem to have compromised the fill factors of these cells. This behavior is a common issue for solution-processed planar cells that can be adequately addressed by low-temperature interface engineering (*169, 170*).

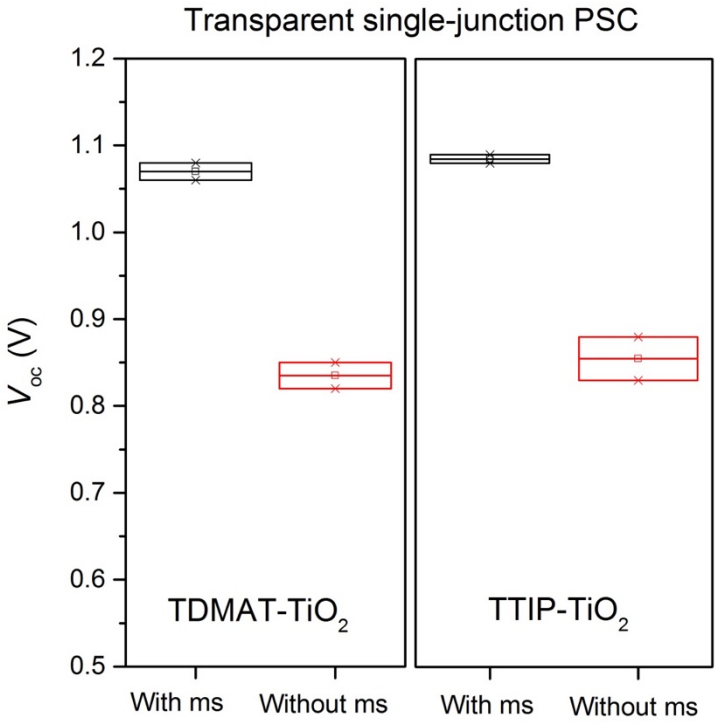

Figure 4.16 V_{oc} yield of transparent single-junction perovskite solar cells (with p^+-Si as the substrate) with and without mesoporous-TiO_2. Results for TDMAT-ALD TiO_2 are shown on the left while results for TTIP-ALD TiO_2 are shown on the right. Both titania compact layers have high work functions with the deposition conditions used in this work.

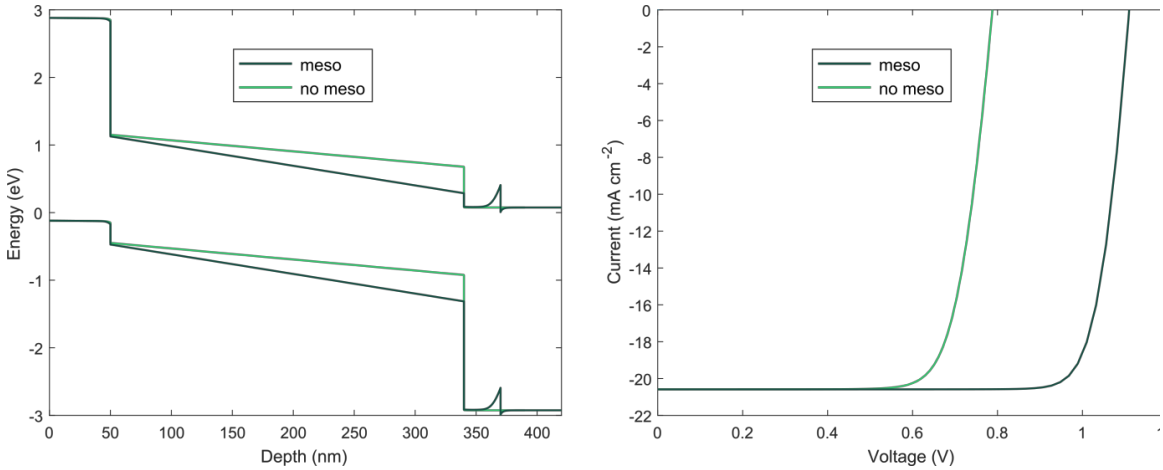

Figure 4.17 Simulated band diagram at 0 V (left) and *J-V* behavior (right) of a single-junction perovskite solar cell with and without an additional "mesoporous" titania layer inserted between the perovskite and high work-function compact titania. This represents a 1D simplification of the complex 3-dimensional mesoporous structure present in our tandem cell design, but captures the qualitative effect of including titania layers with contrasting

work functions. The mesoporous layer functions primarily to maintain the built-in voltage in the perovskite cell, as seen in the band diagram (left) and consequently discrepant open-circuit voltages (right). Here electron affinities of 4.1 eV and 4.5 eV were used for the compact and mesoporous titania layers respectively.

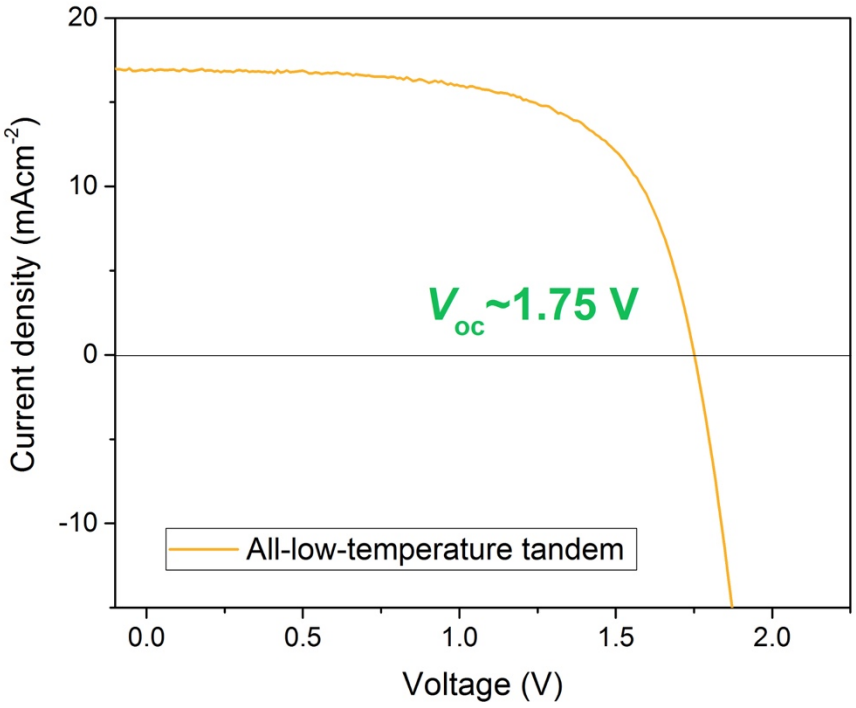

Figure 4.18 *J-V* curve of a monolithic perovskite/Si tandem solar cells with as-deposited $TiCl_4$-ALD TiO_2 (200 °C). The top perovskite subcell has a planar structure without the inclusion of the mesoporous TiO_2 film, and is fabricated with low-temperature processes.

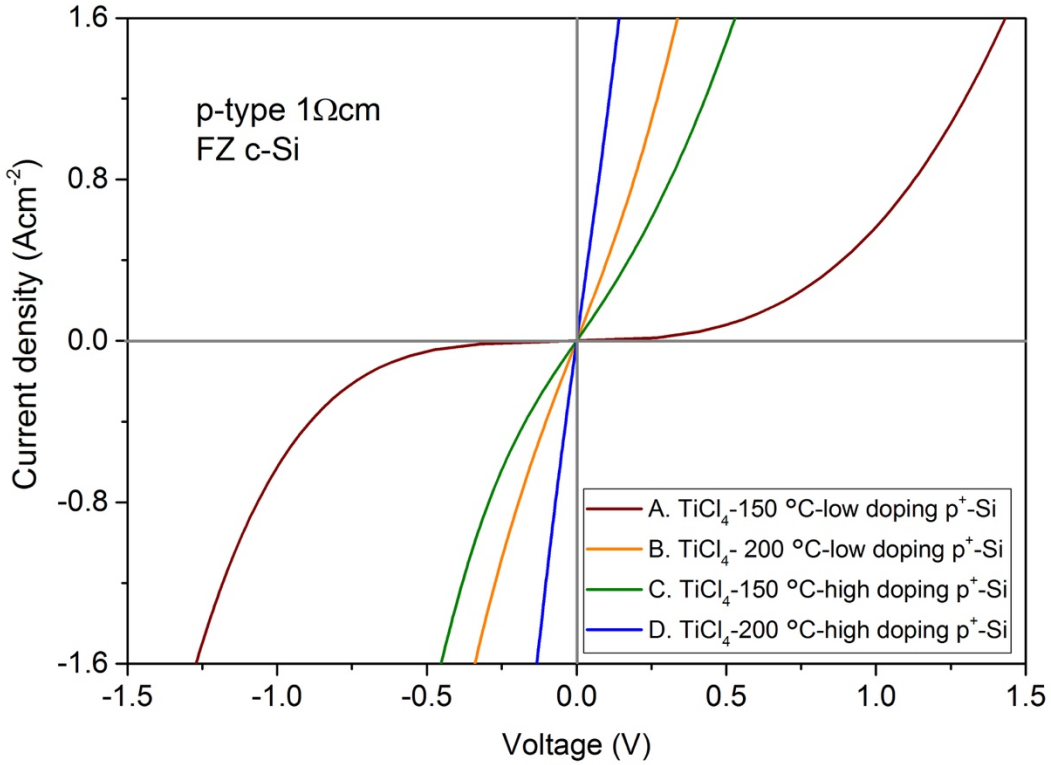

Figure 4.19 *J-V* curves of the $TiCl_4$-ALD TiO_2 deposited at low temperatures on different p+-Si wafers. The samples receive no further heat-treatment. TiO_2 deposited at 150 °C on top of p^+-Si with a doping density of (A) ~9.3×10^{19} cm^{-3}, the extracted contact resistivity is ~850 mΩcm^2 and (C) ~1.7×10^{20} cm^{-3}, the extracted contact resistivity is ~445 mΩcm^2. TiO_2 deposited at 200 °C on top of p+-Si with a doping density of (B) ~9.3×10^{19} cm^{-3}, the extracted contact resistivity is ~210 mΩcm^2 and (D) ~1.7×10^{20} cm^{-3}, the extracted contact resistivity is ~99.6 mΩcm^2.

According to our analysis, an enabling feature of interconnect-free tandems is the presence of intra-gap states that bridge the energetic offset between the Si sub-cell and the adjoining contact layer (TiO_2 in our demonstration). For homojunction Si cells, minority carriers may recombine at the same defects, compromising the Si cell's voltage. Nonetheless, for the homojunction cells with TiO_2, open-circuit voltages of 654 mV were obtained in just a few attempts whilst retaining an adequate contact resistance of 0.96 Ωcm^2 (Fig. 4.20) suggesting that considerable room for improvement utilizing homojunctions may remain in achieving the optimal balance between passivation and contact resistance. For perovskite/Si tandems, the issue of series resistance is much less severe (by a factor of ~5 (*171*)), due to the higher

voltage and lower cell current. For the polysilicon cell, this trade-off is entirely avoided due to the carrier-selective buried oxide layer, which blocks the passage of minority carriers to the TiO_2 interface (*138*). Carrier-selectivity, a common feature among passivating-contact designs, allows the TiO_2 interfacial defect density to be freely tuned for optimal contact resistance without detrimentally affecting the open-circuit voltage of the Si cell. Considering the already superior performance of passivating-contact type cells for use in tandems, the interconnect-free concept seems most promising for such cells as compared to homojunction designs.

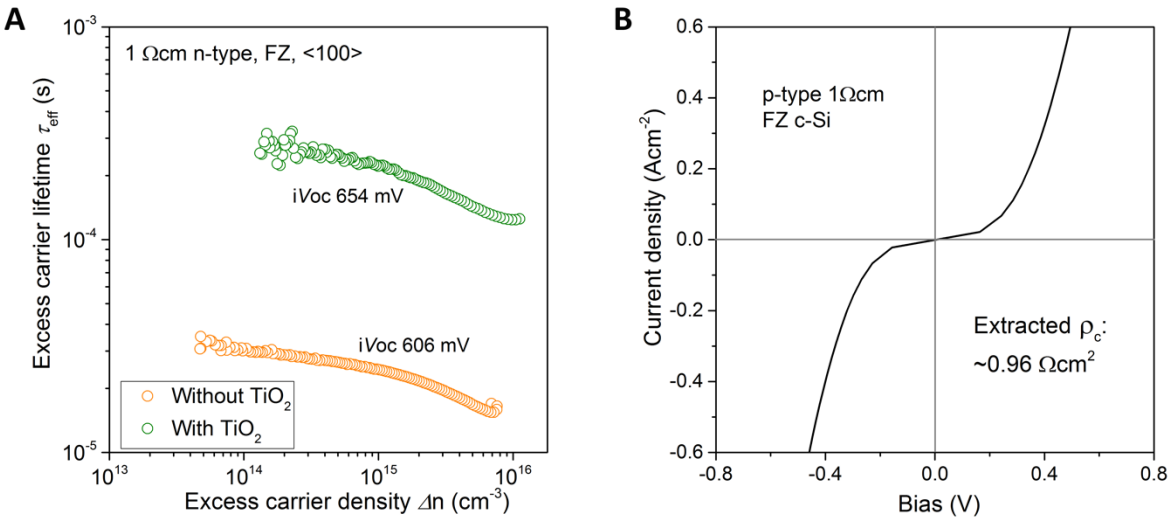

Figure 4.20 (A) Excess carrier lifetime of a Si substrate with and without TiO_2 passivation ($TiCl_4$-ALD TiO_2 deposited at 150 °C without further annealing) as a function of the measured injection level. The implied V_{oc} (iV_{oc}) is increased by ~50 mV with the $TiCl_4$ TiO_2 coating. (B) *J-V* curve of a $TiCl_4$-ALD (150 °C) TiO_2/p^+-Si sample (p^+-Si has a doping density of ~$1.5*10^{19}$ cm^{-3}).

4.3.4 Cell Stability

4.3.4.1 Perovskite Damp Heat Test

Stability is a serious issue for all perovskite devices reported in the literature to date. The stability of our devices with respect to heat and moisture was investigated by performing the damp heat test according to the testing protocol 61215 defined by the International

Electrochemical Commission (IEC) (85 °C in 85% relative humidity). These tests were performed on encapsulated semi-transparent perovskite solar cells, the perovskite cell being the primary source of instability in our tandems. Data showing the evolution of photovoltaic metrics under aging is provided in Fig. 4.21. These devices maintained ~89% of their original output after testing for > 1000 h, putting them very close to passing protocol 61215, which requires 90% retained efficiency, and shows that our cells are well within the stability range established by McGehee *et al.* (*120*) and the more recent work by Ballif *et al.* (*132*). Multiple causes could contribute to the observed performance decreases, including sub-optimal encapsulation, degradation of the organic HTM, migration of extrinsic ions introduced into the HTM, and metal electrode diffusion into the perovskite (*172, 173*).

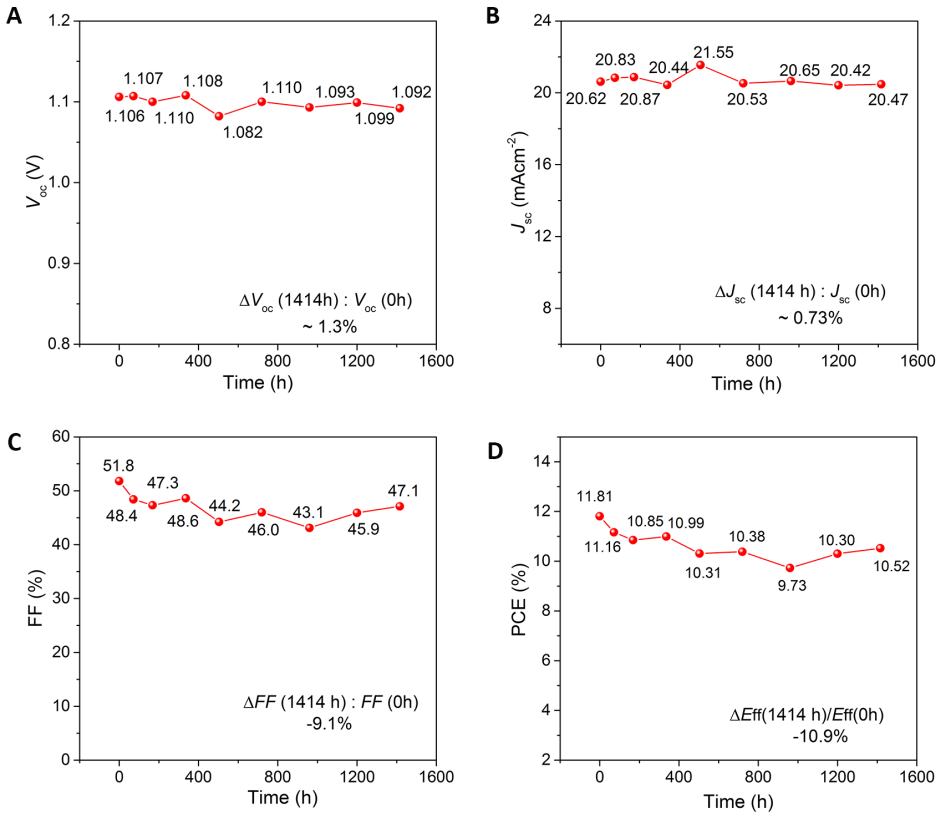

Figure 4.21 Damp heat test (85 °C in a relative humidity level of 85%) of a semitransparent perovskite solar cell. Evolution of the photovoltaic characteristics including (a) V_{oc}, (b) J_{sc}, (c) FF and (d) PCE during damp heat stability of an encapsulated single-junction perovskite device for 1414 h.

4.3.4.2 Si/perovskite Tandem Stability

We also tested the long-term stability of our tandem perovskite/Si homojunction cells. Though there has been a range of studies dealing with the stability of the single-junction perovskite solar cell, the stability of the tandem device, especially the light stability has only been reported in the recent work on tandem device by Ballif et al (*132*). Our perovskite/Si tandem device maintained an efficiency of ~18.4% after an aging period of ~2500 h in total, including overall illumination for ~800 h, corresponding to over 80% of its original output. Notably the cell spent more than 20 h during this aging period under 1-sun illumination in air. In detail, the aging test included four stages (Fig. 4.22). Stage 1 and Stage 3 were stress tests, entailing exposure to air, continuous illumination at full spectrum 1-sun intensity, and biasing near the maximum power point. Stage 2 consisted of storing the devices in the dark in an N_2 cabinet, after which the cells were taken out for *J-V* characterization (1200 h). Stage 4 consisted of light/dark cycles under a constant N_2 flow (with illumination for over 800 h).

Unsurprisingly the fastest degradation occurred in the stress tests of Stage 1 and Stage 3 (Fig. 4.22A and Fig. 4.22C, highlighted in yellow), where moisture, oxygen and the interaction of light with these species are all potential culprits. The performance degradation under these conditions was almost linear, which is consistent with the recently published result shown for the tandem device with record efficiency (*132*). However, we found that such degradation can be mostly reversed after resting the cells in the dark, as seen by the efficiency returning to ~20.4 % as compared to ~20.7% before stress testing in Fig. 4.22C. This indicates that irreversible chemical degradation by moisture and oxygen is a minor factor under short-term exposure to air and illumination. The interaction of light with oxygen and light-enhanced ion migration could then be the major contributors for the reduction during the stress tests. This "dark recovery" has been previously reported for single junction perovskite solar cells (*174, 175*), whilst this is the first time that has been investigated on the perovskite/Si tandem. In Stage 2 (Fig. 4.22B), with storage of the device in dark for ~1200 h, no performance recovery was observed, but the performance degradation was also relatively small (with the efficiency

dropping from 21.9% to 21.4% after ~700 h aging in the dark). A further reduction to ~20.7% efficiency was observed after another ~500 h aging.

The degradation of the tandem device under illumination in N_2 atmosphere was slow over the ~800 h light/dark cycles. A 10% reduction measured from the start of each cycle (20.4% for the starting point of the first cycle and 18.4% for the seventh cycle) was observed over the full light/dark cycling test (7 cycles of approx. 120 h). This is somewhat comparable to the current record tandem cell (*132*), wherein an efficiency drop of ~10% during the course of ~250 h illumination was reported, although a different testing protocol and the phenomenon of dark recovery makes direct comparison difficult. Similarly, we observe clear dark recovery after comparable storage time in all the light/dark cycles. Overall, our perovskite/Si tandem exhibited respectable stability, with over 80% efficiency remaining after aging under various conditions for >2500 h.

Whilst protocols of assessing the perovskite solar cell still vary largely (*175*), our perovskite-based device shows promising stability after industry standard stress tests (including the damp heat test and light soaking at 60°C) and the long-term tracking of our perovskite/Si tandem device performance including over 800 h illumination and dark recovery.

The titania is on the rear side of the top-cell and is therefore almost completely shielded by the perovskite and other front-side layers that strongly absorb UV. This configuration may therefore have benefits in terms of stability, as the photocatalytic effect of TiO_2 (*176, 177*) has been discussed as one of the main causes of as-prepared perovskite degradation.

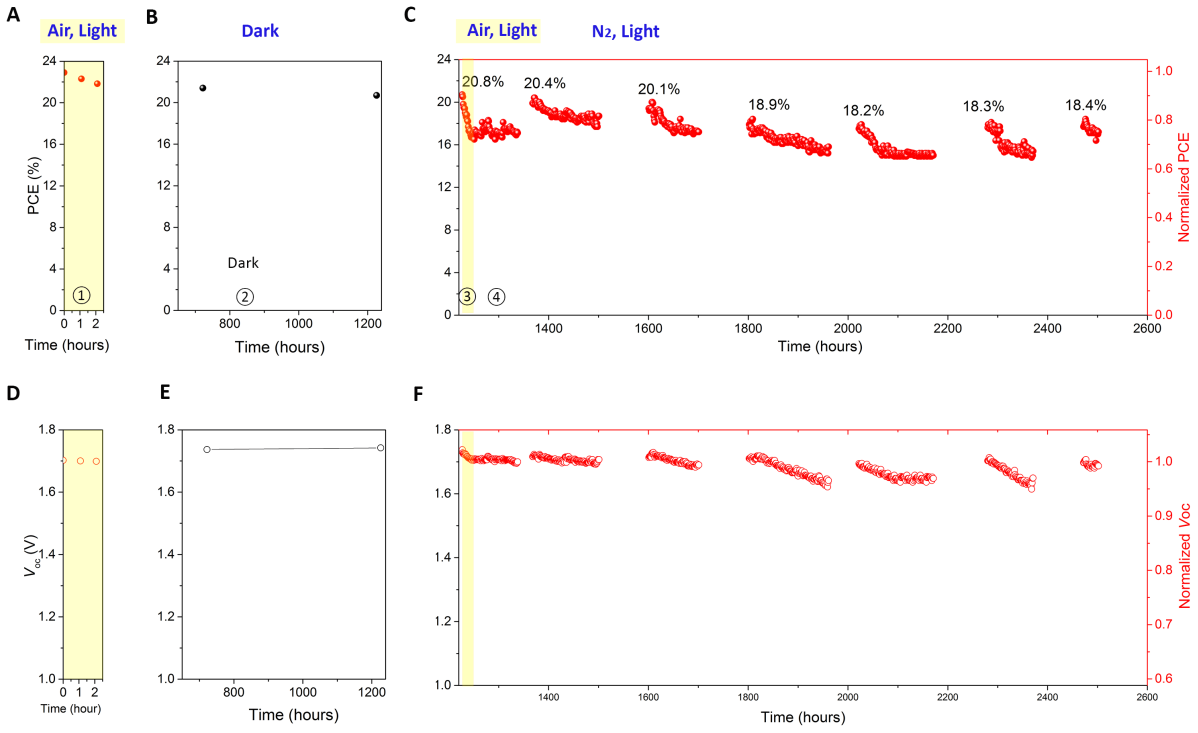

Figure 4.22 PCE evolution of the proof-of-concept perovskite/Si homojunction tandem device undergoing four different aging stages. (A) Stage 1: 1 Sun continuous illumination in air for ~2.1 h, biased near maximum power point); (B) Stage 2: device stored in dark in a N_2 cabinet for ~1224 h; (C) Stage 3: device under 1 Sun continuous illumination in air for ~19 h, biased at ~1.3 V, and Stage 4: device underwent light/dark cycles for seven cycles, with total illumination of over 800 h. The measurement under light was taken at 25 °C. Corresponding V_{oc} evolution (D-F) of the same device under the same conditions.

4.4 Conclusion

In conclusion, we have demonstrated two proof-of-concept 2-terminal perovskite/Si tandem devices that function without a conventional interconnection layer between their sub-cells. In principle this concept may be generalized to other cell designs including those based on the use of HIT silicon, as well as newer passivating-contact Si cells (*146*). Whereas fabrication of an nc-Si tunnel-junction interconnect is relatively straightforward for HIT cells, these layers introduce a small but potentially significant amount of parasitic loss in the region of ~550-700 nm [16] where the nc-Si is absorbing and the perovskite top cell's

absorption is simultaneously incomplete. Optical calculations indicate that this loss can be as large as ~1.0-1.5 mA cm^{-2} under the AM1.5G spectrum for standard tunnel-junction thicknesses. Larger losses can be expected for ITO recombination layers deposited without annealing [16]. The interconnect-free concept thus offers dual advantages of simpler processing and reduced optical losses compared to TCO and tunnel-junction interconnection layers. Sub-optimal optics on our tandem device's front side was identified as the main performance limitation in our demonstration devices, which could be markedly improved by using a silicon cell with front-surface texturing for anti-reflection and thinner, less absorbing hole-transport materials. The contact between TiO_2 and Si should not be substantially affected by micron-scale texturing, making the interconnect-free design described here fully compatible with evaporating a perovskite top-cell cell onto a textured Si wafer, which leads to very low optical losses (*132*). In principle, the desired device properties can also be obtained from a variety of TiO_2 deposition and processing conditions, and from other materials. The publication of a similar scheme using SnO_2 (*178*) instead of TiO_2 whilst this paper was under review demonstrates the wide applicability of the interconnect-free concept. Jointly, our work highlights the potential of emerging perovskite photovoltaics to enable low-cost, high-efficiency tandem devices through straightforward integration with commercially relevant and emerging Si solar cells.

Chapter 5
Tuning the Catalytic Activity of Oxygen- and Chlorine-Evolution Electrocatalysts with Atomic Layer Deposition

5.1 Introduction

Highly active electrocatalysts are required for the cost-effective generation of fuels and commodity chemicals from renewable sources of electricity (*179, 180*). Despite potential advantages (e.g., facile product separation), the industrial use of many heterogeneous electrocatalysts is currently limited in part by suboptimal catalytic activity and/or selectivity. In addition, there are limited methods to tune the selectivity and activity of heterogeneous electrocatalysts (*179*). Methods and design tools such as doping, inducing strain, and mixing metal oxides have been used to improve the catalytic activity of heterogeneous electrocatalysts (*181-184*). The activity of heterogeneous electrocatalysts can also be tuned by applying thin layers of another material, leading to an altered surface charge density on the resulting composite material relative to the bulk charge density of either individual material (*185-190*). This approach has been widely used to alter the catalytic and electronic properties of core/shell nanoparticles, although additional tuning of the particle support structure is necessary to create an efficient heterogeneous electrocatalyst (*191, 192*). Density functional theory calculations have shown that a single atomic layer of TiO_2 on RuO_2 should lead to enhanced selectivity for the chlorine-evolution reaction (CER) relative to the oxygen-evolution reaction (OER) (*186*). Enhanced catalytic activity for the OER has been reported for WO_3 photocatalysts coated with 5 nm of alumina, with the activity increase ascribed to an alteration in the electronic surface-state density (*193*). Enhanced catalytic activity has also

been observed at the interface between TiO_2 and RuO_2, with charge transfer between RuO_2 and TiO_2 resulting in a mixed phase with an intermediate charge density (*182*).

Herein, atomic layer deposition (ALD; a stepwise deposition technique) has been used to tune the surface charge density, and consequently tune the catalytic activity, of electrocatalytic systems in a fashion consistent with estimates based on group electronegativity concepts (see Figs. S1-S5 in the Supplementary Materials for further discussion of ALD, surface homogeneity, and group electronegativity estimates). To test these predictions, the activities of the known electrocatalysts, IrO_2, RuO_2, and F-doped SnO_2 (FTO) were tuned and evaluated for the chlorine-evolution reaction (CER) and the oxygen-evolution reaction (OER). The CER provides a promising approach to infrastructure-free wastewater treatment as well as for the production of chlorine, an important industrial chemical whose global annual demand exceeds seventy million metric tons (*194, 195*). The OER is the limiting half-reaction for water splitting that could provide hydrogen for transportation and could also provide a precursor to energy storage via thermochemical reaction with CO_2 to produce an energy-dense, carbon-neutral fuel (*196*).

5.2 Material Selection, Sample Preparation, and Characterization

5.2.1 Material Selection and Group Electronegativity

Each material tested was selected based on its theoretical group electronegativity (χ). Electronegativities were estimated for heterogeneous electrocatalysts by taking the geometric mean of the electronegativities of the constituent atoms (*187, 197*). Allen scale electronegativities were used because it is superior to other electronegativity scales (e.g. Pauling, Mulliken, Allred-Rochow) at differentiating between the electronegativities of the transition metals (*198-200*). As an example, for TiO_2: Ti ($\chi = 1.38$) and O ($\chi = 3.61$), therefore TiO2 ($\chi \approx (1.38 \times 3.61^2)^{1/3} = 2.62$).

RuO_2 ($\chi \approx 2.72$), was firstly selected because it is the most active catalyst for the OER in the benchmarking literature (Fig. S5) as well as the most active catalyst for the CER (*201*). IrO_2 ($\chi \approx 2.78$) and FTO ($\chi \approx 2.88$) were also investigated because they have higher electronegativities than RuO_2, and therefore using ALD to overcoat these catalysts with TiO_2 ($\chi \approx 2.62$) is expected to shift their surface electronic properties (i.e., the potential of zero charge, EZC) and catalytic activities towards that of RuO_2, the optimal single metal oxide catalyst. In the case of FTO, the electronegativity of SnO_2 was estimated because it is not known how small quantities of F would change the electronegativity of SnO_2. Electronegativity is a useful theoretical concept for estimating the directions in which surface charge availability and the corresponding catalyst-reacting-species bond strength may move, but not to estimate the magnitude of change or any complex details of any physical parameter. These materials were also chosen because TiO_2, IrO_2, RuO_2, and other materials are commonly used to form mixed metal oxide electrodes, most notably the dimensionally stable anode (DSA), in which TiO_2 increases the anode's stability, but does not confer enhanced activity to the aggregated material (*202*).

5.2.2 Sample Preparation

The three catalysts were prepared on substrates that had very low roughness to minimize effects in geometric overpotential measurements due to surface area differences. Specifically, IrO_2 and RuO_2 samples consisted of a ~300 nm metal-oxide film sputter deposited on a (100)-oriented Si substrate. The samples were heated to 300 ^oC and Ir or Ru were sputtered using an RF source under an Ar/O_2 plasma with a constant flow of 20 sccm Ar and 3 sccm O_2 for 22.42 min for Ir, and 13.5 sccm Ar and 1.5 sccm O_2 for 22 min for Ru. The chamber pressure was maintained at 5 mTorr during deposition, and the base pressure of the chamber was held at $< 10^{-7}$ Torr between depositions. The phase purity of the samples was confirmed by X-ray diffraction measurements, as detailed below (Fig. 5.1). TEC 15 FTO

glass substrates were used in the case of FTO-based electrocatalysts. TiO_2 overlayers were then deposited on top of the electrocatalysts.

TiO_2 films were deposited on IrO_2, RuO_2 and FTO at 150 °C using an Ultratech Fiji 200 Plasma ALD System (Veeco, Waltham, MA). The IrO_2, RuO_2, and FTO were prepared as described above. Prior to ALD, one 0.060 sec pulse of H_2O was applied to the sample. Each ALD cycle consisted of a 0.250 sec pulse of tetrakis(dimethylamido)titanium (TDMAT, Sigma-Aldrich, St. Louis, MO, 99.999%, used as received), followed by a 0.060 sec pulse of H_2O (18 MΩ cm, Millipore). A 15 sec purge under a constant 0.13 L/min flow of research-grade N_2 was performed between each precursor pulse. While idle, the ALD system was maintained under a continuous N_2 purge with a background pressure of 0.50 Torr.

Following ALD of TiO_2, a tungsten-carbide-tipped scribe was used to contact a gallium-indium eutectic (Alfa Aesar, Ward Hill, MA, 99.99%, used as received) onto the back side of the IrO_2 and RuO_2 samples. A coiled zinc-plated copper wire (Consolidated Electrical Wire and Cable, Franklin Park, IL) was placed onto the gallium-indium and the wire was covered with one-sided copper foil tape (3M, Maplewood, MN, used as received).

For the FTO electrodes, a coiled zinc-plated copper wire was placed onto the conductive side of the FTO electrode and secured with one-sided copper foil tape.

To protect the contact and define the geometric surface area, circular holes were punched in a strip of 1-inch width 3M vinyl electroplating tape using a 2 or 3 mm diameter circular punch. The entire electrode was then covered with this tape, only exposing the 3 mm diameter circle of the electrode. The wire covered the tape for at least 4 cm, such that neither the wire housing nor the metallic wire was exposed to the electrolyte.

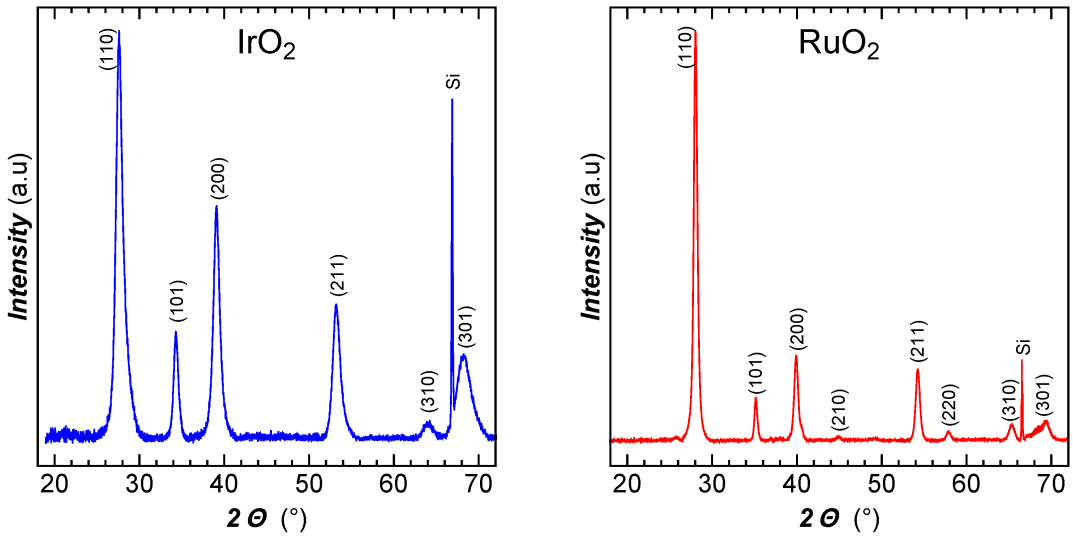

Figure 5.1 X-ray diffraction patterns for typical IrO_2 and RuO_2. All observed peaks were indexed to standard diffraction patterns for IrO_2 and RuO_2, respectively.

5.2.3 Catalyst Microstructure

The microstructure of a heterogeneous electrocatalyst is important to characterize. Increasing a catalyst's surface area, which generally increase the active-site density, can lead to enhanced catalytic activity without changing the intrinsic catalytic activity of the catalyst (*9*). Therefore, understanding a catalyst's surface morphology is vital to discerning the mechanism(s) behind enhanced catalytic performance. The microstructure of a typical IrO_2-based electrocatalyst with a thick (1000 cycle) TiO_2 overlayer is shown in the cross-sectional scanning electron microscopy (SEM) image in Figure 5.2A. The catalyst consists of a crystalline IrO_2 layer with a conformal amorphous TiO_2 overlayer.

5.2.3.1 Atomic Force Microscopy

Atomic Force Microscopy (AFM) measurements were conducted to further characterize the catalysts' microstructure. A Bruker Dimension Icon was used in Peak Force Tunneling AFM Mode (PF-TUNA) for all topography and conductive AFM measurements. Even at low cycle numbers (< 20 cycles) the resulting electrocatalysts were very smooth with low surface

roughness (Fig. 5.2B) such that the surface area as measured by atomic-force microscopy (AFM) was roughly equivalent to the measured geometric surface areas (Table 5.1).

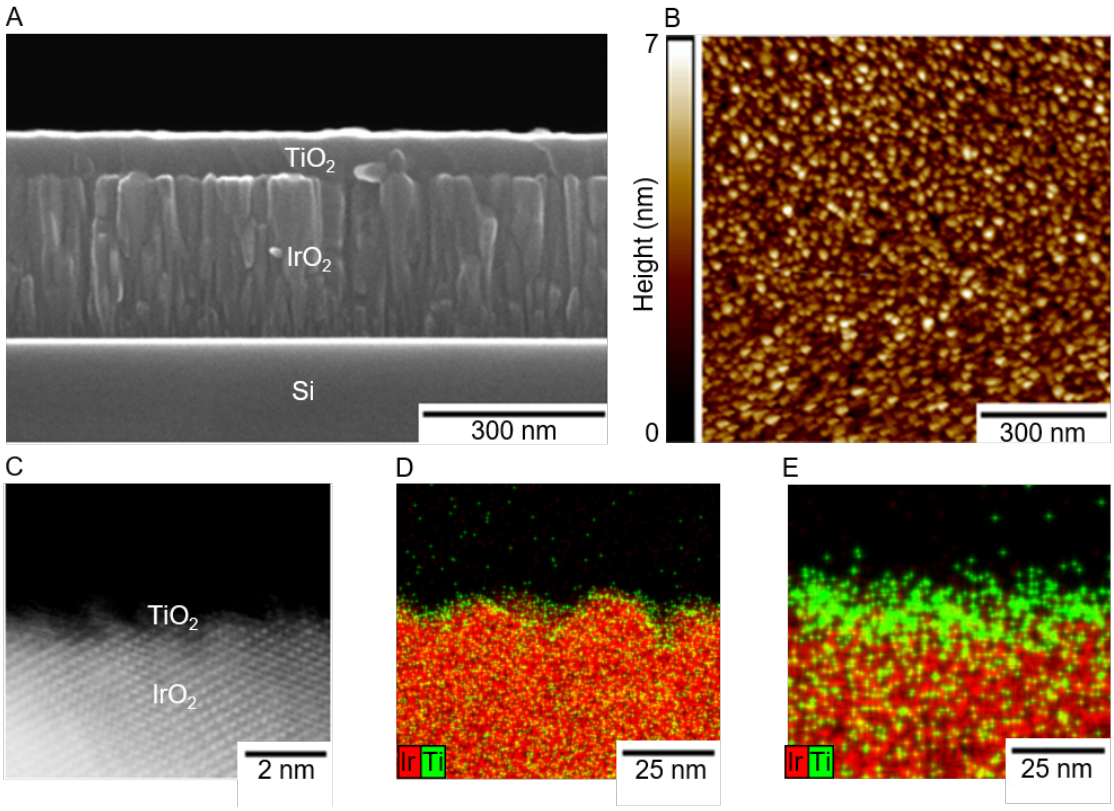

Figure 5.2 Material characterization of typical electrocatalyst samples. (A) SEM image of an IrO_2 catalyst with 1000 ALD TiO_2 cycles. (B) AFM map of IrO_2 with 10 ALD cycles of TiO_2. (C) HAADF-STEM image of an IrO_2-based electrocatalyst with 10 ALD cycles of TiO_2. The underlying crystalline material is IrO_2 while the hair-like material at the surface is TiO_2. (D,E) Energy dispersive X-ray spectroscopy (EDS) maps of IrO_2-based electrocatalysts with 10 and 40 ALD cycles of TiO_2, respectively. The red color indicates Ir and green indicates Ti. Note that green and red intermix throughout this cross section due to the inherent roughness of the sample.

Representative surface topology (Fig. 5.3) and conductive AFM (TUNA current) (Fig. 5.4) for 0, 3, 10, and 1000 ALD TiO_2 cycles are shown for IrO_2, RuO_2, and FTO substrates. AFM images of RuO_2, IrO_2, FTO, and substrates coated with 1000 cycles of TiO_2 were consistent with previously reported images of materials grown under similar conditions (*203-206*).

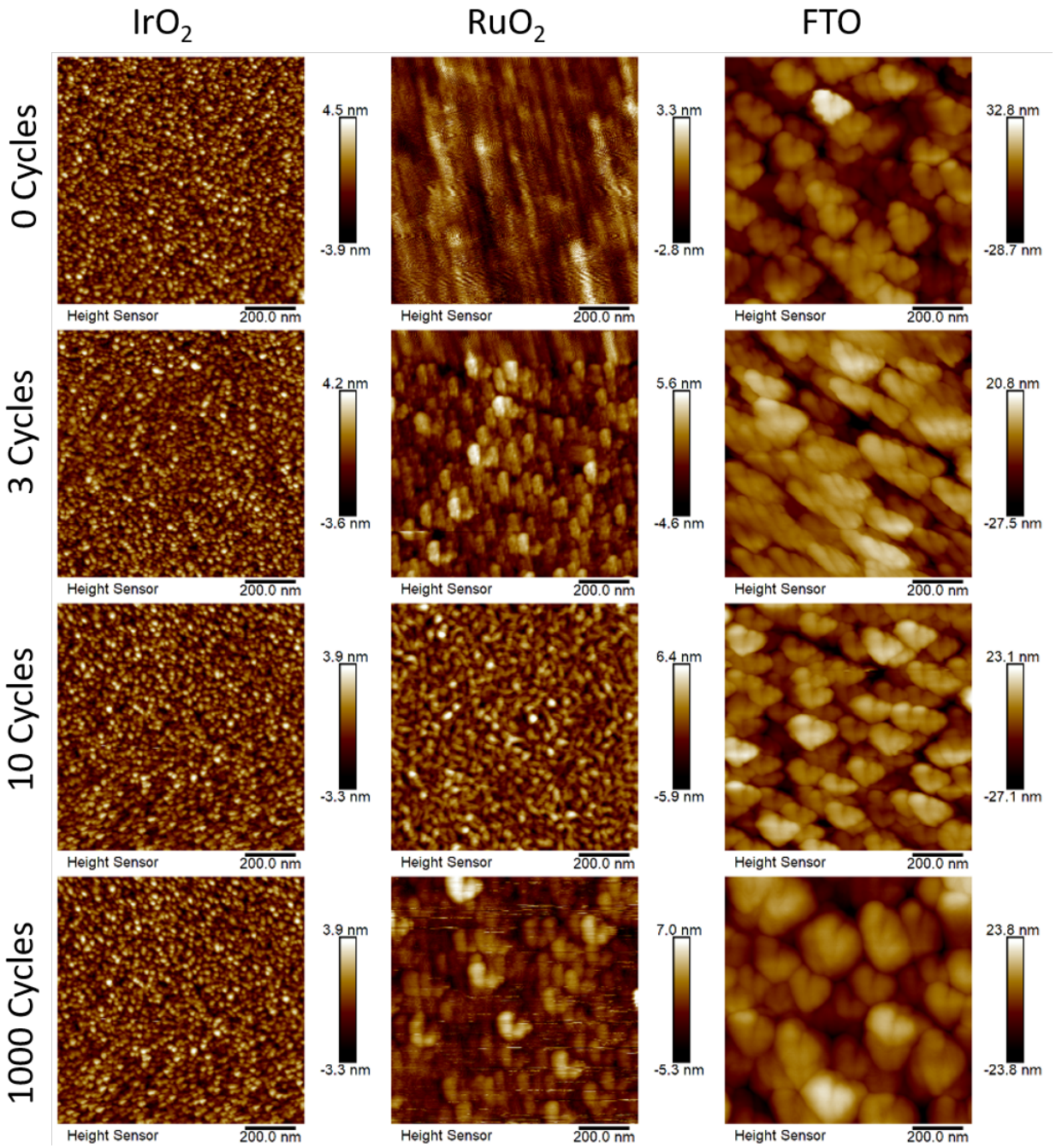

Figure 5.3 Representative topographic atomic force microscopy images of IrO_2, RuO_2, and FTO each with 0, 3, 10, and 1000 ALD cycles of TiO_2.

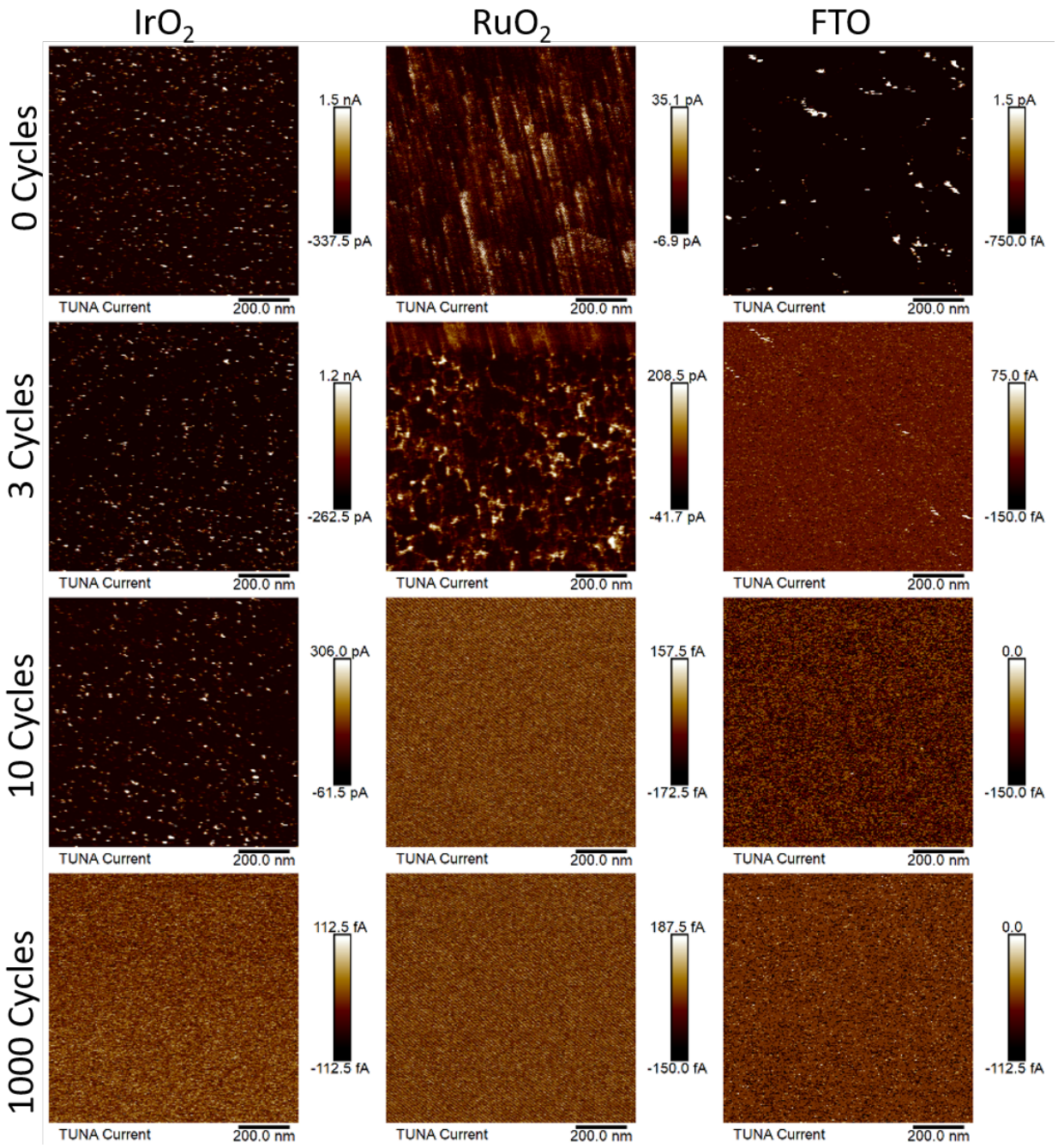

Figure 5.4 Representative conductive atomic force microscopy tunneling current images of IrO_2, RuO_2, and FTO each with 0, 3, 10, and 1000 ALD cycles of TiO_2.

	AFM Measured Surface Area as a Percentage of Geometric Surface Area		
TiO_2 Cycle Number	**IrO_2**	**RuO_2**	**FTO**
0	104.52%	107.75%	108.35%
3	103.87%	102.45%	107.98%
6	103.12%	103.93%	110.24%
10	102.94%	104.08%	108.05%
20	103.32%	104.61%	110.60%
30			108.92%
40	102.70%	102.61%	108.27%
50			108.18%
60	103.60%	101.65%	108.10%
500	102.00%		
1000	102.01%	111.02%	104.15%

Table 5.1 Surface area (measured by AFM) as a percent of geometric surface area. Dividing these values by 100 yields topographic roughness factors.

The surface area as measured by AFM was at most 112% of the geometric surface area (Table 5.1). For IrO_2 and FTO, the surface topography was similar for all cycle numbers of TiO_2. The only observable change as the number of ALD cycles increased was that the conductivtiy and surface area decreased uniformly as TiO_2 was deposited, suggesting that TiO_2 coated the catalysts' surface reasonably evenly. Based on AFM data, no holes were visible in the TiO_2 coating at any cycle number for FTO and IrO_2. The surface topography of bare RuO_2 was rippled (0 cycles), and gradually morphed into a flake-like structure (3-6 cycles), a columnar structure similar to IrO_2 (10-30 cycles), and then back into flakes similar to FTO (>30 cycles). Furthermore, for RuO_2 at 3 ALD cycles some holes in the TiO_2 were clearly visible in both the topological and the conductive AFM images. No such holes were visible at > 3 cycles TiO_2. Conductive AFM showed uniformly drecreasing conductivity with cycle number once no holes were visible (>3 cycles TiO_2).

5.2.3.2 Transmission Electron Microscopy

The growth rate of ALD TiO_2 (0.50-0.65Å/cycle) suggests that for low cycle numbers (< 20 cycles, ~2 nm) the AFM resolution is insufficient to accurately discern the catalysts' surface morphology. Therefore, high-resolution transmission electron microscopy images and energy dispersive x-ray spectroscopy mapswere aquired of 10 and 40 ALD cycles of TiO_2 on IrO_2 (Fig. 5.2C-E and Fig. 5.5). ALD of 10 cycles of TiO_2 on IrO_2 exhibited a semicontinuous film where the majority of imaged areas were covered with TiO_2 with relatively small gaps of what appeared to be uncoated area. However, 40 ALD cycles resulted in a fully continuous film for all areas imaged.

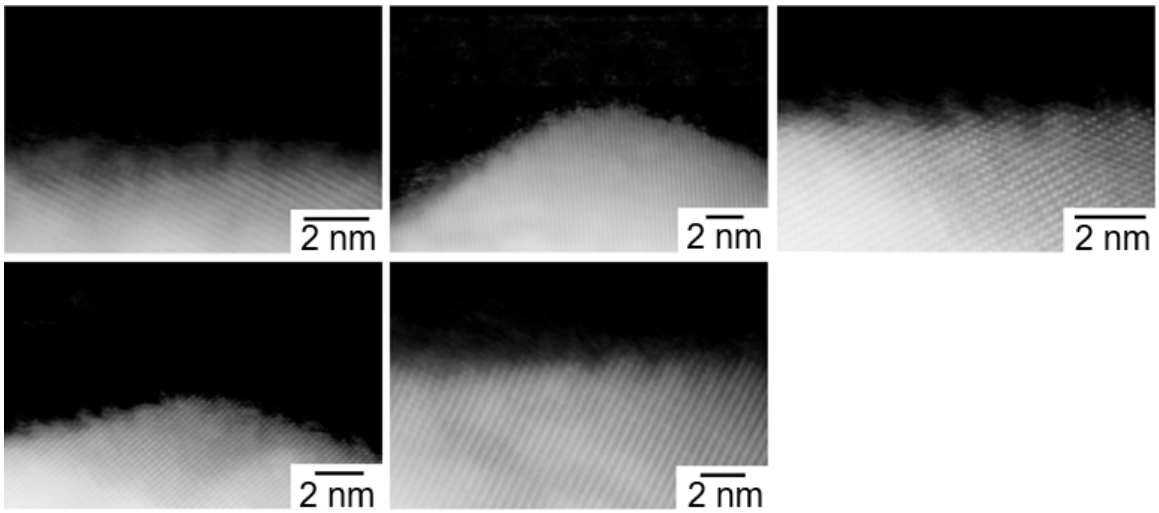

Figure 5.5 High-Angle Annular Dark-Field Scanning Transmission Electron Microscopy (HAADF-STEM) images of different IrO_2 + 10 ALD cycles of TiO_2 samples. The crystalline sublayer is IrO_2 and the "hairy" top layer is amorphous TiO_2.

5.3 Catalyst Performance

After TiO_2 deposition the samples were tested for their catalytic performance for the OER and CER. The three major electrocatalyst figures of merit for catalyst performance are the overpotential, specific activity, and stability. In the following sections, we report the

performance of our electrocatalysts as a function of TiO_2 deposition thickness. Details regarding the electrochemical testing procedure and analysis can be found in Appendix C.

5.3.1 Catalyst Overpotential

Overpotentials (η; the excess potential beyond the equilibrium potential required to reach a given current density) were determined for IrO_2, RuO_2, and FTO as a function of the successive number of TiO_2 ALD cycles for the OER at 10 mA/cm^2_{geo} in 1.0 M H_2SO_4 and for the CER at 1 mA/cm^2_{geo} in 5.0 M NaCl adjusted to pH 2.0 with HCl. Current densities were chosen to produce > 95% measured Faradaic efficiency for each catalyst (Table S2), and current-potential data were corrected for the solution resistance (< 2.0 mV correction) as measured by electrochemical impedance spectroscopy (see Appendix B. 2 for details).

The measured OER overpotentials at 10 mA/cm^2_{geo} for bare RuO_2 and IrO_2 agreed well with values reported for catalysts prepared on similarly flat surfaces, however we are unaware of comparable OER data for FTO or for CER catalysts (*207*). The overpotentials for IrO_2 and FTO, for both the OER and CER, initially showed an improvement (i.e., reduction) with increasing ALD cycle number, before exhibiting an inflection point due to an increase in overpotential at higher ALD cycle numbers (Fig. 5.6). The triangular shape observed between the overpotential and the TiO_2 ALD cycle number is typical of a volcano-type relationship that exemplifies the Sabatier principle (*208*). The overpotential reductions between bare IrO_2 and FTO catalysts and those at the peak of the volcano curve for the OER were $\Delta\eta_{OER} \approx$ -200 mV at 10 cycles and -100 mV at 30 cycles, respectively. For the CER, the observed overpotential reductions were $\Delta\eta_{CER} \approx$ -30 mV at 3 cycles and -100 mV at 10 cycles, for IrO_2 and FTO respectively (Fig. 5.6). A volcano-type relationship between cycle number and overpotential was also observed for RuO_2 facilitating the OER, with $\Delta\eta_{OER} \approx$ -350 mV between 0 and 10 cycles. However, for the CER, the overpotential of the RuO_2-based catalyst increased with TiO_2 ALD cycle number.

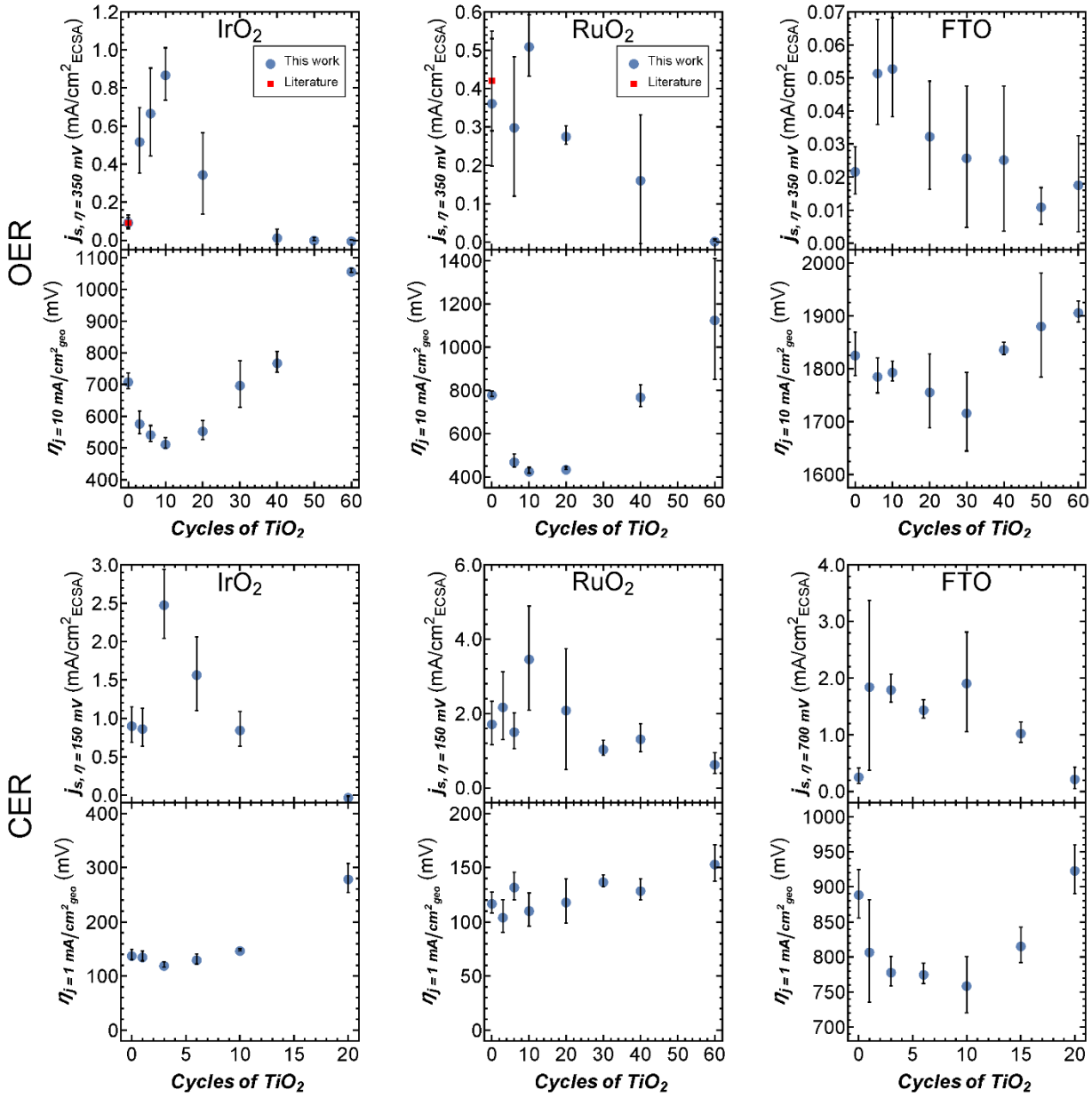

Figure 5.6 Specific activities (j_s) and overpotentials (η) for the OER and CER on IrO_2, RuO_2, and FTO coated at various ALD cycles of TiO_2. Overpotentials were measured at 10 mA/cm^2_{geo} for the OER and at 1 mA/cm^2_{geo} for the CER (normalized to geometric surface area). Specific activities for the OER were measured at 350 mV (IrO_2 and RuO_2) or 900 mV (FTO). Specific activities for the CER were measured at 150 mV (IrO_2 and RuO_2) or 700 mV (FTO). The red squares indicate available literature values.

5.3.1.1 Electronegativity and Catalytic Activity

To better understand how group electronegativities may be correlated with catalytic activity for heterogeneous electrocatalysts, group electronegativities were calculated for oxygen evolution catalysts from this work and for the catalysts compared in Seh *et al.* and plotted against overpotentials at 1 mA/cm^2_{AFMSA} for each catalyst (Fig. 5.7, Appendix B. 2.1 for details). The overpotential and electronegativity show a similar volcano-like relationship as to that of the overpotential and ALD cycles of TiO_2, suggesting that the changes in the thickness of the TiO_2 overlayer may be correlated with changes in the group electronegativity. This is explored further in Section 5.4.

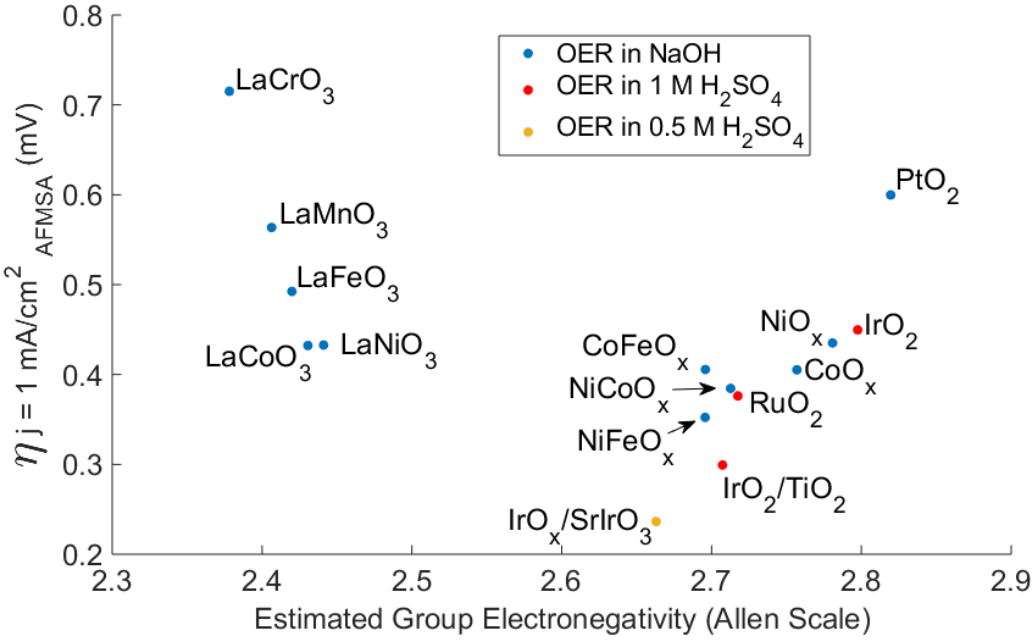

Figure 5.7 Group electronegativity vs overpotential at 1 mA/cm^2_{AFMSA}. Overpotential data was taken from Seh *et al.* (blue and orange circles) and from this work (red circles). For $LaCrO_3$, $LaMnO_3$, $LaFeO_3$, $LaCoO_3$, $LaNiO_3$, RuO_2, IrO_2, and PtO_2 group electronegativites were estimated by taking the geometric mean of the Allen Scale electronegativities of the constituent atoms. For $IrO_x/SrIrO_3$, Ir_2SrO_7 was assumed for group electronegativity calculations (*209*). For IrO_2/TiO_2, $IrTiO_4$ was assumed for group electronegativity calculations For $NiFeO_x$, $NiFe_2O_4$ was was assumed for group electronegativity calculations (*201*). For $NiCoO_x$ $NiCo_2O_4$ was assumed for group electronegativity calculations (*201*). For $NiCoO_x$, $NiCo_2O_4$ was assumed for group electronegativity calculations (*201*). For $CoFeO_x$, $FeCo_2O_4$ was assumed for group

electronegativity calculations (*201*). For CoO_x, $CoO_{1.5}$ was assumed for group electronegativity calculations (*201*). For NiO_x, Ni_2O_3 was assumed for group electronegativity calculations (*201*).

5.3.2 Specific Activity

The specific activity (i.e., the current density normalized to the electrochemically active surface area (ECSA)) is a standard quantity for comparing the OER activity of heterogeneous electrocatalysts. For IrO_2 and RuO_2 catalysts, the OER specific activities of the uncoated catalysts were in good agreement with previously reported values (*201*). We are unaware of reported specific activities for FTO for the OER or for any catalyst for the CER. The specific activities for the OER and CER were characterized by volcano-type relationships as a function of the TiO_2 ALD cycle number (Fig. 5.6). In fact, IrO_2 coated with 10 ALD cycles of TiO_2 showed an 8.7-fold increase in OER specific activity at η = 350 mV relative to uncoated IrO_2, resulting in the highest ECSA-based specific activity reported to date for Ir-based OER catalysts at η = 350 mV in 1.0 M H_2SO_4. Recently, $IrO_x/SrIrO_3$ has been reported as an especially active catalyst using current normalized to atomic force microscopy measured surface area (AFMSA) in 0.5 M H_2SO_4. To compare these catalysts, we measured the roughness of our catalysts using AFM (Table 5.1). For our catalysts, bare IrO_2 exhibited a Tafel slope of ~60 mV/dec in good agreement with previously reported OER catalysts (*210*). As the activity of our IrO_2 based catalyst increased from bare IrO_2 to 10 TiO_2 ALD cycles, the Tafel slope remained constant at ~60 mV/dec while the exchange current density (i_0) increased from ~1×10^{-7} to ~2×10^{-5} mA/cm^2_{AFMSA}. Initially the $IrO_x/SrIrO_3$ catalyst also had an OER Tafel slope of ~60 mV/dec and an i_0 of ~7×10^{-6} mA/cm^2_{AFMSA}. For the $IrO_x/SrIrO_3$, however, after a period of activation the Tafel slope improved dramatically to ~40 mV/dec, which indicates a previously unknown OER mechanism, while the i_0 deteriorated to ~3×10^{-7} mA_{AFMSA} (Fig. 5.8, Table 5.2). In our case, IrO_2 coated with 10 ALD cycles of TiO_2 exhibited lower overpotentials than the freshly prepared $IrO_x/SrIrO_3$ catalyst at current densities < 1 mA/cm^2_{AFMSA} and lower overpotentials than the activated $IrO_x/SrIrO_3$ catalyst at < 0.02 mA/cm^2_{AFMSA}, but substantially higher overpotentials at the more industrially relevant current densities of > 10 mA/cm^2_{AFMSA} (*179, 209*).

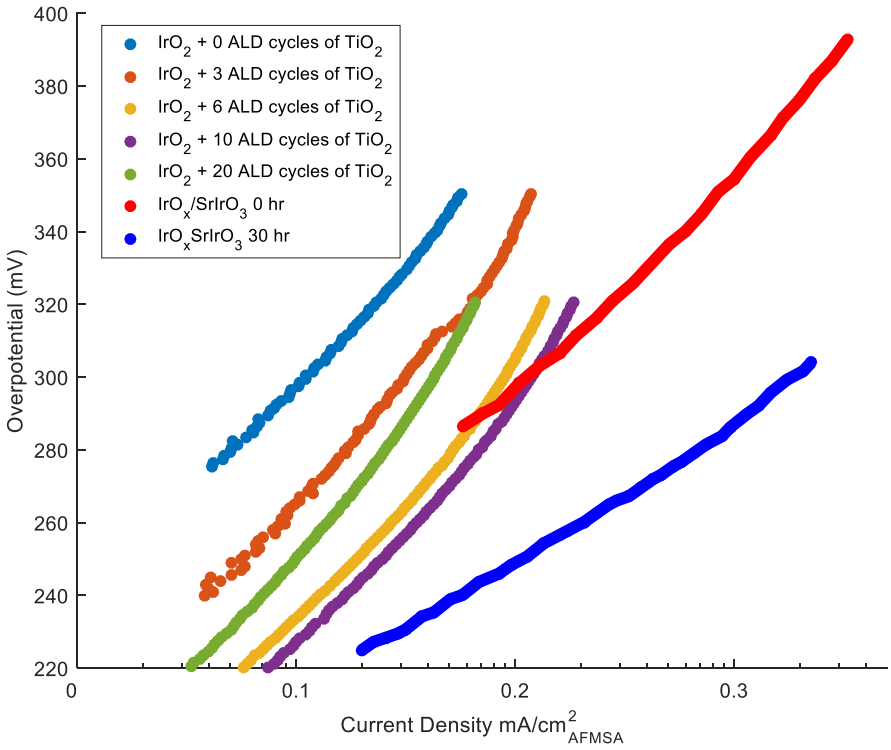

Figure 5.8 Tafel plots from IrO_2 coated with 0 (dark blue), 3 (orange), 6 (yellow), 10 (purple), and 20 (green) ALD cycles of TiO_2 all from this work are shown next to those of $IrO_x/SrIrO_3$ at 0 (red) and 30 (light blue) hrs of activation as taken from literature (*209*). To calculate the current density, the surface area was measured by AFM (Table 4.1).

Catalyst	**i_0 (mA/cm^2_{AFMSA})**	**slope ($mV/mA/cm^2_{AFMSA}$ decade)**
IrO_2 + 0 ALD cycles of TiO_2	1.0×10^{-7}	59
IrO_2 + 3 ALD cycles of TiO_2	8.0×10^{-6}	65
IrO_2 + 6 ALD cycles of TiO_2	2.0×10^{-5}	64
IrO_2 + 10 ALD cycles of TiO_2	2.0×10^{-5}	61
IrO_2 + 20 ALD cycles of TiO_2	8.0×10^{-6}	61
$IrO_x/SrIrO_3$ 0 h	7.0×10^{-6}	57
$IrO_x/SrIrO_3$ 30 h	3.0×10^{-7}	38

Table 5.2 A summary of the Tafel slopes and exchange current densities from this work (IrO_2 + TiO_2 catalyts) and previous work ($SrIrO_3$ catalysts) (*209*). All current density data reported here is based on surface area that is measured by AFM (Table S1).

5.3.3 Stability of Enhanced Catalyst Performance

To test the longevity of the enhanced catalytic performance with TiO_2 deposition, we performed 24 h stability testing at 10 mA/cm^2 for both the CER and the OER for the uncoated catalyst and the most active catalyst for each material system. The stability testing procedures and results are detailed below.

5.3.3.1 24-Hour Stability Test Procedure

For each catalyst, the uncoated and the most active, coated catalysts were tested for 24 h stability. For the OER, IrO_2 with 40 ALD cycles of TiO_2 was also tested. 10 mA/cm^2 in 1 M H_2SO_4 Electrodes were as prepared as described above except, instead of vinyl tape, electrode surface area was defined by Hysol 9460 epoxy (Henkel, Dusseldorf, Germany) (*209*). Geometric surface areas were measured as previously described by scanning the electrode surface using a Ricoh MP 301 scanner (Tokyo, Japan) and estimating the surface area using ImageJ software (*209*). The catalyst stability was assessed by maintaining the electrodes galvanostatically at either 10 mA/cm^2 or 1 mA/cm^2 for the OER and CER, respectively, for 24 hrs. At 0 min, 10 min, 2 h, and 24 h, the electrolyte was replaced with fresh electrolyte, and either O_2(g) or Cl_2(g) was bubbled through the solution as described above. After > 1 min of gas bubbling, electrochemical impedance spectroscopy was preformed to determine the system resistance followed by 5 CVs which were run from the OCV to a potential that yielded 10 mA/cm^2 or 1 mA/cm^2 for the OER and CER, respectively. The voltage required to reach 10 mA/cm^2 for the OER and 1 mA/cm^2 for the CER, respectively, is tabulated in Table 5.3 below. Initial overpotential measurements agree well with overpotential measurements using vinyl tape on electrodes reported in Fig. 5.9 (Table S3). A sample 24 h stability test of 0, 10, and 40 ALD cycles of TiO_2 on IrO_2 under OER conditions is presented in Fig. 5.9 below.

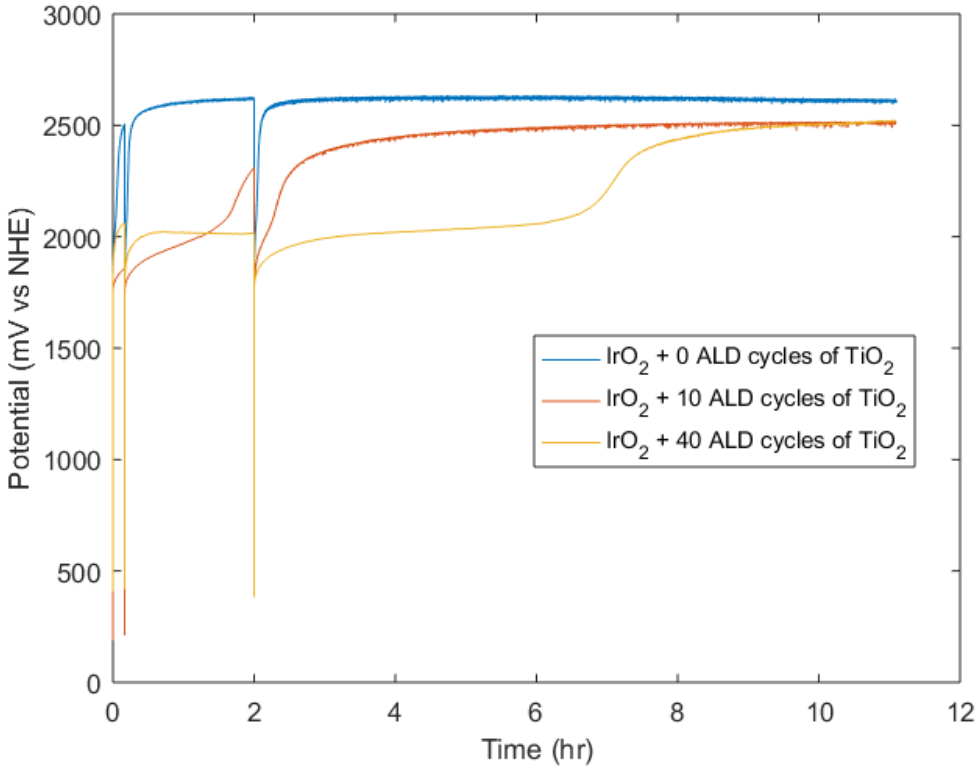

Figure 5.9 Example stability testing data of IrO_2 + 0 (blue), 10 (orange), and 40 (yellow) ALD cycles in 1 M H_2SO_4 at 10 mA/cm^2_{geo}.

OER overpotential to reach 10 mA/cm^2_{geo}					
MO_x + X ALD Cycles of TiO_2	initial	10 min	2 h	24 h	Reported initial value (Fig. 1.)
IrO_2 + 0 cyc	720	670	N/A	N/A	710 ± 30
IrO_2 + 10 cyc	540	510	N/A	N/A	520 ± 20
IrO_2 + 40 cyc	800	610	560	N/A	810 ± 50
RuO_2 + 0 cyc	770	880	N/A	N/A	740 ± 70
RuO2 + 10 cyc	430	470	440	N/A	430 ± 10
FTO + 0 cyc	1870	1820	N/A	N/A	1870 ± 50
FTO + 30 cyc	1740	1620	N/A	N/A	1720 ± 70
CER overpotential to reach 1 mA/cm^2_{geo}					
IrO2 + 0 cyc	160	220	230	N/A	148 ± 6

IrO2 + 3 cyc	120	200	200	190	122 ± 5
RuO2 + 0 cyc	140	220	140	210	116 ± 6
RuO2 + 60 cyc	160	160	100	100	160 ± 10
FTO + 0 cyc	870	980	990	970	890 ± 30
FTO + 10 cyc	760	1150	1000	740	760 ± 40

Table 5.3 Summary of overpotential data as measured from CVs to reach 10 mA/cm^2_{geo} in 1 M H_2SO_4 for the OER and 1 mA/cm^2_{geo} in 5 M NaCl pH 2.0 for CER at 0 min, 10 min, 2 h, and 24 h of testing in constant current mode. The right-most column displays the overpotential that was reported in the main text. N/A indicates that a rapid loss in activity was noticed before the time of measurement.

5.3.3.2 Stability Results

The catalysts investigated herein were not optimized for stability and, as was previously reported for thin IrO_2 and RuO_2 catalyst depositions (*201, 211*), the overpotential on uncoated catalysts for the OER in 1 M H_2SO_4 degraded rapidly after < 1 h of operation at 10 mA/cm^2_{geo}. For thinly coated catalysts (3-10 cycles) the OER stability improved from about 1 h to about 4 h, while for thicker TiO_2 coatings (> 30 cycles) the OER stability increased to > 9 h (Fig. 5.9). For the CER, all catalysts were relatively stable over the 24 h testing period except for the FTO-based catalysts which followed the same trend as the OER, with thicker TiO_2 coatings stabilizing the electrodes.

X-ray photoelectron spectra were taken before and after 24-hour stability testing to understand the longevity of the catalytic enhancement. Figure 5.10 shows XPS spectra of the Ti 2p core-level before and after testing for the catalysts with the lowest overpotential for the OER for each materials system, 10 cycles, 10 cycles, and 30 cycles of TiO_2 for IrO_2, RuO_2, and FTO, respectively. After testing, no Ti species was detectable for any of the electrocatalysts tested in this study, which correlates well with the loss in catalytic performance over the duration of the stability test. The peak in the Ti 2p region for RuO_2 after testing is due to the Ru 3p core-level peaks and not to species associated with TiO_2. XPS spectra were also collected after 24-hour stability tests of the electrodes for the CER.

Unlike for the OER, all electrocatalysts (except for the FTO based catalysts, which performed similarly as for the OER) showed stable performance over the duration of the stability test. XPS spectra after testing indicate that TiO_2 films are still present. A representative XPS spectra of the Ti 2p region for a RuO_2-based electrocatalyst before and after stability testing for the CER is shown in Fig. 5.11.

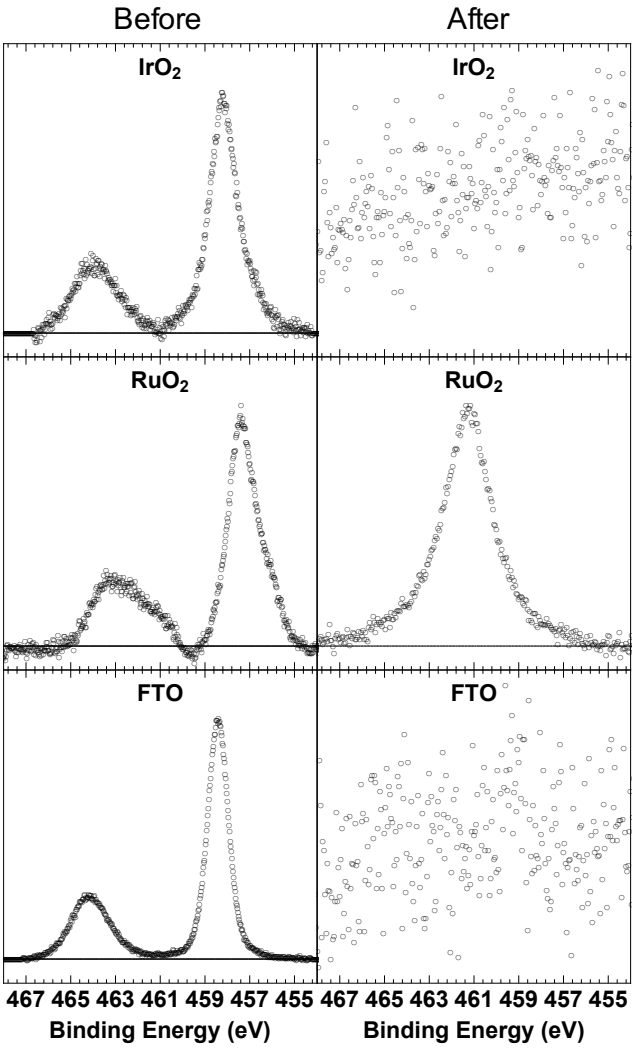

Figure 5.10 X-ray photoelectron spectroscopy of the Ti 2p region for IrO_2, RuO_2, and FTO electrocatalysts with 10 cycles, 10 cycles, and 30 cycles of TiO_2, respectively, before and after stability testing for the OER. Note the peak still visible in the "after" RuO_2 spectra is associated with the Ru 3p core levels.

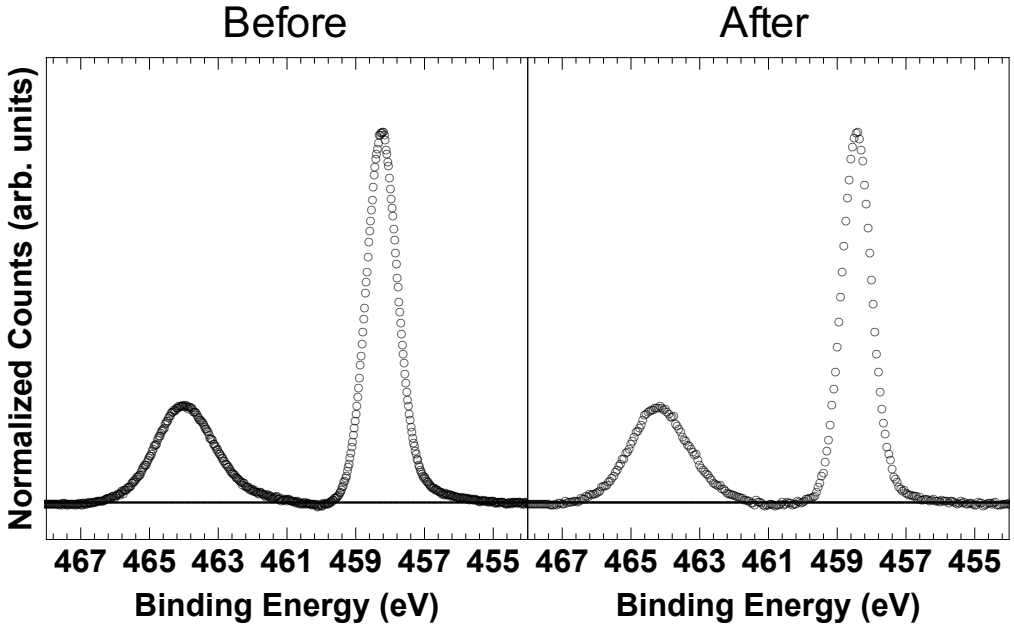

Figure 5.11 X-ray photoelectron spectroscopy of the Ti 2p region for an RuO_2 electrocatalyst with 60 cycles of before and after 24-hour stability testing for the CER. The TiO_2 is still present after testing.

5.4 Catalyst Surface Electronics

The enhancement in catalytic performance observed with deposition of TiO_2 is not readily explained by surface morphological changes of the electrocatalyst. Deposition of TiO_2 does not substantially affect the electrochemically active surface area, a metric believed to be related to active site density, and changes in the surface area alone do not account for the magnitude of the enhancement in the specific activity (Fig. 5.6). Furthermore, while high-angle annular dark-field scanning transmission electron microscopy (HAADF-STEM) images and STEM electron dispersive X-ray spectroscopy (EDS) maps of IrO_2 samples with 10 cycles of TiO_2 (Figs. 5.2C, D) indicate that the TiO_2 film is semi-continuous with small areas of the underlying IrO_2 exposed, deposition of 40 cycles of TiO_2 results in a uniform, continuous film (Fig. 5.2E) and catalysis commensurate with the bare IrO_2 samples. These facts suggest the phenomenon does not arise from surface morphological effects alone,

instead suggesting that TiO_2 is playing a partial role in enhancing the activity of the active sites. To that end we investigated the catalysts' surface electronic properties using the potential of zero charge and x-ray photoelectron spectroscopy.

5.4.1 Potential of Zero Charge Measurements

To investigate the electrocatalysts' surface electronic properties the potential of zero charge (E_{ZC}) of the electrocatalysts was measured as a function of TiO_2 thickness (Fig. 5.12). E_{ZC} is the potential that must be applied to produce a neutral surface and is an indicator of a material's willingness to lose electrons, with more positive E_{ZC} values indicating surfaces that are less willing to lose their electrons (see Appendix B. 7). E_{ZC} thus yields insight into the strength of the bonds on the catalyst surface (*212, 213*). Measured E_{ZC} values for bare RuO_2 and IrO_2 (50 and 30 mV vs. SCE, respectively) were consistent with previously reported values for Ru and Ir (*214*). We are unaware of reported E_{ZC} values for FTO. As the RuO_2 and IrO_2 samples were coated with increasing ALD cycles of TiO_2 the E_{ZC} shifted from lower to higher potentials in both cases and eventually reached the value for bulk TiO_2. This behavior is consistent with the expected trends for equilibrated group electronegativities. The E_{ZC} for bare FTO (450 mV vs SCE) was less than that for bulk TiO_2 and greater than bare IrO_2 or RuO_2. The FTO E_{ZC} decreased with increasing TiO_2 cycles up to 10 cycles and as the TiO_2 cycles increased beyond 10 the E_{ZC} increased until it reached the bulk value of TiO_2 at large cycle numbers. The overall trend of the FTO E_{ZC} increasing to higher values with increasing TiO_2 cycle number is consistent with group electronegativity arguments. However, the intermediate behavior where the E_{ZC} decreases and then increases is not well explained by group electronegativity and could, in part, arise from the complicated behavior of the F dopant atoms (further discussion on the limits of group electronegativity are found in the Supplementary Materials). For all catalysts, the E_{ZC} continued to shift even beyond the point where TEM data indicated that the film is continuous (40 ALD cycles). This suggests that the exposed metal oxide is not fully responsible for the shift in E_{ZC} and that the surface TiO_2 is likely responsible in part for the *Ezc* shift. Shifts in E_{ZC} with incremental TiO_2 deposition suggest that ALD can be used to tune the catalytic performance. These data reveal

that the catalysts with the highest activity for the CER have E_{ZC} values between 50 and 75 mV vs SCE (Fig. 5.12), consistent with the observation that addition of TiO_2 layers to RuO_2 decreased the activity of RuO_2 electrocatalysts (E_{ZC} = 50 mV vs SCE) for the CER. Additionally, active OER and CER catalysts for all systems investigated have E_{ZC} values between 25 and 200 mV vs SCE with the best OER catalysts having a somewhat higher E_{ZC} (~110 mV vs SCE) than the best CER catalysts (~60 mV vs SCE).

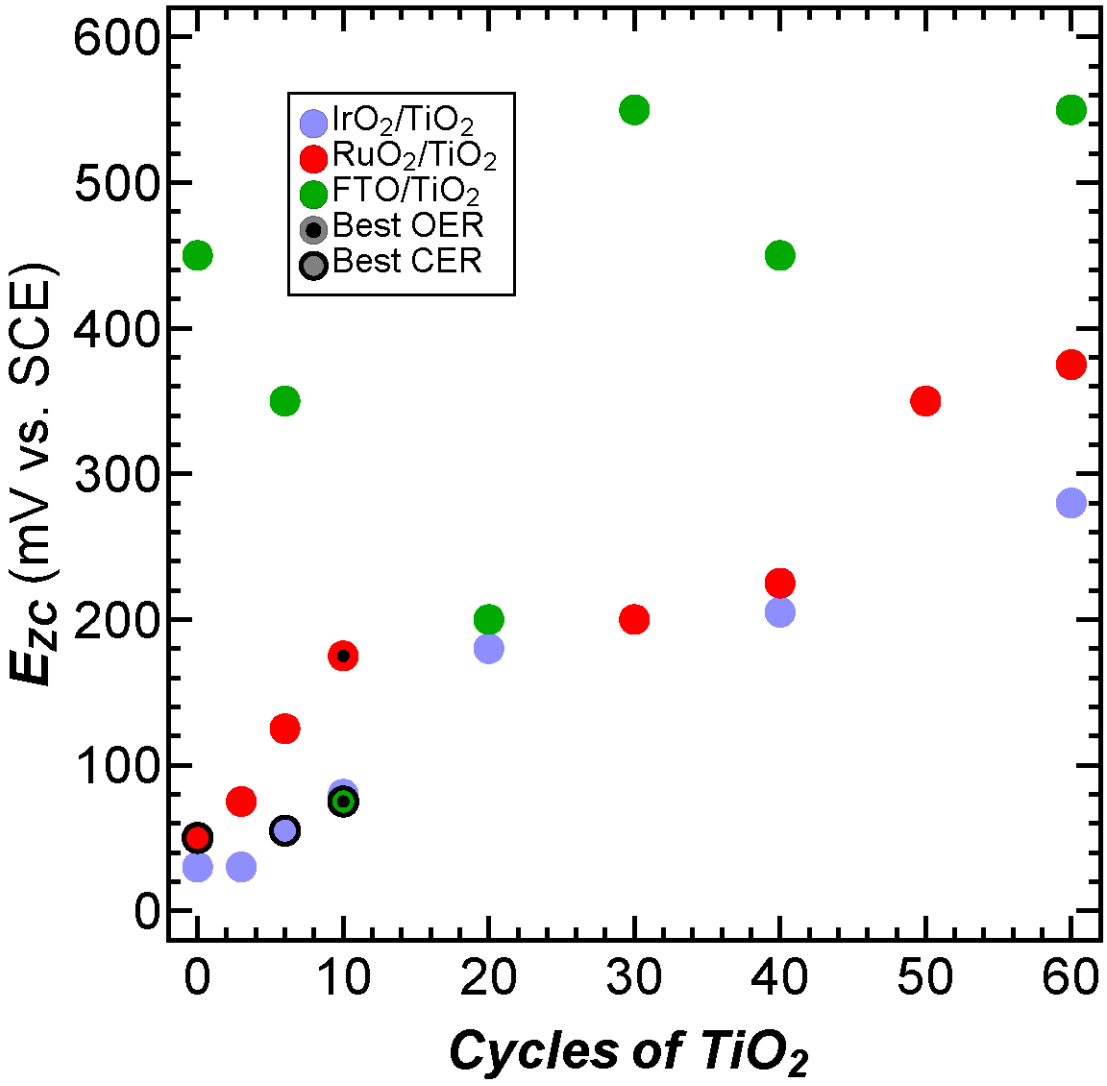

Figure 5.12 E_{ZC} of IrO_2 (blue), RuO_2 (red), and FTO (green) anodes coated with various ALD cycles of TiO_2. Black dots and circles with black borders indicate the catalysts with the highest specific activity for each catalyst for the OER and CER, respectively.

5.4.2 XPS Characterization of TiO_2 Coated Catalysts

To further understand the surface states of the catalysts, X-ray photoelectron spectroscopy was used to measure the Ti oxidation state. Details of the data collection and peak fitting can be found in Appendix D. Analysis of the catalyst XPS is found below.

5.4.2.1 Ti 2p Core-level Photoemission Spectra

Figures 5.13 and 5.14 show the Ti $2p_{3/2}$ and full Ti 2p core-level photoemission, stacked from bottom to top, for increasing ALD TiO_2 thickness, with 0 cycles indicating the bare catalyst substrate. Deposition of low cycle numbers of ALD TiO_2 on IrO_2 and RuO_2 produced Ti core-level peaks that were at ~456.6 eV and ~457.6 eV, which is consistent with previously reported binding energies for Ti^{3+} states (*215, 216*). As the ALD cycle number increased, the Ti oxidation state for these samples gradually increased to its bulk oxidation state (~+4), and signals indicative of bulk TiO_2 were eventually observed (Figs. 5.13 and 5.14). In the case of ALD TiO_2 on FTO, the lower cycle number thicknesses instead produced binding energies primarily at the bulk position, in addition to a peak at a higher binding energy. This additional peak can be ascribed to a mixed phase between the substrate (FTO) and the thin TiO_2 film, in which the chemical nature of the phase produces a more oxidized metal, with the mixed phase most likely dominated by Ti^{4+} sites.

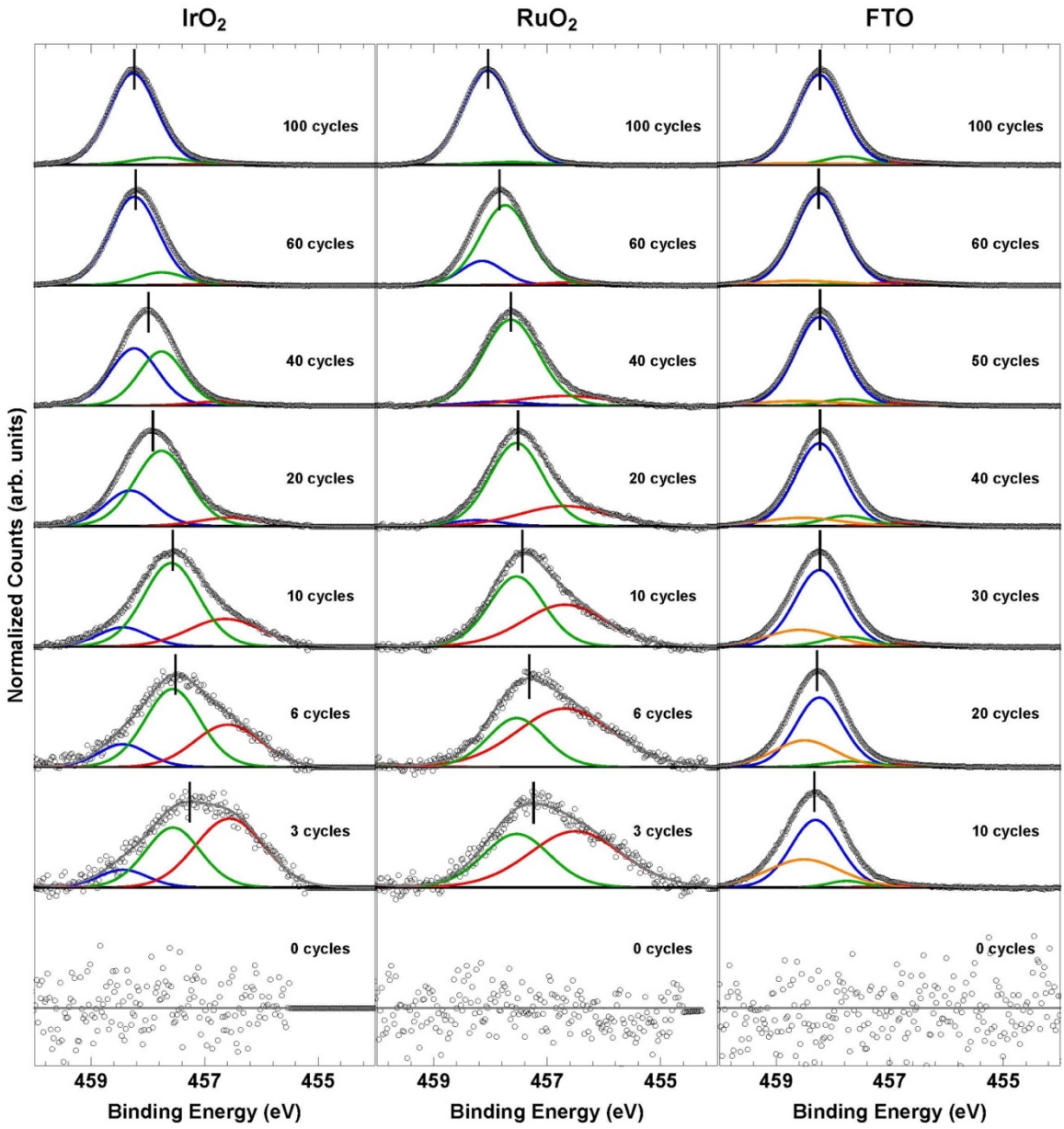

Figure 5.13 X-ray photoelectron spectroscopy of the Ti $2p_{3/2}$ region for IrO_2, RuO_2, and FTO catalysts with varying TiO_2 thicknesses. Bulk TiO_2 is shown as the blue peak in each spectrum. The slightly and highly reduced Ti peaks are shown in green and red, respectively, and the most highly oxidized Ti peak is shown in orange.

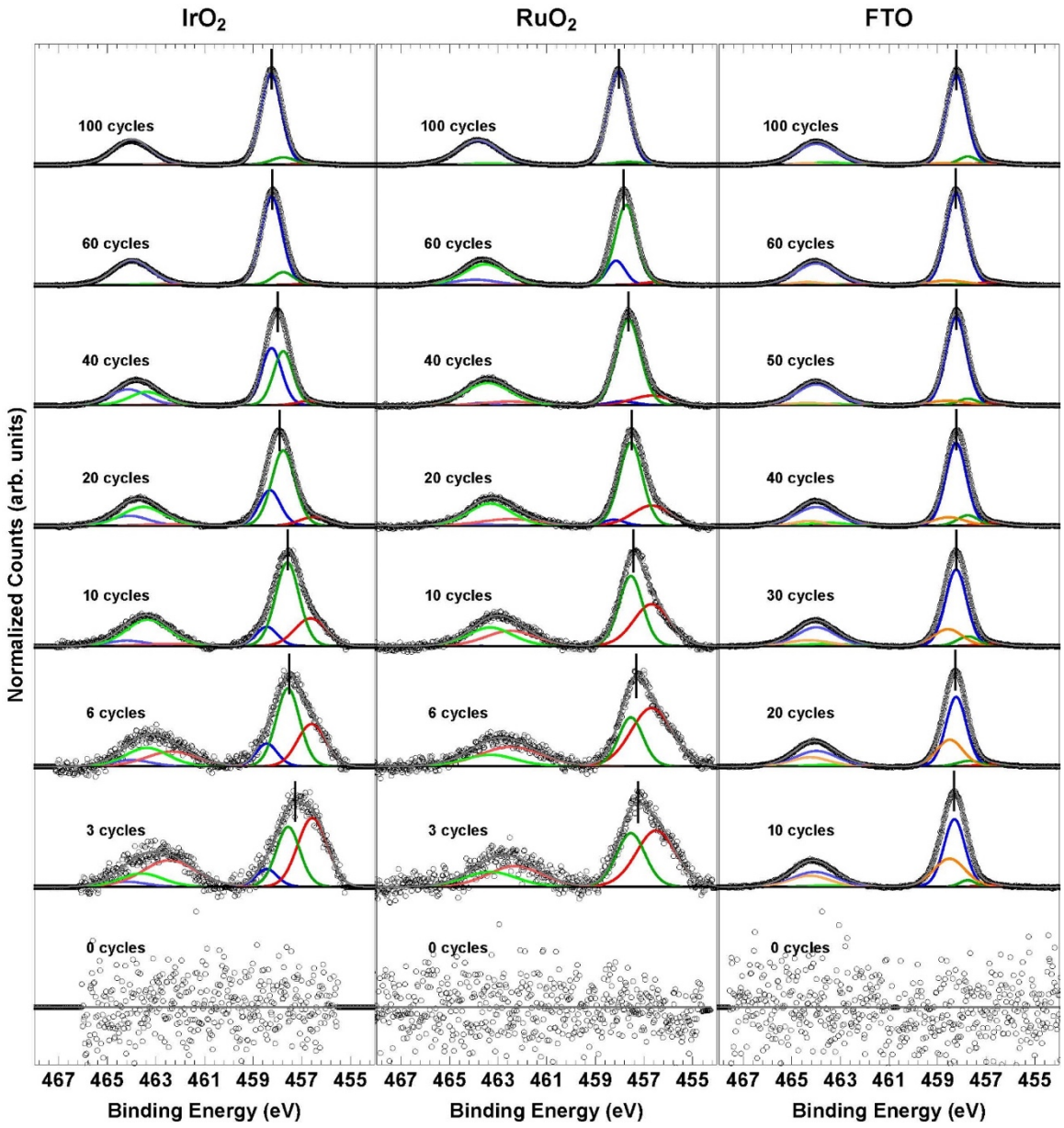

Figure 5.14 X-ray photoelectron spectroscopy of the Ti 2p region for IrO_2, RuO_2, and FTO catalysts. Bulk TiO_2 is shown as the blue peak in each spectrum. The slightly and highly reduced Ti peaks are shown in green and red, respectively, and the most highly oxidized Ti peak is shown in orange.

The variation in the Ti oxidation state with ALD TiO_2 cycles is accompanied by a peak shift of the $Ti2p_{3/2}$ peak relative to the bulk TiO_2 peak position (Fig. 5.15). The $Ti2p_{3/2}$ peak of the IrO_2- and RuO_2-based catalysts shifts from reduced, lower binding energies to the more

oxidized, higher binding energies typical of bulk TiO_2. The FTO-based $Ti2p_{3/2}$ peak shifts from more oxidized, high binding energies at low TiO_2 cycles to lower binding energies for intermediate TiO_2 cycles (10-40 cycles) before increasing again to higher binding energies at large TiO_2 thicknesses (>60 cycles). The $Ti2p_{3/2}$ peak shift is qualitatively consistent with the variation in E_{zc} with TiO_2 cycle number suggesting that the change in the surface charge density is correlated with a change in the Ti oxidation state.

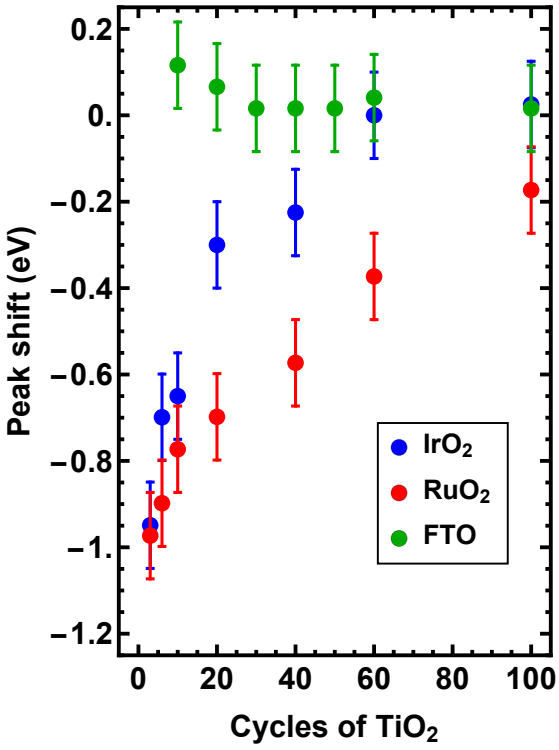

Figure 5.15 Ti $2p_{3/2}$ overall peak shift relative to bulk TiO_2 as a function of TiO_2 cycle thickness for IrO_2, RuO_2, and FTO.

5.4.2.2 Metal-oxide Core-level Emission Spectra

The shift in the Ti $2p_{3/2}$ peak position and variation in the Ti oxidation state with TiO_2 thickness can be explained by charge transfer from the underlying metal oxide substrate. In this scenario, a more reduced Ti species present at low deposited cycles of TiO_2 on IrO_2 and RuO_2 would be accompanied by a more oxidized metal oxide substrate. In order to confirm this hypothesis, we measured the Ir 4f, Ru 3d, and Sn 3d core-level photoemission (Fig.

5.16). Unlike in the case of the Ti 2p spectra, the Ir 4f, Ru 3d, and Sn 3d core-level photoemission exhibited very small changes between the bare metal oxide substrate and those with varying thicknesses of TiO_2. This was reflected in the peak shifts of the main peak for the Ir 4f, Ru 3d, and Sn 3d spectra with TiO_2 thickness relative to that of the bare substrate (Fig. 5.16), which were an order of magnitude lower than those for the Ti 2p core-level photoemission and mostly within the error of the measurement (± 0.1 eV). While peak fitting (see Appendix C) of these spectra indicates that initial deposition of TiO_2 leads to a slightly more oxidized Ir and Ru state, and a slightly more reduced Sn state for FTO, no trend with thickness was observed for any of the substrates, and changes in the oxidation state of the underlying catalyst are likely below the detection limit for the techniques used in this study (Fig 5.16, 5.17, and Table 5.4).

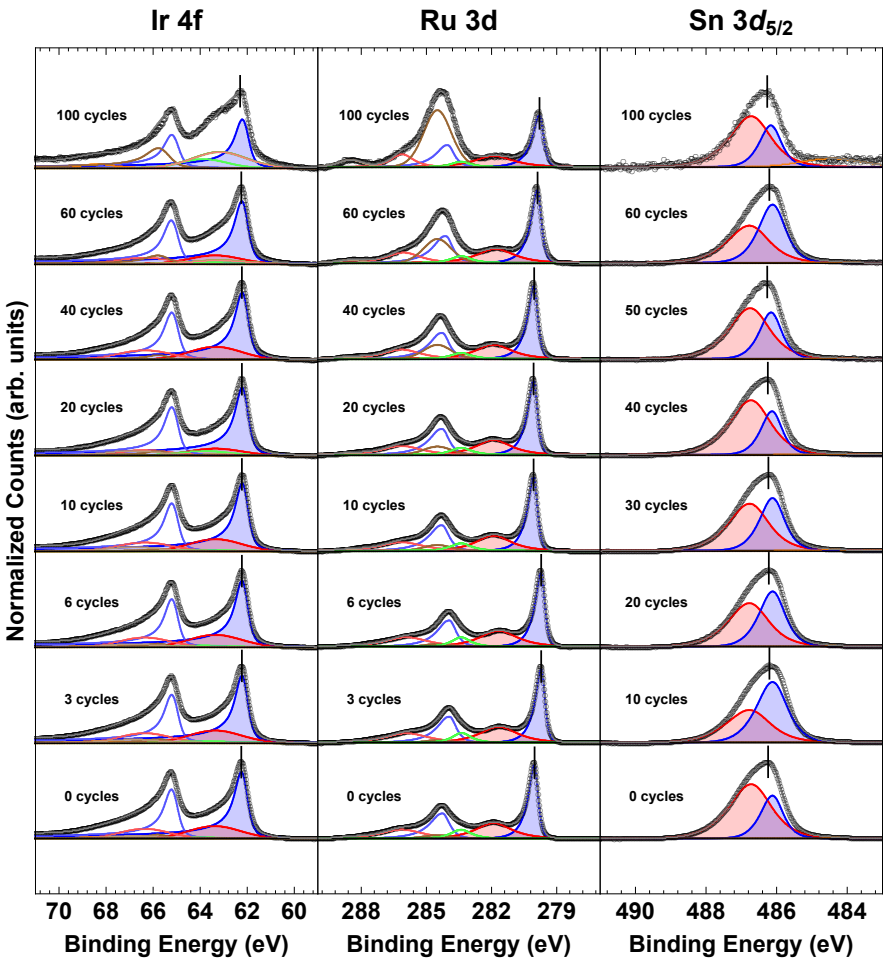

Figure 5.16 X-ray photoelectron spectroscopy of the Ir 4f, Ru 3d, and Sn $3d_{5/2}$ region for IrO_2- RuO_2- and FTO-based electrocatalysts as a function of TiO_2 thickness.

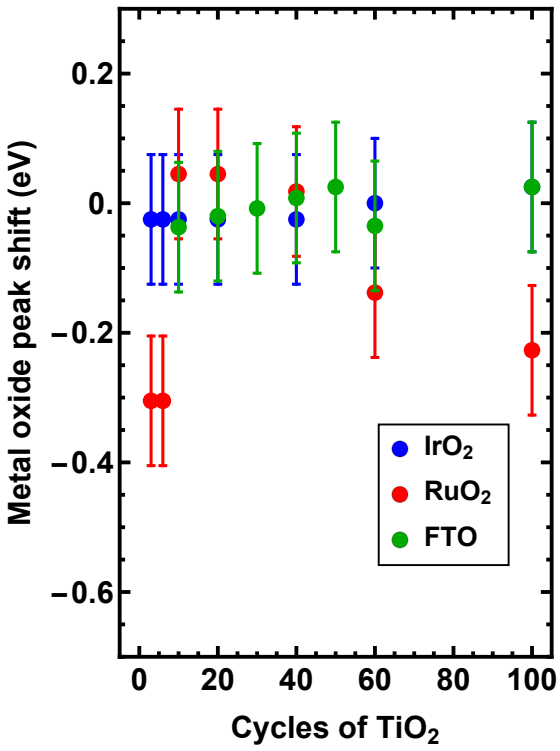

Figure 5.17 Overall peak shift of the main peak of the Ir 4f, Ru 3d, and Sn $3d_{5/2}$ spectra relative to the bare metallic (0 cycle) metal-oxide substrate as a function of TiO_2 cycle thickness for IrO_2, RuO_2, and FTO, respectively.

TiO_2 Cycles	Ir 4f	Ru 3d	Sn 3d
0	4.76	1.42	0.42
3	4.73	1.34	-
6	4.7	1.33	-
10	4.95	1.51	1.30
20	8.78	1.58	0.81
30	-	-	0.69
40	4.65	1.59	0.41
50	-	-	0.50
60	6.86	1.62	1.01
100	∞	1.52	0.435

Table 5.4 The areal peak ratios of the main peak to the satellite peak for the Ir 4f, Ru 3d, and Sn 3d core-level photoemission.

5.5 Conclusion

In summation, surface characterization suggests that atomic layer deposition of low cycle numbers of TiO_2 can tune surface electron densities of the catalyst in a direction consistent with predictions from group electronegativity concepts (Fig. 5.6). Given that concomitant changes in electrochemical activity were observed with deposition of TiO_2, this approach is a promising method to tune the performance of other electrocatalysts (beyond metal oxides) for diverse reactions, including those critical for renewable energy storage and wastewater treatment.

Chapter 6

Conclusion and Outlook

Throughout this thesis we have presented analyses and developed technologies for high-efficiency photovoltaics and electrocatalysis with the goal of enabling a pathway to a net-zero carbon emission energy system. Such an energy system relies on a renewable electricity grid and thus our research in photovoltaics centered around increased efficiency, which is a primary driver in reducing the levelized cost of electricity, the metric by which all electricity generating technologies are ultimately evaluated. We developed two new models for evaluating the photovoltaic efficiency limits in new (and existing) materials and demonstrated the first interconnect-free tandem silicon/perovskite solar cell with a 24.1% efficiency. Our work also focused on new methods to improve electrocatalysis which is key to enabling the clean production of fuels and commodity chemicals. Our technique allows for the tuning of the catalytic activity of multiple electrocatalysts for a variety of reactions.

In Chapter 2, we presented a modified detailed balance model in which we took into account the non-ideal absorption profile of photovoltaic materials. We showed that there is an intimate relationship between the sub-gap absorption tail and a photovoltaic's efficiency and luminescence. In particular, we found that significant sub-gap absorption (Urbach parameter, $\gamma > k_B T$) nullifies the notion of a single forbiddgen gap and leads to a distribution of band gaps that limits the quasi-Fermi level splitting and thus the open-circuit voltage. The generalized absorption parameterization used in this model can be directly fit to the experimentally measured absorption of real materials. Thus in tandem with our model, careful measurement of the sub-gap absorption (and/or emission) profile can yield insights into the efficiency limits of a candidate photovoltaic material.

We further analyzed material efficiency limits in Chapter 3, where we examined the effects of excitons on photovoltaic performance using cuprous oxide (Cu_2O) as a case study. Excitons are the fundamental optical excitation in a slew of emerging materials with large

exciton binding energies (>>100 meV, e.g. the transition metal dichalcogenides)). In Cu_2O, for example, we found that the quasi-equilibrium excitation density is comprised of greater than 20% excitions under photovoltaic operating conditions. Excitonic signatures were found in the photoluminescence of Cu_2O and in the spectral response of Cu_2O/Zn(O,S) photovoltaics. Using a device physics model that accounted for excitonic effects, we found that the ultimate photovoltaic efficiency of Cu_2O solar cells is underestimated by 2 absolute percent when excitons are neglected.

In Chapter 4, we demonstrated a novel tandem device architecture in which the top and bottom cells are interconnected without the use of a tunnel junction or recombination layer. We realized this device using a perovskite top cell fabricated directly on top the silicon bottom cell. The electron selective contact, a TiO_2 layer deposited by atomic layer deposition, spontaneously formed a recombination layer in the form of an atomic-scale defect layer at the Si/TiO_2 interface. Tandem photovoltaics incorporating this interconnect-free design reached photovoltaic efficiencies in excess of 24% with thousands of hours of stability. The interconnect-free design is compatible with other solar cell types (e.g. HIT cells) as well as textured cells and has superior optical and processing properties compared to the traditional ITO contact used in other silicon/perovskite tandems. Importantly, our simulations show that the interconnect free tandem design enables a pathway to low cost, high efficiency (>30%) silicon/perovskite tandems.

Finally, in Chapter 5 we develop a method to tune the catalytic activity of heterogeneous electrocatalysts for the chlorine-evolution and oxygen-evolution reactions. Specifically, we showed that atomic layer deposition of TiO_2 (~3-30 cycles) on RuO_2, IrO_2, and FTO electrocatalysts resulted in significant enhancement of the catalytic activity (an 8.7-fold increase in the case of IrO_2 for the OER) and a reduction in hundreds of mVs in overpotential compared to the uncoated catalysts. The enhancement in catalytic performance was associated with an alteration of the surface electronics of the catalyst in a manner consistent with simple arguments in group electronegativity. Our results suggest that atomic layer

deposition may be a promising tool to tune the catalytic performance of other catalysts (beyond metal oxides) for a variety of important chemical reactions.

This work took important steps towards a net-zero carbon energy system but the road to realizing such a system is an arduous one. Although adoption of solar photovoltaics is on the rise, the majority of global electricity generation is still derived from dirty fossil fuel sources and while our results on electrocatalyst enhancement are promising, many new electrocatalysts must be developed if traditional CO_2-intensive reactions are to be replaced. Beyond electricity generation and fuel/chemical production, many CO_2 emissions are difficult to eliminate (e.g. those associated with steel and cement production) (*6*). It is my sincere hope that this work inspires smart people, like the ones I have worked aside at Caltech, to continue to be driven to reduce societies reliance on a centuries-old, dirty energy system.

Appendix A

Band Tailing Code

The Mathematica code used for calculating the modified detailed balance model of Chapter 2 is provided in the following pages.

om

Band Tailing and Solar Cell Performance

Created by Stefan Omelchenko on May 10, 2018
Last updated: May 10, 2018

```
Clear["Global`*"]
```

In[323]:=
```
Needs["NumericalCalculus`"]
```

Motivation

In[167]:=
```
MaterialEgs = Import[
   "/Users/Stefan/Documents/Caltech/Data/Calculations/Detailed Balance/Urbach
     Parameters vs Record Vocs.xlsx", {"Data", 1, Range[3, 12], 6}];
MaterialUrbPar =
  Import[
    "/Users/Stefan/Documents/Caltech/Data/Calculations/Detailed
      Balance/Urbach Parameters vs Record Vocs.xlsx",
    {"Data", 1, Range[3, 12], 4}] * 10^-3;
```

In[169]:=
```
MaterialSQVocs = Table[
  kB * Tcell * Log[AbsSolFluxSQ[MaterialEgs[[i]]] / R0SQ[MaterialEgs[[i]]] + 1],
  {i, Length[MaterialEgs]}]
```

Out[169]=
```
{1.15659, 1.25002, 1.0819, 0.876749,
 1.29668, 1.60544, 1.26871, 1.51197, 1.41831, 1.5587}
```

In[170]:=
```
MaterialCalcVocs =
 Table[OpenCircuit[AM15Photonflux[En], MaterialEgs[[i]], 1., MaterialUrbPar[[i]],
   Tcell, α0L, 1., MaterialEgs[[i]] * 0.6], {i, Length[MaterialEgs]}]
```

NIntegrate: The integrand AM15Photonflux[En] EQE[1.42, En, 1., 0.0067, 0.852, 300., α0L, 1.] has evaluated to non-numerical values for all sampling points in the region with boundaries {{0.310206, 4.43151}}.

NIntegrate: The integrand b[En, 300., 0.852] EQE[1.42, En, 1., 0.0067, 0.852, 300., α0L, 1.] has evaluated to non-numerical values for all sampling points in the region with boundaries {{0, 5}}.

NIntegrate: The integrand b[En, 300., 0.] EQE[1.42, En, 1., 0.0067, 0., 300., α0L, 1.] has evaluated to non-numerical values for all sampling points in the region with boundaries {{0, 5}}.

General: Further output of NIntegrate::inumr will be suppressed during this calculation.

FindRoot: The function value
$\{1.602\times10^{-20}(-1.\ \text{NIntegrate}[b[\text{En, Tcell, 0.}]\ \text{EQE}[1.42, \text{En, 1., 0.0067, 0., 300., }\alpha0\text{L, 1.}], \{\text{En, 0., 5.}\}] - 1.\ \text{NIntegrate}[\text{AM15Photonflux[En] EQE}[1.42, \text{En, 1., 0.0067, 0.852, 300., }\alpha0\text{L, 1.}], \{\text{En, Emin, Emax}\}] + \text{NIntegrate}[b[\text{En, Tcell, 0.852}]\ \text{EQE}[1.42, \text{En, 1., 0.0067, 0.852, 300., }\alpha0\text{L, 1.}], \{\text{En, 0., 5.}\}])\}$ is not a list of numbers with dimensions {1} at {V} = {0.852}.

ReplaceAll: {J[AM15Photonflux[En], 1.42, 1., 0.0067, V, 300., α0L, 1.]} is neither a list of replacement rules nor a valid dispatch table, and so cannot be used for replacing.

FindRoot: The function value
$\{1.602\times10^{-20}(-1.\ \text{NIntegrate}[b[\text{En, Tcell, 0.}]\ \text{EQE}[1.52, \text{En, 1., 0.024, 0., 300., }\alpha0\text{L, 1.}], \{\text{En, 0., 5.}\}] - 1.\ \text{NIntegrate}[\text{AM15Photonflux[En] EQE}[1.52, \text{En, 1., 0.024, 0.912, 300., }\alpha0\text{L, 1.}], \{\text{En, Emin, Emax}\}] + \text{NIntegrate}[b[\text{En, Tcell, 0.912}]\ \text{EQE}[1.52, \text{En, 1., 0.024, 0.912, 300., }\alpha0\text{L, 1.}], \{\text{En, 0., 5.}\}])\}$ is not a list of numbers with dimensions {1} at {V} = {0.912}.

ReplaceAll: {J[AM15Photonflux[En], 1.52, 1., 0.024, V, 300., α0L, 1.]} is neither a list of replacement rules nor a valid dispatch table, and so cannot be used for replacing.

FindRoot: The function value
$\{1.602\times10^{-20}(-1.\ \text{NIntegrate}[b[\text{En, Tcell, 0.}]\ \text{EQE}[1.34, \text{En, 1., 0.0071, 0., 300., }\alpha0\text{L, 1.}], \{\text{En, 0., 5.}\}] - 1.\ \text{NIntegrate}[\text{AM15Photonflux[En] EQE}[1.34, \text{En, 1., 0.0071, 0.804, 300., }\alpha0\text{L, 1.}], \{\text{En, Emin, Emax}\}] + \text{NIntegrate}[b[\text{En, Tcell, 0.804}]\ \text{EQE}[1.34, \text{En, 1., 0.0071, 0.804, 300., }\alpha0\text{L, 1.}], \{\text{En, 0., 5.}\}])\}$ is not a list of numbers with dimensions {1} at {V} = {0.804}.

General: Further output of FindRoot::nlnum will be suppressed during this calculation.

ReplaceAll: {J[AM15Photonflux[En], 1.34, 1., 0.0071, V, 300., α0L, 1.]} is neither a list of replacement rules nor a valid dispatch table, and so cannot be used for replacing.

General: Further output of ReplaceAll::reps will be suppressed during this calculation.

Out[170]=
```
{V /. J[AM15Photonflux[En], 1.42, 1., 0.0067, V, 300., α0L, 1.],
 V /. J[AM15Photonflux[En], 1.52, 1., 0.024, V, 300., α0L, 1.],
 V /. J[AM15Photonflux[En], 1.34, 1., 0.0071, V, 300., α0L, 1.],
 V /. J[AM15Photonflux[En], 1.12, 1., 0.011, V, 300., α0L, 1.],
 V /. J[AM15Photonflux[En], 1.57, 1., 0.015, V, 300., α0L, 1.],
 V /. J[AM15Photonflux[En], 1.9, 1., 0.014, V, 300., α0L, 1.],
 V /. J[AM15Photonflux[En], 1.54, 1., 0.065, V, 300., α0L, 1.],
 V /. J[AM15Photonflux[En], 1.8, 1., 0.048, V, 300., α0L, 1.],
 V /. J[AM15Photonflux[En], 1.7, 1., 0.051, V, 300., α0L, 1.],
 V /. J[AM15Photonflux[En], 1.85, 1., 0.051, V, 300., α0L, 1.]}
```

In[171]:=
```
ExpPV = Import[
  "/Users/Stefan/Documents/Caltech/Data/Calculations/Detailed Balance/Urbach
    Parameters vs Record Vocs.xlsx",
  {"Data", 1, Range[3, 12], {1, 2, 4, 6, 7, 15}}]
```

Out[171]=
```
{{GaAs, 1.122, 6.7, 1.42, 0.298, 0.03459}, {CIGS, 0.82, 24., 1.52, 0.7, 0.43002},
 {InP, 0.878, 7.1, 1.34, 0.462, 0.2039}, {c-Si, 0.75, 11., 1.12, 0.37, 0.126749},
 {Ch3NH3PbI3, 1.05, 15., 1.57, 0.52, 0.24668}, {Cu2O, 1.39, 14., 1.9, 0.51, 0.21544},
 {CZTS, 0.683, 65., 1.54, 0.857, 0.58571}, {a-Si, 0.89, 48., 1.8, 0.91, 0.62197},
 {a-Si, 0.79, 51., 1.7, 0.91, 0.62831}, {a-Si, 0.87, 51., 1.85, 0.98, 0.6887}}
```

```
VocTicks[min_, max_] :=
 Table[If[Mod[i * 10, 2] < 0.0001, {i, NumberForm[i, {2, 1}], {.025, 0}, Black},
   {i, "", {.0125, 0}, Black}], {i, Floor[min], Ceiling[max], 0.05}]
E0LinLTicks[min_, max_] := Table[If[Mod[i, 10] < 0.0001, {i, i, {.025, 0}, Black},
   {i, "", {.0125, 0}, Black}], {i, Floor[min], Ceiling[max], 2}]
ListPlot[Evaluate[Table[{ExpPV[[i, 3]], ExpPV[[i, 5]]}, {i, 1, Length[ExpPV]}]],
 PlotRange → {{-2, 70}, {-0.05, 1.20}},
 PlotMarkers → {Graphics[{Disk[]}], 1/30},
 PlotStyle → Red,
 Frame → True,
 FrameLabel → {{"E_g-qV_oc (eV)", None}, {"γ (meV)", None}},
 FrameTicks → {{VocTicks, None}, {E0LinLTicks, None}},
 FrameStyle → Black,
 BaseStyle → Directive[FontSize → 18],
 Epilog → {{Text[
     Style["GaAs (1.42 eV)", FontSize → 12, FontFamily → "Arial"], {17, 0.298}]},
   {Text[Style["CIGS (1.52 eV)", FontSize → 12, FontFamily → "Arial"], {34, 0.7}]},
   {Text[
     Style["InP \n(1.34 eV)", FontSize → 12, FontFamily → "Arial"], {7.1, 0.58}]},
   {Text[Style["c-Si (1.12 eV)", FontSize → 12, FontFamily → "Arial"],
     {20.75, 0.37}]},
   {Text[Style["CH_3NH_3PbI_3 (1.57 eV)", FontSize → 12, FontFamily → "Arial"],
     {29, 0.54}]},
   {Text[Style["Cu_2O (1.9 eV)", FontSize → 12, FontFamily → "Arial"], {23, 0.465}]},
   {Text[
     Style["a-Si (1.7-1.85 eV)", FontSize → 12, FontFamily → "Arial"], {38, 0.97}]},
   {Text[Style["CZTS (1.54 eV)", FontSize → 12, FontFamily → "Arial"],
     {60, 0.79}]}},
 AspectRatio → .75,
 ImageSize → 400]
```

Out[174]=

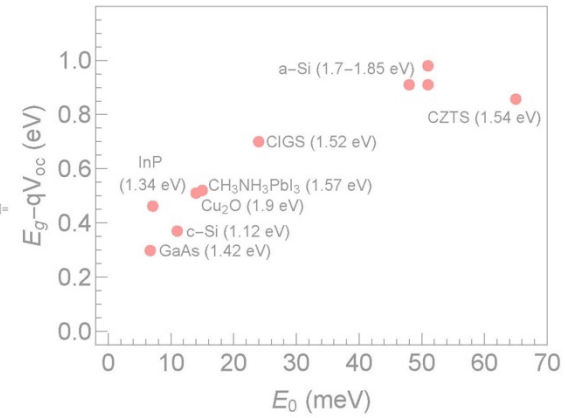

```
ListPlot[Evaluate[Table[{ExpPV[[i, 3]], ExpPV[[i, 6]]}, {i, 1, Length[ExpPV]}]],
 PlotRange → {{-2, 70}, {-0.05, 1.0}},
 PlotMarkers → {Graphics[{Disk[]}], 1/30},
 PlotStyle → Red,
 Frame → True,
 FrameLabel → {{"qV_oc,S-Q - qV_oc,Exp (eV)", None}, {"γ (meV)", None}},
 FrameTicks → {{VocTicks, None}, {E0LinLTicks, None}},
 FrameStyle → Black,
 BaseStyle → Directive[FontSize → 18],
 Epilog → {{Text[
     Style["GaAs (1.42 eV)", FontSize → 12, FontFamily → "Arial"], {17, 0.038}]},
   {Text[Style["CIGS (1.52 eV)", FontSize → 12, FontFamily → "Arial"], {34, 0.44}]},
   {Text[
     Style["InP \n(1.34 eV)", FontSize → 12, FontFamily → "Arial"], {7.1, 0.3}]},
   {Text[Style["c-Si (1.12 eV)", FontSize → 12, FontFamily → "Arial"],
     {20.75, 0.13}]},
   {Text[Style["CH3NH3PbI3 (1.57 eV)", FontSize → 12, FontFamily → "Arial"],
     {29, 0.20}]},
   {Text[Style["Cu2O (1.9 eV)", FontSize → 12, FontFamily → "Arial"], {25, 0.25}]},
   {Text[
     Style["a-Si (1.7-1.85 eV)", FontSize → 12, FontFamily → "Arial"], {38, 0.69}]},
   {Text[Style["CZTS \n (1.54 eV)", FontSize → 12, FontFamily → "Arial"],
     {64, 0.68}]}},
 AspectRatio → .75,
 ImageSize → 400]
```

Out[175]=

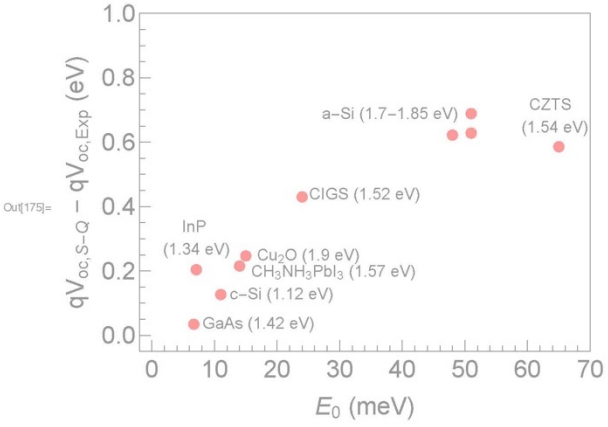

Fundamental Constants and Solar Cell

Parameters

```
q = 1.602 × 10^(-19); (*C*)
h = 6.626 × 10^(-34) / q;(*eV s *)
c = 3. × 10^8; (*m/s*)
kB = 1.38 × 10^-23 / q;(* eV/K*)

Tcell = 300.; (*K*)
Tsun = 5760.; (*K*)

α0 = 10 000.; (*cm^-1*)
L = 0.001; (*cm*)
```

Governing Equations

```
Clear[AM15Photonflux]
```

In[176]:=
```
SunSolidAngle = 2.16 × 10^-5;
b[En_?NumericQ, T_?NumericQ, V_?NumericQ] :=
 2. π / (h^3 * c^2) * En^2 / (Exp[(En - V) / (kB * T)] - 1) (*Blackbody flux*)

AM15λ =
  Import["/Users/Stefan/Documents/Caltech/Data/Calculations/AM15_Spectrum.xlsx",
   {"Data", 1}];
AM15λinterp = Interpolation[AM15λ, InterpolationOrder → 1];
AM15Photonflux[E_?NumericQ] :=
  (10.^9) * (h * c) * AM15λinterp[h * c * 10.^9 / E] / (q * E^3); (*#photons/cm^2/nm*)
λmin = AM15λ[[1, 1]];
λmax = AM15λ[[-3, 1]];
Emin = h * c / (4000. × 10^-9);
Emax = h * c / (280. × 10^-9);

SolarConstantBB = 0.1 * q * SunSolidAngle * NIntegrate[b[En, Tsun, 0], {En, 0, ∞}]
(*mW/cm^2*)
SolarConstantAM =
 0.1 * NIntegrate[AM15λinterp[λ], {λ, λmin, λmax}] // Quiet(*mW/cm^2*)
```

Out[185]= 100.267

Out[186]= 100.477

```
Plot[{SunSolidAngle * b[En, Tsun, 0], AM15Photonflux[En]},
 {En, Emin, Emax}, PlotRange → All,
 PlotStyle → {Red, Blue},
 Filling → {1 → Axis, 2 → None},
 FillingStyle → LightRed,
 Frame → True,
 FrameLabel → {"Photon Energy (eV)", "Photon flux (# photons/m²/eV)"},
 PlotLabel → "Blackbody @ 300K", BaseStyle → {FontWeight → "Bold", FontSize → 12},
 AspectRatio → 1]
```

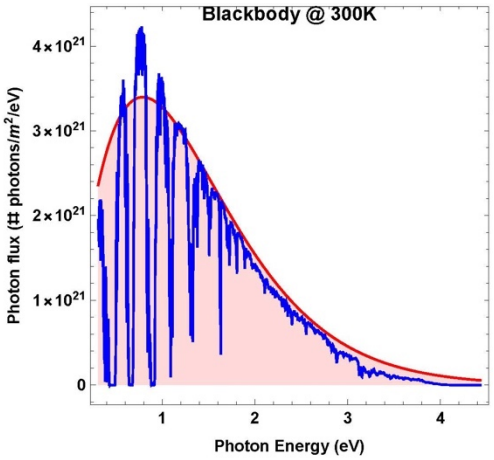

Generalizable Absorption Model

In[187]:=
```
G[Δe_?NumericQ, θ_?NumericQ] :=
  Re[1. / (2. * Gamma[1. + 1. / θ]) * NIntegrate[Exp[-Abs[Δep]^θ] * Sqrt[Δe - Δep],
      {Δep, -∞, ∞}, PrecisionGoal → MachinePrecision] // Quiet];
thetas = {1., 1.25, 1.5, 2.};
epsilons = Subdivide[-5000., 5000., 100001];
```

In[190]:=
```
Gs = If[FileExistsQ[
    "/Users/Stefan/Documents/Caltech/Data/Calculations/Detailed Balance/Direct
      Gap_Band Edge Sharpness/Bandfilling/Gfile.dat"],
   Import["/Users/Stefan/Documents/Caltech/Data/Calculations/Detailed
      Balance/Direct Gap_Band Edge Sharpness/Bandfilling/Gfile.dat"],
   Table[G[epsilons[[j]], thetas[[i]]], {i, 1, 4}, {j, Length[epsilons]}]
  ]
```

Out[190]=
```
{{0., 0., 0., 0., 0., 0., 0., 0., 0., 0., 0., 0., 0., ··· 99974 ···,
  70.7015, 70.7022, 70.7029, 70.7036, 70.7043, 70.705, 70.7057, 70.7064,
  70.7071, 70.7078, 70.7086, 70.7093, 70.71, 70.7107}, ··· 2 ···, {··· 1 ···}}
```

large output | show less | show more | show all | set size limit...

```
Export["/Users/Stefan/Documents/Caltech/Data/Calculations/Detailed
   Balance/Direct Gap_Band Edge Sharpness/Bandfilling/Gfile.dat", Gs]
```

```
/Users/Stefan/Documents/Caltech/Data/Calculations/Detailed
  Balance/Direct Gap_Band Edge Sharpness/Bandfilling/Gfile.dat
```

In[191]:=
```
Gfuncs = Table[Interpolation[Transpose[{epsilons, Gs[[i]]}]], {i, Length[Gs]}]
```

Out[191]=
```
{InterpolatingFunction[ Domain: {{-5.00×10^3, 5.00×10^3}}
                        Output: scalar ],
 InterpolatingFunction[ Domain: {{-5.00×10^3, 5.00×10^3}}
                        Output: scalar ],
 InterpolatingFunction[ Domain: {{-5.00×10^3, 5.00×10^3}}
                        Output: scalar ],
 InterpolatingFunction[ Domain: {{-5.00×10^3, 5.00×10^3}}
                        Output: scalar ]}
```

```
α[Eg_?NumericQ, En_?NumericQ, θi_, γ_?NumericQ, V_?NumericQ, T_?NumericQ] :=
 Block[{Δε},
  Δε = (En - Eg) / γ;
  Sqrt[γ] Gfuncs[[θi]][Δε] * Tanh[(En - V) / (4. * kB * T)]
 ]

a[Eg_?NumericQ, En_?NumericQ, θi_,
  γ_?NumericQ, V_?NumericQ, T_?NumericQ, α0L_?NumericQ] :=
 1 - Exp[-2 α[Eg, En, θi, γ, V, T] * α0L]
```

```
EQE[Eg_?NumericQ, En_?NumericQ, θi_, γ_?NumericQ,
  V_?NumericQ, T_, α0L_?NumericQ, IQE_?NumericQ] :=
 a[Eg, En, θi, γ, V, T, α0L] * IQE


AbsSolFlux[Spectrum_, Eg_, θi_, γ_, V_?NumericQ, T_, α0L_, IQE_] :=
 NIntegrate[Spectrum * EQE[Eg, En, θi, γ, V, T, α0L, IQE], {En, Emin, Emax}] // Quiet
R0[Eg_, θi_, γ_, V_?NumericQ, T_, α0L_, IQE_] :=
 NIntegrate[b[En, Tcell, V] * EQE[Eg, En, θi, γ, V, T, α0L, IQE], {En, 0, 5}] // Quiet

J[Spectrum_, Eg_, θi_, γ_, V_?NumericQ, T_, α0L_, IQE_] :=
 0.1 * q * (-AbsSolFlux[Spectrum, Eg, θi, γ, V, T, α0L, IQE] +
    R0[Eg, θi, γ, V, T, α0L, IQE] - R0[Eg, θi, γ, 0., T, α0L, IQE])
OpenCircuit[Spectrum_, Eg_, θi_, γ_, T_, α0L_, IQE_, guess_] :=
 V /. FindRoot[J[Spectrum, Eg, θi, γ, V, T, α0L, IQE], {V, guess}][[1]]
Mpp[Spectrum_, Eg_, θi_, γ_, T_, α0L_, IQE_, guess_] :=
 FindMinimum[{V * J[Spectrum, Eg, θi, γ, V, T, α0L, IQE], 0. < V < Eg},
  {V, guess}, AccuracyGoal → 5]

J[AM15Photonflux[En], 1.5, 1, 10.^-3, 0, Tcell, 10., 1.] // AbsoluteTiming
q * 0.1 * AbsSolFlux[AM15Photonflux[En], 1.5, 1, 10.^-3, 0, Tcell, 10., 1.] //
 AbsoluteTiming
```

```
{0.070132, -28.8887}
```

```
{0.04827, 28.8887}
```

■ S-Q

```
aSQ[Eg_?NumericQ, En_?NumericQ] := Piecewise[{{0, En < Eg}, {1, En ≥ Eg}}]

AbsSolFluxSQ[Eg_] := NIntegrate[AM15Photonflux[En], {En, Eg, Emax}] // Quiet
R0SQ[Eg_] := NIntegrate[b[En, Tcell, 0], {En, Eg, Emax}] // Quiet
JSQ[Eg_, V_?NumericQ] :=
 0.1 * q * (-AbsSolFluxSQ[Eg] + NIntegrate[b[En, Tcell, V], {En, Eg, Emax}] - R0SQ[Eg]) //
  Quiet
```

Analysis

We'll consider Urbach parameters γas a fraction of $k_B T$ and $\alpha_0 L$ for that of GaAs

In[192]:=
```
UrbPars = kB * Tcell * {0.1, 0.5, 1., 2., 3.};
α0L = α0 * L;
```

EQE

```
EgTicks[min_, max_] := Table[
  If[Mod[i * 10, 5] < 0.0001, {i, ToString[NumberForm[i, {2, 1}]], {0, .025}, Black},
   {i, "", {0, .0125}, Black}], {i, Floor[min], Ceiling[max], 0.1}]
EQETicks[min_, max_] := Table[If[Mod[i * 10, 2] < 0.0001,
   {i, ToString[NumberForm[i, {2, 1}]], {0, .025}, Black},
   {i, "", {0, .0125}, Black}], {i, Floor[min], Ceiling[max], 0.05}]
EQELogTicks[min_, max_] := Table[If[Mod[i, 5] < 0.0001, {i, Superscript[10, i],
    {0, .025}, Black}, {i, "", {0, .0125}, Black}], {i, Floor[min], Ceiling[max], 1}]
```

In[194]:=
```
frame[legend_] :=
  Framed[Style[legend, 16, FontWeight → Plain], FrameMargins → 0, Background → None];
```

In[536]:=
```
EQERegPlot =
 Plot[Flatten[{aSQ[1.5, En], EQE[1.5, En, 1., #, 0., Tcell, α0L, 1.] & /@ UrbPars}],
  {En, 0, 3}, Evaluated → True,
  PlotRange → {{0, 2.5}, {-0.05, 1.05}},
  PlotStyle → Join[{Directive[Black, Dashed]},
    Table[ColorData["Rainbow"][i / Length[UrbPars]], {i, 1, Length[UrbPars]}]],
  Frame → True,
  FrameTicks → {{EQETicks, None}, {EgTicks, None}},
  FrameLabel → {"Photon Energy (eV)", "EQE"},
  FrameStyle → Black,
  BaseStyle → {FontSize → 18},
  PlotLegends → Placed[LineLegend[Join[{Directive[Black, Dashed]},
      Table[ColorData["Rainbow"][i / Length[UrbPars]], {i, 1, Length[UrbPars]}]],
     {"S-Q", "0.1", "0.5", "1", "2", "3"}, LegendLabel → "γ (k_B T_cell)",
     LegendMarkerSize → 25, LegendFunction → frame,
     LegendLayout → {"Column", 1}, Spacings → 0.2], Scaled[{0.25, 0.6}]],
  ImageSize → 400,
  ImagePadding → {{60, 20}, {60, 10}},
  AspectRatio → 1]
```

Out[536]=

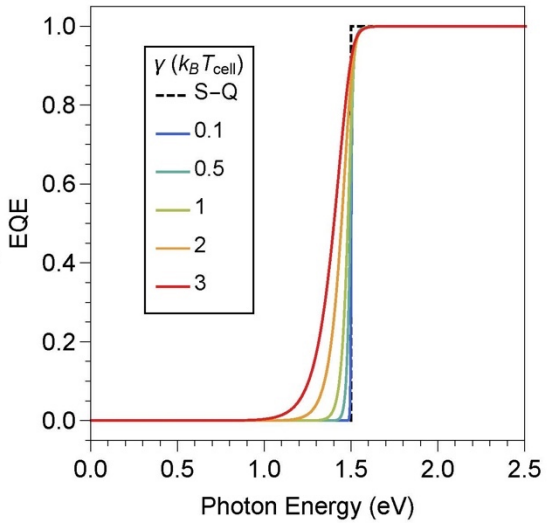

In[550]:=
```
Export["/Users/Stefan/Documents/Caltech/Data/Calculations/Detailed
    Balance/Direct Gap_Band Edge Sharpness/Bandfilling/EQE Reg Plot.tiff",
  EQERegPlot, "TIFF", ImageResolution → 300];
```

```
ParametricPlot[{En, Log10[EQE[1.5, En, 1., #, 0., Tcell, α0L, 1.]]} & /@ UrbPars,
 {En, 0, 2.5}, Evaluated → True,
 PlotRange → {{0, 2.5}, {1, -16}},
 PlotStyle →
  Table[ColorData["Rainbow"][i / Length[UrbPars]], {i, 1, Length[UrbPars]}],
 Frame → True,
 FrameTicks → {{Automatic, None}, {EgTicks, None}},
 FrameLabel → {"Photon Energy (eV)", "EQE"},
 FrameStyle → Black,
 BaseStyle → {FontSize → 18},

 ImagePadding → {{60, 20}, {60, 10}},
 AspectRatio → 1]
```

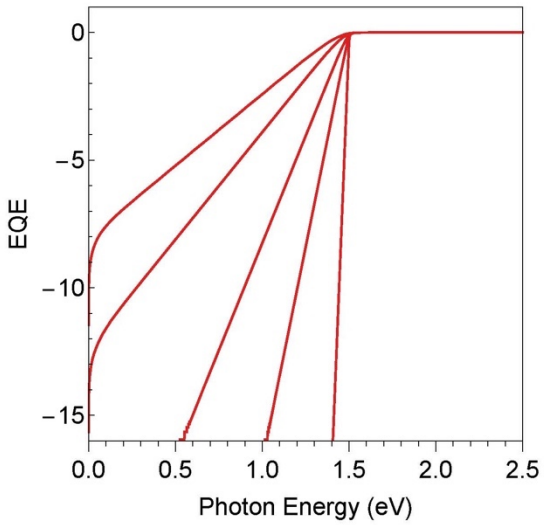

■ Urbach parameter effect on device performance

```
logspace[a_, b_, n_] := 10.0^Range[a, b, (b - a) / (n - 1.)]
```

Calculate the solar cell characteristics as a function of E_g and γ

In[435]:=
```
Egs = Subdivide[0.5, 2.5, 40.];
γs = logspace[-3., 1., 41.];
```

```
Jsc = Table[
   0.1 * q * AbsSolFlux[AM15Photonflux[En], Egs[[i]], 1, γs[[j]], 0., Tcell, α0L, 1.],
   {i, Length[Egs]}, {j, Length[γs]}];
Export["/Users/Stefan/Documents/Caltech/Data/Calculations/Detailed Balance/Direct
    Gap_Band Edge Sharpness/Bandfilling/FOM/Jsc.dat", Jsc, "Data"];

J0 = Table[0.1 * q * R0[Egs[[i]], 1., γs[[j]], 0., Tcell, α0L, 1.],
   {i, Length[Egs]}, {j, Length[γs]}];
Export["/Users/Stefan/Documents/Caltech/Data/Calculations/Detailed Balance/Direct
    Gap_Band Edge Sharpness/Bandfilling/FOM/J0.dat", J0, "Data"];


Voc = Table[OpenCircuit[AM15Photonflux[En], Egs[[i]], 1., γs[[j]],
    Tcell, α0L, 1., Egs[[i]] * 0.6], {i, Length[Egs]}, {j, Length[γs]}];
Export["/Users/Stefan/Documents/Caltech/Data/Calculations/Detailed Balance/Direct
    Gap_Band Edge Sharpness/Bandfilling/FOM/Voc.dat", Voc, "Data"];


maxPV = Flatten[Reap[Do[
      vguess = Egs[[i]] - 0.4;
      Sow[Flatten[Reap[Do[
            Sow[
             output = Mpp[AM15Photonflux[En],
               Egs[[i]], 1., γs[[j]], Tcell, α0L, 1., vguess], j];
            vguess = V /. output[[2]], {j, 1, Length[γs]}]][[2, All]], 1], i],
      {i, 1, Length[Egs]}]][[2, All]], 1];

Vmax = Table[V /. maxPV[[i, j]][[2]], {i, Length[Egs]}, {j, Length[γs]}];
maxPow = Table[maxPV[[i, j]][[1]], {i, Length[Egs]}, {j, Length[γs]}];
Export[
  "/Users/Stefan/Documents/Caltech/Data/Calculations/Detailed Balance/Direct
    Gap_Band Edge Sharpness/Bandfilling/FOM/Vmax.dat", Vmax, "Data"];
Export["/Users/Stefan/Documents/Caltech/Data/Calculations/Detailed Balance/Direct
    Gap_Band Edge Sharpness/Bandfilling/FOM/maxPow.dat", maxPow, "Data"];
```

... FindMinimum: Failed to converge to the requested accuracy or precision within 500 iterations.

... FindMinimum: Failed to converge to the requested accuracy or precision within 500 iterations.

... FindMinimum: Failed to converge to the requested accuracy or precision within 500 iterations.

... General: Further output of FindMinimum::cvmit will be suppressed during this calculation.

In[471]:=
```
Eff = Table[100 * Abs[maxPow[[i, j]]] / SolarConstantAM,
   {i, Length[Egs]}, {j, Length[γs]}];
Export["/Users/Stefan/Documents/Caltech/Data/Calculations/Detailed Balance/Direct
    Gap_Band Edge Sharpness/Bandfilling/FOM/Eff.dat", Eff, "Data"];
```

Calculate the traditional SQ limit

In[438]:=

```
sqJsc = Table[0.1 * q * AbsSolFluxSQ[Egs[[i]]], {i, Length[Egs]}] // Quiet;
sqJ0 = Table[0.1 * q * R0SQ[Egs[[i]]], {i, Length[Egs]}] // Quiet;
sqVoc = Table[kB * Tcell * Log[sqJsc[[i]] / sqJ0[[i]] + 1], {i, Length[Egs]}];
sqVmax = Table[FindMinimum[V * (-sqJsc[[i]] + sqJ0[[i]] * (Exp[V / (kB * Tcell)] - 1)),
    {V, sqVoc[[i]]}], {i, Length[Egs]}];
sqEff = Table[100 * Abs[sqVmax[[i, 1]]] / SolarConstantAM, {i, Length[Egs]}] // Quiet;

(*Save S-Q data*)
Export[
  "/Users/Stefan/Documents/Caltech/Data/Calculations/Detailed Balance/Direct
    Gap_Band Edge Sharpness/Bandfilling/FOM/SQ Voc.dat", sqVoc, "Data"];
Export["/Users/Stefan/Documents/Caltech/Data/Calculations/Detailed Balance/Direct
    Gap_Band Edge Sharpness/Bandfilling/FOM/SQ Jsc.dat", sqJsc, "Data"];
Export["/Users/Stefan/Documents/Caltech/Data/Calculations/Detailed Balance/Direct
    Gap_Band Edge Sharpness/Bandfilling/FOM/SQ J0.dat", sqJ0, "Data"];
Export["/Users/Stefan/Documents/Caltech/Data/Calculations/Detailed Balance/Direct
    Gap_Band Edge Sharpness/Bandfilling/FOM/SQ Eff.dat", sqEff, "Data"];
```

... FindMinimum: The line search decreased the step size to within the tolerance specified by AccuracyGoal and PrecisionGoal but was unable to find a sufficient decrease in the function. You may need more than MachinePrecision digits of working precision to meet these tolerances.

... FindMinimum: The line search decreased the step size to within the tolerance specified by AccuracyGoal and PrecisionGoal but was unable to find a sufficient decrease in the function. You may need more than MachinePrecision digits of working precision to meet these tolerances.

... FindMinimum: The line search decreased the step size to within the tolerance specified by AccuracyGoal and PrecisionGoal but was unable to find a sufficient decrease in the function. You may need more than MachinePrecision digits of working precision to meet these tolerances.

... General: Further output of FindMinimum::lstol will be suppressed during this calculation.

```
Export["/Users/Stefan/Documents/Caltech/Data/Calculations/Detailed Balance/Direct
    Gap_Band Edge Sharpness/Bandfilling/FOM/Vmax.dat", Vmax, "Data"];
```

Effect on FOM

In[460]:=
```
(*Import Data*)
Jsc = Import[
   "/Users/Stefan/Documents/Caltech/Data/Calculations/Detailed Balance/Direct
     Gap_Band Edge Sharpness/Bandfilling/FOM/Jsc.dat"];
J0 = Import["/Users/Stefan/Documents/Caltech/Data/Calculations/Detailed
     Balance/Direct Gap_Band Edge Sharpness/Bandfilling/FOM/J0.dat"];
Voc = Import["/Users/Stefan/Documents/Caltech/Data/Calculations/Detailed
     Balance/Direct Gap_Band Edge Sharpness/Bandfilling/FOM/Voc.dat"];
Vmax = Import["/Users/Stefan/Documents/Caltech/Data/Calculations/Detailed
     Balance/Direct Gap_Band Edge
     Sharpness/Bandfilling/FOM/Vmax.dat", "Data"];
maxPow = Import["/Users/Stefan/Documents/Caltech/Data/Calculations/Detailed
     Balance/Direct Gap_Band Edge
     Sharpness/Bandfilling/FOM/maxPow.dat", "Data"];
```

In[465]:=
```
logTicks = Flatten[Table[i * Table[10^j, {j, -3, 1}], {i, 1, 9}]];
UrbTicks = Table[If[IntegerQ[Log10[logTicks[[i]]]],
    {Log10[logTicks[[i]]], Superscript[10, Log10[logTicks[[i]]]], {0, .025}, Black},
    {Log10[logTicks[[i]]], "", {0, .0125}, Black}], {i, 1, Length[logTicks]}];
```

In[505]:=
```
ContourJ0 = ListContourPlot[ J0,
  DataRange → {{-3, 0}, {0.5, 2.5}},
  PlotRangePadding → None,
  Contours → 100,
  ContourStyle → None,
  Frame → True,
  FrameTicks → {{EgTicks, None}, {UrbTicks, None}},
  FrameStyle → Black,
  FrameLabel → {"γ (eV)", "E_g (eV)"},
  ColorFunction → "SolarColors",
  BaseStyle → Directive[Black, FontSize → 18],
  PlotLegends → BarLegend[{"SolarColors", {0, 650}}, LegendLabel → "mA/cm²",
    LegendMarkerSize → 250, LabelStyle → Directive[FontSize → 14, Black]],
  PlotLabel → Style["J₀", Black],
  ImageSize → 400,
  ImagePadding → {{85, 15}, {60, 10}}]
```

Out[505]=

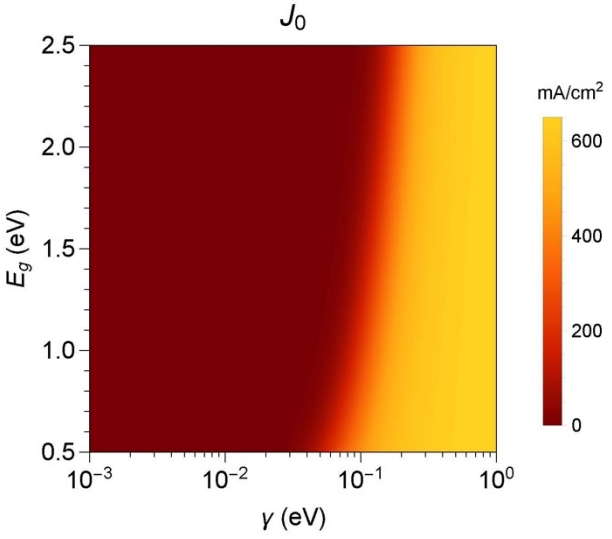

In[502]:=
```
ContourJsc = ListContourPlot[ Jsc,
  DataRange → {{-3, 0}, {0.5, 2.5}},
  PlotRangePadding → None,
  Contours → 100,
  ContourStyle → None,
  ColorFunction → "SolarColors",
  Frame → True,
  FrameLabel → {"γ (eV)", "Eg (eV)"},
  FrameTicks → {{EgTicks, None}, {UrbTicks, None}},
  FrameStyle → Black,
  BaseStyle → Directive[Black, FontSize → 18],
  PlotLegends → BarLegend[{"SolarColors", {0, 100}}, LegendLabel → "mA/cm²",
    LegendMarkerSize → 250, LabelStyle → Directive[FontSize → 14, Black]],
  PlotLabel → Style["Jsc", Black],
  ImageSize → 400,
  ImagePadding → {{85, 15}, {60, 10}}]
```

Out[502]=

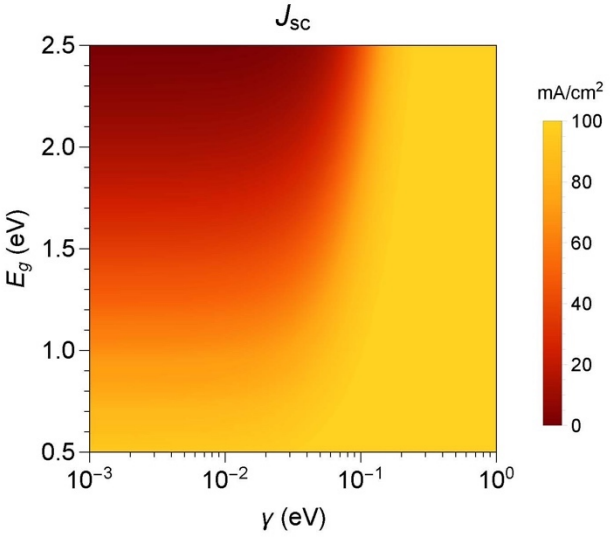

In[503]:=
```
ContourVoc = ListContourPlot[Voc,
  DataRange -> {{-3, 0}, {0, 2.5}},
  PlotRange → {{-3, 0}, {0.5, 2.5}},
  PlotRangePadding → None,
  Contours → 100,
  ContourStyle → None,
  Frame → True,
  FrameStyle → Black,
  FrameTicks → {{EgTicks, None}, {UrbTicks, None}},
  FrameLabel → {"γ (eV)", "Eg (eV)"},
  ColorFunction → "SolarColors",
  BaseStyle → Directive[Black, FontSize → 18],
  PlotLegends → BarLegend[{"SolarColors", {0, 2.5}}, LegendLabel → "Volts",
    LegendMarkerSize → 250, LabelStyle → Directive[FontSize → 14, Black]],
  PlotLabel → Style["Voc", Black],
  ImageSize → 400,
  ImagePadding → {{85, 15}, {60, 10}}]
```

Out[503]=

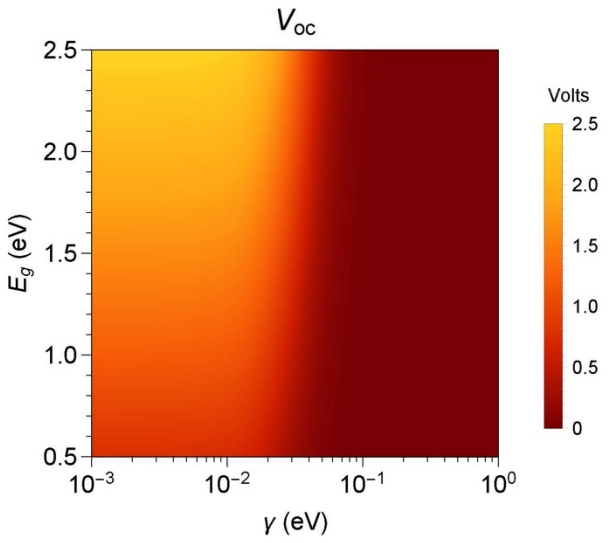

In[504]:=
```
ContourEff = ListContourPlot[Eff,
  DataRange → {{-3, 0}, {0.5, 2.5}},
  PlotRangePadding → None,
  Contours → 100,
  ContourStyle → None,
  Frame → True,
  FrameTicks → {{EgTicks, None}, {UrbTicks, None}},
  FrameStyle → Black,
  FrameLabel → {"γ (eV)", "Eg (eV)"},
  ColorFunction → "SolarColors",
  BaseStyle → Directive[Black, FontSize → 18],
  PlotLegends → BarLegend[{"SolarColors", {0, 35}}, LegendLabel → "Percent",
    LegendMarkerSize → 250, LabelStyle → Directive[FontSize → 14, Black]],
  PlotLabel → Style["η", Black],
  ImageSize → 400,
  ImagePadding → {{85, 15}, {60, 10}}]
```

Out[504]=

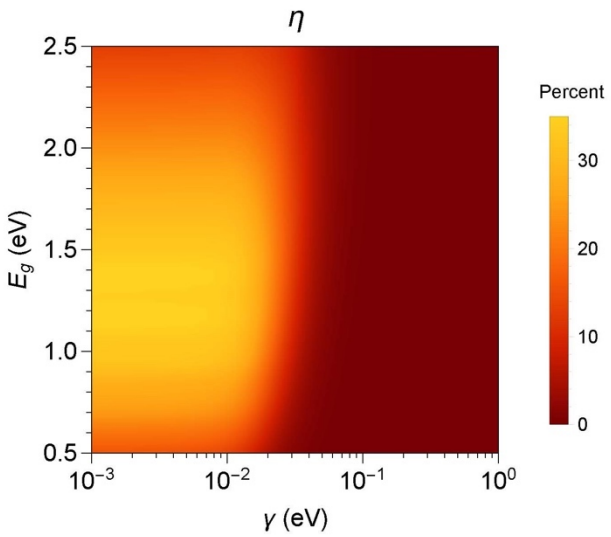

```
In[520]:= Export["/Users/Stefan/Documents/Caltech/Data/Calculations/Detailed
      Balance/Direct Gap_Band Edge Sharpness/Bandfilling/Contour Voc.tiff",
    ContourVoc, "TIFF", ImageResolution → 300];
  Export["/Users/Stefan/Documents/Caltech/Data/Calculations/Detailed
      Balance/Direct Gap_Band Edge Sharpness/Bandfilling/Contour Jsc.tiff",
    ContourJsc, "TIFF", ImageResolution → 300];
  Export["/Users/Stefan/Documents/Caltech/Data/Calculations/Detailed
      Balance/Direct Gap_Band Edge Sharpness/Bandfilling/Contour Eff.tiff",
    ContourEff, "TIFF", ImageResolution → 300];
```

Line cuts at $E_g = 1.5$ eV

```
In[474]:= (*Where Eg = 1.5*)

In[475]:= index15 = FirstPosition[Egs, 1.5][[1]];

  (*Plot ticks*)

In[476]:= MakeInteger[x_] := If[Round[x] == x, ToString[Round@x], x]
  E0Ticks =  Table[If[IntegerQ[Log10[logTicks[[i]]]],
      {logTicks[[i]], Superscript[10, Log10[logTicks[[i]]]], {.025, 0}, Black},
      {logTicks[[i]], "", {.0125, 0}, Black}], {i, 1, Length[logTicks]}];
  J0Ticks[min_, max_] := Table[If[Mod[i, 100] < 0.0001, {i, i, {.025, 0}, Black},
     {i, "", {.0125, 0}, Black}], {i, Floor[min], Ceiling[max], 20}]
  J0LogTicks = Table[If[Mod[i, 5] < 0.0001, {10^i, Superscript[10, i],
       {0, .025}, Black}, {10^i, "", {0, .0125}, Black}], {i, -21, 5, 1}];
  JscTicks[min_, max_] := Table[If[Mod[i, 20] < 0.0001, {i, i, {.025, 0}, Black},
     {i, "", {.0125, 0}, Black}], {i, Floor[min], Ceiling[max], 5}]
  EffTicks = Table[If[Mod[i, 5] < 0.0001, {i, MakeInteger[i], {.025, 0}, Black},
      {i, "", {.0125, 0}, Black}], {i, -1.25, 35, 1.25}];

In[482]:= (*kBT lines for plots*)

In[483]:= kBTLine = Line[{{Log[kB * Tcell], -20}, {Log[kB * Tcell], 600}}];
  kBTLogLine =
    Line[{{Log[kB * Tcell], Log[10^-21]}, {Log[kB * Tcell], Log[10^6]}}];
  LineStyle = Directive[{Red, Dashed, Thick}];

In[486]:= (*Line cut lots*)

In[528]:= lineVoc = ListLogLinearPlot[Transpose[{γs, Voc[[index15, All]]}],
    Joined → True,
    PlotRange → {{10^-3, 10^0}, {-0.05, 1.45}},
    PlotStyle → Thick,
    Frame → True,
    FrameLabel → {{"V_oc  (V)", None}, {"γ  (eV)", None}},
    FrameTicks → {{VocTicks, None}, {E0Ticks, None}},
    FrameStyle → Black,
```

```
  BaseStyle → Directive[FontSize → 18],
  Epilog → {{LineStyle, kBTLine}},
  AspectRatio → 1,
  ImageSize → 400,
  ImagePadding → {{85, 15}, {60, 10}}]

γsJ0 = logspace[-3., 1., 1001.];

lineJ0 = ListLogLogPlot[Transpose[{γsJ0,
    Table[0.1 * q * R0[1.5, 1., γsJ0[[j]], 0., Tcell, α0L, 1.], {j, Length[γsJ0]}]}],
  Joined → True,
  PlotRange → {{10^-3, 10^0}, {10^-20, 10^6}},
  PlotStyle → Thick,
  Frame → True,
  FrameLabel → {{"J₀ (mA/cm²)", None}, {"γ (eV)", None}},
  FrameTicks → {{J0LogTicks, None}, {E0Ticks, None}},
  FrameStyle → Black,
  BaseStyle → Directive[FontSize → 18],
  Epilog → {{LineStyle, kBTLogLine}},
  AspectRatio → 1,
  ImageSize → 400,
  ImagePadding → {{85, 15}, {60, 10}}]

lineJsc = ListLogLinearPlot[Transpose[{γs, Jsc[[index15, All]]}],
  Joined → True,
  PlotRange → {{10^-3, 10^0}, {-5, 125}},
  Frame → True,
  FrameLabel → {{"Jsc (mA/cm²)", None}, {"γ (eV)", None}},
  FrameTicks → {{JscTicks, None}, {E0Ticks, None}},
  FrameStyle → Black,
  BaseStyle → Directive[FontSize → 18],
  Epilog → {{LineStyle, kBTLine}},
  AspectRatio → 1,
  ImageSize → 400,
  ImagePadding → {{85, 15}, {60, 10}}]

lineEff = ListLogLinearPlot[Transpose[{γs, Eff[[index15, All]]}],
  Joined → True,
  PlotRange → {{10^-3, 10^0}, {-1.25, 36.25}},
  PlotStyle → Thick,
  Frame → True,
  FrameLabel → {{"η (%)", None}, {"γ (eV)", None}},
  FrameTicks → {{EffTicks, None}, {E0Ticks, None}},
```

```
FrameStyle → Black,
BaseStyle → Directive[FontSize → 18],
Epilog → {{LineStyle, kBTLine}},
AspectRatio → 1,
ImageSize → 400,
ImagePadding → {{85, 15}, {60, 10}}]
```

Out[528]=

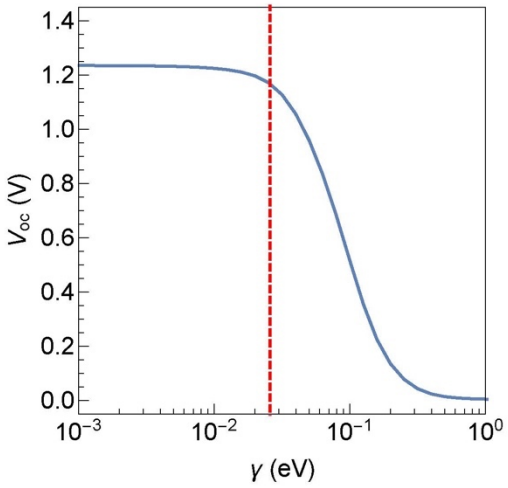

Out[530]=

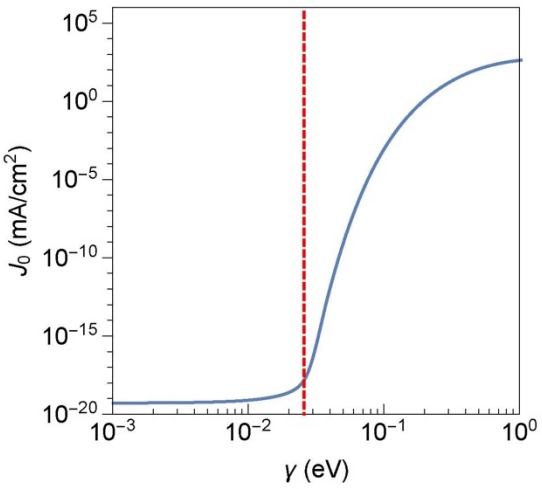

Out[531]=

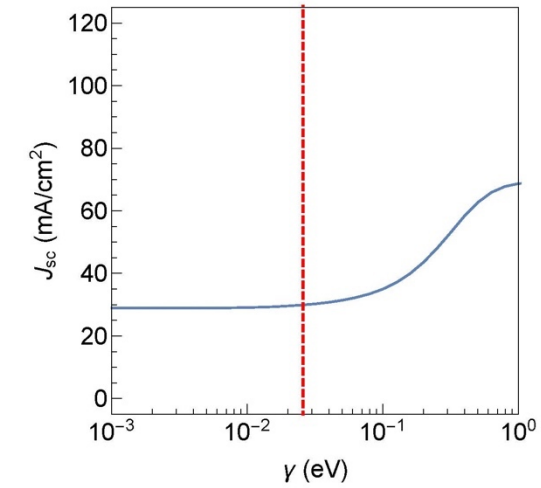

Out[532]=

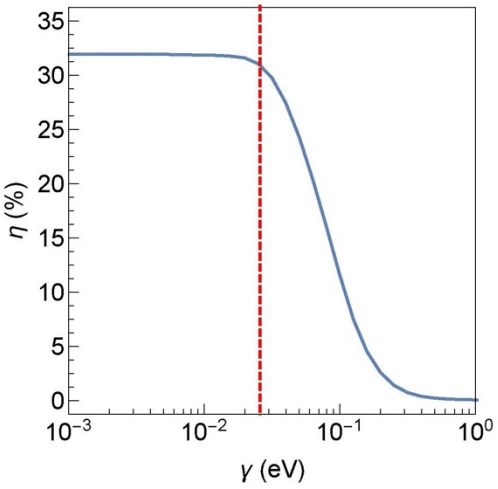

In[533]:=
```
Export["/Users/Stefan/Documents/Caltech/Data/Calculations/Detailed
    Balance/Direct Gap_Band Edge Sharpness/Bandfilling/Line Voc.pdf",
  lineVoc, "PDF", ImageResolution → 300];
Export["/Users/Stefan/Documents/Caltech/Data/Calculations/Detailed
    Balance/Direct Gap_Band Edge Sharpness/Bandfilling/Line Jsc.pdf",
  lineJsc, "PDF", ImageResolution → 300];
Export["/Users/Stefan/Documents/Caltech/Data/Calculations/Detailed
    Balance/Direct Gap_Band Edge Sharpness/Bandfilling/Line Eff.pdf",
  lineEff, "PDF", ImageResolution → 300];
```

■ Effect on S-Q Limit

```
(*Calculate Eff for relevant γ*)
```

In[430]:=
```
γkBT = kB * Tcell * {0.1, 0.2, 0.5, 1., 2., 3.};
```

In[453]:=
```
VmaxComp = Flatten[Reap[Do[
      vguess = Egs[[i]] - 0.3;
      Sow[Flatten[Reap[Do[
            Sow[
             output = Mpp[AM15Photonflux[En],
               Egs[[i]], 1., γkBT[[j]], Tcell, α0L, 1., vguess], j];
            vguess = V /. output[[2]], {j, 1, Length[γkBT]}]][[2, All]], 1], i],
      {i, 1, Length[Egs]}]][[2, All]], 1];
EffComp = Table[100 * Abs[VmaxComp[[i, j]][[1]]] / SolarConstantAM,
   {i, Length[Egs]}, {j, Length[γkBT]}];
```

... FindMinimum: Failed to converge to the requested accuracy or precision within 500 iterations.

... FindMinimum: Failed to converge to the requested accuracy or precision within 500 iterations.

```
Export["/Users/Stefan/Documents/Caltech/Data/Calculations/Detailed Balance/Direct
    Gap_Band Edge Sharpness/Bandfilling/FOM/EffComp.dat", EffComp, "Data"];
```

In[431]:=
```
(*Define color scheme*)
kBTColors = Flatten[{Directive[Black, Dashed],
    Table[ColorData["Rainbow"][i / Length[γkBT]], {i, 1, Length[γkBT]}]}];
```

In[433]:=
```
EffComp = Import[
   "/Users/Stefan/Documents/Caltech/Data/Calculations/Detailed Balance/Direct
     Gap_Band Edge Sharpness/Bandfilling/FOM/EffComp.dat"];
```

In[541]:=
```
kBTColors
```

Out[541]= {Directive[■, Dashing[{Small, Small}]], ■, ■, ■, ■, ■, ■}

In[551]:=
```
effPlot = ListPlot[{Transpose[{Egs, sqEff}],
   Transpose[{Egs, EffComp[[All, 1]]}],
   Transpose[{Egs, EffComp[[All, 2]]}],
   Transpose[{Egs, EffComp[[All, 3]]}],
   Transpose[{Egs, EffComp[[All, 4]]}],
   Transpose[{Egs, EffComp[[All, 5]]}],
   Transpose[{Egs, EffComp[[All, 6]]}]},
  Joined → True,
  PlotRange → {{0.4, 2.5}, {-1, 36}},
  PlotStyle → kBTColors,
  Frame → True,
  FrameLabel → {{"η (%)", None}, {"Eg (eV)", None}},
  FrameTicks → {{EffTicks, None}, {EgTicks, None}},
  FrameStyle → Black,
  BaseStyle → Directive[FontSize → 18],
  AspectRatio → 1,
  ImageSize → 400,
  ImagePadding → {{60, 20}, {60, 10}}]
```

Out[551]=

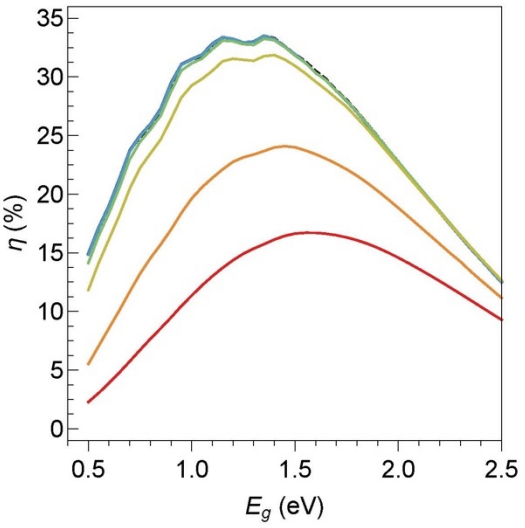

In[552]:=
```
Export[
 "/Users/Stefan/Documents/Caltech/Data/Calculations/Detailed Balance/Direct
   Gap_Band Edge Sharpness/Bandfilling/EffPlot.pdf",
 effPlot, "PDF", ImageResolution → 300]
```

Out[552]=
```
/Users/Stefan/Documents/Caltech/Data/Calculations/Detailed
 Balance/Direct Gap_Band Edge Sharpness/Bandfilling/EffPlot.pdf
```

Effect on Cell Emission and Sub-gap Recombination

In[195]:=
```
eg = 1.5;

CellEmission[Eg_, En_?NumericQ, θi_, γ_?NumericQ, Voc_?NumericQ, T_, α0L_, IQE_] :=
 UnitStep[En] b[En, T, Voc] * EQE[Eg, En, θi, γ, Voc, T, α0L, IQE]
```

In[197]:=
```
γCellEm = Join[Range[0.1, 1.4, 0.05], Range[1.6, 2.6, 0.2]] * kB * Tcell;
γLabel = NumberForm[#, {3, 2}] & /@ (γCellEm / (kB * Tcell));
```

In[199]:=
```
vocCellEm = Table[OpenCircuit[AM15Photonflux[En], eg, 1.,
    γCellEm[[j]], Tcell, α0L, 1., eg * 0.6], {j, Length[γCellEm]}];
MaxCellEm = Table[FindMaximum[CellEmission[eg, En, 1., γCellEm[[i]],
      vocCellEm[[i]], Tcell, α0L, 1.], {En, eg}] // Quiet, {i, 1, Length[γCellEm]}];
```

In[201]:=
```
(*Plot to see peak shift*)
```

In[356]:=
```
cellEmPlotData =
  Join[Table[{CellEmission[eg, En, 1., γCellEm[[i]], vocCellEm[[i]], Tcell, α0L, 1.] /
      MaxCellEm[[i, 1]],
     EQE[eg, En, 1, γCellEm[[i]], 0, Tcell, α0L, 1.]}, {i, 3, 27, 8}],
   Table[{CellEmission[eg, En, 1., γCellEm[[i]], vocCellEm[[i]],
      Tcell, α0L, 1.] / MaxCellEm[[i, 1]],
     EQE[eg, En, 1, γCellEm[[i]], 0, Tcell, α0L, 1.]}, {i, 29, 33, 2}]];
cellEmPlotDataLabel = Join[Table[γLabel[[i]], {i, 3, 27, 8}],
   Table[γLabel[[i]], {i, 29, 33, 2}]];
```

```
In[319]:= Table[cellEmPlotData[[i]] + 1.25 * (i - 1), {i, Length[cellEmPlotData]}]
```

```
Out[319]= {{0. + 2.45312 × 10^-23 CellEmission[1.5, En, 1., 0.00516854, 1.23117, 300., 10., 1.],
    0. + EQE[1.5, En, 1, 0.00516854, 0, 300., 10., 1.],
    0. + EQE[1.5, En, 1, 0.00516854, 0, 300., 10., 1.]},
   {1.25 + 4.76721 × 10^-23 CellEmission[1.5, En, 1., 0.0155056, 1.2115, 300., 10., 1.],
    1.25 + EQE[1.5, En, 1, 0.0155056, 0, 300., 10., 1.],
    1.25 + EQE[1.5, En, 1, 0.0155056, 0, 300., 10., 1.]},
   {2.5 + 1.44601 × 10^-22 CellEmission[1.5, En, 1., 0.0258427, 1.16717, 300., 10., 1.],
    2.5 + EQE[1.5, En, 1, 0.0258427, 0, 300., 10., 1.],
    2.5 + EQE[1.5, En, 1, 0.0258427, 0, 300., 10., 1.]},
   {3.75 + 1.27849 × 10^-22 CellEmission[1.5, En, 1., 0.0361798, 1.08979, 300., 10., 1.],
    3.75 + EQE[1.5, En, 1, 0.0361798, 0, 300., 10., 1.],
    3.75 + EQE[1.5, En, 1, 0.0361798, 0, 300., 10., 1.]},
   {5. + 1.08362 × 10^-22 CellEmission[1.5, En, 1., 0.0465169, 0.994103, 300., 10., 1.],
    5. + EQE[1.5, En, 1, 0.0465169, 0, 300., 10., 1.],
    5. + EQE[1.5, En, 1, 0.0465169, 0, 300., 10., 1.]},
   {6.25 + 1.02921 × 10^-22 CellEmission[1.5, En, 1., 0.0568539, 0.893631, 300., 10., 1.],
    6.25 + EQE[1.5, En, 1, 0.0568539, 0, 300., 10., 1.],
    6.25 + EQE[1.5, En, 1, 0.0568539, 0, 300., 10., 1.]},
   {7.5 + 1.00864 × 10^-22 CellEmission[1.5, En, 1., 0.067191, 0.794316, 300., 10., 1.],
    7.5 + EQE[1.5, En, 1, 0.067191, 0, 300., 10., 1.],
    7.5 + EQE[1.5, En, 1, 0.067191, 0, 300., 10., 1.]}}
```

```
qePL = Plot[
  {{0.` + 2.4531240141113867`*^-23 CellEmission[1.5`, En, 1.`, 0.005168539325842697`,
      1.2311652285964143`, 300.`, 10.`, 1.`],
    0.` + EQE[1.5`, En, 1, 0.005168539325842697`, 0, 300.`, 10.`, 1.`],
    0.` + EQE[1.5`, En, 1, 0.005168539325842697`, 0, 300.`, 10.`, 1.`]},
   {1.25` + 4.7672148597989585`*^-23 CellEmission[1.5`, En, 1.`,
      0.01550561797752809`, 1.2115030121401194`, 300.`, 10.`, 1.`],
    1.25` + EQE[1.5`, En, 1, 0.01550561797752809`, 0, 300.`, 10.`, 1.`],
    1.25` + EQE[1.5`, En, 1, 0.01550561797752809`, 0, 300.`, 10.`, 1.`]},
   {2.5` + 1.4460132197045965`*^-22 CellEmission[1.5`, En, 1.`,
      0.025842696629213485`, 1.1671733433009777`, 300.`, 10.`, 1.`],
    2.5` + EQE[1.5`, En, 1, 0.025842696629213485`, 0, 300.`, 10.`, 1.`],
    2.5` + EQE[1.5`, En, 1, 0.025842696629213485`, 0, 300.`, 10.`, 1.`]},
   {3.75` + 1.2784881673479119`*^-22 CellEmission[1.5`, En, 1.`,
      0.03617977528089888`, 1.089787637880022`, 300.`, 10.`, 1.`],
    3.75` + EQE[1.5`, En, 1, 0.03617977528089888`, 0, 300.`, 10.`, 1.`],
    3.75` + EQE[1.5`, En, 1, 0.03617977528089888`, 0, 300.`, 10.`, 1.`]},
   {5.` + 1.0836176735170156`*^-22 CellEmission[1.5`, En, 1.`,
      0.04651685393258428`, 0.9941028449265771`, 300.`, 10.`, 1.`],
    5.` + EQE[1.5`, En, 1, 0.04651685393258428`, 0, 300.`, 10.`, 1.`],
```

```
  5.` + EQE[1.5`, En, 1, 0.04651685393258428`, 0, 300.`, 10.`, 1.`]},
 {6.25` + 1.0292075667953865`*^-22 CellEmission[1.5`, En, 1.`,
     0.05685393258426967`, 0.8936314145219935`, 300.`, 10.`, 1.`],
  6.25` + EQE[1.5`, En, 1, 0.05685393258426967`, 0, 300.`, 10.`, 1.`],
  6.25` + EQE[1.5`, En, 1, 0.05685393258426967`, 0, 300.`, 10.`, 1.`]},
 {7.5` + 1.0086387456367333`*^-22 CellEmission[1.5`, En, 1.`,
     0.06719101123595507`, 0.7943164317689941`, 300.`, 10.`, 1.`],
  7.5` + EQE[1.5`, En, 1, 0.06719101123595507`, 0, 300.`, 10.`, 1.`], 7.5` +
   EQE[1.5`, En, 1, 0.06719101123595507`, 0, 300.`, 10.`, 1.`]}}, {En, 0.5, 2.5},
Evaluated → True,
PlotPoints → 50,
PlotRange → {{0.5, 2.5}, All},
PlotStyle → Flatten[
  Table[{Directive[ColorData["Rainbow"][i / Length[cellEmPlotData]], Dashed],
    Directive[ColorData["Rainbow"][i / Length[cellEmPlotData]]],
    Directive[ColorData["Rainbow"][i / Length[cellEmPlotData]], DotDashed]},
   {i, 1, Length[cellEmPlotData]}]],
Frame → True,
FrameLabel → {{"Emission Intensity (a.u.)", None}, {"γ (eV)", None}},
FrameTicks → {{None, None}, {Automatic, None}},
FrameStyle → Black,
BaseStyle → Directive[FontSize → 18],
Epilog → {{Table[Style[Text["γ=" <> ToString[cellEmPlotDataLabel[[i]]] <> " k_BT",
      {2.25, 0.17 + 1.25 (i - 1)}], 14, ColorData["Rainbow"][
      i / Length[cellEmPlotData]]], {i, Length[cellEmPlotData]}]}},
AspectRatio → 1,
ImageSize → 400,
ImagePadding → {{70, 15}, {60, 15}}]
```

Out[424]=

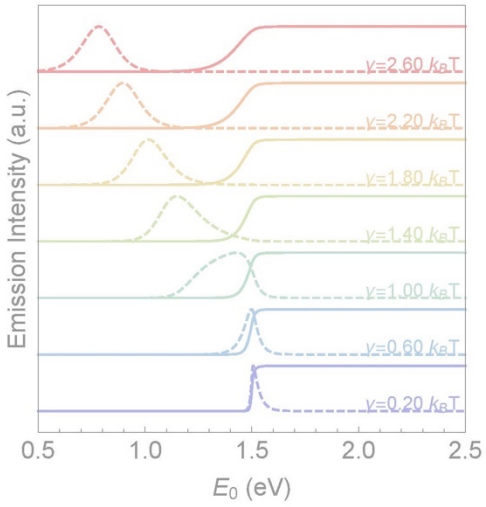


```
(*Calculate Eg distribution*)
```

In[410]:=
```
egpoints = Subdivide[0.5, 3., 500];
qedata =
  Join[
   Table[EQE[eg, egpoints[[j]], 1, γCellEm[[i]], 0, Tcell, α0L, 1.],
    {i, 3, 27, 8}, {j, Length[egpoints]}],
   Table[EQE[eg, egpoints[[j]], 1, γCellEm[[i]], 0, Tcell, α0L, 1.],
    {i, 29, 33, 2}, {j, Length[egpoints]}]];
```

In[412]:=
```
dqe = Table[DerivativeFilter[qedata[[i]], {1}], {i, Length[qedata]}];
```

```
derivplot =
 ListPlot[Table[Transpose[{egpoints, dqe[[i]] / Max[dqe[[i]]] + 1.25 * (i - 1)}],
   {i, Length[dqe]}], PlotRange → {{0.5, 2.5}, All},
  Joined → True,
  PlotRange → {{0.5, 2.5}, All},
  PlotStyle → Table[Directive[ColorData["Rainbow"][i / Length[cellEmPlotData]],
     DotDashed], {i, 1, Length[cellEmPlotData]}],
  Frame → True,
  FrameLabel → {{"Emission Intensity (a.u.)", None}, {"γ (eV)", None}},
  FrameTicks → {{None, None}, {Automatic, None}},
  FrameStyle → Black,
  BaseStyle → Directive[FontSize → 18],
  AspectRatio → 1,
  ImageSize → 400,
  ImagePadding → {{70, 15}, {60, 15}}]
```

Out[455]=

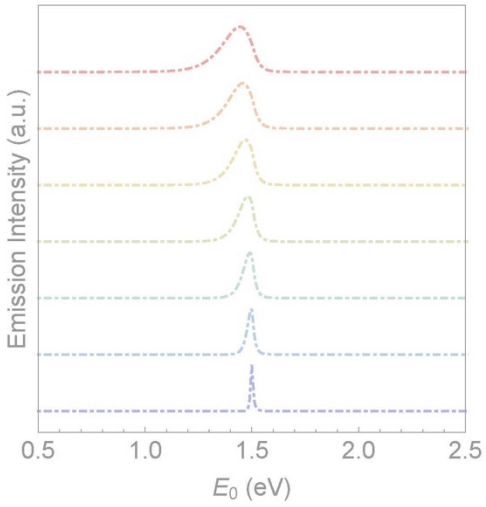

In[456]:=
```
(*Combine plots*)
emcomb = Show[qePL, derivplot]
```

Out[456]=

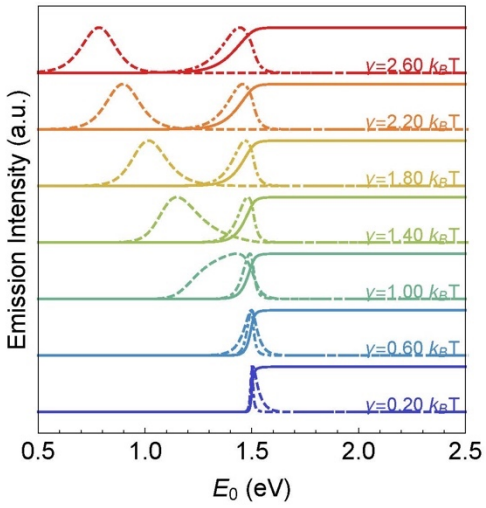

In[457]:=
```
Export[
 "/Users/Stefan/Documents/Caltech/Data/Calculations/Detailed Balance/Direct
   Gap_Band Edge Sharpness/Bandfilling/Emission.pdf", emcomb, "PDF"]
```

Out[457]=
```
/Users/Stefan/Documents/Caltech/Data/Calculations/Detailed
  Balance/Direct Gap_Band Edge Sharpness/Bandfilling/Emission.pdf
```

Emission Max and Peak Position

```
Clear[PeakPos, peakPos, peakMax]
```

```
Eg, En, θi, γs[[i]], vocs[[i]], T, α0L, IQE
```

```
PeakPos[Spectrum_, Eg_, θi_, T_, α0L_, IQE_] :=
 Block[{indexEg, γs, vocs, maxEmPos},
  γs = logspace[-3., 0., 51];
  indexEg = FirstPosition[Egs, Eg];
  vocs = OpenCircuit[AM15Photonflux[En], Eg, θi, #, T, α0L, IQE, Eg * 0.6] & /@ γs;
  maxEmPos =
   Table[FindMaximum[CellEmission[Eg, En, θi, γs[[i]], vocs[[i]], T, α0L, IQE],
       {En, Eg}] // Quiet, {i, 1, Length[γs]}];
  peakPos = Table[En /. maxEmPos[[i, 2]], {i, Length[γs]}];
  peakMax = Table[maxEmPos[[i, 1]], {i, Length[γs]}];
 ]
```

```
PeakPos[AM15Photonflux[En], 1.5, 1, Tcell, α0L, 1.]
peakVoc = Block[{JL, Jdark},
   JL = Table[0.1 * q * AbsSolFluxSQ[peakPos[[i]]], {i, Length[peakPos]}] // Quiet;
   Jdark = Table[0.1 * q * R0SQ[peakPos[[i]]], {i, Length[peakPos]}] // Quiet;
   Table[kB * Tcell * Log[JL[[i]] / Jdark[[i]] + 1], {i, Length[peakPos]}]
  ];
```

… FindRoot: The line search decreased the step size to within tolerance specified by AccuracyGoal and PrecisionGoal but was unable to find a sufficient decrease in the merit function. You may need more than MachinePrecision digits of working precision to meet these tolerances.

… FindRoot: The line search decreased the step size to within tolerance specified by AccuracyGoal and PrecisionGoal but was unable to find a sufficient decrease in the merit function. You may need more than MachinePrecision digits of working precision to meet these tolerances.

```
ListLogLinearPlot[
 {Transpose[{logspace[-3., 0., 51], peakPos}], Transpose[{γs, Voc[[index15]]}],
  Transpose[{logspace[-3., 0., 51], peakVoc}]}, Joined → True,
 PlotRange → {{10^-3, 10^0}, All},
 PlotStyle → Thick,
 Frame → True,
 FrameLabel → {{"Peak Position (eV)", None}, {"γ (eV)", None}},
 FrameTicks → {{EgTicks, None}, {E0Ticks, None}},
 FrameStyle → Black,
 BaseStyle → Directive[FontSize → 18],
 Epilog → {{LineStyle, kBTLine},
   {Text[
     Style["Eg=1.5 eV", FontFamily → "Arial", FontSize → 20], Scaled[{0.2, 0.1}]]}},
 PlotLegends → Placed[LineLegend[Automatic, {"PL Peak", "Voc", "Voc from PL"},
    LegendFunction → frame], {0.75, 0.8}],
 AspectRatio → 1,
 ImageSize → 400,
 ImagePadding → {{85, 15}, {60, 10}}]
```

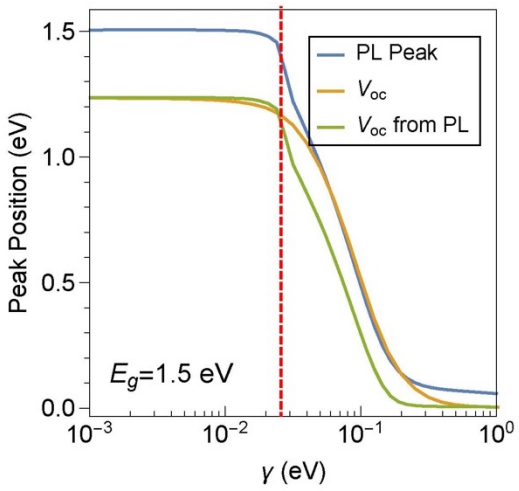

```
ListLogLogPlot[Transpose[{γs, peakMax}],
 Joined → True,
 PlotRange → {{10^-3, 10^0}, {-1.25, 36.25}},
 PlotStyle → Thick,
 Frame → True,
 FrameLabel → {{"Emission Peak Maximum (a.u.)", None}, {"γ (eV)", None}},
 FrameTicks → {{None, None}, {E0Ticks, None}},
 FrameStyle → Black,
 BaseStyle → Directive[FontSize → 18],
 Epilog → {{LineStyle, kBTLine}},
 AspectRatio → 1,
 ImageSize → 400,
 ImagePadding → {{85, 15}, {60, 10}}]
```

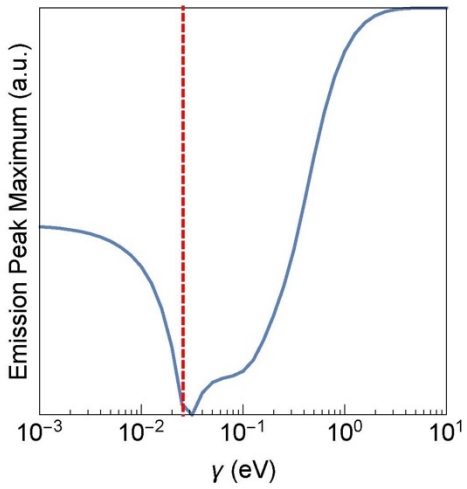

Emission Peak Shift

In[568]:=
```
PeakShift[Spectrum_, Eg_, θi_, γstart_, γend_, γstep_, T_, α0L_, IQE_] :=
 Block[{maxEmPos, γs, vocs, shifts},
  γs = kB * Tcell * Range[γstart, γend, γstep];
  vocs = OpenCircuit[AM15Photonflux[En], Eg, θi, #, T, α0L, IQE, Eg * 0.6] & /@ γs;

  maxEmPos =
   Table[FindMaximum[CellEmission[Eg, En, θi, γs[[i]], vocs[[i]], T, α0L, IQE],
      {En, Eg}] // Quiet, {i, 1, Length[γs]}];
  shifts = Table[Eg - En /. maxEmPos[[i, 2]], {i, 1, Length[γs]}];
  ListPlot[Transpose[{Range[γstart, γend, γstep], shifts}],
   Joined → True,
   PlotRange → {{-0.1, 3.0}, {-0.05, 1}},
   Frame → True,
   FrameTicks → {{Automatic, None}, {Automatic, None}},
   FrameLabel → {{"Emission Peak Shift (eV)", None}, {"γ (kBTcell)", None}},
   FrameStyle → Black,
   BaseStyle → Directive[FontSize → 18],
   Epilog → {LineStyle, Line[{{1, -0.1}, {1, 1}}]},
   AspectRatio → 1]]
```

In[569]:=
```
PeakShift[AM15Photonflux[En], eg, 1., 0.05, 3., 0.05, Tcell, α0L, 1.]
```

… FindRoot: The line search decreased the step size to within tolerance specified by AccuracyGoal and PrecisionGoal but was unable to find a sufficient decrease in the merit function. You may need more than MachinePrecision digits of working precision to meet these tolerances.

Out[569]=

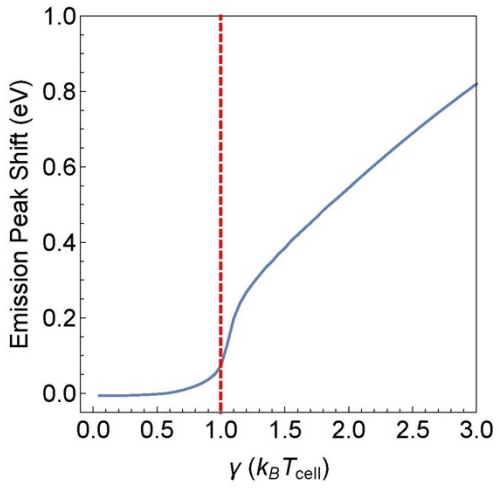

```
PeakShift[Spectrum_, Eg_, θi_, γstart_, γend_, γstep_, T_, α0L_, IQE_] :=
 Block[{maxEmPos, γs, vocs, shifts},
  γs = kB * Tcell * Range[γstart, γend, γstep];
  vocs = OpenCircuit[AM15Photonflux[En], Eg, θi, #, T, α0L, IQE, Eg * 0.6] & /@ γs;

  maxEmPos =
   Table[FindMaximum[CellEmission[Eg, En, θi, γs[[i]], vocs[[i]], T, α0L, IQE],
      {En, Eg}] // Quiet, {i, 1, Length[γs]}];
  shifts = Table[Eg - En /. maxEmPos[[i, 2]], {i, 1, Length[γs]}];
  ListPlot[Transpose[{Range[γstart, γend, γstep], shifts}],
   Joined → True,
   PlotRange → {{-0.1, 3.0}, {-0.05, 1}},
   Frame → True,
   FrameTicks → {{Automatic, None}, {Automatic, None}},
   FrameLabel → {{"Emission Peak Shift (eV)", None}, {"γ (k_B T_cell)", None}},
   FrameStyle → Black,
   BaseStyle → Directive[FontSize → 18],
   Epilog → {LineStyle, Line[{{1, -0.1}, {1, 1}}]},
   AspectRatio → 1]]
```

Effect on peak shape and emission width

```
Plot[Table[CellEmission[eg, En, 1., γCellEm[[2 i]], vocCellEm[[2 i]], Tcell, α0L, 1.] /
    MaxCellEm[[2 i, 1]] + 1.25 * (i - 1), {i, 1, 12}], {En, 0.5, 2.5},
 Evaluated → True,
 PlotRange → All,
 PlotStyle → Table[ColorData["Rainbow"][i / 12], {i, 1, 12}],
 Frame → True,
 FrameLabel → {{"Emission Intensity (a.u.)", None}, {"γ (eV)", None}},
 FrameTicks → {{None, None}, {Automatic, None}},
 FrameStyle → Black,
 BaseStyle → Directive[FontSize → 18],
 Epilog → {Table[Style[Text["γ=" <> ToString[γLabel[[2 i]]] <> " kBT",
      {2.25, 0.17 + 1.25 (i - 1)}], 14, ColorData["Rainbow"][i / 12]], {i, 1, 12}]},
 AspectRatio → 1,
 ImageSize → 400,
 ImagePadding → {{70, 10}, {60, 10}}]
```

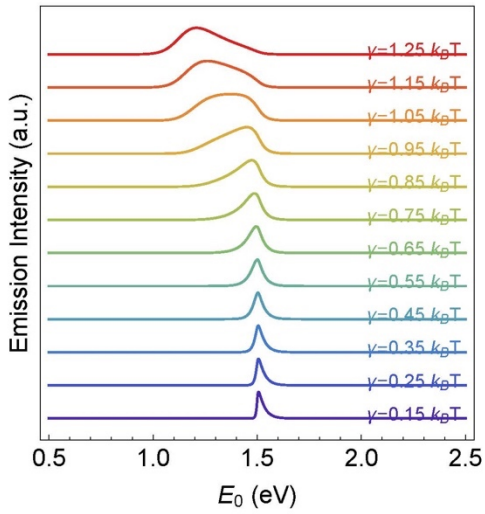


```
(*Peak FWHM*)
```

```
Clear[findAllRoots]
SyntaxInformation[findAllRoots] = {"LocalVariables" → {"Plot", {2, 2}},
   "ArgumentsPattern" → {_, _, OptionsPattern[]}};
SetAttributes[findAllRoots, HoldAll];

Options[findAllRoots] = Join[{"ShowPlot" → False, PlotRange → All},
   FilterRules[Options[Plot], Except[PlotRange]]];

findAllRoots[fn_, {l_, lmin_, lmax_}, opts : OptionsPattern[]] :=
 Module[{pl, p, x, localFunction, brackets},
  localFunction = ReleaseHold[Hold[fn] /. HoldPattern[l] :↦ x];
  If[lmin ≠ lmax, pl = Plot[localFunction, {x, lmin, lmax},
     Evaluate@FilterRules[Join[{opts}, Options[findAllRoots]], Options[Plot]]];
   p = Cases[pl, Line[{x__}] :↦ x, Infinity];
   If[OptionValue["ShowPlot"],
    Print[Show[pl, PlotLabel → "Finding roots for this function",
      ImageSize → 200, BaseStyle → {FontSize → 8}]]], p = {}];
  brackets = Map[First, Select[(*This Split trick pretends that two points on
       the curve are "equal" if the function values have _opposite _ sign.Pairs
       of such sign-changes form the brackets for the subsequent FindRoot*)
     Split[p, Sign[Last[#2]] == -Sign[Last[#1]] &], Length[#1] == 2 &], {2}];
  x /. Apply[FindRoot[localFunction == 0, {x, ##1}] &, brackets, {1}] /. x → {}]

FWHM[Spectrum_, Eg_, θi_, γstart_, γend_, γnum_, T_, α0L_, IQE_] :=
 Module[{maxEmPos, γs, vocs, roots},

  γs = logspace[γstart, γend, γnum];
  vocs = Table[
    OpenCircuit[Spectrum, Eg, θi, γs[[i]], T, α0L, IQE, Eg * 0.6], {i, Length[γs]}];
  maxEmPos =  Table[FindMaximum[CellEmission[Eg, En, θi, γs[[i]],
       vocs[[i]], T, α0L, IQE], {En, Eg}] // Quiet, {i, 1, Length[γs]}];
  roots = Table[findAllRoots[ CellEmission[Eg, En, θi, γs[[i]], vocs[[i]], T,
       α0L, IQE] / maxEmPos[[i, 1]] - 0.5, {En, 0., 1.7}], {i, Length[γs]}];
  Table[roots[[i, 2]] - roots[[i, 1]], {i, Length[γs]}]
 ]
```

```
fwhms = FWHM[AM15Photonflux[En], 1.5, 1., -3., 0., 51, Tcell, α0L, 1.]
```

... FindRoot: The line search decreased the step size to within tolerance specified by AccuracyGoal and PrecisionGoal but was unable to find a sufficient decrease in the merit function. You may need more than MachinePrecision digits of working precision to meet these tolerances.

... FindRoot: The line search decreased the step size to within tolerance specified by AccuracyGoal and PrecisionGoal but was unable to find a sufficient decrease in the merit function. You may need more than MachinePrecision digits of working precision to meet these tolerances.

```
{0.0299343, 0.0300174, 0.030127, 0.0302691, 0.0304509, 0.0306823, 0.0309766,
 0.0313458, 0.0318051, 0.0323736, 0.0330761, 0.0339457, 0.0350276, 0.0363844,
 0.038106, 0.0403244, 0.0432403, 0.0471717, 0.0526469, 0.060602, 0.0726894,
 0.0917767, 0.126669, 0.207139, 0.309831, 0.274021, 0.216092, 0.193808,
 0.184408, 0.181092, 0.18076, 0.18219, 0.183675, 0.184513, 0.182912, 0.17743,
 0.167646, 0.155123, 0.142239, 0.13104, 0.122214, 0.115672, 0.110919, 0.10738,
 0.104594, 0.102232, 0.100085, 0.09803, 0.096016, 0.0940409, 0.0921421}
```

```
ListLogLinearPlot[Transpose[{logspace[-3, 0., 51], fwhms}],
 Joined → True,
 Axes → False,
 PlotRange → {{10^-3, 10^0}, {0, 0.35}},
 Frame → True,
 FrameTicks → {{Automatic, None}, {E0Ticks, None}},
 FrameLabel → {{"Emission Peak FWHM (eV)", None}, {"γ (eV)", None}},
 FrameStyle → Black,
 BaseStyle → Directive[FontSize → 18],
 Epilog → {LineStyle, Line[{{1, -0.1}, {1, 1}}]},
 AspectRatio → 1]
```

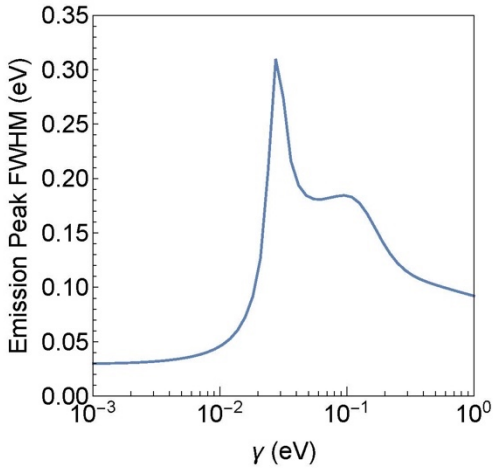

Sub-gap Emission Fraction

In[554]:=
```
SubGapRecomb[Spectrum_, Eg_, θi_, γ_, T_, α0L_, IQE_] := Block[{voc, sg, tot},
  voc = OpenCircuit[Spectrum, Eg, θi, γ, T, α0L, IQE, Eg * 0.6];
  sg =
   NIntegrate[b[En, T, voc] * EQE[Eg, En, θi, γ, voc, T, α0L, IQE], {En, Emin, Eg}];
  tot = NIntegrate[b[En, T, voc] * EQE[Eg, En, θi, γ, voc, T, α0L, IQE],
    {En, Emin, Emax}];
  sg / tot]
```

In[555]:=
```
sgr = SubGapRecomb[AM15Photonflux[En], eg, 1., #, Tcell, α0L, 1.] & /@
    logspace[-3., 1., 101.]; // Quiet
```

In[558]:=
```
ListLogLinearPlot[Transpose[{logspace[-3., 1., 101.], sgr}],
 Joined → True,
 PlotRange → {{10^-3, 10^0}, {0, 1.05}},
 Frame → True,
 FrameLabel → {{"PL_{E<E_g}/PL_{Tot}", None}, {"γ (eV)", None}},
 FrameTicks → {{VocTicks, None}, {E0Ticks, None}},
 FrameStyle → Black,
 BaseStyle → Directive[FontSize → 18],
 Epilog → {LineStyle, Line[{Log@{kB * Tcell, 10^-20}, Log@{kB * Tcell, 10^28}}]},
 AspectRatio → 1,
 ImageSize → 400,
 ImagePadding → {{70, 15}, {60, 10}}]
```

Out[558]=

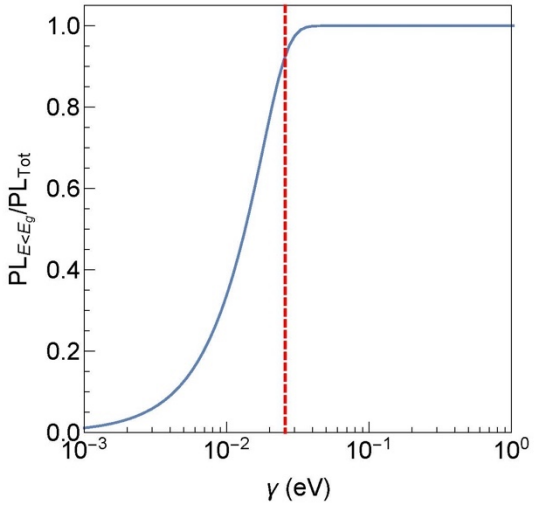

Effect of Urbach Parameter on J-V curves

In[560]:=
```
VBottTicks =
  Table[If[Mod[i * 10, 5] < 0.0001, {i, NumberForm[i, {2, 1}], {.025, 0}, Black},
    {i, "", {.0125, 0}, Black}], {i, 0, 1.5, 0.1}];
VTopTicks = Table[If[Mod[i * 10, 5] < 0.0001, {i, "", {.025, 0}, Black},
    {i, "", {.0125, 0}, Black}], {i, 0, 1.5, 0.1}];
JLTicks = Table[If[Mod[i, 10] < 0.0001, {i, i, {.025, 0}, Black},
    {i, "", {.0125, 0}, Black}], {i, 0, 50, 2}];
JRTicks = Table[If[Mod[i, 10] < 0.0001, {i, "", {.025, 0}, Black},
    {i, "", {.0125, 0}, Black}], {i, 0, 50, 2}];
```

In[564]:=
```
Plot[{-JSQ[1.5, V],
  -J[AM15Photonflux[En], 1.5, 1, 0.1 * kB * Tcell, V, Tcell, α0L, 1.],
  -J[AM15Photonflux[En], 1.5, 1, 0.2 * kB * Tcell, V, Tcell, α0L, 1.],
  -J[AM15Photonflux[En], 1.5, 1, 0.5 * kB * Tcell, V, Tcell, α0L, 1.],
  -J[AM15Photonflux[En], 1.5, 1, kB * Tcell, V, Tcell, α0L, 1.],
  -J[AM15Photonflux[En], 1.5, 1, 2 * kB * Tcell, V, Tcell, α0L, 1.],
  -J[AM15Photonflux[En], 1.5, 1, 3 * kB * Tcell, V, Tcell, α0L, 1.]}, {V, 0, 1.3},
 PlotPoints → 10,
 PlotRange → {{0, 1.5}, {-2, 50}},
 PlotStyle → kBTColors,
 Frame → True,
 FrameLabel → {{"J (mAcm^-2)", None}, {"V (V)", None}},
 FrameTicks → {{JLTicks, JRTicks}, {VBottTicks, VTopTicks}},
 FrameStyle → Black,
 BaseStyle → Directive[FontSize → 18],
 PlotLegends → Placed[LineLegend[kBTColors, {"S-Q", "0.1", "0.5", "1", "2", "3"},
    LegendFunction → frame, LegendLabel → "γ (k_B T_cell)", LegendMarkerSize → 15,
    LegendLayout → {"Column", 1}, Spacings → 0.1], Scaled[{0.2, 0.3}]],
 Epilog -> {Text[Style["E_g=1.5 eV", FontFamily → "Arial", FontSize → 20],
    Scaled[{0.775, 0.9}]]},
 AspectRatio → 1,
 ImageSize → 400,
 ImagePadding → {{60, 15}, {60, 10}}]
```

Out[564]=

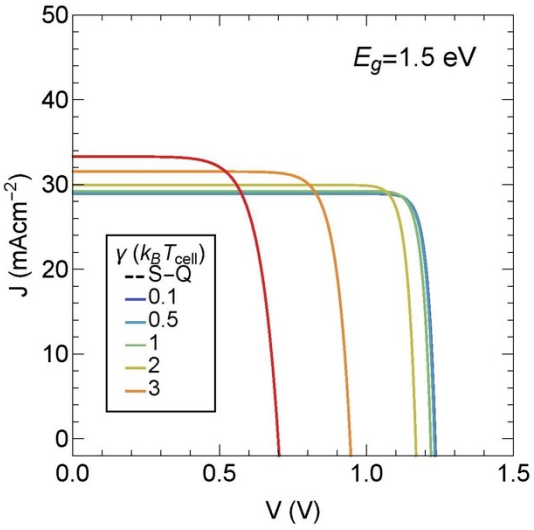

```
vocUrbPars =
 Table[OpenCircuit[AM15Photonflux[En], 1.5, 1, #, Tcell, α0L, 1, 1.5 * 0.6],
    {i, Length[UrbPars]}] & /@ UrbPars
```

```
{{1.23361, 1.23361, 1.23361, 1.23361, 1.23361},
 {1.2181, 1.2181, 1.2181, 1.2181, 1.2181},
 {1.16706, 1.16706, 1.16706, 1.16706, 1.16706},
 {0.943528, 0.943528, 0.943528, 0.943528, 0.943528},
 {0.698818, 0.698818, 0.698818, 0.698818, 0.698818}}
```

In[565]:=

```
FFEffect[Eg_] := Module[{indexEg, ffs},
  indexEg = FirstPosition[Egs, Eg];
  ffs =
   Flatten[Table[Abs[maxPow[[indexEg, i]] / (Voc[[indexEg, i]] * Jsc[[indexEg, i]])],
     {i, Length[Vmax]}]];

  ListLogLinearPlot[Transpose[{γs, ffs}],
   Joined → True,
   PlotRange → {{10^-3, 10}, {-0.05, 1}},
   Frame → True,
   FrameTicks → {{EQETicks, None}, {E0Ticks, None}},
   FrameLabel → {{"FF", None}, {"γ (eV)", None}},
   FrameStyle → Black,
   BaseStyle → Directive[FontSize → 18],
   Epilog → {LineStyle, kBTLine},
   AspectRatio → 1]]
```

In[566]:=
```
FFEffect[1.5]
```

Out[566]=

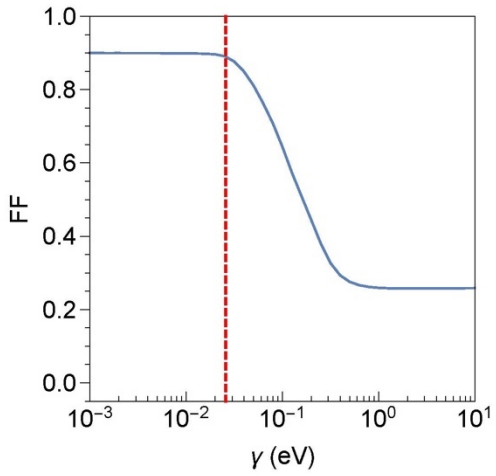

In[567]:=
```
maxPow[[index15, -1]] / (Voc[[index15, -1]] * Jsc[[index15, -1]])
```

Out[567]=
```
-0.258517
```

```
FFContour = ListContourPlot[Abs[maxPow / (Voc * Jsc)] * 100,
  DataRange → {{-3, 0}, {0.5, 2.5}},
  PlotRangePadding → None,
  Contours → 100,
  ContourStyle → None,
  Frame → True,
  FrameTicks → {{EgTicks, None}, {UrbTicks, None}},
  FrameStyle → Black,
  FrameLabel → {"γ (eV)", "Eg (eV)"},
  ColorFunction → "SolarColors",
  BaseStyle → Directive[Black, FontSize → 18],
  PlotLegends → BarLegend[{"SolarColors", {0, 100}}, LegendLabel → "Percent",
    LegendMarkerSize → 250, LabelStyle → Directive[FontSize → 14, Black]],
  PlotLabel → Style["FF", Black],
  ImageSize → 400,
  ImagePadding → {{70, 15}, {60, 10}}]
```

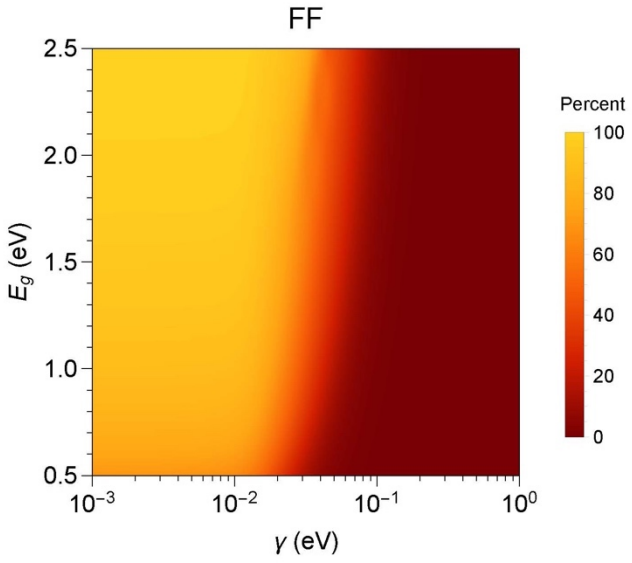

■ Effect in Weakly Absorbing Limit

In[570]:= `α0Ls = {0.01, 0.1, 0.3, 1, 10};`

In[571]:=
```
Plot[EQE[1.5, En, 1., 0.1 * kB * Tcell, 0., Tcell, #, 1.] & /@ α0Ls,
 {En, 0, 3}, Evaluated → True,
 PlotRange → {{0, 2.5}, {-0.05, 1.05}},
 PlotStyle → Table[ColorData["Rainbow"][i / Length[α0Ls]], {i, 1, Length[α0Ls]}],
 Frame → True,
 FrameLabel → {"Incident Photon Energy (eV)", "EQE"},
 FrameTicks → {{EQETicks, None}, {EgTicks, None}},
 FrameStyle → Black,
 BaseStyle → {FontSize → 16},
 PlotLegends → Placed[
   LineLegend[Table[ColorData["Rainbow"][i / Length[α0Ls]], {i, 1, Length[α0Ls]}],
    Table[ToString[α0Ls[[i]]], {i, Length[α0Ls]}], LegendLabel → "α0L",
    LegendFunction → frame, LegendLayout → "Column"], Scaled[{0.3, 0.5}]],
 Epilog → {Text[Style["γ=0.1 kBTcell", FontFamily → "Arial",
     FontSize → 20, FontWeight → Plain], Scaled[{0.275, 0.9}]]},
 ImageSize → 400,
 ImagePadding → {{75, 15}, {55, 10}},
 AspectRatio → 1]
```

Out[571]=

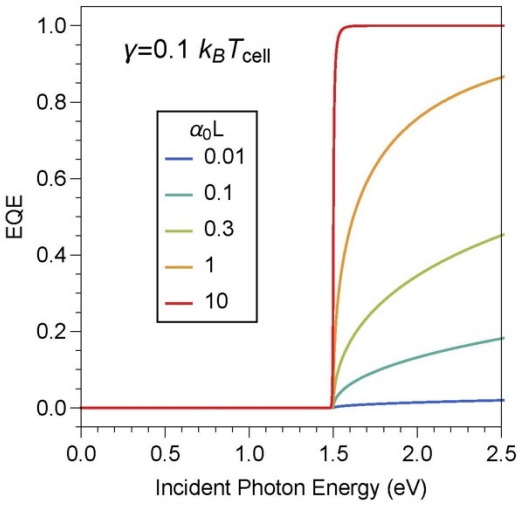

In[572]:=
```
Plot[EQE[1.5, En, 1., 1.2 * kB * Tcell, 0., Tcell, #, 1.] & /@ α0Ls,
 {En, 0, 3}, Evaluated → True,
 PlotRange → {{0, 2.5}, {-0.05, 1.05}},
 PlotStyle → Table[ColorData["Rainbow"][i / Length[α0Ls]], {i, 1, Length[α0Ls]}],
 Frame → True,
 FrameLabel → {None, "EQE"},
 FrameTicks → {{EQETicks, None}, {None, None}},
 FrameStyle → Black,
 BaseStyle → {FontSize → 16},
 PlotLegends → Placed[
   LineLegend[Table[ColorData["Rainbow"][i / Length[α0Ls]], {i, 1, Length[α0Ls]}],
    Table[ToString[α0Ls[[i]]], {i, Length[α0Ls]}], LegendLabel → "α0L",
    LegendFunction → frame, LegendLayout → "Column"], Scaled[{0.3, 0.5}]],
 Epilog → {Text[Style["γ=1.2 kBTcell", FontFamily → "Arial",
     FontSize → 20, FontWeight → Plain], Scaled[{0.275, 0.9}]]},
 ImageSize → 400,
 ImagePadding → {{75, 10}, {55, 10}},
 AspectRatio → 1]
```

Out[572]=

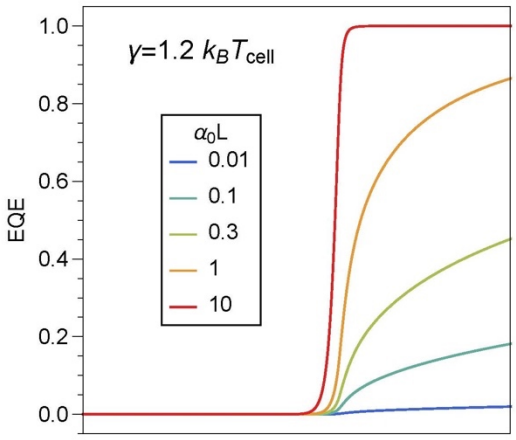

```
weakαJsc = Table[
   0.1 * q * AbsSolFlux[AM15Photonflux[En], 1.5, 1, γs[[j]], 0., Tcell, α0Ls[[i]], 1.],
   {i, Length[α0Ls]}, {j, Length[γs]}];
Export["/Users/Stefan/Documents/Caltech/Data/Calculations/Detailed Balance/Direct
    Gap_Band Edge Sharpness/Bandfilling/FOM/weakαJsc.dat", weakαJsc, "Data"];

weakαJ0 = Table[0.1 * q * R0[1.5, 1., γs[[j]], 0., Tcell, α0Ls[[i]], 1.],
   {i, Length[α0Ls]}, {j, Length[γs]}];
Export["/Users/Stefan/Documents/Caltech/Data/Calculations/Detailed Balance/Direct
    Gap_Band Edge Sharpness/Bandfilling/FOM/weakαJ0.dat", weakαJ0, "Data"];
```

In[630]:=
```
weakαVoc = Table[OpenCircuit[AM15Photonflux[En], 1.5, 1., γs[[j]],
    Tcell, α0Ls[[i]], 1., 1.5 * 0.6], {i, Length[α0Ls]}, {j, Length[γs]}];
Export["/Users/Stefan/Documents/Caltech/Data/Calculations/Detailed Balance/Direct
    Gap_Band Edge Sharpness/Bandfilling/FOM/weakαVoc.dat", weakαVoc, "Data"];

weakαVmax = Flatten[Reap[Do[
      vguess = 1.5 - 0.4;
      Sow[Flatten[Reap[Do[
            Sow[
             output = Mpp[AM15Photonflux[En],
               1.5, 1., γs[[j]], Tcell, α0Ls[[i]], 1., vguess], j];
            vguess = V /. output[[2]], {j, 1, Length[γs]}]][[2, All]], 1], i],
      {i, 1, Length[α0Ls]}]][[2, All]], 1];
Export[
  "/Users/Stefan/Documents/Caltech/Data/Calculations/Detailed Balance/Direct
    Gap_Band Edge Sharpness/Bandfilling/FOM/weakαVmax.dat", weakαVmax, "Data"];

weakαEff = Table[100 * Abs[weakαVmax[[i, j]][[1]]] / SolarConstantAM,
   {i, Length[α0Ls]}, {j, Length[γs]}];
Export["/Users/Stefan/Documents/Caltech/Data/Calculations/Detailed Balance/Direct
    Gap_Band Edge Sharpness/Bandfilling/FOM/weakαEff.dat", weakαEff, "Data"];
```

In[603]:=
```
weakαEff = Import[
   "/Users/Stefan/Documents/Caltech/Data/Calculations/Detailed Balance/Direct
     Gap_Band Edge Sharpness/Bandfilling/FOM/weakαEff.dat"];
```

In[636]:=
```
ListLogLinearPlot[Table[Transpose[{γs, weakαVoc[[i]]}], {i, Length[α0Ls]}],
 Joined → True,
 PlotRange → {{10^-3, 10^1}, {-0.05, 1.45}},
 PlotStyle → Table[ColorData["Rainbow"][i / Length[α0Ls]], {i, 1, Length[α0Ls]}],
 Frame → True,
 FrameLabel → {{"Voc (V)", None}, {"γ (eV)", None}},
 FrameTicks → {{VocTicks, None}, {E0Ticks, None}},
 FrameStyle → Black,
```

```
  BaseStyle → Directive[FontSize → 18],
  PlotLegends → Placed[
    LineLegend[Table[ColorData["Rainbow"][i / Length[α0Ls]], {i, 1, Length[α0Ls]}],
     Table[ToString[α0Ls[[i]]], {i, Length[α0Ls]}], LegendLabel → "α₀L",
     LegendFunction → frame, LegendLayout → "Column"], Scaled[{0.75, 0.475}]],
  Epilog → {{LineStyle, kBTLine}},
  AspectRatio → 1,
  ImageSize → 400,
  ImagePadding → {{85, 15}, {60, 10}}]

ListLogLogPlot[Table[Transpose[{γs, weakαJ0[[i]]}], {i, Length[α0Ls]}],
  Joined → True,
  PlotRange → {{10^-3, 10}, {10^-21, 10^6}},
  PlotStyle → Table[ColorData["Rainbow"][i / Length[α0Ls]], {i, 1, Length[α0Ls]}],
  Frame → True,
  FrameLabel → {{"J₀ (mA/cm²)", None}, {"γ (eV)", None}},
  FrameTicks → {{J0LogTicks, None}, {E0Ticks, None}},
  FrameStyle → Black,
  BaseStyle → Directive[FontSize → 18],
  PlotLegends → Placed[
    LineLegend[Table[ColorData["Rainbow"][i / Length[α0Ls]], {i, 1, Length[α0Ls]}],
     Table[ToString[α0Ls[[i]]], {i, Length[α0Ls]}], LegendLabel → "α₀L",
     LegendFunction → frame, LegendLayout → "Column"], Scaled[{0.725, 0.475}]],
  Epilog → {{LineStyle, kBTLogLine}, {Text[Style["Eg=1.5 eV",
       FontFamily → "Arial", FontSize → 20], Scaled[{0.225, 0.9}]]}},
  AspectRatio → 1,
  ImageSize → 400,
  ImagePadding → {{85, 15}, {60, 10}}]

ListLogLinearPlot[Table[Transpose[{γs, weakαJsc[[i]]}], {i, Length[α0Ls]}],
  Joined → True,
  PlotRange → {{10^-3, 10}, {-5, 120}},
  PlotStyle → Table[ColorData["Rainbow"][i / Length[α0Ls]], {i, 1, Length[α0Ls]}],
  Frame → True,
  FrameLabel → {{"Jsc (mA/cm²)", None}, {"γ (eV)", None}},
  FrameTicks → {{JscTicks, None}, {E0Ticks, None}},
  FrameStyle → Black,
  BaseStyle → Directive[FontSize → 18],
  Epilog → {{LineStyle, kBTLine}},
  AspectRatio → 1,
  ImageSize → 400,
  ImagePadding → {{85, 15}, {60, 10}}]
```

```
ListLogLinearPlot[Table[Transpose[{γs, weakαEff[[i]]}], {i, Length[α0Ls]}],
 Joined → True,
 PlotRange → {{10^-3, 10}, {-1.25, 35}},
 PlotStyle → Table[ColorData["Rainbow"][i / Length[α0Ls]], {i, 1, Length[α0Ls]}],
 Frame → True,
 FrameLabel → {{"η (%)", None}, {"γ (eV)", None}},
 FrameTicks → {{EffTicks, None}, {E0Ticks, None}},
 FrameStyle → Black,
 BaseStyle → Directive[FontSize → 18],
 Epilog → {{LineStyle, kBTLine}},
 AspectRatio → 1,
 ImageSize → 400,
 ImagePadding → {{85, 15}, {60, 10}}]
```

Out[636]=

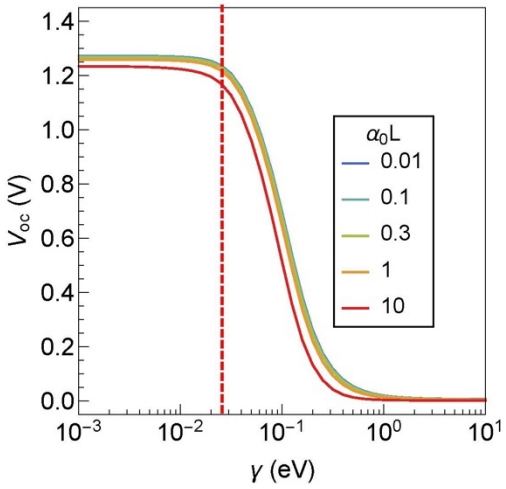

Out[637]=

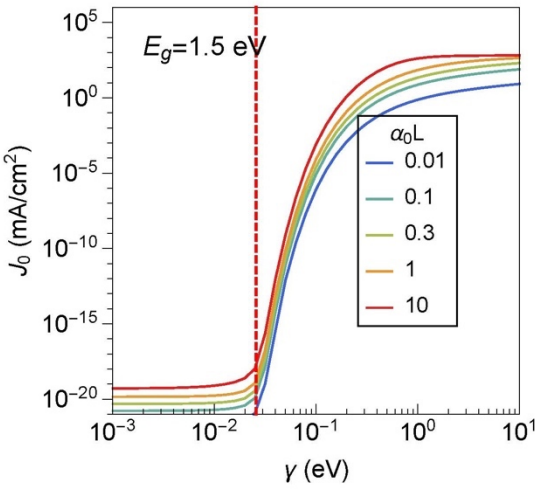

Out[638]=

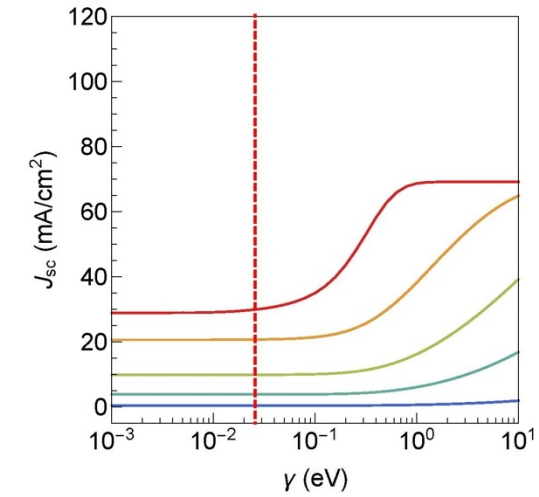

Out[639]=

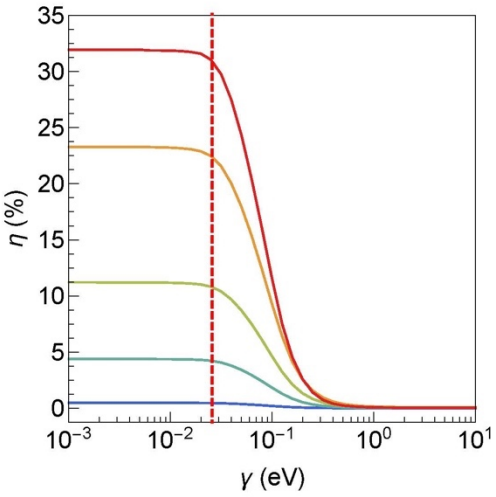

■ Effect with imperfect sub-gap radiative efficiency

In[591]:=
```
iqe[Eg_, En_, NumericQ?ℊ_] := Piecewise[{{ℊ, En < Eg}, {1, En >= Eg}}]
ℊs = Table[10.^-i, {i, 0, 8, 2}]
```

Out[592]= $\{1., 0.01, 0.0001, 1.\times10^{-6}, 1.\times10^{-8}\}$

```
iqeJsc = Table[0.1 * q * AbsSolFlux[AM15Photonflux[En], 1.5, 1, ɣs[[j]], 0.,
      Tcell, α0L, iqe[1.5, En, ℊs[[i]]]], {i, Length[ℊs]}, {j, Length[ɣs]}];
Export["/Users/Stefan/Documents/Caltech/Data/Calculations/Detailed Balance/Direct
    Gap_Band Edge Sharpness/Bandfilling/FOM/iqeJsc.dat", iqeJsc, "Data"];

iqeJ0 = Table[0.1 * q * R0[1.5, 1., ɣs[[j]], 0., Tcell, α0L, iqe[1.5, En, ℊs[[i]]]],
   {i, Length[ℊs]}, {j, Length[ɣs]}];
Export["/Users/Stefan/Documents/Caltech/Data/Calculations/Detailed Balance/Direct
    Gap_Band Edge Sharpness/Bandfilling/FOM/iqeJ0.dat", iqeJ0, "Data"];

iqeVoc = Table[OpenCircuit[AM15Photonflux[En], 1.5, 1., ɣs[[j]], Tcell, α0L,
    iqe[1.5, En, ℊs[[i]]], 1.5 * 0.6], {i, Length[ℊs]}, {j, Length[ɣs]}];
Export["/Users/Stefan/Documents/Caltech/Data/Calculations/Detailed Balance/Direct
    Gap_Band Edge Sharpness/Bandfilling/FOM/iqeVoc.dat", iqeVoc, "Data"];
```

```
iqeVmax = Flatten[Reap[Do[
      vguess = 1.5 - 0.4;
      Sow[Flatten[Reap[Do[
           Sow[
            output = Mpp[AM15Photonflux[En], 1.5, 1.,
              γs[[j]], Tcell, α0L, iqe[1.5, En, ℰs[[i]]], vguess], j];
           vguess = V /. output[[2]], {j, 1, Length[γs]}]][[2, All]], 1], i],
      {i, 1, Length[ℰs]}]][[2, All]], 1];
Export[
  "/Users/Stefan/Documents/Caltech/Data/Calculations/Detailed Balance/Direct
    Gap_Band Edge Sharpness/Bandfilling/FOM/iqeVmax.dat", iqeVmax, "Data"];

iqeEff = Table[100 * Abs[iqeVmax[[i, j]][[1]]] / SolarConstantAM,
   {i, Length[ℰs]}, {j, Length[γs]}];
Export["/Users/Stefan/Documents/Caltech/Data/Calculations/Detailed Balance/Direct
    Gap_Band Edge Sharpness/Bandfilling/FOM/iqeEff.dat", iqeEff, "Data"];
```

In[588]:=
```
iqeJsc = Import[
   "/Users/Stefan/Documents/Caltech/Data/Calculations/Detailed Balance/Direct
     Gap_Band Edge Sharpness/Bandfilling/FOM/iqeJsc.dat"];
iqeVoc = Import["/Users/Stefan/Documents/Caltech/Data/Calculations/Detailed
     Balance/Direct Gap_Band Edge Sharpness/Bandfilling/FOM/iqeVoc.dat"];
iqeEff = Import["/Users/Stefan/Documents/Caltech/Data/Calculations/Detailed
     Balance/Direct Gap_Band Edge Sharpness/Bandfilling/FOM/iqeEff.dat"];
```

In[626]:=
```
ListLogLinearPlot[Table[Transpose[{γs, iqeVoc[[i]]}],
  {i, Length[ℰs]}],
 Joined → True,
 PlotRange → {{10^-3, 10^1}, {-0.05, 1.45}},
 PlotStyle → Table[ColorData["Rainbow"][i / Length[ℰs]], {i, 1, Length[ℰs]}],
 Frame → True,
 FrameLabel → {{"V_oc (V)", None}, {"γ (eV)", None}},
 FrameTicks → {{VocTicks, None}, {E0Ticks, None}},
 FrameStyle → Black,
 BaseStyle → Directive[FontSize → 18],
 PlotLegends →
  Placed[LineLegend[Table[ColorData["Rainbow"][i / Length[ℰs]], {i, 1, Length[ℰs]}],
    {"1", "10^-2", "10^-4", "10^-6", "10^-8"}, LegendLabel → "IQE",
    LegendFunction → frame, LegendLayout → "Column"], Scaled[{0.2, 0.475}]],
 Epilog → {{LineStyle, kBTLine}},
 AspectRatio → 1,
 ImageSize → 400,
 ImagePadding → {{85, 15}, {60, 10}}]

ListLogLogPlot[Table[Transpose[{γs, iqeJ0[[i]]}], {i, Length[ℰs]}],
```

```
  Joined → True,
  PlotRange → {{10^-3, 10}, {10^-21, 10^6}},
  PlotStyle → Table[ColorData["Rainbow"][i / Length[γs]], {i, 1, Length[γs]}],
  Frame → True,
  FrameLabel → {{"J₀ (mA/cm²)", None}, {"γ (eV)", None}},
  FrameTicks → {{J0LogTicks, None}, {E0Ticks, None}},
  FrameStyle → Black,
  BaseStyle → Directive[FontSize → 18],
  PlotLegends →
   Placed[LineLegend[Table[ColorData["Rainbow"][i / Length[γs]], {i, 1, Length[γs]}],
     {"1", "10⁻²", "10⁻⁴", "10⁻⁶", "10⁻⁸"}, LegendLabel → "IQE",
     LegendFunction → frame, LegendLayout → "Column"], Scaled[{0.225, 0.475}]],
  Epilog → {{LineStyle, kBTLogLine}, {Text[Style["E_g=1.5 eV",
       FontFamily → "Arial", FontSize → 20], Scaled[{0.225, 0.9}]]}},
  AspectRatio → 1,
  ImageSize → 400,
  ImagePadding → {{85, 15}, {60, 10}}]

ListLogLinearPlot[Table[Transpose[{γs, iqeJsc[[i]]}], {i, Length[γs]}],
  Joined → True,
  PlotRange → {{10^-3, 10}, {-5, 120}},
  PlotStyle → Table[ColorData["Rainbow"][i / Length[γs]], {i, 1, Length[γs]}],
  Frame → True,
  FrameLabel → {{"J_sc (mA/cm²)", None}, {"γ (eV)", None}},
  FrameTicks → {{JscTicks, None}, {E0Ticks, None}},
  FrameStyle → Black,
  BaseStyle → Directive[FontSize → 18],
  Epilog → {{LineStyle, kBTLine}},
  AspectRatio → 1,
  ImageSize → 400,
  ImagePadding → {{85, 15}, {60, 10}}]

ListLogLinearPlot[Table[Transpose[{γs, iqeEff[[i]]}], {i, Length[γs]}],
  Joined → True,
  PlotRange → {{10^-3, 10}, {-1.25, 35}},
  PlotStyle → Table[ColorData["Rainbow"][i / Length[γs]], {i, 1, Length[γs]}],
  Frame → True,
  FrameLabel → {{"η (%)", None}, {"γ (eV)", None}},
  FrameTicks → {{EffTicks, None}, {E0Ticks, None}},
  FrameStyle → Black,
  BaseStyle → Directive[FontSize → 18],
  Epilog → {{LineStyle, kBTLine}},
  AspectRatio → 1,
```

```
ImageSize → 400,
ImagePadding → {{85, 15}, {60, 10}}]
```

Out[626]=

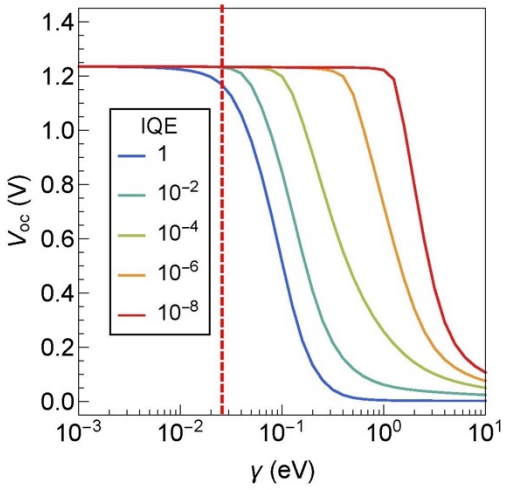

... **Part**: Part specification iqeJ0⟦1⟧ is longer than depth of object.

... **Transpose**: The first two levels of {{0.001, 0.00125893, 0.00158489, 0.00199526, 0.00251189, 0.00316228, 0.00398107, 0.00501187, 0.00630957, 0.00794328, 0.01, ≪19≫, 1., 1.25893, 1.58489, 1.99526, 2.51189, 3.16228, 3.98107, 5.01187, 6.30957, 7.94328, 10.}, iqeJ0⟦1⟧} cannot be transposed.

... **Part**: Part specification iqeJ0⟦2⟧ is longer than depth of object.

... **Transpose**: The first two levels of {{0.001, 0.00125893, 0.00158489, 0.00199526, 0.00251189, 0.00316228, 0.00398107, 0.00501187, 0.00630957, 0.00794328, 0.01, ≪19≫, 1., 1.25893, 1.58489, 1.99526, 2.51189, 3.16228, 3.98107, 5.01187, 6.30957, 7.94328, 10.}, iqeJ0⟦2⟧} cannot be transposed.

... **Part**: Part specification iqeJ0⟦3⟧ is longer than depth of object.

... **General**: Further output of Part::partd will be suppressed during this calculation.

... **Transpose**: The first two levels of {{0.001, 0.00125893, 0.00158489, 0.00199526, 0.00251189, 0.00316228, 0.00398107, 0.00501187, 0.00630957, 0.00794328, 0.01, ≪19≫, 1., 1.25893, 1.58489, 1.99526, 2.51189, 3.16228, 3.98107, 5.01187, 6.30957, 7.94328, 10.}, iqeJ0⟦3⟧} cannot be transposed.

... **General**: Further output of Transpose::nmtx will be suppressed during this calculation.

Out[627]=

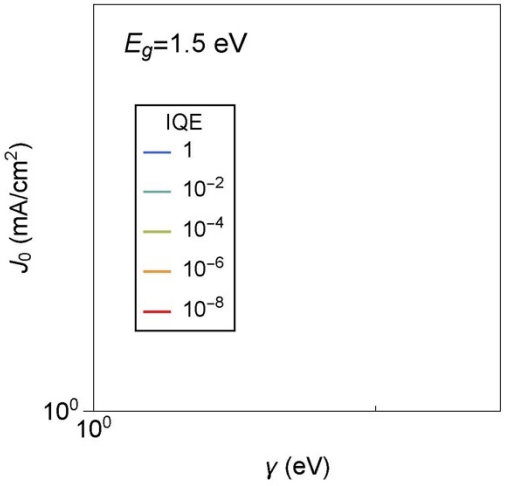

Out[628]=

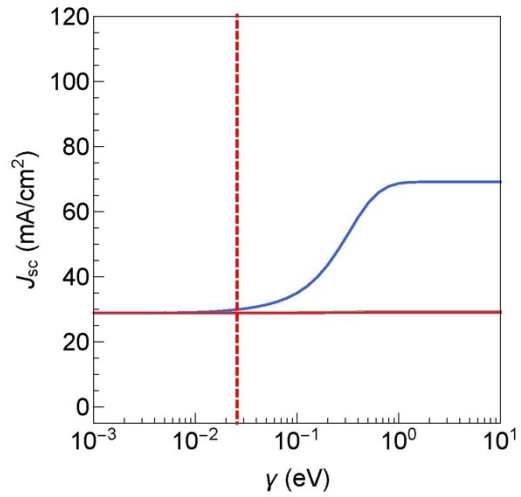

Out[629]=

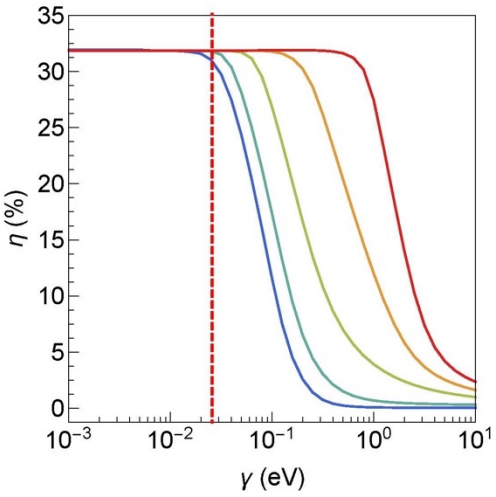

Appendix B
Floating Zone Crystal Growth

B.1 Zone Melting Background

Zone melting or zone refining, is a crystal growth technique developed by William Pfann at Bell Labs for the purification of germanium for use in transistors (*217*). Unlike in a normal freezing process (Fig. B1, top) where solidification occurs as the solid-liquid interface advances, in zone melting (Fig. B2, top) a molten zone is passed along the length of a solid. As the zone advances, new, previously unmelted solid is melted at the leading solid-liquid interface joining the molten zone and leaving behind a purer, recrystallized solid at the trailing solid-liquid interface.

The distribution of solute (impurities) in a solid is largely governed by its distribution coefficient k, the ratio of solute in a material's solid phase to that in its liquid phase. $k < 1$, indicates that an impurity will result in the lowering of the freezing temperature of the liquid phase of a material. This is typical for most materials. In a normal freezing process, where we have assumed that there is no diffusion in the solid and the solute concentration is uniform in the liquid, the concentration C of solute in the solid after a fraction g depends on the distribution coefficient as follows (*217*):

$$\frac{C}{C_0} = k(1-g)^{k-1} \tag{1}$$

where, C_0 is the original solute concentration in the liquid. This results in a non-uniform distribution of solutes for a solid that has undergone normal freezing (Fig. B.1, bottom). The concentration of solute across the length of the solid is much different in a zone melting process. A single pass of the zone melting process results in (*217*):

$$\frac{C}{C_0} = 1 - (1 - k)e^{-kx/l} \quad (2)$$

where, l is the length of the molten zone. As can be seen from Fig. B.2, for $k < 1$, this results in a region of purification and a region of uniform impurity distribution in the solid. As the molten zone proceeds along the rod, it freezes out (at $x = 0$) a concentration kC_0 but melts unpure material at the leading edge of the molten zone, thus increasing the concentration of impurities in the zone and subsequently solidifies out higher concentrations. This process of purification continues (at an ever-decreasing rate) until the concentration of impurities in the molten zone becomes C_0/k and the solid freezing out has the same impurity concentration as that being melted. After this point is reached the impurity concentration remains constant in the solid until the end of the road ($x = L-l$) is reached and normal freezing occurs. Using multiple passes of the molten zone the degree of purification and size of the purification region can be greatly extended.

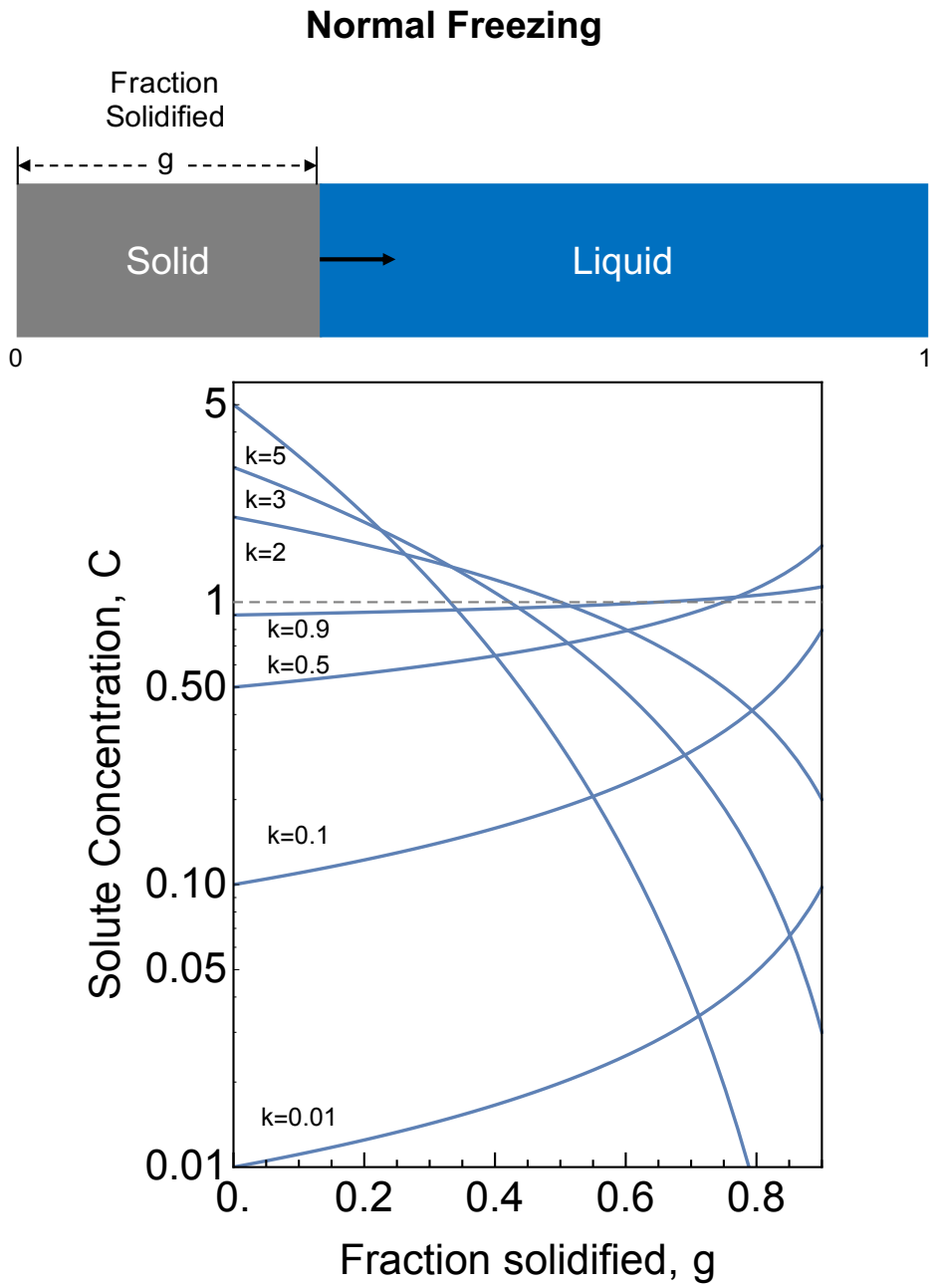

Figure B.1 (Top) Diagram of the typical solidification process, known as normal freezing. The distribution of solute (impurities) in the solid is controlled by the distribution coefficient *k*, the rate of the advance of the solid-liquid interface, and the mixing in the liquid. (Bottom) The solute concentration for a normal freezing process as a function of the fraction of solidification for different distribution coefficients *k*.

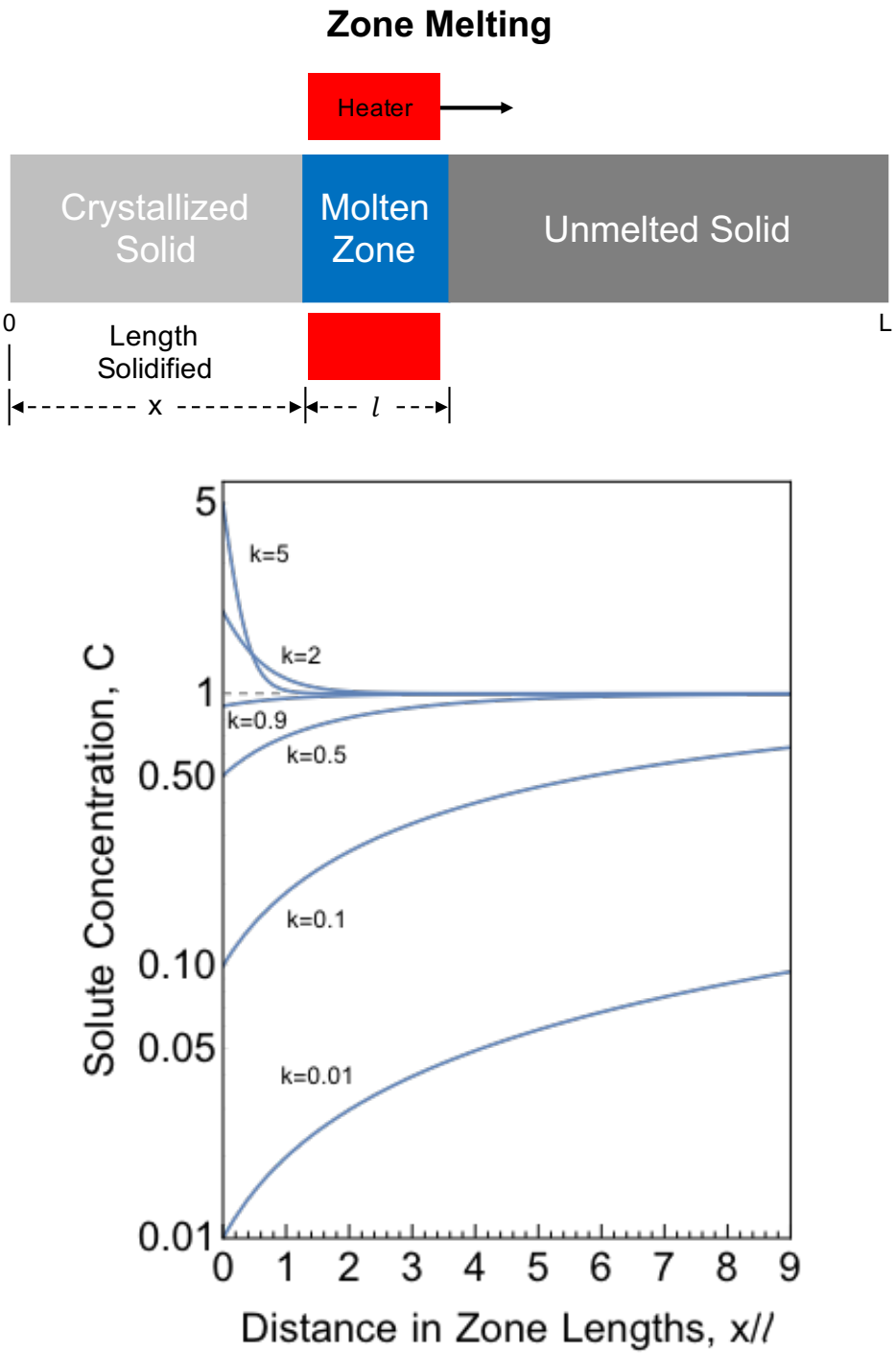

Figure B.2 (Top) Diagram of the zone melting process, in which a molten zone is passed along the length of a solid. (Bottom) The solute concentration for the zone melting process as a function of the fraction of solidification for different distribution coefficients *k*. Zone melting results in regions of purification and uniform solute distribution.

B.2 The Floating Zone Method

The floating zone method is a technique that developed out of traditional zone melting for materials that are reactive or effective solvents when molten. The floating zone technique was originally developed for the growth and purification of single crystalline silicon and is still widely used for the growth of high-quality silicon in industry today. As the name implies, the floating-zone technique, as depicted in Fig. B.3, employs a molten zone suspended between two vertical rods that is held in place by only its own surface tension.

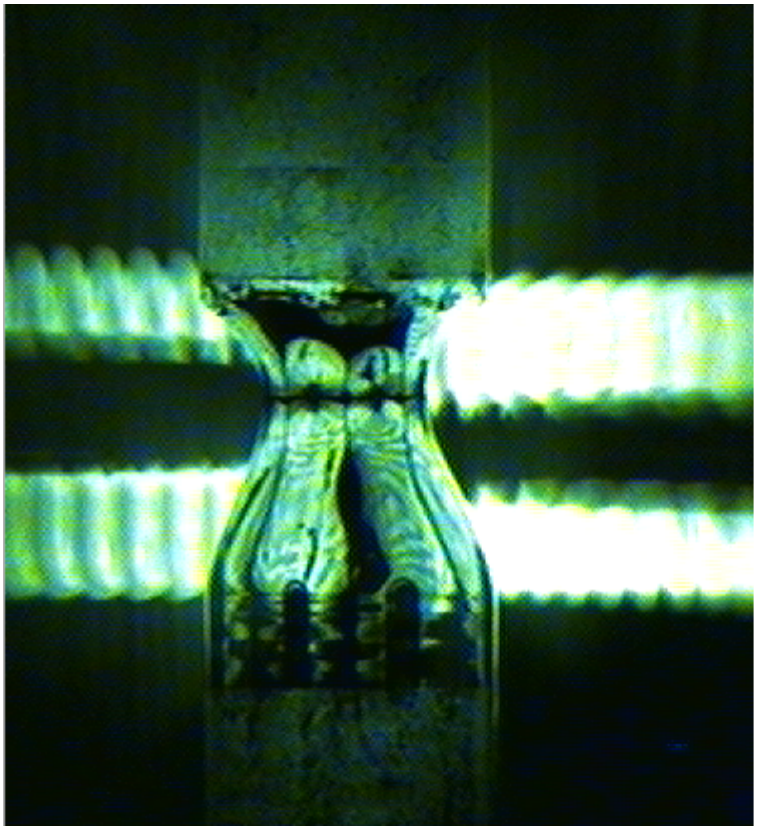

Figure B.3 Image of a floating zone during growth of single crystalline Cu_2O. The bright regions in the background are the halogen lamps which serve as the heat source.

A typical floating zone apparatus is depicted in Fig. B.4. As in regular zone melting, the solid sample to be refined is generally suspended in a quartz tube which allows for control of the growth atmosphere and viewing the crystal during growth. The heating sources for the

floating zone technique vary but induction, electron beam, and optical heaters are the most common. Research-grade floating zone growth furnaces are now available commercially from Crystal Systems Inc.

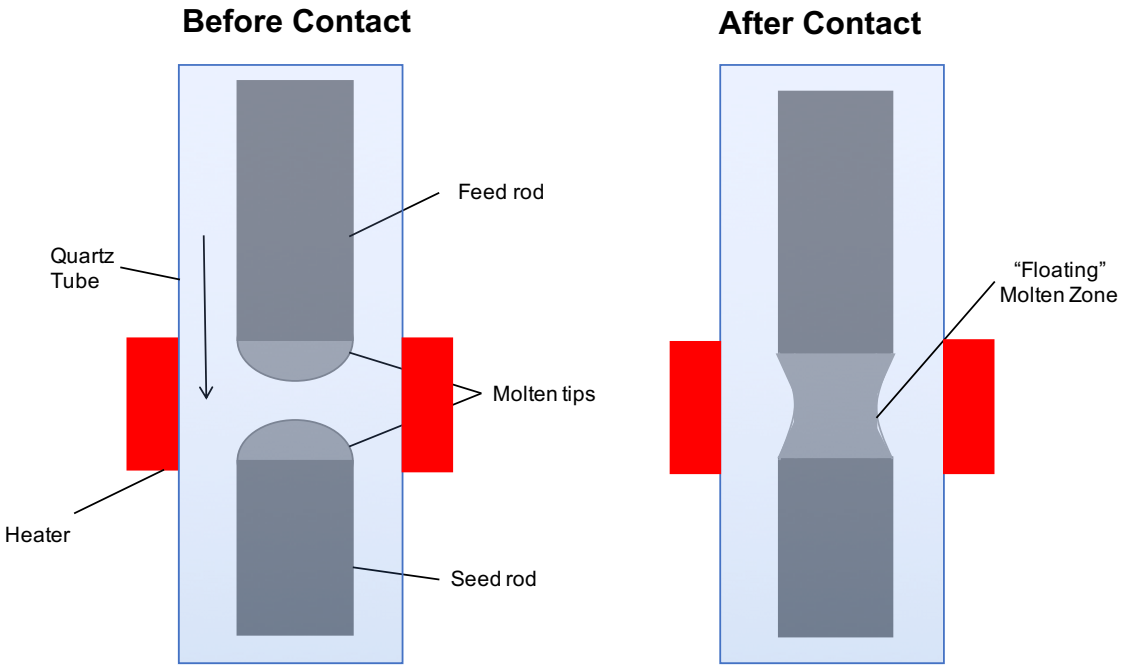

Figure B.4 Typical floating zone setup before (left) and after (right) the feed and seed rods are brought into contact

B.2.1 General Growth Process Overview

The floating zone growth process begins with two solid cylindrical rods: a so-called seed rod and a feed rod. Ideally, the seed rod is single crystalline in nature, providing a "seed" for the crystal orientation of the new growth. If a single crystalline seed is not available, a polycrystalline rod may be used as the seed. A polycrystalline rod can effectively function as a single crystalline seed if a single grain is isolated (e.g. by sharpening the rod to a point) or if the grain size is large enough that the seed rod only "sees" one grain. The feed rod plays the role of the unmelted solid in Fig. B.2, providing the material feedstock for the refined

crystal. In most cases the feed rod is considerably longer than the seed rod, which need only provide the growth template, so that a sufficiently large crystal can be grown.

At the beginning of growth, the feed rod and seed rod are separated. The rods are then brought into close proximity and heat is applied so that the tips of the rods become molten (Fig. B.4, left) and typically made to rotate to improve heating uniformity. Once molten, the rods are slowly moved together until the molten tips touch and a molten zone is formed (Fig. B.4, right). The molten zone is then moved up the length of the feed rod at the selected growth rate generally slowly (~1-20 mm/hr) to allow sufficient time for recrystallization. When the end of the feed rod is reached the feed rod is separated from the newly grown crystal, unless multiple passes are to be made.

B.3 The Caltech System

B.3.1 The Floating Zone Furnace

The floating zone furnace that was used in this work is a Crystal Systems Inc. Model FZ-T-4000-H-VII-VPO-PC housed in the Molecular Materials Research Center at the Beckman Institute at Caltech. The furnace (Fig. B.5) is an optical floating zone furnace which employs four 1 kW halogen lamps as the heating source. The lamps are focused by 4 ellipsoidal mirrors (Fig. 4B) to produce a heating zone on the order of ~1-3 mm. The optical heating system is capable of reaching temperatures up to 2000 ºC, although measurement of the actual temperature of the molten zone is very difficult as the lamps operate on a percentage of full power rating system.

In this setup, the seed rod is affixed to a sample post and the feed rod is hung from a malleable hook, which allows for adjustment in the alignment of the rods. Growth is accomplished by moving the lamp assembly up along the length of the feed rod and be monitored by a CCD camera that is part of the lamp assembly. The growth atmosphere is controlled by gas housing and can be configured to be air, O_2, Ar, or vacuum at a variety of pressures.

The manual provided by Crystal Systems Inc. is thorough and provides step by step instructions for operating the furnace and is available on the MMRC website. Tips for successful growth are provided later in this appendix.

Figure B.5 The optical floating zone furnace from Crystal Systems Inc. Adapted from (*218*).

B.3.2 Growth of Feed Rods

In order to ensure a stable molten zone, an appropriate sized and shape feed rod must be fabricated. The stability and shapes of the molten zone have been treated theoretically (*219, 220*) and verified experimentally. While there is no theoretical upper limit to the diameter of the feed rod, large diameters generally are more difficult to stabilize because of the large heat requirement necessary to melt the entire cross section. A general rule of thumb is to use feed and seed rods with the same diameter. The Crystal Systems Inc. system supports 0.5 cm and 1 cm seed rods, and thus those sized feed rods were also targeted.

Feed rods were grown in the Bridgeman vertical tube furnace (Fig. B.6). The vertical tube furnace includes a crane assembly that can be programmed to ensure the length of the rod is evenly heated in the furnace's primary heating zone. Operation instructions for the vertical tube furnace and crane assembly are available on the MMRC website.

Figure B.6 The Bridgeman vertical tube furnace and crane assembly (*218*).

Rods were suspended from the crane via a hook. To attach the sample rod to the furnace hook, a hole was (carefully) drilled into the rod and a metallic wire was fed through the hole and tied to make a support ring. It is important to note that the wire must be mechanically

stable enough to support the sample rod during the feed rod growth and floating zone processes. Metals that oxidize and become brittle may not be suitable for this purpose and therefore, platinum is generally because of its high temperature stability and resistance to oxidation.

B.3.3 Tips for Floating Zone Growth

Floating zone growth, and crystal growth in general, is somewhat of a black magic. Although the theory of the floating zone growth technique is well established, there is no way to predict a priori the growth parameters necessary to create a stable molten zone for a given material. As such, the floating zone process is often time consuming and requires lots of trial and error (read frustrating). I have provided tips below that should ease some of the pain.

0. **Be patient –** Read the above. Crystal growth is hard and floating zone growth is slow even when it works. But if things go work

1. **Read the literature –** The crystal growth community is large and it has been around a long time. Someone has probably tried to grow what you are trying to grow before or at least something similar and although their system was likely different their growth parameters can be used as a guide.

2. **Be clean –** Impurities are bad and can have a major effect on the outcome of your growth. Clean the quartz tube when growing a new material and have dedicated tools (tweezers, beakers, etc.) for each material system.

3. **Alignment of Feed and Seed Rods –** In alignment of the feed and seed rod during the growth is one of, if not the most, important factors that dictates the stability of the molten zone. If the feed and seed rods are misaligned along the rotational (vertical) axis then it is very hard to stabilize the zone and uneven heating may occur. Spend the time to carefully align the feed and seed rods before growth begins and adjust the feed rod accordingly during growth if it becomes off-axis.

4. **Correctly Size the Seed (and Feed) Rod –** As mentioned above, misalignment along the vertical axis can lead to an unstable molten zone. Because the Crystal Systems Inc. float zone furnace uses seed rod sample holders of a fixed diameter (0.5 cm and 1 cm), attempting to use a seed rod of a larger or smaller size will result in the seed rods rotation axis differing from that of the sample holder and consequently the feed rod (see Fig B.7). Maintaining a stable zone during growth under such conditions is extremely difficult.

5. **Ensure the Seed and Feed Rods are Cylindrical –** This helps with alignment. See tips 3 and 4, above.

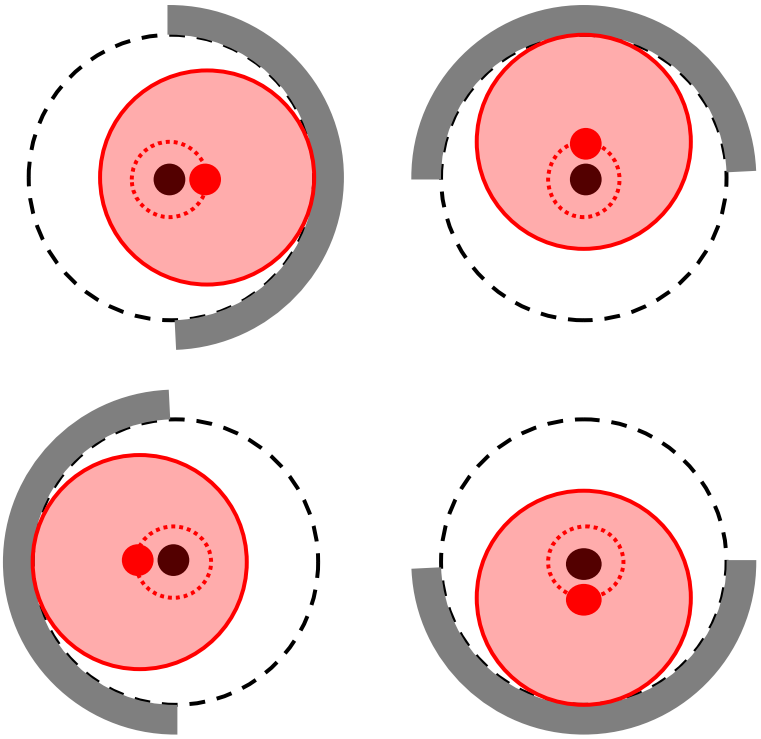

Figure B.7 Top view of a seed rod sample holder (gray) with an improperly sized seed rod (red) during different stages of rotation. The sample holder is sized for a sample of the size traced out by the black dashed circle. The center of a seed rod this size is collinear with the rotational axis (black dot) of the sample holder and feed rod. The improperly sized seed rod, however, has a rotational axis (red dot) different than that of the sample holder. Thus, rotation of the sample holder leads to the center of the seed rod tracing a circle around the axis of rotation of the float zone assembly (black dot). This leads to a "wobbly", unstable molten zone.

Appendix C

Electrochemical Methods for Catalysis

C.1 Experimental Setup and Catalyst Testing

With assistance from a large-gauge needle guide, the lead of each electrode was inserted through a rubber septum, and the electrode was placed in a 25 mL, 14/20, 4-necked, round bottom flask (Chemglass, Vineland, NJ). The flask was filled with 15 mL of 1.0 M H_2SO_4 or 5.0 M NaCl at pH 2.0 (adjusted using HCl and measured using a calibrated Thermo Scientific Orion 3 Star pH probe). A saturated calomel electrode (SCE; CH Instruments, Austin, TX) reference electrode was washed and placed in the solution.

For OER and CER experiments, O_2(g) or Cl_2(g) was flowed through a bubbler that contained either 1.0 M H_2SO_4 or 5.0 M NaCl at pH 2.0, respectively, and then into the reactor using a Teflon tube that extended ~1 cm below the surface of the electrolyte. To ensure that the reactor was pressurized to 1 atm, gas could freely escape through an identical Teflon tube that went from the reactor flask to the back of the fume hood. Prior to data collection, the gas was bubbled through the solution for > 1 min. The counter electrode was a 0.5 mm diameter coiled platinum wire (Sigma Aldrich, 99.9%). All purging and experiments were performed under continuous stirring. The distance between the working electrode and reference electrode was 1.0 cm.

To measure overpotential, the following experiments were run on a Bio-Logic (Seyssinet-Pariset, France) potentiostat/galvanostat model VSP-300 with EIS capability:

1) Open circuit voltage for 30 sec.

2) Two cyclic voltammograms (CVs) to clean the electrode, scanning from 1.0 to 1.45 vs SCE for RuO_2 and IrO_2 in 1.0 M H_2SO_4 (prior to OER); from 1.2 to 1.8 vs SCE for FTO in

1.0 M H_2SO_4 (prior to OER); from 1.1 to 1.2 V vs SCE for RuO_2 and IrO_2 in 5.0 M NaCl at pH 2.0 (prior to CER); and from 1.1 to 2.0 V for FTO in 5.0 M NaCl at pH 2.0 (prior to CER).

3) Hold the potential at open circuit for 30 sec.

4) Two CVs to measure the overpotential, scanning from 1.0 to 2.5 vs SCE for RuO_2 and IrO_2 in 1.0 M H_2SO_4 (OER), 1.5 to 3.5 for FTO in 1.0 M H_2SO_4 (OER), 1.1 to 1.35 V vs SCE for RuO_2 and IrO_2 in 5.0M NaCl at pH 2.0 (CER), and for 1.1 to 3.0 V FTO in 5.0 M NaCl at pH 2.0 (CER).

All CVs were conducted at a 5 mV/sec scan rate and were corrected for solution resistance as described below, unless otherwise stated. The system resistance was also measured for each sample prior to each experiment. For each electrode, at least 4 replicates were tested.

C.2 Calculating Overpotentials

For the OER, standard conditions were assumed, and the thermodynamic potential of 1230 mV vs RHE was used to determine the OER overpotential at 10 mA/cm^2.

For the CER, the activity for Cl^- was estimated to be 4.36 using the Pitzer model (*221*) and the fugacity of 1 atm Cl_2 was taken to be 0.07267 (*222*). Using these values, a thermodynamic potential of 1288 mV vs NHE was calculated from the Nernst equation.

C.2.1 Electronegativity and Overpotential Calculations

Group electronegativities were calculated for oxygen evolution catalysts from this work and for the catalysts compared in Seh *et al.* and plotted against overpotentials at 1 mA/cm^2_{AFMSA} for each catalystLike in Seh *et al*., for catalysts with no AFM data, if they were prepared on flat substrates (e.g. (100) silicon), a roughness factor of 1 was assumed(*179*). In the case of catalysts with undefined elemental ratios, XPS data on the oxidation state was used to

estimate elemental composition, and then fractional compositions were rounded to the nearest half. If there was no XPS data, Pourbaix diagrams were consulted and the predominant species at the relevant potentials were used for group electronegativity calculations. In most cases, assumptions were the same as the assumptions made for active site composition in Seh *et al*. For layered catalysts (e.g. $IrO_x/SrIrO_3$) the geometric mean of all the atoms in the overlayer and underlayer was used as the group electronegativity of the material. Overpotentials at 1 mA/cm^2_{AFMSA} was either taken from Seh *et al.* or from this work. Most overpotential data presented in Fig. 5.6 was collected in a basic electrolyte (blue circles), for catalysts tested in acidic electrolytes, red circles indicate values from this work measured in 1 M H_2SO_4 and the orange circle indicates the catalyst tested in 0.5 M H_2SO_4 from Seitz *et al.* (*209*). Electronegativity, like other theoretical constructs that are related to bond strength, demonstrates a nice volcano type correlation with activity for the oxygen evolution reaction (*209*).

C.3 Calculating Faradaic Efficiency

For the OER, the faradaic efficiency of the electrodes was measured as previously described using a pneumatic trough (*223*). A graduated cylinder was filled with electrolyte and placed upside down in a bath of electrolyte. The working electrode was inserted to a height > 1 cm into the cylinder. The reference electrode was placed near the cylinder and the counter electrode was placed > 5 cm away from the cylinder. The cylinder was closed to the bulk solution except for the pour spout of the cylinder, hence ions were allowed to pass freely. The electrode was biased to pass 10 mA of current at 10 mA/cm^2_{geo}, and the resulting oxygen bubbles were collected in the cylinder for 1 h. The resulting head-space volume was measured and compared using the ideal gas law to the expected total charge passed. Similar to other studies, 105-115% faradaic efficiencies were measured (Table S2). The excess is attributed to electrolyte sticking to the cylinder walls, narrowing the diameter of the cylinder.

For the CER, electrodes were operated at a constant current of 1mA/cm^2_{geo} for 10 min in 15 mL of 5.0 M NaCl at pH 2.0, which, given 100% faradaic efficiency, should yield 22.08 ppm Cl_2(g) in our experimental configuration. Immediately after the reaction, one milliliter of electrolyte was transferred to a 25 mL beaker and chlorine was measured by titrating excess potassium iodide with a starch indicator using 0.50 mN $Na_2S_2O_3$ (*224*). Greater than 90% faradaic efficiency was measured for samples with 40-60 ALD cycles of TiO_2 and greater than 95% faradaic efficiency was measured for samples with fewer than 40 ALD cycles of TiO_2 (Table B.1).

	OER			**CER**		
TiO_2 Cycle Number	**IrO_2**	**RuO_2**	**FTO**	**IrO_2**	**RuO_2**	**FTO**
0	108%	122%	114%	101%	95%	97%
1			86%	96%	99%	102%
3	120%	122%	97%	99%	96%	96%
6	120%	107%	103%	101%	96%	98%
10	114%	122%	114%	96%	99%	96%
15		114%				
20	117%	122%	114%	104%	95%	98%
25			114%			
30	120%	114%	114%			
40	108%	114%	114%	95%	91%	91%
50	103%	114%				
60	120%	114%	103%	91%	95%	113%
100	114%	107%	114%	92%	91%	15%

Table C.1 Faradaic efficiencies for the OER and CER

C.4 Determination of Solution and System Resistance

The solution resistance was estimated using electrochemical impedance spectroscopy on a coiled Pt wire working electrode and Pt wire counter electrode system. The wire coil was 3

mm in diameter to simulate the working electrode and was placed 1 cm from the SCE reference electrode to simulate the distance between working and reference electrode. Measurements were taken in 5.0 M NaCl at pH 2.0 under 1 atm Cl_2 (CER) or in 1.0 M H_2SO_4 under 1 atm O_2 (OER). No correction was performed for the resistance of the Pt electrodes, due to the low resistivity (< 0.0001 Ω/cm) of Pt. For 5.0 M NaCl at pH 2.0, a solution resistance of 3.45 ± 0.02 Ω was measured. For 1.0 M H_2SO_4, a solution resistance of 1.91 ± 0.02 Ω was measured. These values were used to correct the electrodes for the IR drop. No correction was made for the electrode resistivity, as it is an intrinsic electrode property. Typical corrections from solution resistance were ~1.4 mV and ~0.3 mV for the OER at 10 mA/cm^2_{geo} and the CER at 1 mA/cm^2_{geo} respectively.

The system resistance was also measured as described above, but instead of Pt wire TiO_2 coated IrO_2, RuO_2, and FTO electrodes were used as the working electrodes. The measured solution resistance was a lower bound for the system resistances (Fig. B.1). Data was not corrected for system resistance because this is an intrinsic property of the electrode. Neither the magnitude nor the shape of the change in overpotential or specific activity shown in Fig. 1 were explained by the magnitude or the pattern of the system resistivity which would have resulted in corrections of < 10 mV for the OER and < 3 mV for the CER.

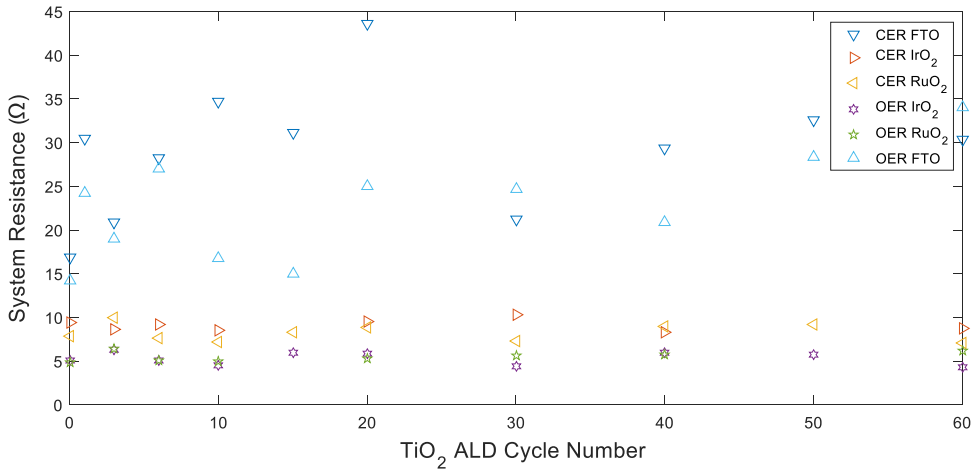

Figure C.1 System resistance as measured by electrochemical impedance spectroscopy in 5.0 M NaCl at pH 2.0 (CER) and 1.0 M H_2SO_4 (OER). The resistivity of the system did

not appreciably change between 0 and 60 ALD cycles of TiO_2. For IrO_2 based electrodes, the average system resistance was 9.1 ± 0.6 Ω for CER condtions and 5.4 ± 0.6 Ω for OER conditions. For RuO_2 based electrodes, the average system resistance was 8.0 ± 1.0 Ω for CER condtions and as 5.3 ± 0.7 Ω for OER conditions. For FTO-based electrodes, the average system resistance was 30 ± 7 Ω for CER condtions and 23 ± 6 Ω for OER conditions.

C.5 Determination of the Double Layer Capacitance and Electrochemically Active Surface Area

In order to make a fair comparison between values herein and in the benchmarking study, the double-layer capacitance (C_d) was measured and linearly related to the electrochemically active surface area (ECSA) by Eq. B1 in the same manner as described in the benchmarking literature (*201*). For the OER, briefly, C_d was measured by plotting the non-Faradaic current vs scan rate and extracting the slope of the linear best-fit line. An initial CV was conducted to identify the non-faradaic region, which in general was a 50 mV window around the open-circuit potential (E_{oc}). Scans were then conducted at scan rates of 0.005, 0.01, 0.025, 0.05, 0.1, 0.2, 0.4, and 0.8 V/s and 100% of the current was collected for each step (Fig. B.2). Between potential sweeps, the working electrode was held at E_{oc} for 30 sec. The non-faradaic current at E_{oc} for each scan rate was plotted versus scan rate (Fig. B.3). The average of the absolute value of the positive and negative slopes of the linear fits of the data was taken to be C_d. Because of the narrow potential window between oxidation of Cl^- and reduction of Cl_2, C_d was determined from electrochemical impedience spectroscpy at E_{oc}. Nyquist plots were fit to a resistor in series with a parallel combination of a capacitor and a shunt resistor (Fig. B.3). The resulting capacitance was taken as the C_d. In both cases C_d values were used as described previously to calculate the ECSA (*201*). Briefly, C_d was divided by the specific capacitance (C_s) of an average metal substrate in an acidic electrolyte (Fig. B.4, Eq. B.1). Few literature values exist for C_s in concentrated acidic brine, and C_s does not change appreciably with ionic strength for H_2SO_4. Both the CER and OER electrolytes were acidic, so the same value of C_s was used to calculate the ECSA for both the CER and OER:

$$ECSA = C_d/C_s \quad (1)$$

where C_S is specific capacitance (i.e., 0.035 mF/cm^2 for 1.0 M H_2SO_4 and 5.0 M NaCl, pH 2.0). To ensure mutual comparability, we chose the same C_s value that was used in the benchmarking literature for the OER (*201*).

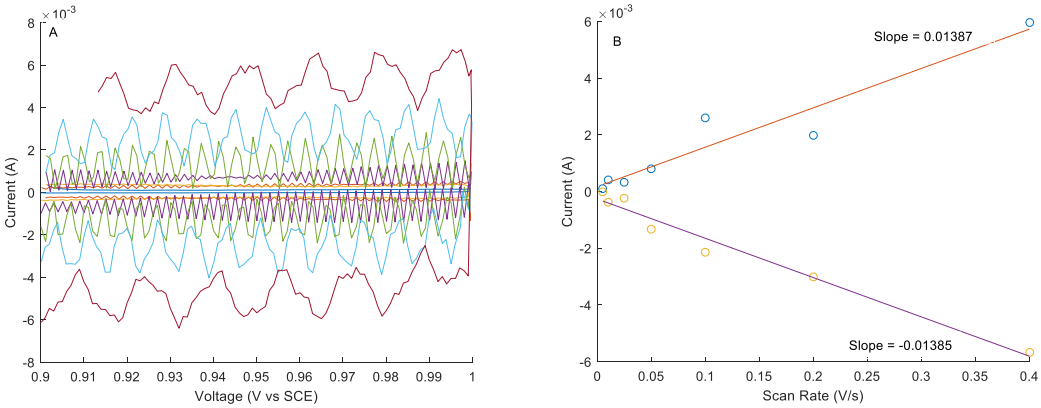

Figure C.2 Example double-layer capicitance measurements for determining ECSA for IrO_2 with 10 cycles of ALD TiO_2 in 1.0 M H_2SO_4. (Left) Cyclic voltamogramms in the non-Faradaic region at 0.005, 0.01, 0.025, 0.05, 0.1, 0.2, 04, and 0.8 V/s. (Right) Cathodic (yellow disks) and anodic (blue disks) charging currents measured at 0.95 V vs SCE plotted as a function of scan rate.

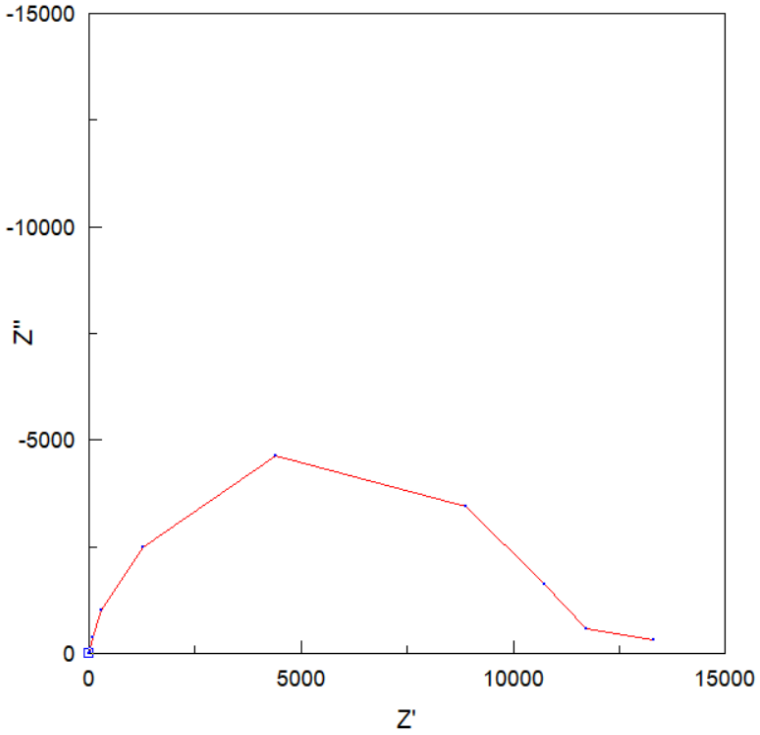

Figure C.3 Example impedence spectroscopy for IrO_2 with 0 cycles of ALD TiO_2 in 5.0 M NaCl pH 2.0 at E_{oc}. These data were fit to a resistor in series with a parallel combination of a capacitor and a shunt resistor. The resulting capacitance was taken as the C_d which in this case was was 3.24×10^{-6} F.

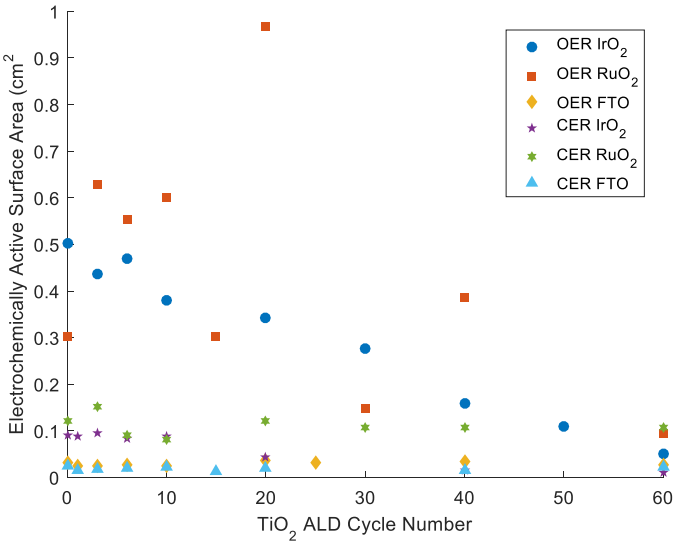

Figure C.4 ECSA for IrO_2, RuO_2, and FTO based catalysts in 1.0 M H_2SO_4 and 5.0 M NaCl, pH 2.0. All catalysts presented here had a geometric surface area of 0.13 cm^2, yielding electrochemical roughness factors between 0.1 and 6.0.

C.6 Calculating Specific Activities using ECSA and Surface Area Measured by AFM

As discussed in detail in prevous reports, reporting overpotential data relative to geometric current density can be misleading because geometric overpotentials can be influenced both by the roughness and the intrinsic activty of the catalyst (*179, 209*). Specific activities (Fig. 5.5) were calculated as previously described, by normalizing the current from cyclic voltamagrams to the electrochemically active surface area (*201*). For RuO_2 and IrO_2 based catalysts, specific activities were calculated at 350 mV overpotential for the OER, and at 150 mV overpotential for the CER. For FTO, specific activities were calculated at 900 mV overpotential for the OER, and at 700 mV vs NHE for the CER.

Alteratively, specific activities were calculated by normalizing the measured current density to the topographic surface area measured by atomic force microscopy (AFM; see Section

5.2.3.1) for direct comparison with catalysts reported by Seitz et al (*209*). Roughness factors for these calculations are reported in Table 5.1.

C.7 Determination of E_{ZC} by Electrochemical Impedance Spectroscopy

To ensure high capacitance values, 5.0 M $NaNO_3$ at pH 2.0 was prepared by dissolving $NaNO_3$ (J.T. Baker, Center Valley, PA, 99.6%, used as received) in 900 mL of water (18 MΩ cm, Millipore, Billerica, MA), adjusting the pH using HNO_3 (Sigma Aldrich, ≥ 60%, used as received), and diluting with water to 1 L. Working electrodes were prepared as described above. A working electrode, an SCE reference electrode (CH instruments), a coiled platinum wire counter electrode (Sigma Aldrich), and 20 mL of $NaNO_3$ solution were added to a 25 mL 4 neck 14/20 round bottom flask reactor. The reactor was gently bubbled with N_2 for at least 15 min before experiments, as well as during experiments. The impedance was measured using a Bio-Logic potentiostat/galvanostat model VSP-300 with EIS capability. All studies were performed at 25 ± 2 °C. Impedance spectra were recorded in the frequency range of 1 MHz to 10 mHz, with a modulation amplitude of 5 mV. An initial potential range of 1.1 to 0 V vs SCE, with a step size of 25 mV, was performed to identify the E_{ZC} region. A narrower potential range (typically ± 200 mV around the apparent E_{ZC}) was then used to measure the E_{ZC} value.

EIS data were fit as described previously, using *ZView* software, to an R_s-(R_p-C) circuit, where R_s is solution resistance at high frequencies, C is capacitor that represents double-layer capacitance in mid-range frequencies, and R_p is charge transfer resistance at low frequencies (Figs. S5 and S6) (*225*).

As previously reported, for FTO, IrO_2, and RuO_2 the capacitance values extracted from impedance spectroscopy are expected to approximate a traditional double layer capacitance (C_{DL}) to first order (*226, 227*). For samples with partial, semi-continuous and continuous TiO_2 coatings (Fig. 5.3-5.5), the TiO_2 layers are so thin for reasonably active catalysts (<

1.95 nm or 30 ALD cycles of TiO_2), the TiO_2 is assumed to be fully carrier-depleted within the potentials in question, so the changes in C_{DL} measured by impedance may be used to approximate a traditional E_{ZC}.

To confirm this assumption, Mott-Schottky analysis of the capacitance data was performed for the various samples. For an equivalent circuit comprising a series resistor combined with a parallel combination of a capacitor (C) and a shunt resistance, the inverse of the square of the capacitance (Farads) taken from the fit of the full frequency range on the nyquist plots was plotted against the potential with respect to NHE, E_{NHE}. For the low-cycle numbers of ALD TiO_2 on the substrates, a local maximum was observed, corresponding to the local minimum of Q vs $E_{NHE,}$ and thus the E_{ZC}. However, for samples in which 100 or 1000 cycles of ALD TiO_2 were deposited, corresponding to ~6.5 and ~65 nm respectively, a linear plot from Q^{-2} vs E_{NHE} was obtained. These plots were analyzed through application of the Mott-Schottky equation (Eq. B2), where ε_0 is the permittivity of free space, ε is the specific permittivity of TiO_2, A is the area of the electrode, q is the (unsigned) charge on an electron, N_d is the dopant density, V_{fb} is the flat band potential, k_b is the Boltzmann constant, T is temperature, and V is the applied potential, and C is the capacitance.

$$\frac{1}{C^2} = \frac{2}{\varepsilon\varepsilon_0 A^2 q N_d}\left(V - V_{fb} - \frac{k_b T}{q}\right) \qquad (2)$$

From the 500 and 1000 TiO_2 ALD cycle samples, a value of N_d = (8.1 ± 4.2) X 10^{19} cm^{-3} was found, and the flat-band potential for the TiO_2, V_{fb}, was calculated to be 282 ± 15 mV positive of NHE. From these parameters, in conjunction with Eq. B3 and at an applied potential of 0.25 V vs NHE (the lowest E_{ZC} value), the TiO_2 in question would have a depletion width of 7.3 ± 1.4 nm, which is substantially higher than the actual thickness of TiO_2 present in any of the catalytically relevant samples analyzed here (< 60 TiO_2 ALD cycles, or less than 3.9 nm).

$$W = \sqrt{\frac{2\epsilon\epsilon_0 V_{bi}}{q N_d}} \qquad (3)$$

Within the framework of this analysis, the TiO_2 film deposited on the substrates is under full depletion throughout the course of these experiments, and the capacitive effects from this film may therefore be ignored when the potential of zero charge is calculated by impedance spectroscopy.

Because E_{ZC} is believed to be a fundamental property of a material, changing the electrolyte may change the absolute value of the E_{ZC}, but should not change the trend in the values of materials measured in the same electrolyte (*212*).

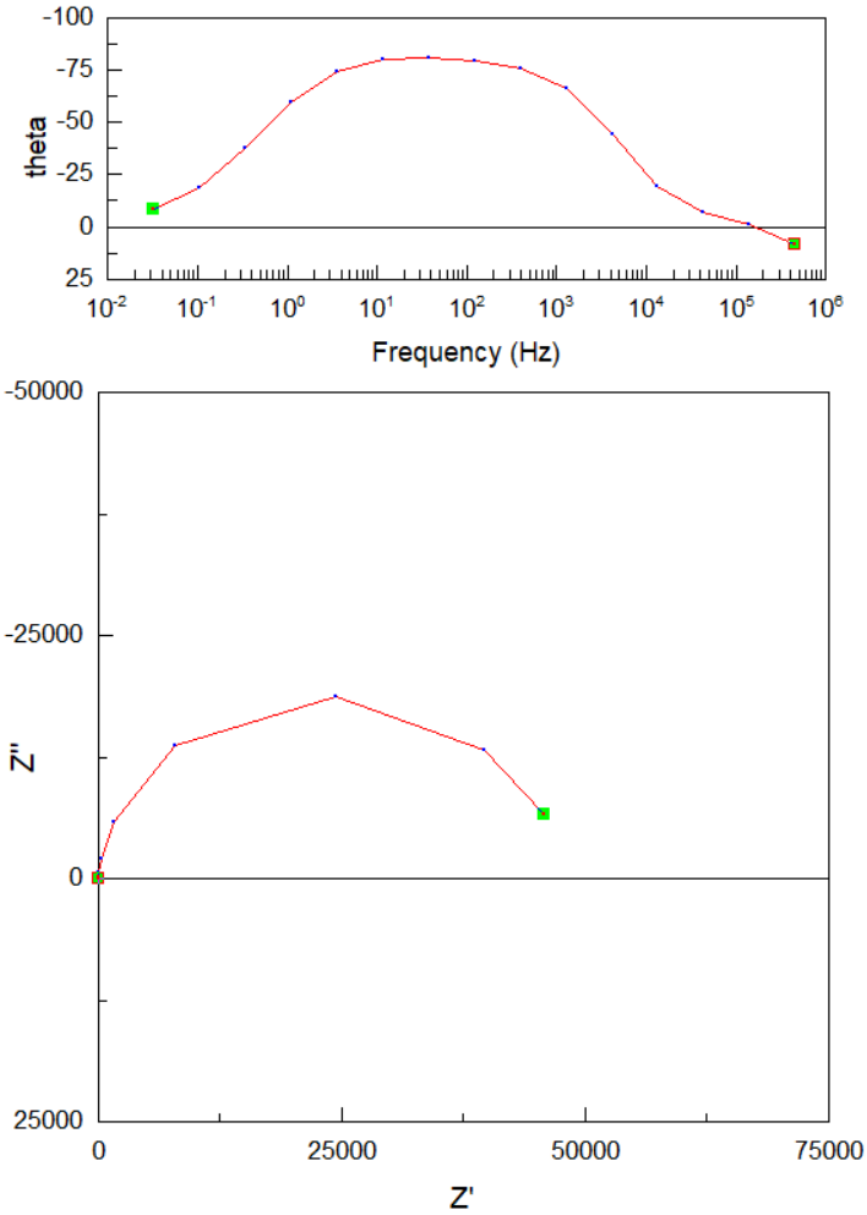

Figure C.5 Sample Bode (above) and Nyquist (below) plots of electrochemical impedence spectroscopy data of IrO_2 coated with 10 ALD cycles of TiO_2. The Bode plot shows the frequency of the alternating current signal (Hz) versus the phase shift of the impedance response (degrees). The Nyquist plot shows the real (*Z*') and imaginary (*Z*") components of the impedance response to the alternating current signal. Data presented in the figure were collected at 105 mV vs SCE in 5.0 M $NaNO_3$ at pH 2.0. The resulting equivelent circuit [R_s-(R_p-*C*)] fit of these data yielded a capacitance of 5.8×10^{-6} F.

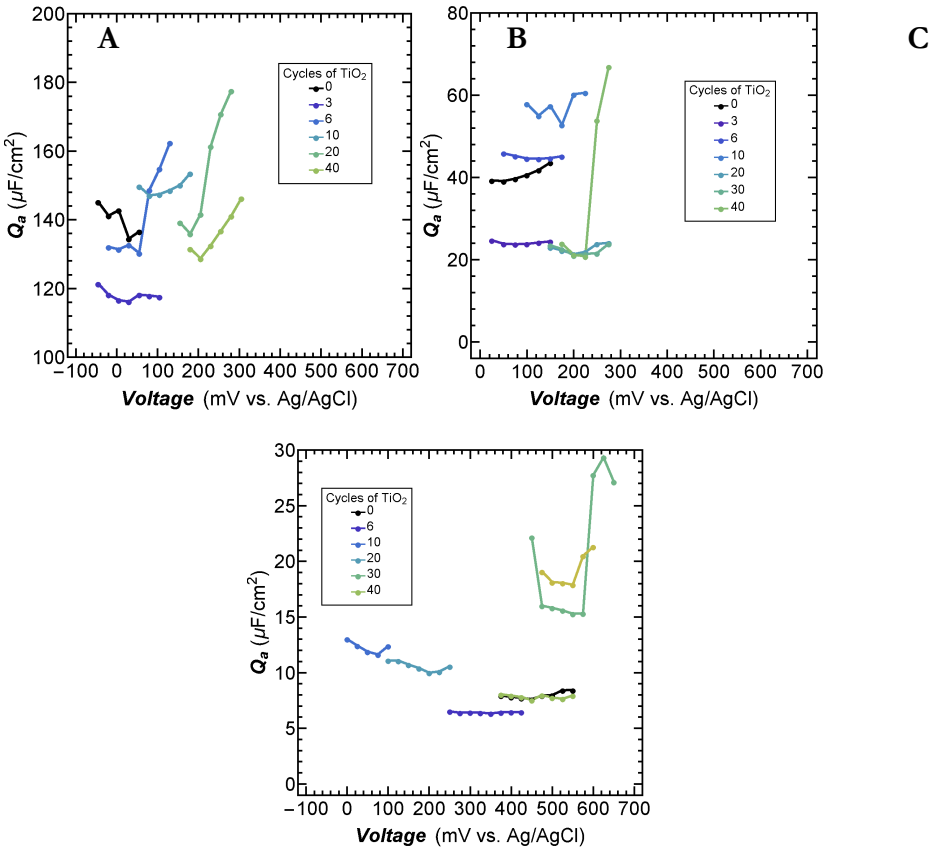

Figure C.6 Electrochemical impedance spectroscopy of (A) IrO_2, (B) RuO_2, (C) and FTO coated with various ALD cycles of TiO_2 at 25 mV intervals in 5.0 M $NaNO_3$ at pH 2.0. The resulting Nyquist plots were modeled as R_s-(C-R_p) circuits. The calculated capacitance values (dots) for each sample (set of dots) are shown here. The minimum value of each curve represents the E_{ZC}. The magnitude of the capacitance represents the surface area of the sample.

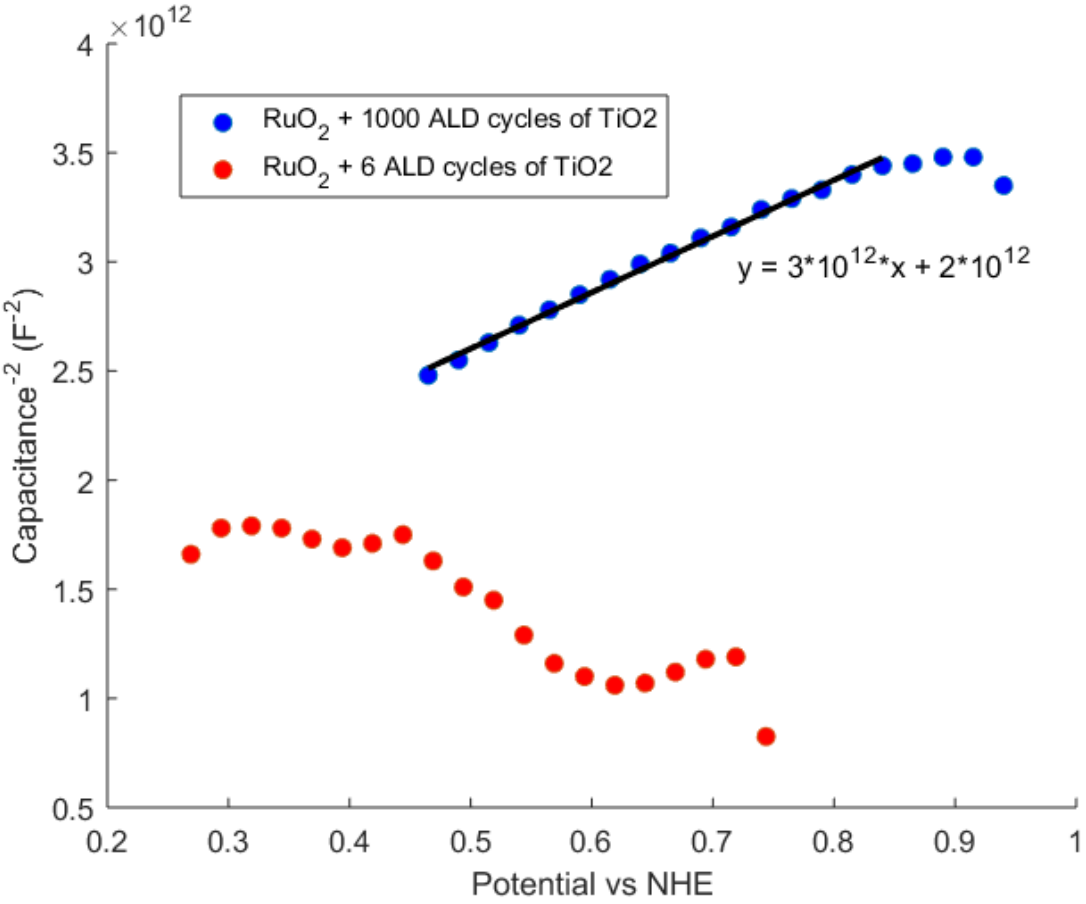

Figure C.7 Sample Mott-Schottky (E vs $1/C^2$) plots of RuO_2 with 0 (red), 1000 (blue) ALD TiO_2 cycles. The fit, using a geometric surface area of 7.1 X 10^{-6} m^2, yielded N_d = of 5.4 X 10^{19} cm^{-3}.

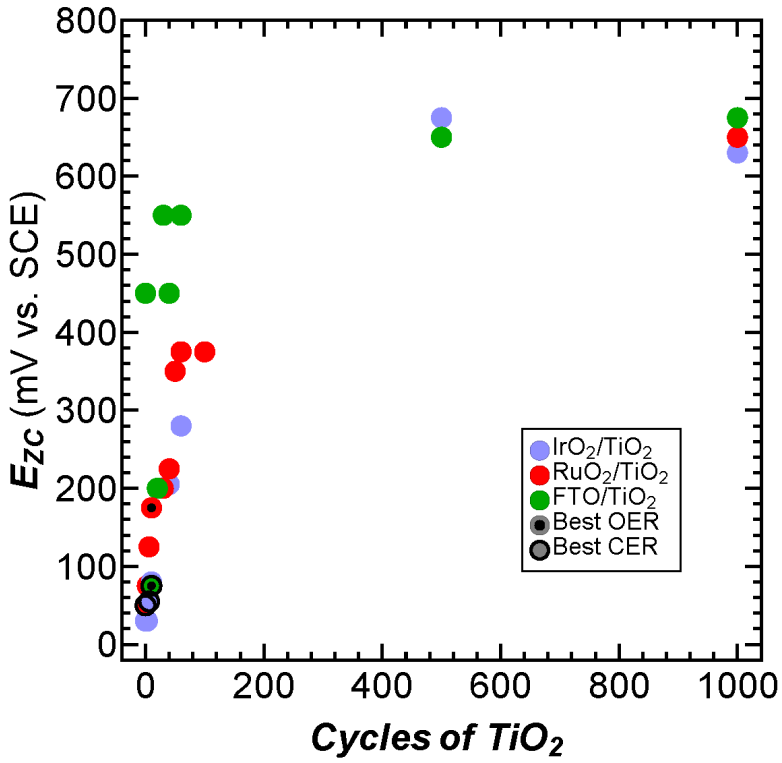

Figure C.8 Potential of zero charge as a function of TiO_2 cycle number for IrO_2, RuO_2, and FTO electrocatalysts. Black dots and disks with black borders indicate the catalysts with the highest specific activity for each substrate for the OER and CER, respectively.

For thick (>100 cycles) ALD TiO_2 films, the E_{ZC} values converged, indicating that all surfaces were electronically similar, bulk TiO_2. For The CER, the most active catalysts had E_{ZC} values of ~55, ~50, and ~75 mV vs SCE (IrO_2 + 3 ALD TiO_2 cycles, RuO_2 + 0 ALD TiO_2 cycles, and FTO + 10 ALD TiO_2 cycles respectively) and for the OER the optimal E_{ZC} was ~80, ~175, and ~75 mV vs SCE (IrO_2 + 10 ALD TiO_2 cycles, RuO_2 + 10 ALD TiO_2 cycles, and FTO + 10 ALD TiO_2 cycles respectively) (Figs. B.7 and B.8).

Appendix D Details of XPS Analysis

D.1 XPS Data Collection and Peak Fitting

X-ray photoelectron spectroscopy (XPS) data were collected using a Kratos AXIS Ultra spectrometer (Kratos Analytical, Manchester, UK) equipped with a hybrid magnetic and electrostatic electron lens system, a delay-line detector (DLD), and a monochromatic Al K□ ± X-ray source (1486.7 eV). Data were collected at pressures of ~2 x 10^{-9} Torr with photoelectrons collected along the sample surface normal. The analyzer pass energy was 80 eV for survey spectra and 10 eV for high-resolution spectra, which were collected at a resolution of 50 meV. The instrument energy scale and work function were calibrated using clean Au, Ag, and Cu standards. The instrument was operated by Vision Manager software v. 2.2.10 revision 5.

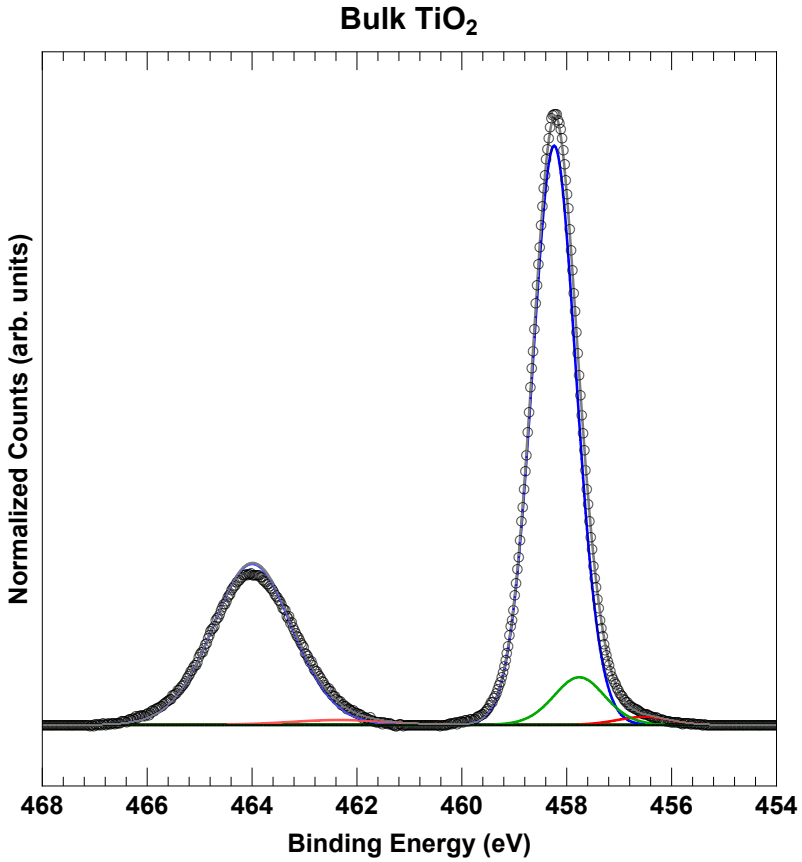

Figure D.1 X-ray photoelectron spectroscopy of the Ti 2p region for a bulk TiO_2 film. The peak associated with Ti^{4+} is shown in blue. The slightly and highly reduced Ti peaks are shown in green and red, respectively, and the most highly oxidized Ti peak is shown in orange.

XPS data were analyzed using CasaXPS software (CASA Software Ltd). The Ti 2p core-level photoemission spectra were fit constraining the peak separation and the peak area ratio between Ti $2p^{3/2}$ and Ti $2p^{1/2}$ peaks to 5.75 eV and 2:1, respectively. The peak area ratios were allowed to deviate 5% from the 2:1 ratio to account for inaccuracies in the background. All peaks were fit using a Gaussian-Lorentzian with 30% Lorentzian character. A bulk TiO_2 sample (1000 cycles) was used as a standard to determine the peak positions for the Ti $2p_{3/2}$ core-level photoemission (Fig. C.1). The bulk TiO_2 sample fit exhibited a main peak at 458.24 eV, which is consistent with reports of the peak position for TiO_2 and therefore was ascribed to the Ti^{4+} oxidation state, and two additional peaks at lower binding energies, 457.6 eV and 456.6 eV, respectively, associated with a more reduced Ti state, likely Ti^{3+}(*215, 216, 228, 229*). These peaks were propagated through for IrO_2 for all thicknesses of TiO_2. In addition to these peaks, a fourth peak at slightly higher binding energy (458.5 eV) was needed to fit the FTO spectra.

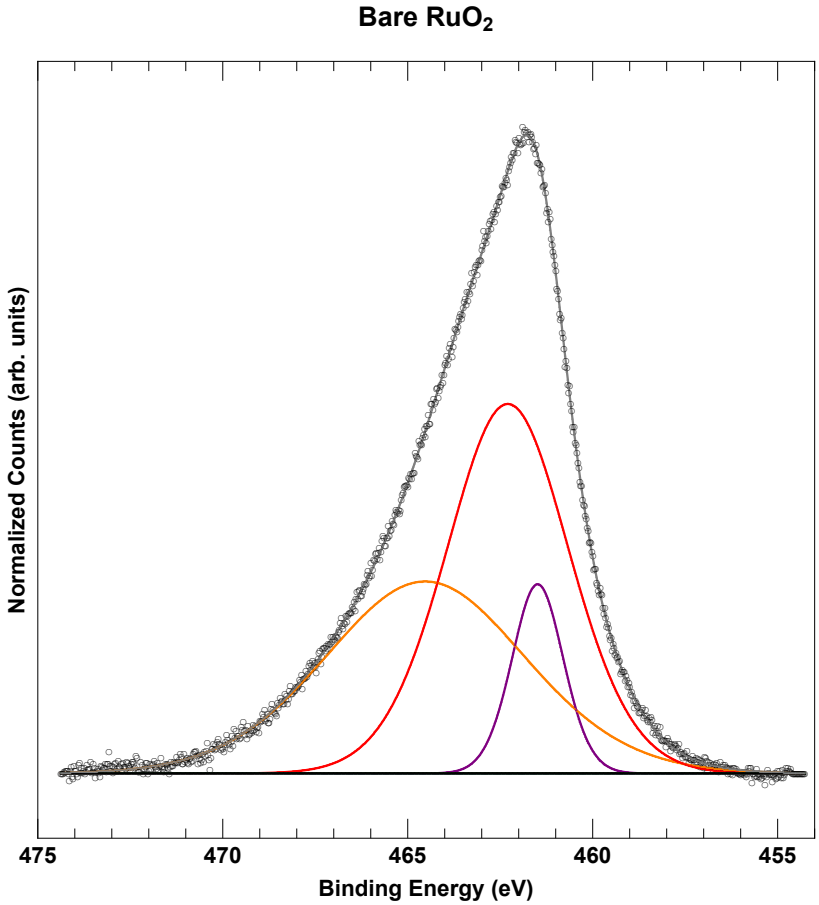

Figure D.2 X-ray photoelectron spectroscopy of the Ti 2p region for a bare RuO_2 film. The 3 orange, red, and purple peaks define the Ru 3p core level photoemission associated with RuO_2.

In the case of RuO_2, the Ru 3p core level exhibited a broad peak in the Ti 2p region (Fig. C.2), which was well-fit by 3 Gaussian-Lorentzian peaks at 461.5 eV, 462.3 eV, and 464.5 eV, respectively. These Ru 3p core level photoemission peaks were propagated through for the fits of the spectra with ALD TiO_2. In addition to the 3 peaks associated with the Ru 3p core level, the spectra were also fit with the 3 peaks associated with bulk TiO_2, as described above. To deconvolute the effect of Ru 3p core level photoemission from the TiO_2 signal, the Ru 3p core level peaks were subtracted from the spectra resulting in spectra corresponding purely to the Ti 2p core level photoemission.

The photoemission from the underlying metal oxide substrates was also measured. Peak fitting was performed on the bare metal oxide substrate and then propagated through to the spectra with ALD TiO_2. The Ir 4f and Ru 3d photoemission core-level spectra were fit according to previous reports in the literature (*230, 231*).

BIBLIOGRAPHY

1. M. I. Hoffert *et al.*, Energy implications of future stabilization of atmospheric CO2 content. *Nature* **395**, 881 (1998).
2. "International Energy Outlook 2015," (Energy Information Administration, 2015).
3. H. D. Matthews, K. Caldeira, Stabilizing climate requires near-zero emissions. *Geophysical Research Letters* **35**, (2008).
4. R. Joeri *et al.*, Zero emission targets as long-term global goals for climate protection. *Environmental Research Letters* **10**, 105007 (2015).
5. United Nations, *The Paris Agreement* (2016).
6. S. J. Davis *et al.*, Net-zero emissions energy systems. *Science* **360**, (2018).
7. "International Energy Outlook 2018," (U.S. Energy Information Administration 2018).
8. "The Outlook for Energy: A View to 2040," (Exonn Mobil, 2018).
9. Z. W. Seh *et al.*, Combining theory and experiment in electrocatalysis: Insights into materials design. *Science* **355**, (2017).
10. "Technology roadmap: energy and GHG reductions in the chemical industry via catalytic processes," (International Energy Agency (IEA),
International Council of Chemical Associations,
DECHEMA, Paris (France), 2013).
11. IEA, "Key World Energy Statistics," (IEA, 2017).
12. J. Tsao, N. S. Lewis, G. Crabtree, "Solar FAQs," (Sandia National Lab, 2006).
13. BP, "Statitstical Review of World Energy," (BP 2018).
14. "Photovoltaics Report," (Frauenhofer Institute for Solar Energy, 2018).
15. . (DOE Solar Energy Technologies Office, 2017).
16. N. S. Lewis, Research opportunities to advance solar energy utilization. *Science* **351**, 353-362 (2016).
17. "Lazard's Levelized Cost of Storage Analysis - Version 3.0," (Lazard, 2017).
18. K. Yoshikawa *et al.*, Silicon heterojunction solar cell with interdigitated back contacts for a photoconversion efficiency over 26%. **2**, 17032 (2017).
19. A. Richter, M. Hermle, S. W. Glunz, Reassessment of the limiting efficiency for crystalline silicon solar cells. *IEEE Journal of Photovoltaics* **3**, 1184-1191 (2013).
20. "Solar intermittency: Australia's clean energy challenge," (Global CCS Institute).
21. S. M. Sze, K. K. Ng, *Physics of semiconductor devices*. (Wiley-Interscience, Hoboken, N.J., ed. 3rd, 2007), pp. x, 815 p.
22. P. Würfel, U. Würfel, *Physics of solar cells : from basic principles to advanced concepts*. Physics textbook (Wiley-VCH, Weinheim, ed. 2nd, updated and expanded, 2009), pp. xii, 244 p.
23. J. Nelson, *The physics of solar cells*. (Imperial College Press ;
Distributed by World Scientific Pub. Co., London
River Edge, NJ, 2003), pp. xix, 363 p.
24. D. Z. Morris. (Fortune, 2016).

25. . (Germany Trade and Invest, 2017).
26. . (California Energy Commission 2018).
27. J. Fauvarque, The Chlorine Industry *Pure Appl. Chem.* **68**, 1713-1720 (1996).
28. "Chemical Economics Handbook: Chlorine/Dosium Hydroxide," (IHS Markit, 2018).
29. W. Shockley, H. J. Queisser, Detailed Balance Limit of Efficiency of p-n Junction Solar Cells. *Journal of Applied Physics* **32**, 510-519 (1961).
30. . (NREL, 2017).
31. M. V. Kurik, Urbach rule. *physica status solidi (a)* **8**, 9-45 (1971).
32. C. H. Grein, S. John, Temperature dependence of the Urbach optical absorption edge: A theory of multiple phonon absorption and emission sidebands. *Phys. Rev. B.* **39**, 1140-1151 (1989).
33. S. John, C. Soukoulis, M. H. Cohen, E. N. Economou, Theory of Electron Band Tails and the Urbach Optical-Absorption Edge. *Physical Review Letters* **57**, 1777-1780 (1986).
34. O. D. Miller, E. Yablonovitch, S. R. Kurtz, Strong Internal and External Luminescence as Solar Cells Approach the Shockley–Queisser Limit. *IEEE Journal of Photovoltaics* **2**, 303-311 (2012).
35. M. Beaudoin, A. J. G. DeVries, S. R. Johnson, H. Laman, T. Tiedje, Optical absorption edge of semi-insulating GaAs and InP at high temperatures. *Appl. Phys. Lett.* **70**, 3540-3542 (1997).
36. I. Strzalkowski, S. Joshi, C. R. Crowell, Dielectric constant and its temperature dependence for GaAs, CdTe, and ZnSe. *Appl. Phys. Lett.* **28**, 350-352 (1976).
37. M. A. Green, Self-consistent optical parameters of intrinsic silicon at 300K including temperature coefficients. *Sol. Energy Mater. Sol. Cells* **92**, 1305-1310 (2008).
38. S. W. Lee *et al.*, Improved Cu_2O-Based Solar Cells Using Atomic Layer Deposition to Control the Cu Oxidation State at the p-n Junction. *Advanced Energy Materials* **4**, 1301916-n/a (2014).
39. S. De Wolf *et al.*, Organometallic Halide Perovskites: Sharp Optical Absorption Edge and Its Relation to Photovoltaic Performance. *The Journal of Physical Chemistry Letters* **5**, 1035-1039 (2014).
40. J. T. Heath, J. D. Cohen, W. N. Shafarman, D. X. Liao, A. A. Rockett, Effect of Ga content on defect states in CuIn1−xGaxSe2 photovoltaic devices. *Appl. Phys. Lett.* **80**, 4540-4542 (2002).
41. M. K. van Veen, R. E. I. Schropp, Beneficial effect of a low deposition temperature of hot-wire deposited intrinsic amorphous silicon for solar cells. *J. Appl. Phys.* **93**, 121-125 (2002).
42. C. Yan *et al.*, Beyond 11% Efficient Sulfide Kesterite Cu2ZnxCd1–xSnS4 Solar Cell: Effects of Cadmium Alloying. *ACS Energy Letters* **2**, 930-936 (2017).
43. F. Urbach, The Long-Wavelength Edge of Photographic Sensitivity and of the Electronic Absorption of Solids. *Physical Review* **92**, 1324-1324 (1953).
44. J. K. Katahara, H. W. Hillhouse, Quasi-Fermi level splitting and sub-bandgap absorptivity from semiconductor photoluminescence. *J. Appl. Phys.* **116**, 173504 (2014).

45. P. Wurfel, The chemical potential of radiation. *Journal of Physics C: Solid State Physics* **15**, 3967 (1982).
46. J. Jean *et al.*, Radiative Efficiency Limit with Band Tailing Exceeds 30% for Quantum Dot Solar Cells. *ACS Energy Letters* **2**, 2616-2624 (2017).
47. Z. Yuan, L. Shi, Y. Zhang, in *2015 IEEE 42nd Photovoltaic Specialist Conference (PVSC)*. (2015), pp. 1-5.
48. U. Rau, B. Blank, T. C. M. Müller, T. Kirchartz, Efficiency Potential of Photovoltaic Materials and Devices Unveiled by Detailed-Balance Analysis. *Physical Review Applied* **7**, 044016 (2017).
49. M. Bernardi, M. Palummo, J. C. Grossman, Semiconducting monolayer materials as a tunable platform for excitonic solar cells. *ACS Nano* **6**, 10082-10089 (2012).
50. D. Jariwala, V. K. Sangwan, L. J. Lauhon, T. J. Marks, M. C. Hersam, Emerging Device Applications for Semiconducting Two-Dimensional Transition Metal Dicalchogenides. *ACS Nano*, 1102-1120 (2014).
51. C.-H. Lee *et al.*, Atomically thin p–n junctions with van der Waals heterointerfaces. *Nat. Nanotechnol.* **9**, 676-681 (2014).
52. M. A. Green, Improved value for the silicon free exciton binding energy. *AIP Advances* **3**, 112104 (2013).
53. K. Zanio, in *Semiconductors and Semimetals,* Z. Kenneth, Ed. (Elsevier, 1978), vol. Volume 13, pp. iii.
54. S. B. Nam *et al.*, Free-exciton energy spectrum in GaAs. *Phys. Rev. B.* **13**, 761-767 (1976).
55. R. Corkish, D. S. P. Chan, M. A. Green, Excitons in silicon diodes and solar cells: A three-particle theory. *J. Appl. Phys.* **79**, 195-203 (1996).
56. Y. Zhang, A. Mascarenhas, S. Deb, Effects of excitons on solar cells. *J. Appl. Phys.* **84**, 3966-3971 (1998).
57. S. Z. Karazhanov, Y. Zhang, A. Mascarenhas, S. Deb, The effect of excitons on CdTe solar cells. *J. Appl. Phys.* **87**, 8786-8792 (2000).
58. G. M. Kavoulakis, Y.-C. Chang, G. Baym, Fine structure of excitons in Cu_2O. *Phys. Rev. B.* **55**, 7593-7599 (1997).
59. A. Mysyrowicz, D. Hulin, A. Antonetti, Long Exciton Lifetime in Cu_2O. *Phys. Rev. Lett.* **43**, 1123-1126 (1979).
60. T. Kazimierczuk, D. Frohlich, S. Scheel, H. Stolz, M. Bayer, Giant Rydberg excitons in the copper oxide Cu_2O. *Nature* **514**, 343-347 (2014).
61. S. David, G. M. Kavoulakis, Bose–Einstein condensation of excitons in Cu_2O: progress over 30 years. *Rep. Prog. Phys.* **77**, 116501 (2014).
62. S. a. t. A. Moskalenko, D. W. Snoke, *Bose-Einstein condensation of excitons and biexcitons : and coherent nonlinear optics with excitons*. (Cambridge University Press, Cambridge, UK ; New York, 2000), pp. xiii, 415 p.
63. E. Tselepis, E. Fortin, A. Mysyrowicz, Exciton-mediated photovoltaic effect in Cu_2O/Cu. *Phys. Rev. Lett.* **59**, 2107-2110 (1987).
64. C. Klingshirn, M. Jörger, T. Fleck, A. Jolk, Exciton transport in Cu_2O, exciton detection by field ionization in a Schottky barrier and intraexcitonic transitions. *Solid State Commun.* **134**, 155-158 (2005).

65. L. C. Olsen, F. W. Addis, W. Miller, Experimental and theoretical studies of Cu_2O solar cells. *Solar Cells* **7**, 247-279 (1982).
66. A. Luque, S. Hegedus, *Handbook of photovoltaic science and engineering*. (Wiley, Chichester, West Sussex, U.K., ed. 2nd, 2011), pp. xxxii, 1132 p.
67. E. O. Kane, Pollmann-B\"uttner variational method for excitonic polarons. *Phys. Rev. B.* **18**, 6849-6855 (1978).
68. V. T. Agekyan, Spectroscopic properties of semiconductor crystals with direct forbidden energy gap. *physica status solidi (a)* **43**, 11-42 (1977).
69. M. O'Keeffe, W. J. Moore, Thermodynamics of the Formation and Migration of Defects in Cuprous Oxide. *The Journal of Chemical Physics* **36**, 3009-3013 (1962).
70. B. Zhu, X. Chen, X. Cui, Exciton Binding Energy of Monolayer WS2. *Scientific Reports* **5**, 9218 (2015).
71. A. Chernikov *et al.*, Exciton Binding Energy and Nonhydrogenic Rydberg Series in Monolayer WS2. *Phys. Rev. Lett.* **076802**, 1-5 (2014).
72. A. Ramasubramaniam, Large excitonic effects in monolayers of molybdenum and tungsten dichalcogenides. *Phys. Rev. B.* **86**, 115409 (2012).
73. H.-P. Komsa, A. V. Krasheninnikov, Effects of confinement and environment on the electronic structure and exciton binding energy of MoS_2 from first principles. *Phys. Rev. B.* **86**, 241201 (2012).
74. J. I. Jang, J. P. Wolfe, Auger recombination and biexcitons in Cu_2O: A case for dark excitonic matter. *Phys. Rev. B.* **74**, 045211 (2006).
75. M. N. Saha, On a Physical Theory of Stellar Spectra. *Proceedings of the Royal Society of London. Series A* **99**, 135-153 (1921).
76. M. Combescot, Thermodynamics of an electron—hole system in semiconductors. *physica status solidi (b)* **86**, 349-358 (1978).
77. V. D'Innocenzo *et al.*, Excitons versus free charges in organo-lead tri-halide perovskites. *Nature Communications* **5**, 3586 (2014).
78. E. F. Gross, F. I. Kreingol'd, V. L. Makarov, Resonant Interaction Between Ortho- and Para-excitons with Participation of Phonons in a Cu_2O Crystal. *JETP Letters* **15**, 269 (1972).
79. P. D. Bloch, C. Schwab, Direct Evidence for Phonon-Assisted Transitions to the 1s Paraexciton Level of the Yellow Exciton Series in Cu_2O. *Phys. Rev. Lett.* **41**, 514-517 (1978).
80. J. I. Jang, University of Illinois at Urbana-Champaign, (2005).
81. K. Karpinska, P. H. M. van Loosdrecht, I. P. Handayani, A. Revcolevschi, Para-excitons in —a new approach. *J. Lumin.* **112**, 17-20 (2005).
82. D. W. Snoke, A. J. Shields, M. Cardona, Phonon-absorption recombination luminescence of room-temperature excitons in Cu_2O. *Phys. Rev. B.* **45**, 11693-11697 (1992).
83. S. Koirala, N. Naka, K. Tanaka, Correlated lifetimes of free paraexcitons and excitons trapped at oxygen vacancies in cuprous oxide. *J. Lumin.* **134**, 524-527 (2013).
84. Y. Tolstova, S. T. Omelchenko, R. E. Blackwell, A. M. Shing, H. A. Atwater, Polycrystalline Cu_2O photovoltaic devices incorporating Zn(O,S) window layers. *Sol. Energy Mater. Sol. Cells* **160**, 340-345 (2017).

85. C. Xiang *et al.*, 820 mV open-circuit voltages from Cu_2O/CH3CN junctions. *Energy & Environmental Science* **4**, 1311-1318 (2011).
86. S. S. Wilson *et al.*, Interface stoichiometry control to improve device voltage and modify band alignment in ZnO/Cu2O heterojunction solar cells. *Energy & Environmental Science* **7**, 3606-3610 (2014).
87. E. F. Gross, F. I. Kreingol'd, Exciton Luminescence in Cu_2O Crystals. *JETP Letters* **7**, 218 (1968).
88. Y. Petroff, P. Y. Yu, Y. R. Shen, Luminescence of Cu_2O-Excitonic Molecules, or Not? *Phys. Rev. Lett.* **29**, 1558-1562 (1972).
89. Y. Petroff, P. Y. Yu, Y. R. Shen, Study of photoluminescence in Cu_2O. *Phys. Rev. B.* **12**, 2488-2495 (1975).
90. T. Ito, T. Masumi, Detailed Examination of Relaxation Processes of Excitons in Photoluminescence Spectra of Cu_2O. *J. Phys. Soc. Jpn.* **66**, 2185-2193 (1997).
91. D. E. Kane, R. M. Swanson, The effect of excitons on apparent band gap narrowing and transport in semiconductors. *J. Appl. Phys.* **73**, 1193-1197 (1993).
92. H. Raebiger, S. Lany, A. Zunger, Origins of the *p*-type nature and cation deficiency in Cu_2O and related materials. *Phys. Rev. B.* **76**, 045209 (2007).
93. S. A. Moskalenko, D. W. Snoke, *Bose-Einstein Condensation of Excitons and Biexcitons and Coherent Nonlinear Optics with Excitons*. (Cambridge University Press, New York, New York, 2000).
94. H. Shimada, T. Masumi, Hall Mobility of Positive Holes in Cu_2O. *J. Phys. Soc. Jpn.* **58**, 1717-1724 (1989).
95. F. Biccari, Universita di Roma, (2009).
96. T. Minami, Y. Nishi, T. Miyata, Impact of incorporating sodium into polycrystalline p-type Cu_2O for heterojunction solar cell applications. *Appl. Phys. Lett.* **105**, 212104 (2014).
97. F. Biccari, C. Malerba, A. Mittiga, Chlorine doping of Cu_2O. *Sol. Energy Mater. Sol. Cells* **94**, 1947-1952 (2010).
98. D. W. Snoke, J. L. Lin, J. P. Wolfe, Coexistence of Bose-Einstein paraexcitons with Maxwell-Boltzmann orthoexcitons in Cu_2O. *Phys. Rev. B.* **43**, 1226-1228 (1991).
99. E. Nolle, Recombination Through Exciton States in Semiconductors. *Soviet Physics - Solid State* **9**, 90-94 (1967).
100. D. Trivich, E. Y. Wang, R. J. Komp, K. Weng, A. Kakar, Cuprous oxide photovoltaic cells. *J. Electrochem. Soc.* **124**, C318 (1977).
101. D. P. Trauernicht, J. P. Wolfe, Drift and diffusion of paraexcitons in Cu_2O: Deformation-potential scattering in the low-temperature regime. *Phys. Rev. B.* **33**, 8506-8521 (1986).
102. C. Malerba *et al.*, Absorption coefficient of bulk and thin film Cu_2O. *Sol. Energy Mater. Sol. Cells* **95**, 2848-2854 (2011).
103. M. Tadatsugu, N. Yuki, M. Toshihiro, Heterojunction solar cell with 6% efficiency based on an n-type aluminum–gallium–oxide thin film and p-type sodium-doped Cu_2O sheet. *Applied Physics Express* **8**, 022301 (2015).
104. M. Tadatsugu, N. Yuki, M. Toshihiro, Efficiency enhancement using a Zn 1− x Ge x -O thin film as an n-type window layer in Cu_2O-based heterojunction solar cells. *Applied Physics Express* **9**, 052301 (2016).

105. Y. S. Lee *et al.*, Atomic Layer Deposited Gallium Oxide Buffer Layer Enables 1.2 V Open-Circuit Voltage in Cuprous Oxide Solar Cells. *Adv. Mater.* **26**, 4704-4710 (2014).
106. T. Kirchartz, K. Ding, U. Rau, in *Advanced Characterization Techniques for Thin Film Solar Cells*. (Wiley-VCH Verlag GmbH & Co. KGaA, 2011), pp. 33-60.
107. I. Almansouri, A. Ho-Baillie, S. P. Bremner, M. A. Green, Supercharging Silicon Solar Cell Performance by Means of Multijunction Concept. *IEEE Journal of Photovoltaics* **5**, 968-976 (2015).
108. N. Jain, M. K. Hudait, III-V Multijunction Solar Cell Integration with Silicon: Present Status, Challenges and Future Outlook. *Energy Havesting and Systems* **1**, (2014).
109. S. Essig *et al.*, Realization of GaInP/Si Dual-Junction Solar Cells With 29.8% 1-Sun Efficiency. *IEEE Journal of Photovoltaics* **6**, 1012-1019 (2016).
110. Z. Ren *et al.*, Numerical Analysis of Radiative Recombination and Reabsorption in GaAs/Si Tandem. *IEEE Journal of Photovoltaics* **5**, 1079-1086 (2015).
111. S. Essig *et al.*, Wafer-Bonded GaInP/GaAs//Si Solar Cells With 30% Efficiency Under Concentrated Sunlight. *IEEE Journal of Photovoltaics* **5**, 977-981 (2015).
112. J. M. Gee, G. F. Virshup, in *Conference Record of the Twentieth IEEE Photovoltaic Specialists Conference*. (1988), pp. 754-758 vol.751.
113. T. J. Grassman, D. J. Chmielewski, S. D. Carnevale, J. A. Carlin, S. A. Ringel, GaAs_{0.75}P_{0.25}/Si Dual-Junction Solar Cells Grown by MBE and MOCVD. *IEEE Journal of Photovoltaics* **6**, 326-331 (2016).
114. K. N. Yaung, M. Vaisman, J. Lang, M. L. Lee, GaAsP solar cells on GaP/Si with low threading dislocation density. *Appl. Phys. Lett.* **109**, 032107 (2016).
115. R. M. France, F. Dimroth, T. J. Grassman, R. R. King, Metamorphic epitaxy for multijunction solar cells. *MRS Bull.* **41**, 202-209 (2016).
116. S. Essig *et al.*, Raising the one-sun conversion efficiency of III–V/Si solar cells to 32.8% for two junctions and 35.9% for three junctions. *Nature Energy* **2**, 17144 (2017).
117. A. Kojima, K. Teshima, Y. Shirai, T. Miyasaka, Organometal Halide Perovskites as Visible-Light Sensitizers for Photovoltaic Cells. *Journal of the American Chemical Society* **131**, 6050-6051 (2009).
118. J.-H. Im, C.-R. Lee, J.-W. Lee, S.-W. Park, N.-G. Park, 6.5% efficient perovskite quantum-dot-sensitized solar cell. *Nanoscale* **3**, 4088-4093 (2011).
119. M. M. Lee, J. Teuscher, T. Miyasaka, T. N. Murakami, H. J. Snaith, Efficient Hybrid Solar Cells Based on Meso-Superstructured Organometal Halide Perovskites. *Science* **338**, 643 (2012).
120. K. A. Bush *et al.*, 23.6%-efficient monolithic perovskite/silicon tandem solar cells with improved stability. *Nature Energy* **2**, 17009 (2017).
121. J. H. Noh, S. H. Im, J. H. Heo, T. N. Mandal, S. I. Seok, Chemical Management for Colorful, Efficient, and Stable Inorganic–Organic Hybrid Nanostructured Solar Cells. *Nano Lett.* **13**, 1764-1769 (2013).
122. https://www.oxfordpv.com/news/oxford-pv-sets-world-record-perovskite-solar-cell.

123. R. G. Wilks, M. Bär, Perovskite solar cells: Danger from within. *Nature Energy* **2**, 16204 (2017).
124. P. Löper *et al.*, Organic–inorganic halide perovskite/crystalline silicon four-terminal tandem solar cells. *PCCP* **17**, 1619-1629 (2015).
125. F. Lang *et al.*, Perovskite Solar Cells with Large-Area CVD-Graphene for Tandem Solar Cells. *The Journal of Physical Chemistry Letters* **6**, 2745-2750 (2015).
126. T. Duong *et al.*, Semitransparent Perovskite Solar Cell With Sputtered Front and Rear Electrodes for a Four-Terminal Tandem. *IEEE Journal of Photovoltaics* **6**, 679-687 (2016).
127. D. P. McMeekin *et al.*, A mixed-cation lead mixed-halide perovskite absorber for tandem solar cells. *Science* **351**, 151-155 (2016).
128. T. Duong *et al.*, Rubidium Multication Perovskite with Optimized Bandgap for Perovskite-Silicon Tandem with over 26% Efficiency. *Advanced Energy Materials* **7**, 1700228-n/a (2017).
129. C. Amano, H. Sugiura, A. Yamamoto, M. Yamaguchi, 20.2% efficiency Al0.4Ga0.6As/GaAs tandem solar cells grown by molecular beam epitaxy. *Applied Physics Letters* **51**, 1998-2000 (1987).
130. J. P. Mailoa *et al.*, A 2-terminal perovskite/silicon multijunction solar cell enabled by a silicon tunnel junction. *Applied Physics Letters* **106**, 121105 (2015).
131. F. Sahli *et al.*, Improved Optics in Monolithic Perovskite/Silicon Tandem Solar Cells with a Nanocrystalline Silicon Recombination Junction. *Advanced Energy Materials*, 1701609-n/a.
132. F. Sahli *et al.*, Fully textured monolithic perovskite/silicon tandem solar cells with 25.2% power conversion efficiency. *Nature Materials*, (2018).
133. Y. Wu *et al.*, Monolithic perovskite/silicon-homojunction tandem solar cell with over 22% efficiency. *Energy & Environmental Science* **10**, 2472-2479 (2017).
134. S. Albrecht *et al.*, Monolithic perovskite/silicon-heterojunction tandem solar cells processed at low temperature. *Energy & Environmental Science*, (2015).
135. J. Werner *et al.*, Efficient Monolithic Perovskite/Silicon Tandem Solar Cell With Cell Area > 1 cm2. *The Journal of Physical Chemistry Letters*, (2015).
136. S. Hu *et al.*, Amorphous TiO₂ coatings stabilize Si, GaAs, and GaP photoanodes for efficient water oxidation. *Science* **344**, 1005-1009 (2014).
137. M. T. McDowell *et al.*, The Influence of Structure and Processing on the Behavior of TiO2 Protective Layers for Stabilization of n-Si/TiO2/Ni Photoanodes for Water Oxidation. *ACS Applied Materials & Interfaces* **7**, 15189-15199 (2015).
138. D. Yan, A. Cuevas, Y. Wan, J. Bullock, Passivating contacts for silicon solar cells based on boron-diffused recrystallized amorphous silicon and thin dielectric interlayers. *Solar Energy Materials and Solar Cells* **152**, 73-79 (2016).
139. J. Peng *et al.*, Interface passivation using ultrathin polymer-fullerene films for high-efficiency perovskite solar cells with negligible hysteresis. *Energy & Environmental Science*, (2017).
140. M. Saliba *et al.*, Incorporation of rubidium cations into perovskite solar cells improves photovoltaic performance. *Science*, (2016).

141. M. Xiao *et al.*, A Fast Deposition-Crystallization Procedure for Highly Efficient Lead Iodide Perovskite Thin-Film Solar Cells. *Angewandte Chemie International Edition* **53**, 9898-9903 (2014).
142. H. Shen *et al.*, Mechanically-stacked perovskite/CIGS tandem solar cells with efficiency of 23.9% and reduced oxygen sensitivity. *Energy & Environmental Science* **11**, 394-406 (2018).
143. W. Jérémie, N. Bjoern, B. Christophe, Perovskite/Silicon Tandem Solar Cells: Marriage of Convenience or True Love Story? – An Overview. *Advanced Materials Interfaces* **5**, 1700731 (2018).
144. Z. Yang *et al.*, Composition-Tuned Wide Bandgap Perovskites: From Grain Engineering to Stability and Performance Improvement. *Advanced Functional Materials* **0**, 1803130.
145. S. Bandana, S. S. Chetan, N-type solar cells: advantages, issues, and current scenarios. *Materials Research Express* **4**, 072001 (2017).
146. J. Melskens *et al.*, Passivating Contacts for Crystalline Silicon Solar Cells: From Concepts and Materials to Prospects. *IEEE Journal of Photovoltaics* **8**, 373-388 (2018).
147. Z. C. Holman, A. Descoeudres, S. D. Wolf, C. Ballif, Record Infrared Internal Quantum Efficiency in Silicon Heterojunction Solar Cells With Dielectric/Metal Rear Reflectors. *IEEE Journal of Photovoltaics* **3**, 1243-1249 (2013).
148. J. Yan, D. C. Gilmer, S. A. Campbell, W. L. Gladfelter, P. G. Schmid, Structural and electrical characterization of TiO2 grown from titanium tetrakis-isopropoxide (TTIP) and TTIP/H2O ambients. *Journal of Vacuum Science & Technology B: Microelectronics and Nanometer Structures Processing, Measurement, and Phenomena* **14**, 1706-1711 (1996).
149. J. Jhaveri *et al.*, in *2013 IEEE 39th Photovoltaic Specialists Conference (PVSC)*. (2013), pp. 3292-3296.
150. J. A. Willemen, M. Zeman, J. W. Metselaar, in *Proceedings of 1994 IEEE 1st World Conference on Photovoltaic Energy Conversion - WCPEC (A Joint Conference of PVSC, PVSEC and PSEC)*. (1994), vol. 1, pp. 599-602 vol.591.
151. J. A. Willemem, Simulation of amorphous Silicon single and multijuntion solar cells. *Thesis*, (1998).
152. R. H. Cox, H. Strack, Ohmic contacts for GaAs devices. *Solid-State Electronics* **10**, 1213-1218 (1967).
153. M. Perego, G. Seguini, G. Scarel, M. Fanciulli, F. Wallrapp, Energy band alignment at TiO2/Si interface with various interlayers. *Journal of Applied Physics* **103**, 043509 (2008).
154. S. Hu *et al.*, Electrical, Photoelectrochemical, and Photoelectron Spectroscopic Investigation of the Interfacial Transport and Energetics of Amorphous TiO2/Si Heterojunctions. *The Journal of Physical Chemistry C* **120**, 3117-3129 (2016).
155. B. Mei *et al.*, Crystalline TiO2: A Generic and Effective Electron-Conducting Protection Layer for Photoanodes and -cathodes. *The Journal of Physical Chemistry C* **119**, 15019-15027 (2015).

156. O. Hiroaki, N. Yoshiteru, H. Yoshihiro, Design Parameters of a-Si: H High-Voltage Photovoltaic Cells. *Japanese Journal of Applied Physics* **19**, 545 (1980).
157. S. Ahmed, M. R. Melloch, E. S. Harmon, D. T. McInturff, J. M. Woodall, Use of nonstoichiometry to form GaAs tunnel junctions. *Applied Physics Letters* **71**, 3667-3669 (1997).
158. J. M. O. Zide *et al.*, Increased efficiency in multijunction solar cells through the incorporation of semimetallic ErAs nanoparticles into the tunnel junction. *Applied Physics Letters* **88**, 162103 (2006).
159. M. Burgelman, P. Nollet, S. Degrave, Modelling polycrystalline semiconductor solar cells. *Thin Solid Films* **361-362**, 527-532 (2000).
160. R. T. Tung, The physics and chemistry of the Schottky barrier height. *Applied Physics Reviews* **1**, 011304 (2014).
161. S. Kamohara, D. Park, C. Hu, in *1998 IEEE International Reliability Physics Symposium Proceedings. 36th Annual (Cat. No.98CH36173)*. (1998), pp. 57-61.
162. U. Diebold, The surface science of titanium dioxide. *Surface Science Reports* **48**, 53-229 (2003).
163. L.-Å. Ragnarsson, P. Lundgren, Electrical characterization of Pb centers in (100)Si–SiO2 structures: The influence of surface potential on passivation during post metallization anneal. *Journal of Applied Physics* **88**, 938-942 (2000).
164. Y. W. Chen *et al.*, Atomic layer-deposited tunnel oxide stabilizes silicon photoanodes for water oxidation. *Nature Materials* **10**, 539 (2011).
165. Y. Wu *et al.*, On the Origin of Hysteresis in Perovskite Solar Cells. *Advanced Functional Materials* **26**, 6807-6813 (2016).
166. P. Kohn *et al.*, Low temperature crystallisation of mesoporous TiO2. *Nanoscale* **5**, 10518-10524 (2013).
167. H. Lee *et al.*, Low-Temperature Fabrication of TiO2 Electrodes for Flexible Dye-Sensitized Solar Cells Using an Electrospray Process. *ACS Applied Materials & Interfaces* **4**, 3308-3315 (2012).
168. D. Pérez-del-Rey, P. P. Boix, M. Sessolo, A. Hadipour, H. J. Bolink, Interfacial Modification for High-Efficiency Vapor-Phase-Deposited Perovskite Solar Cells Based on a Metal Oxide Buffer Layer. *The Journal of Physical Chemistry Letters* **9**, 1041-1046 (2018).
169. L. Qiu *et al.*, Engineering Interface Structure to Improve Efficiency and Stability of Organometal Halide Perovskite Solar Cells. *The Journal of Physical Chemistry B* **122**, 511-520 (2018).
170. Y. Shuai *et al.*, A Biopolymer Heparin Sodium Interlayer Anchoring TiO2 and MAPbI3 Enhances Trap Passivation and Device Stability in Perovskite Solar Cells. *Advanced Materials* **30**, 1706924 (2018).
171. M. A. Green, Accuracy of analytical expressions for solar cell fill factors. *Solar Cells* **7**, 337-340 (1982).
172. J. A. Christians *et al.*, Tailored interfaces of unencapsulated perovskite solar cells for >1,000 hour operational stability. *Nature Energy* **3**, 68-74 (2018).
173. Z. Li *et al.*, Extrinsic ion migration in perovskite solar cells. *Energy & Environmental Science* **10**, 1234-1242 (2017).

174. K. Domanski *et al.*, Migration of cations induces reversible performance losses over day/night cycling in perovskite solar cells. *Energy & Environmental Science* **10**, 604-613 (2017).
175. K. Domanski, E. A. Alharbi, A. Hagfeldt, M. Grätzel, W. Tress, Systematic investigation of the impact of operation conditions on the degradation behaviour of perovskite solar cells. *Nature Energy* **3**, 61-67 (2018).
176. T. Leijtens *et al.*, Overcoming ultraviolet light instability of sensitized TiO2 with meso-superstructured organometal tri-halide perovskite solar cells. *Nature Communications* **4**, 2885 (2013).
177. Y. Sun *et al.*, Enhanced UV-light stability of organometal halide perovskite solar cells with interface modification and a UV absorption layer. *Journal of Materials Chemistry C* **5**, 8682-8687 (2017).
178. J. Zheng *et al.*, Large area efficient interface layer free monolithic perovskite/homo-junction-silicon tandem solar cell with over 20% efficiency. *Energy & Environmental Science*, (2018).
179. Z. W. Seh *et al.*, Combining theory and experiment in electrocatalysis: Insights into materials design. *Science* **355**, eaad4998 (2017).
180. Y. Yang, J. Shin, J. T. Jasper, M. R. Hoffmann, Multilayer Heterojunction Anodes for Saline Wastewater Treatment: Design Strategies and Reactive Species Generation Mechanisms. *Environmental Science & Technology* **50**, 8780-8787 (2016).
181. K. Gong, F. Du, Z. Xia, M. Durstock, L. Dai, Nitrogen-Doped Carbon Nanotube Arrays with High Electrocatalytic Activity for Oxygen Reduction. *Science* **323**, 760-764 (2009).
182. L.-Å. Näslund *et al.*, The Role of TiO_2 Doping on RuO_2-Coated Electrodes for the Water Oxidation Reaction. *The Journal of Physical Chemistry C* **117**, 6126-6135 (2013).
183. A. R. Zeradjanin, N. Menzel, W. Schuhmann, P. Strasser, On the faradaic selectivity and the role of surface inhomogeneity during the chlorine evolution reaction on ternary Ti-Ru-Ir mixed metal oxide electrocatalysts. *PCCP* **16**, 13741-13747 (2014).
184. H. Li *et al.*, Activating and optimizing MoS_2 basal planes for hydrogen evolution through the formation of strained sulphur vacancies. *Nature Materials* **15**, 48-+ (2016).
185. L. Giordano, F. Cinquini, G. Pacchioni, Tuning the surface metal work function by deposition of ultrathin oxide films: Density functional calculations. *Phys. Rev. B.* **73**, 045414 (2006).
186. K. S. Exner, J. Anton, T. Jacob, H. Over, Controlling Selectivity in the Chlorine Evolution Reaction over RuO_2-Based Catalysts. *Angewandte Chemie-International Edition* **53**, 11032-11035 (2014).
187. R. T. Sanderson, Electronegativities in inorganic chemistry: (II). *J. Chem. Educ.* **31**, 2 (1954).
188. R. T. Sanderson, An Interpretation of Bond Lengths and a Classification of Bonds. *Science* **114**, 670-672 (1951).
189. R. T. Sanderson, *Chemical bonds and bond energy*. Physical chemistry, a series of monographs (Academic Press, New York, ed. 2d, 1976), pp. xii, 218 p.

190. R. T. Sanderson, *Chemical periodicity*. Reinhold physical and inorganic chemistry textbook series (Reinhold Pub. Corp., New York,, 1960), pp. 330 p.
191. Z. Zhuang, W. Sheng, Y. Yan, Synthesis of Monodispere Au@Co_3O_4 Core-Shell Nanocrystals and Their Enhanced Catalytic Activity for Oxygen Evolution Reaction. *Adv. Mater.* **26**, 3950-3955 (2014).
192. L. Bu *et al.*, Biaxially strained PtPb/Pt core/shell nanoplate boosts oxygen reduction catalysis. *Science* **354**, 1410-1414 (2016).
193. W. Kim *et al.*, Promoting water photooxidation on transparent WO_3 thin films using an alumina overlayer. *Energy & Environmental Science* **6**, 3732-3739 (2013).
194. K. Cho, D. Kwon, M. R. Hoffmann, Electrochemical treatment of human waste coupled with molecular hydrogen production. *Rsc Advances* **4**, 4596-4608 (2014).
195. Y. P. Khalil, Changing Regulations and Energy Costs Impact the Global Chlor-alkali Industry. *Engineering 360*, (2015).
196. M. A. Pellow, C. J. M. Emmott, C. J. Barnhart, S. M. Benson, Hydrogen or batteries for grid storage? A net energy analysis. *Energy & Environmental Science* **8**, 1938-1952 (2015).
197. J. Noh, S. Back, J. Kim, Y. Jung, Active learning with non-ab initio input features toward efficient CO 2 reduction catalysts. *Chemical Science* **9**, 5152-5159 (2018).
198. L. R. Murphy, T. L. Meek, A. L. Allred, L. C. Allen, Evaluation and Test of Pauling's Electronegativity Scale. *The Journal of Physical Chemistry A* **104**, 5867-5871 (2000).
199. J. B. Mann, T. L. Meek, E. T. Knight, J. F. Capitani, L. C. Allen, Configuration Energies of the d-block Elements. *J. Am. Chem. Soc.* **122**, 5132-5137 (2000).
200. L. C. Allen, Electronegativity is the average one-electron energy of the valence-shell electrons in ground-state free atoms. *J. Am. Chem. Soc.* **111**, 9003-9014 (1989).
201. C. C. L. McCrory *et al.*, Benchmarking Hydrogen Evolving Reaction and Oxygen Evolving Reaction Electrocatalysts for Solar Water Splitting Devices. *J. Am. Chem. Soc.* **137**, 4347-4357 (2015).
202. S. Trasatti, Electrocatalysis: understanding the success of DSA®. *Electrochim. Acta* **45**, 2377-2385 (2000).
203. B. R. Chalamala *et al.*, Effect of growth conditions on surface morphology and photoelectric work function characteristics of iridium oxide thin films. *Appl. Phys. Lett.* **74**, 1394-1396 (1999).
204. M. M. Jevtić, E. V. Jelenković, K. Y. Tong, G. K. H. Pang, Noise and structural properties of reactively sputtered RuO_2 thin films. *Thin Solid Films* **496**, 214-220 (2006).
205. F. E. Akkad, S. Joseph, Physicochemical characterization of point defects in fluorine doped tin oxide films. *J. Appl. Phys.* **112**, 023501 (2012).
206. T. Uustare, J. Aarik, A. Aidla, V. Sammelselg, Morphology and structure of TiO_2 thin films grown by atomic layer deposition. *Journal of Crystal Growth* **148**, 268-275 (1995).
207. K. A. Stoerzinger, L. Qiao, M. D. Biegalski, Y. Shao-Horn, Orientation-Dependent Oxygen Evolution Activities of Rutile IrO2 and RuO2. *The Journal of Physical Chemistry Letters* **5**, 1636-1641 (2014).

208. A. J. Medford *et al.*, From the Sabatier principle to a predictive theory of transition-metal heterogeneous catalysis. *J. Catal.* **328**, 36-42 (2015).
209. L. C. Seitz *et al.*, A highly active and stable $IrO_x/SrIrO_3$ catalyst for the oxygen evolution reaction. *Science* **353**, 1011-1014 (2016).
210. J.-M. Hu, J.-Q. Zhang, C.-N. Cao, Oxygen evolution reaction on IrO_2-based DSA® type electrodes: kinetics analysis of Tafel lines and EIS. *International Journal of Hydrogen Energy* **29**, 791-797 (2004).
211. C. C. L. McCrory, S. Jung, J. C. Peters, T. F. Jaramillo, Benchmarking Heterogeneous Electrocatalysts for the Oxygen Evolution Reaction. *Journal of the American Chemical Society* **135**, 16977-16987 (2013).
212. S. Trasatti, Work function, electronegativity, and electrochemical behaviour of metals: II. Potentials of zero charge and "electrochemical" work functions. *Journal of Electroanalytical Chemistry and Interfacial Electrochemistry* **33**, 351-378 (1971).
213. S. Trasatti, Work function, electronegativity, and electrochemical behaviour of metals: III. Electrolytic hydrogen evolution in acid solutions. *Journal of Electroanalytical Chemistry and Interfacial Electrochemistry* **39**, 163-184 (1972).
214. A. N. Frumkin, O. A. Petrii, Potentials of zero total and zero free charge of platinum group metals. *Electrochimica Acta* **20**, 347-359 (1975).
215. F. Werfel, O. Brummer, Corundum Structure Oxides Studied by XPS. *Phys. Scr.* **28**, 92-96 (1983).
216. D. Gonbeau *et al.*, XPS Study of Thin-Films of Titanium Oxysulfides. *Surf. Sci.* **254**, 81-89 (1991).
217. W. G. Pfann, *Zone Melting*. (John Wiley & Sons, Inc. , New York, 1958).
218. .
219. W. Heywang, G. Ziegler, Zur Stabilität senkrechter Schmelzzonen. *Z. Naturforsch., A: Phys. Sci.* **9**, 561-562 (1954).
220. W. Heywang, G. Ziegler, Zur Stabilität senkrechter Schmelzzonen. *Z. Naturforsch., A: Phys. Sci.* **11**, 238 (1956).
221. K. S. Pitzer, G. Mayorga, Thermodynamics of electrolytes. II. Activity and osmotic coefficients for strong electrolytes with one or both ions univalent. *The Journal of Physical Chemistry* **77**, 2300-2308 (1973).
222. S. A. Angus, B; de Reuck, K M, *Chlorine: international thermodynamic tables of the fluid state*. (Elsevier Science, Burlington, MA, 1985), pp. 181.
223. J. Jia *et al.*, Solar water splitting by photovoltaic-electrolysis with a solar-to-hydrogen efficiency over 30%. *Nature Communications* **7**, 13237 (2016).
224. American Public Health Association., American Water Works Association., Water Pollution Control Federation., Water Environment Federation. (American Public Health Association, New York, 1960), pp. volumes.
225. A. Łukomska, J. Sobkowski, Potential of zero charge of monocrystalline copper electrodes in perchlorate solutions. *J. Electroanal. Chem.* **567**, 95-102 (2004).
226. J. E. N. Swallow *et al.*, Self-Compensation in Transparent Conducting F-Doped SnO_2. *Adv. Funct. Mater.*, 1701900-n/a.
227. L. F. Mattheiss, Electronic structure of RuO_2, OsO_2, and IrO_2. *Phys. Rev. B.* **13**, 2433-2450 (1976).

228. A. P. Dementjev *et al.*, Altered Layer as Sensitive Initial Chemical-State Indicator. *J Vac Sci Technol A* **12**, 423-425 (1994).
229. M. V. Kuznetsov, J. F. Zhuravlev, V. A. Gubanov, XPS Analysis of Adsorption of Oxygen Molecules on the Surface of Ti and TiN_x Films in Vacuum. *J. Electron. Spectrosc. Relat. Phenom.* **58**, 169-176 (1992).
230. P. Verena *et al.*, The electronic structure of iridium and its oxides. *Surface and Interface Analysis* **48**, 261-273 (2016).
231. B. V. Crist, *Handbook of monochromatic XPS spectra*. (Wiley, Chichester ; New York, 2000).